Poromechanics and adsorption : application to coal swelling during carbon geological storage

Laurent Brochard

UNIVERSITÉ PARIS-EST

ÉCOLE DOCTORALE SCIENCE INGÉNIERIE ET ENVIRONNEMENT

THÈSE

présentée pour l'obtention du diplôme de

DOCTEUR

DE

L'UNIVERSITÉ PARIS-EST

Spécialité: *Structures et Matériaux*

par

Laurent BROCHARD

Sujet de la thèse :

Poromécanique et adsorption : Application au gonflement du charbon lors du stockage géologique du carbone

Thèse soutenue le 31 octobre 2011 devant le jury composé de :

Rapporteurs :	**Pr. Jan CARMELIET** **Dr. Benoit COASNE**
Examinateurs :	**Pr. Alexander V. NEIMARK** **Dr. Matthieu VANDAMME**
Directeur de thèse :	**Dr. Teddy FEN-CHONG**
Co-directeur de thèse :	**Dr. Roland PELLENQ**

À ma famille & ma femme

À la mémoire d'Olivier Coussy

Remerciements

S'il est une personne à remercier en tout premier lieu, il s'agit d'Olivier Coussy. Olivier fut mon professeur en Master puis mon directeur de thèse. C'est lui qui m'a convaincu de me lancer dans l'aventure de la thèse avec l'enthousiasme qui le caractérisait. Sa disparition tragique en janvier 2010 a laissé un vide pour sa famille, ses amis, ses collègues, ses étudiants et pour moi. Je regrette qu'Olivier ne puisse pas lire cette thèse qui lui tenait particulièrement à cœur. Je me souviens avec quelle passion il savait m'encourager dans mon travail. Il aura été pour moi le meilleur directeur de thèse et je lui en serai toujours reconnaissant.

Je souhaite exprimer toute ma gratitude à Matthieu Vandamme qui m'a encadré au quotidien durant ces trois années. Matthieu, je te remercie pour tout le temps que tu m'a accordé, pour tes conseils, ton soutien sans faille et ta gentillesse. Bien qu'étant ton tout premier doctorant, tu as su m'orienter avec brio. Cette thèse est aussi le fruit de ton investissement personnel pendant ces trois années. Un grand merci à toi! Je remercie également Roland Pellenq, mon co-directeur de thèse, qui m'a suivi malgré la distance. A Paris, Marseille, Boston ou Kobe, il a toujours été possible de trouver un moment pour avancer sur la thèse. Je te remercie pour ton enthousiasme, tes conseils avisés et ta bienveillance. J'adresse mes remerciements à Teddy Fen-Chong qui a assuré la direction de ma thèse après le décès d'Olivier. Ce n'est pas une position facile que d'assurer la direction d'une thèse déjà bien avancée. Je te remercie d'avoir accepté cette responsabilité, pour ton soutien, tes conseils et ta sympathie.

Je remercie l'ensemble des membres de mon jury pour leurs critiques et suggestions constructives: Jan Carmeliet et Benoît Coasne qui ont accepté d'être mes rapporteurs, ainsi que Alexander Neimark qui a bien voulu compléter ce jury. Un merci également à Brice Lecampion qui n'a pas pu participer à ce jury mais a eu la gentillesse de transmettre un rapport à l'attention du jury. J'en profite également pour remercier l'entreprise Schlumberger, pour avoir su titiller la curiosité d'Olivier au sujet du gonflement du charbon. De fil en aiguille c'est devenu un sujet de thèse passionnant aussi bien pour l'enjeu scientifique que sociétal.

Je tiens à remercier Karam Sab ainsi que l'ensemble des membres du laboratoire Navier qui m'a accueilli pendant ces trois années et où j'aurai le plaisir de revenir à l'issu de mon post-doctorat. La liste est longue et je m'excuse par avance pour ceux que j'aurais oubliés. J'ai une pensée particulière pour Nadine Catoire et sa famille suite à la disparition de Claude. Je remercie Jean-François Caron, responsable de l'équipe structure qui m'a accueillie pendant la thèse; ainsi que Michel Bornert et Luc Dormieux, responsables de l'équipe multiéchelle qui m'accueillera à mon retour. Je remercie mes collègues de bureau: Si-Hai, Lina, Pooneh, Fernanda et Rana qui ont su me supporter au quotidien et avec qui j'ai passé des moments inoubliables. Je remercie les 'jeunes' du laboratoire: Mathieu, Wafa, Rabie, Navid, Sahar, Philippe, Haysam, Benoit, Laurent, Achille, Natalia, Florian, Saeid, Grégory; les anciens 'jeunes': Arthur, Sebastien, Salma, Mohammad H., Tiffany, Corinne, Sylvain, Cyril, Siavash, Mohammad M., Irina, Sophie; les 'permanents': Patrick, Adélaïde, Alain

E., François, Robert, Marie-Françoise, Géraldine, Alain T., Jean-Michel, Frédéric, Anaël, Gilles, Boumediene, Olivier, Bruno, Sabine, Denis, Amina, Honoré, Pierre, Gwendal; et tous ceux que je n'ai pas cités mais avec qui j'ai pu partager un déjeuner, enseigner ou discuter autour d'un café. J'ai eu beaucoup de plaisir à vous côtoyer, à découvrir autant de richesse humaine et à nouer des amitiés au delà du cadre professionnel.

Enfin, je remercie du fond du cœur ma femme, ma famille et belle-famille ainsi que l'ensemble de mes amis pour leur soutien, leurs encouragements et leur affection. Vous êtes ce qu'il y a de plus cher dans la vie.

Merci à tous,
Laurent

Abstract

The geological storage of carbon in coal seams is a transitory solution to mitigate climate change. The feasibility of this type of storage at an affordable cost is still uncertain, in particular because the rate of injection of carbon dioxide in coal seams is low. Pilot projects have shown that the permeability of the reservoir decreases during injection, as a consequence of the swelling of the coal matrix induced by the preferential adsorption of carbon dioxide over the methane in place. This PhD thesis is dedicated to the study of this swelling. A first theoretical work consisted in extending the constitutive equations of classical poromechanics to cases for which adsorption on surfaces or in micropores becomes significant. We showed that the poromechanical behavior of the medium can only be determined if the dependence of adsorption on the strain of the porous medium is known. The coupling between adsorption and strain is little studied in the literature and is difficult to measure experimentally. In this work, we used molecular simulations which make it convenient to control independently the bulk pressure of the adsorbed fluid and the strain of the porous medium. By performing molecular simulations of adsorption in model one-dimensional systems, we validated the derived constitutive equations. We also showed that adsorption can depend on the strain of the medium in a complex manner and depends significantly on the structure of the micropores. Based on the simulation results on a realistic molecular model of coal, we concluded that the swelling of coal in presence of fluid can be explained by adsorption in micropores but not by adsorption in mesopores. We studied numerically the coupling between adsorption and strain in coal. The swelling estimated by combining the simulated adsorption isotherms with the derived poromechanical equations compared well with data obtained experimentally. We also simulated adsorption of mixtures of carbon dioxide and methane in coal at temperatures and pressures representative of the underground conditions. The results of those simulations were used to estimate the differential swelling during the injection of carbon dioxide in coal seams at various depths.

Keywords: poromechanics, adsorption, coal swelling, molecular simulation, ECBM, CO_2 storage.

Résumé

Le stockage géologique du carbone dans les veines de charbon est une solution transitoire pour lutter contre le réchauffement climatique. La faisabilité de ce stockage à un coût abordable reste incertaine, en particulier parce que l'injection de dioxyde de carbone dans les veines de charbon est lente. Les projets pilotes ont montré que la perméabilité du réservoir diminue lors de l'injection, suite au gonflement du charbon induit par l'adsorption préférentielle du dioxyde de carbone par rapport au méthane présent naturellement. Ce mémoire de thèse est consacré à l'étude de ce gonflement. Un premier travail théorique a consisté à étendre les équations constitutives de poromécanique classique dans les cas où l'adsorption sur des surfaces ou dans des micropores devient significative. Nous avons montré que le comportement poromécanique du solide ne peut être compris que si la dépendance de l'adsorption en fonction de la déformation du milieu poreux est connue. Le couplage entre adsorption et déformation est peu étudié dans la littérature et difficile à mesurer expérimentalement. Dans ce travail, nous avons utilisé la simulation moléculaire qui permet facilement de contrôler indépendamment la pression du fluide adsorbé et la déformation du milieu poreux. À l'aide de simulations moléculaires d'adsorption dans des systèmes modèles unidimensionnels, nous avons validé les nouvelles équations constitutives. Nous avons montré également que l'adsorption peut dépendre de la déformation de façon complexe et qu'elle est très sensible à la structure des micropores. Les résultats de simulations moléculaires d'adsorption dans un modèle moléculaire réaliste de la matrice organique du charbon nous ont permis de montrer que le gonflement du charbon en présence de fluide peut être expliqué par l'adsorption dans les micropores, mais pas dans les mésopores. Nous avons étudié numériquement le couplage entre adsorption et déformation dans le charbon. Le gonflement estimé en associant les simulations moléculaires d'adsorption aux nouvelles équations constitutives de poromécanique est en bon accord avec les mesures expérimentales. De même, nous avons simulé l'adsorption de mélanges de dioxyde de carbone et de méthane dans le charbon à des températures et pressions représentatives des conditions souterraines. Le résultat de ces simulations a permis d'estimer le gonflement différentiel durant l'injection de carbone pour des veines de charbon à différentes profondeurs.

Mots clefs: poromécanique, adsorption, gonflement du charbon, simulation moléculaire, ECBM, stockage de CO_2.

Résumé long

Afin de lutter contre le réchauffement climatique, un ensemble de solutions sont envisagées permettant de réduire les émissions anthropiques de dioxyde de carbone. Parmi ces solutions, la capture et le stockage géologique du carbone est une technique qui consiste à capturer le dioxyde de carbone d'origine industrielle et à le stocker dans des réservoirs géologiques pendant au moins plusieurs centaines d'années. C'est une solution transitoire permettant aux industries de répartir dans le temps les investissements nécessaires pour se convertir à des modes de production propres. Les veines de charbons sont des sites de stockage possibles, dans lesquels l'injection de dioxyde de carbone s'accompagne d'une production de méthane, naturellement présent dans les veines. Toutefois, la faisabilité à coût abordable de ce type de stockage est incertaine. L'un des principaux problèmes rencontrés lors des projets pilotes est la perte d'injectivité : en l'espace d'une année, la quantité de dioxyde de carbone injectée par unité de temps diminue d'un facteur deux environ, tandis que la pression d'injection est constante. Les veines de charbon sont constituées de roches fracturées et le réseau de fractures assure l'essentiel du transport de fluide. La perte d'injectivité constatée est due à la fermeture des fractures suite au gonflement de la matrice organique du charbon. En effet, la matrice de charbon gonfle deux à trois fois plus lorsqu'elle est immergée dans du dioxyde de carbone que lorsqu'elle est immergée dans du méthane. Ce gonflement est lié au phénomène d'adsorption, c'est à dire à la variation de concentration du fluide près du solide : l'hélium qui n'est pas adsorbé dans le charbon n'induit pas de gonflement ; le méthane est adsorbé modérément et le dioxyde de carbone est fortement adsorbé. Ce travail de thèse a pour objectif l'étude du gonflement du charbon et la mise en place d'un modèle physique de ce gonflement. Comprendre et savoir estimer de gonflement du charbon est crucial pour anticiper correctement le comportement d'un réservoir, pouvoir envisager des solutions au problème d'injectivité, et in fine savoir si le déploiement industriel du stockage de carbone dans les veines de charbon est économiquement possible.

Le phénomène d'adsorption a pour origine les interactions moléculaires entre les molécules du fluide et les atomes du solide. A l'échelle nanométrique, les interactions inter-atomiques et intermoléculaires déterminent entièrement le comportement des atomes et molécules. Chaque particule évolue en fonction de son énergie d'interaction avec les autres particules et le comportement global d'une assemblée de particules est très complexe et dépend d'un grand nombre de degrés de liberté. La physique statistique fournit une description statistique des systèmes atomiques et moléculaires et montre que le comportement macroscopique de ces systèmes ne dépend que de quelques grandeurs macroscopiques. La description macroscopique n'est autre que la thermodynamique classique. La physique statistique établit que les configurations moléculaires accessibles sont distribuées suivant la distribution de probabilité de Boltzmann-Gibbs. D'après cette distribution pour un système à température imposée, une configuration moléculaire est d'autant plus probable que l'énergie d'interaction entre les molécules est basse. Ainsi lorsque des molécules d'un fluide interagissent avec les atomes d'un solide, ces molécules s'arrangent pour minimiser l'énergie d'interaction totale.

Lorsque l'affinité entre le fluide et le solide est grande, l'énergie d'interaction avec le solide est basse et les molécules de fluide se concentrent préférentiellement à l'interface avec le solide. C'est le phénomène d'adsorption.

L'adsorption peut-être simulée numériquement au moyen de simulations moléculaires. Dans cette thèse, nous avons utilisé la méthode dite de Monte Carlo pour simuler l'adsorption. La méthode de Monte Carlo est basée sur l'algorithme de Metropolis qui permet d'échantillonner les configurations moléculaires suivant la distribution de probabilité de Boltzmann-Gibbs. Les simulations de Monte Carlo permettent de simuler des systèmes en équilibre dans différents ensembles statistiques comme par exemple des systèmes ouverts pouvant échanger des particules avec un réservoir extérieur (cas d'un fluide adsorbé). Les résultats d'une simulation moléculaire dépendent entièrement des énergies d'interaction entre les particules. Dès lors, la validité d'une simulation moléculaire dépend de la pertinence des potentiels effectifs utilisés pour représenter les interactions. Pour l'adsorption de méthane et de dioxyde de carbone dans le charbon, les interactions en jeu sont : la répulsion stérique, la liaison chimique, les interactions électrostatiques, et les forces de dispersion de London. Ces interactions sont représentées avec des potentiels effectifs, comme le potentiel de Lennard-Jones pour la répulsion stérique et les forces de dispersion, ou des charges ponctuelles pour les interactions électrostatiques.

A l'échelle macroscopique, l'adsorption est caractérisée par la quantité adsorbée. Les modèles d'adsorption classiques relient la quantité adsorbée à la pression du fluide. Les modèles de Langmuir et de BET pour l'adsorption sur des surfaces et le modèle de Dubinin-Radushkevich pour l'adsorption dans des micropores sont souvent utilisés pour interpréter les isothermes mesurés expérimentalement. Ces modèles classiques ne tiennent pas compte de la déformation du solide induite par l'adsorption. Pourtant, au-delà du charbon, de nombreux solides poreux se déforment en raison de l'adsorption : le bois, les argiles, les solides hybrides poreux... L'adsorption induit bien des contraintes mécaniques. Pour une adsorption sur une surface, l'adsorption modifie la contrainte de surface à l'interface entre le fluide et le solide. Lorsque les couches adsorbées de deux interfaces distinctes se recouvrent l'adsorption induit également une contrainte normale aux interfaces. Pour des pores plans, cette contrainte orthogonale est la pression de disjonction. Les notions de contrainte de surface et de pression de disjonction ne sont pas suffisantes pour traiter le cas de l'adsorption dans le charbon. En effet, la matrice organique du charbon contient des micropores de morphologie complexe. A l'échelle moléculaire, l'équation du viriel permet de relier la contrainte macroscopique aux interactions entre particules, et d'interpréter les notions de contrainte de surface et de pression de disjonction. Si l'équation du viriel permet de calculer la contrainte dans un système moléculaire, cette équation reste focalisée sur les molécules une à une et ne permet pas de relier adsorption macroscopique et déformation macroscopique et de comprendre par exemple pourquoi le charbon gonfle.

Dans la littérature il existe des modèles de déformation induite par l'adsorption. La majeure partie de ces modèles s'appuient sur les notions de contrainte de surface ou de pression de disjonction et ainsi sont valables pour des solides mésoporeux ou bien des micropores plans, respectivement. Quelques modèles cependant traitent des micropores non plans. Toutefois, les cas étudiés avec ces modèles diffèrent de celui du charbon : squelette solide incompressible, système à états de déformation discrets ou encore solide en immersion dans un fluide. Dans cette thèse, l'objectif est de mettre en place un cadre théorique qui couple mécanique et adsorption et puisse être appliqué au cas du stockage de carbone dans du charbon.

Dans ce travail de thèse, nous nous sommes appuyés sur la poromécanique classique, dont les équations constitutives sont utilisées habituellement pour l'étude des réservoirs géotechniques. Un

premier travail théorique a consisté à étendre les équations constitutives de la poromécanique classique à l'adsorption sur des surfaces et dans des micropores quelconques. D'après la poromécanique classique, un solide poreux immergé dans un fluide se contracte proportionnellement à la pression, indépendamment de la composition du fluide. En revanche, d'après les équations constitutives étendues à l'adsorption, le milieu peut aussi bien se contracter que gonfler et le comportement mécanique dépend de la nature du fluide. Ainsi, alors que le gonflement du charbon immergé dans différents fluides n'est pas compatible avec les équations de poromécanique classique, ce gonflement peut théoriquement être expliqué par les équations étendues à l'adsorption. Quelques calculs d'ordre de grandeur permettent de montrer que la déformation induite par l'adsorption de surface dans un solide mésoporeux n'est véritablement significative que pour des solides particulièrement souples avec une grande surface spécifique. Dans le cas du charbon, seule l'adsorption dans les micropores est à même d'induire les gonflements observés expérimentalement. D'après les nouvelles équations constitutives, la relation entre adsorption et mécanique est une relation intégrale complexe. L'effet mécanique de l'adsorption ne peut être compris que si le comportement de l'adsorption en fonction de la déformation et des potentiels chimiques des composants du fluide est connu. Cependant, quelques comportements simples peuvent être décrits: Si l'adsorption est une fonction croissante de la déformation, le fluide induit un effet de disjonction qui tend à faire gonfler le milieu poreux. A l'inverse, si l'adsorption est une fonction décroissante de la déformation, le fluide induit un effet de jonction qui tend à contracter le milieu poreux. Cependant, comment l'adsorption dépend de la déformation est peu étudié dans la littérature et cette dépendance est difficile à mesurer expérimentalement. Dans cette thèse, nous avons utilisé la simulation moléculaire qui est une technique intéressante complémentaire des expériences de laboratoire permettant de contrôler indépendamment la pression du fluide adsorbé et la déformation du milieu poreux.

Une première série de simulations moléculaires a été réalisée pour étudier des systèmes modèles : des solide microporeux unidimensionnels dans lesquels un fluide de Lennard-Jones est adsorbé. Ces systèmes modèles peuvent être simulés rapidement avec une grande précision et permettent de se faire une première idée du couplage entre adsorption et déformation. Un premier solide unidimensionnel est étudié, dans lequel tous les micropores sont identiques. Pour ce solide, le couplage entre adsorption et déformation est complexe et difficile à modéliser analytiquement. Ce comportement complexe peut être expliqué qualitativement par la commensurabilité de la taille des pores à la taille des molécules de fluide. Les contraintes induites par l'adsorption sont également complexes. Suivant les conditions de pression et de déformation, le fluide induit un effet de disjonction ou de jonction. Malgré ce comportement complexe, les contraintes estimées à partir des équations poromécaniques étendues à l'adsorption sont en parfait accord avec les contraintes mesurées avec l'équation du viriel validant ainsi les nouvelles équations constitutives. Un second solide unidimensionnel est étudié, dans lequel les micropores sont de tailles aléatoires. Pour ce second solide, l'adsorption dépend linéairement de la déformation et induit un effet de disjonction indépendant de la déformation. Une étude détaillée permet de mettre en évidence que les micropores ont des déformations locales complexes en fonction de leur commensurabilité aux molécules de fluide, mais le comportement macroscopique qui résulte de la combinaison de tous ces comportements microscopiques est relativement simple. Par ailleurs, les pores les plus petits ne pouvant accueillir qu'une seule molécule de fluide jouent un rôle prédominant dans le comportement macroscopique et permettent de comprendre pourquoi le fluide induit un effet macroscopique de disjonction.

Afin d'utiliser les équations poromécaniques dans le cas du charbon, des simulations moléculaires d'adsorption de méthane et de dioxyde de carbone dans un modèle moléculaire représentatif de la matrice organique du charbon sont réalisées. Toutefois le charbon n'est pas un matériau de

structure et de composition bien précise, mais une famille de matériaux caractérisés par une teneur massique en carbone importante. Aussi la modélisation moléculaire mise en place ne peut être représentative de toutes les variétés de charbon, mais elle donne une première idée du couplage entre adsorption et déformation. Les résultats d'adsorption de méthane pur et de dioxyde de carbone pur sont comparés à des isothermes expérimentales. Cette comparaison a permis de confirmer la validité de la modélisation moléculaire mise en place et de montrer que l'essentiel de l'adsorption dans les charbons a lieu dans les micropores, l'adsorption à la surface des mésopores étant négligeable. Le couplage entre adsorption et déformation est étudié par simulation moléculaire et conclut à un comportement linéaire pour des déformations positives. La matrice organique du charbon étant quasi-amorphe, ce résultat est cohérent avec les résultats obtenus avec les systèmes modèles unidimensionnels. Une analyse inverse d'expériences d'immersion où sont mesurés à la fois les quantités adsorbées et le gonflement confirme le résultat des simulations moléculaires. Une particularité apparait cependant dans le cas de l'adsorption de dioxyde de carbone lorsque les conditions de température et de pression sont proches des conditions du point critique. L'agrégation des molécules de dioxyde de carbone dans ces conditions pourrait expliquer la particularité observée.

Le gonflement induit par l'adsorption calculé à partir des équations constitutives de poromécanique étendue à l'adsorption et des quantités adsorbées issues des simulations moléculaires sont en bon accord avec les gonflements mesurés expérimentalement. Ainsi l'approche mise en place dans cette thèse fournit une estimation satisfaisante du comportement mécanique du charbon sous adsorption de méthane et de dioxyde de carbone. La même démarche est mise en œuvre pour estimer le gonflement différentiel induit lors d'une opération de stockage de carbone: l'adsorption de mélanges de méthane et de dioxyde de carbone à des températures et pressions représentatives des conditions souterraines est estimée par simulation moléculaire. Les résultats de simulations, associés aux nouvelles équations poromécaniques nous ont permis d'estimer le gonflement différentiel du charbon lors du remplacement progressif du méthane par du dioxyde de carbone pour des sites de stockage de carbone situés à différentes profondeurs. Cette approche en soi n'est pas suffisante pour modéliser le comportement d'un réservoir dans son ensemble, mais constitue l'élément central indispensable à une telle modélisation.

Contents

List of Figures

List of Tables

Chapter 1

Introduction

THIS CHAPTER *presents the industrial context of this thesis. In order to mitigate climate change, the geological storage of carbon is a transitory solution to reduce the anthropic emissions of carbon dioxide. Large amounts of carbon dioxide can be stored in oil and/or gas fields, in saline aquifers and in coal seams by using conventional techniques of the oil industry. However, industrial application of carbon storage requires developing appropriate financing mechanisms and ensuring the sequestration of carbon for hundreds of years. This latter objective can only be reached by better understanding the physical processes at stake. In this thesis, we focus on the case of carbon storage in coal seams, for which the feasibility at affordable cost is still to be proved. Coal seams are non-conventional reservoirs of methane. The storage of carbon dioxide in these reservoirs enhances the recovery of methane, which is an additional benefit of this type of carbon storage. One of the main issues encountered with this type of storage is the loss of permeability of the reservoir during the injection of carbon dioxide. In a coal seam, the natural fractures in the rocks are responsible for most of the transport properties of the rock. The loss of permeability observed in-situ is due to the closure of those fractures, which itself is a consequence of the swelling of the coal matrix during the injection. Indeed, the porous coal matrix swells two to three times as much in presence of carbon dioxide as in presence of methane. The swelling of coal is attributed to an adsorption of fluid. The objective of this thesis is to understand how adsorption in a porous medium can induce strain and to propose an adsorption-induced strain model applicable to the case of carbon storage in coal seams.*

Ce chapitre *présente le contexte industriel de ce travail de thèse. Afin de lutter contre le changement climatique, la séquestration géologique du carbone est une solution transitoire permettant de réduire les émissions anthropiques de dioxyde de carbone. Le carbone peut-être stocké en quantités suffisantes dans des puits de pétrole et/ou de gaz, dans des aquifères salins et dans des veines de charbon à l'aide des techniques usuelles d'exploitation pétrolière. Toutefois, le déploiement industriel de la séquestration du carbone nécessite de mettre en place des mécanismes de financement adéquats et de pouvoir assurer la séquestration pendant des centaines d'années. Assurer la séquestration sur le long terme nécessite une meilleure compréhension des phénomènes physiques en jeu. Dans cette thèse, nous nous intéressons au cas du stockage dans les veines de charbon, dont la faisabilité à un coût abordable reste à démontrer. Les veines de charbon sont des réservoirs non conventionnels de méthane. Le stockage de carbone dans ces réservoirs permet d'améliorer la récupération de méthane, ce qui constitue un intérêt supplémentaire pour ce type de stockage de carbone. L'un des principaux problèmes rencontrés par ce type de stockage est la perte de perméabilité du réservoir lors de l'injection de dioxyde de carbone. Dans une veine de charbon le transport de fluide est assuré principalement par les fractures naturellement présentes dans la roche. La perte de perméabilité observée in-situ est due à la fermeture de ces fractures lors de l'injection de dioxyde de carbone, suite au gonflement du charbon durant l'injection. En effet, la matrice poreuse du charbon gonfle deux à trois fois plus en présence de dioxyde de carbone qu'en présence de méthane. Le gonflement du charbon est attribué à l'adsorption de fluide. L'objet de cette thèse est de comprendre comment l'adsorption dans un milieu poreux induit une déformation et de proposer un modèle applicable au cas du stockage de carbone dans les veines de charbon.*

Outline of Chapter 1

1.1 Carbon capture and storage

1.1.1 Overview

The fossil fuels are the main source of energy for mankind: they represent 81% of the total primary energy supply worlwide[1]; the conversion to alternative carbon-free sources of energy is going to last for decades. Developed countries have set quantitative objectives for the development of renewable energies. For instance, the directive on renewable energy[2] in the European Union has set an objective of 20% of renewable energy in the total energy consumption in 2020. But electricity obtained from solar and off-shore wind energies is two to three times as expensive as electricity obtained from burning coal (DOE/EIA, 2010) and can only be produced intermittently; on-shore wind energy, hydroelectricity and geothermal energy are limited in terms of capacity; nuclear energy faces risks and waste management issues. Though in decline, the known reserves of fossil fuels, especially of coal, remain important: according to the Organisation for Economic Co-operation and Development (OECD, 2008), *"the estimates of world reserves life expectancies – at growth rate in primary production varying between 0% and 5% – are roughly of 216 to 49 years for coal"*. Moreover, electricity can be produced from coal steadily. Therefore, although the International Panel on Climate Change (IPCC) recommends limiting the carbon dioxide emissions as soon as possible (Bernstein et al., 2007), it is very likely that developing countries with large reserves of coal, such as China, will go on consuming coal. Without any mitigation policy, five emission scenarios of the IPCC out of six lead to a global warming larger than 2°C in 2100. *"Mitigation efforts and investments over the next two to three decades will have a large impact on opportunities to achieve lower stabilization levels."* A transitory solution to avoid excessive emissions of carbon dioxide is Carbon Capture and Storage (CCS).

Carbon Capture and Storage consists in separating carbon dioxide (CO_2) from the flue gas of industrial sources and in transporting it to a storage site, where carbon dioxide must remain isolated from the atmosphere for at least several hundred years (Metz et al., 2005). The purpose of long term sequestration is to limit the anthropic emissions of carbon dioxide and thus to avoid an excessive climate change. We display in Figure 1.1 a schematic representation of CCS. Fossil fuel power-plants and heavy industries are concentrated sources of carbon dioxide, while the transport sector, housing and office buildings lead to distributed emissions. The concentrated sources can be equipped to separate carbon dioxide from the other gases produced. This carbon dioxide can then be transported to storage sites through a network of pipelines and/or tankers. Storage sites can be geological formations, oceans deeper than 1000 m, or carbonation plants in which CO_2 is transformed into solid inorganic carbonate. Storage in oceans modifies the ocean chemistry in the region of injection, and the ecological impact of this storage is very uncertain (Seibel and Walsh, 2001). Regarding mineral carbonation, the chemical process requires as much alkaline oxides (such as calcium oxide) as the amount of CO_2 to be stored: this oxide must be mined on large scale surface operations. Moreover, CO_2 storage by carbonation would consume 30 to 50% of the energy output of a power plant whose flue gas would be treated, thus leading to a storage cost ranging from 50 to 100$ per ton of CO_2 avoided[3] (tCO_2). By contrast, geological storage is inexpensive with a storage cost lower than 10$/$tCO_2$. Moreover, such a storage does not require additional

[1] Source: International Energy Agency, world statistics for 2008 – http://www.iea.org

[2] Directive 2009/28/EC of the European Parliament and of the Council of 23 April 2009 on the promotion of the use of energy from renewable sources

[3] The cost 'per ton of CO_2 avoided' is the ratio between the total cost of a project and the amount of CO_2 that will not be emitted thanks to the project. Since the compression and the injection of CO_2 consumes energy and therefore emits CO_2, the amount of stored CO_2 is larger than the amount of CO_2 avoided.

resources on top of appropriate underground space, and its ecological impact is limited because of the depth of the sites considered, provided the integrity of the reservoir is maintained. Accordingly, the geological storage is the only storage which is already experimented on industrial scales. In April 2011, there were twenty-four geological storage demonstration projects in operation[4], out of which nine were large scale projects injecting more than 500 thousand tons of CO_2 per year. Three types of geological formations are considered for CO_2 storage:

Oil and gas reservoirs enable to store CO_2 with limited risks of leakage since they hold or have previously held fluids, which proves that these reservoirs are well sealed. Moreover, the injection of CO_2 enhances the recovery of gas and oil from the reservoir, thus improving the profitability of such storage sites.

Deep saline aquifers are reservoirs of water saturated with salt that are disconnected from shallower reservoirs of freshwater. These reservoirs offer a very large storage capacity and are well distributed around the world.

Unminable coal beds are unconventional reservoirs of natural gas. Storage of carbon dioxide in coal seams enhances the recovery of natural gas. This technique is called 'Enhanced Coal Bed Methane' (ECBM) recovery. In this work we study this last type of storage.

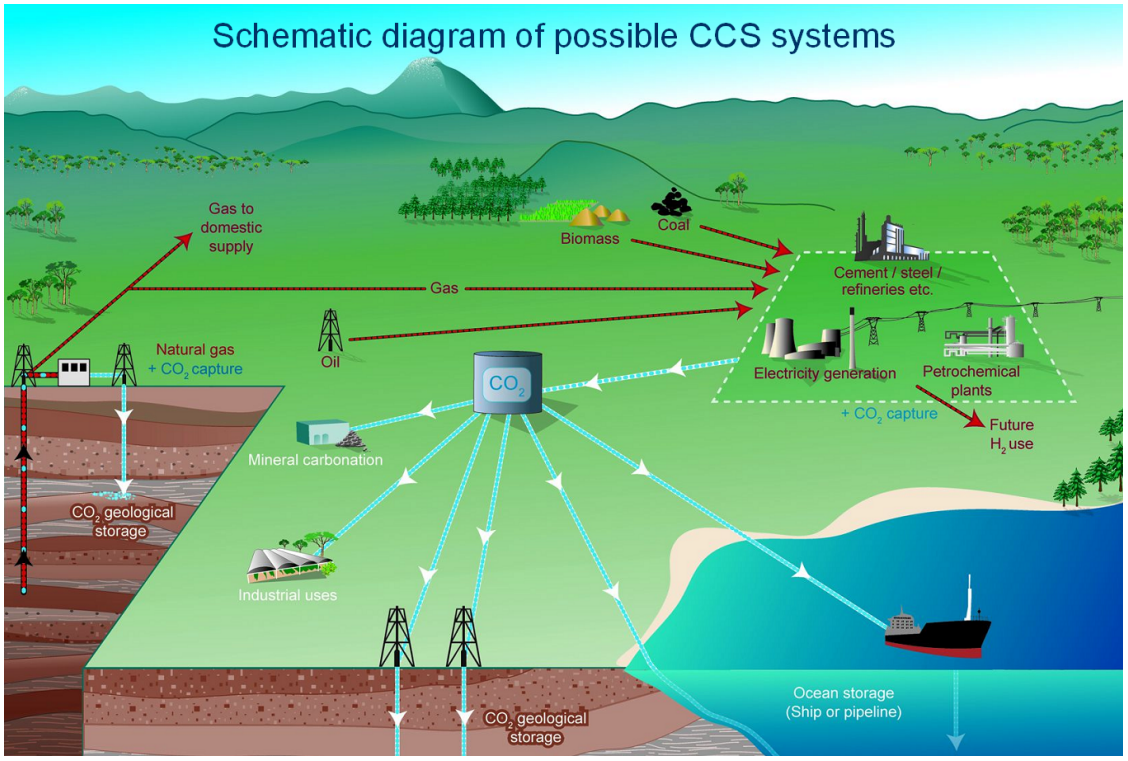

FIGURE 1.1. *Overview of the possible Carbon Capture and Storage systems. Credit: special report on CCS of the International Panel on Climate Change, Fig. TS.1 (Metz et al., 2005).*

CCS is expected to contribute significantly to the global effort to mitigate climate change. The special report on CCS of the IPCC (Metz et al., 2005) investigated several scenarios to mitigate climate change, in which the contribution of CCS ranged from 15% to 55% of the cumulative mitigation effort in 2100. The International Energy Agency (IEA) estimates that CCS should

[4]International Energy Agency Greenhouse Gas R&D Programme – http://www.ieaghg.org

contribute about 15% to 20% of the total greenhouse gas emissions reductions in 2050 (IEA, 2008). There are different reasons for this significant contribution: the inertia of industry to adopt carbon-free solutions, the global capacity of geological sites to store CO_2, and the fact that the technologies required for CCS are readily available.

The conversion of the current economies to carbon-free energies requires huge investments. Carbon capture and storage can help streamlining the existing industrial base and spreading over time the investments in new carbon-free power plants and industries. Thus CCS is a transitory cost-effective solution that can help achieving greenhouse gas concentration stabilization. IPCC estimates that including CCS in a mitigation portfolio would reduce the cost of stabilizing CO_2 concentration by 30% (Metz et al., 2005). According to the IEA, *"without CCS, overall costs to halve emissions by 2050 rise by* 70%*"* (IEA, 2010).

The global capacity of geological formations to store carbon dioxide is large compared to the cumulated anthropic emissions of carbon dioxide. The estimates of capacity (Metz et al., 2005) range from 1700 Gt of CO_2 to more than 10000 Gt of CO_2, the former corresponding to about 50 years of CO_2 emissions at the current rate of emission (Bernstein et al., 2007). For cost reasons, the distance between the emission sites and the storage sites may determine whether CCS will be developed. The potential sites of injection are distributed in sedimentary basins over all continents, and major sources and prospective sites are separated by distances lower than 300 km (Metz et al., 2005).

The technology needed to perform geological storage is similar to the technology used in the petroleum industry. Enhanced Oil Recovery (EOR), which consists in injecting fluids in geological formations in order to improve the recovery of oil, has been used since the 1970's. Carbon dioxide is one of the fluids injected in EOR because it is a good solvent for oil. Therefore, there is no major technological hurdle to the development of geological storage of carbon dioxide.

1.1.2 Issues

Even if geological storage appears as necessary to mitigate global warming, there remain important questions regarding the environmental impact, the scientific understanding, the social acceptability and the financing of the projects. We address in this section some of the main issues.

One issue with geological storage is the long term stability of the sequestered carbon dioxide. In order to mitigate global warming, CO_2 must remain isolated from the atmosphere for a period of time much longer than the characteristic time of climate change. The characteristic time of climate change due to CO_2 emissions is about a century (Bernstein et al., 2007). Accordingly, carbon storage must prevent any release of the sequestered carbon before at least a few centuries. According to IPCC, *"a fraction retained on the order of* $90-99\%$ *for 100 years or* $60-95\%$ *for 500 years could still make [...] impermanent storage valuable for the mitigation of climate change"*. The current projects of geological storage aim at storing carbon dioxide over thousands of years. From the engineering point of view, the selection of an appropriate injection site, the use of well-tested sealing and a proper monitoring should reduce the risk of any large release. For instance, any injection site should be located under a cap rock with very low permeability; any wellbore to the surface should be sealed with materials that would keep their integrity for centuries while exposed to carbon dioxide; any fault through which CO_2 might escape should be monitored and any release should be dealt with carefully to avoid any impact on the ecosystems and populations. Figure 1.2 illustrates the different leakage scenarios in the case of geological storage in saline aquifers, and

the remediation techniques for each scenario. The hazard on health and ecosystems posed by a potential leak of CO_2 from an injection site is a concern for the public.

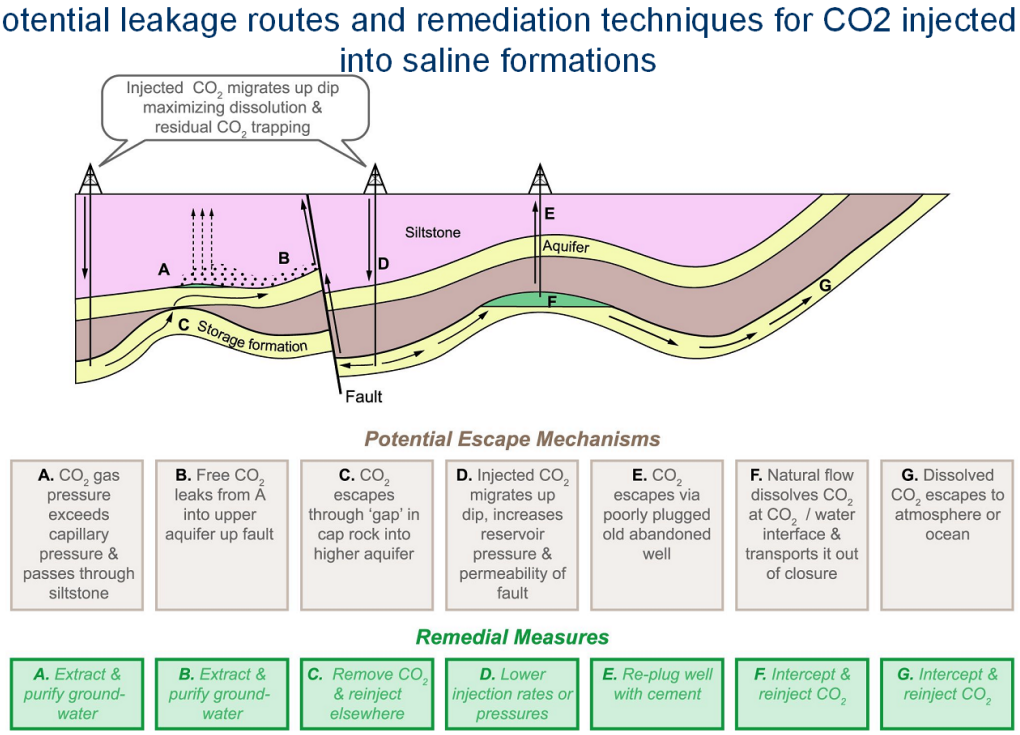

FIGURE 1.2. *Potential leakage routes for geological storage in saline aquifers. Credit: special report on CCS of the International Panel on Climate Change, Fig. TS.8 (Metz et al., 2005).*

A second issue is the potential alteration of the underground environment due to the presence of CO_2. Several alterations have been identified (Gaus, 2010, André et al., 2010), which affect the physical parameters (such as porosity, permeability, mechanical strength) of the rocks:

Acid-induced reactions: CO_2 dissolves in water and forms carbonic acid which lowers the pH. This acidification can induce chemical reactions such as dissolution of carbonates (Bemer and Lombard, 2010), clays and feldspars but also formation of gypsum or of secondary carbonates which are a mineral trapping of CO_2. Carbonation of calcium silicate hydrates, the main component of cement paste is also an issue since cement is used to seal the wellbores after injection.

Reactions due to brine concentration: The water in place in the host rock is brine, i.e., water saturated or nearly saturated with salt. CO_2 is not miscible with water, but, during the injection process, some of the water molecules dissolve in the pure CO_2. Such a dissolution leads to an increase in the salt concentration in the brine, which eventually makes the salt crystallize. When crystallized salt accumulates in the porous space, the permeability of the host rock is modified (Pruess and Müller, 2009, Pruess, 2009).

Clay desiccation: The injection of CO_2 may remove water from the cap rock and therefore dry the rock. Clay may shrink in such conditions: such a phenomenon, known as dessication in soil mechanics, may open transport pathways through the cap rock, thus leading to a leakage of carbon dioxide (Botan et al., 2010).

Reaction with pure CO_2: Pure CO_2 can also trigger chemical reactions with rocks: carbonation of cement, reaction of water dissolved in CO_2 with iron and silicate minerals, and so on...

Coal swelling: The injection of carbon dioxide in coal makes the coal matrix swell, which reduces the permeability of the coal bed. In this work we focus on the swelling of coal induced by an injection of carbon dioxide.

Understanding all these alterations and how they affect the transport properties and storage capacity of rocks is central for field application of CCS. The economical analysis of CCS projects is based on estimations of storage capacities and of evolution of injection rates over the injection process. Moreover, a better understanding of the alterations can also help to assess the risk of leakage and the risk of contamination of subsurface ecosystems, thus favoring the social acceptability of CCS projects.

A third issue with CCS is the financing of the projects. Indeed, CCS is quite expensive. The most recent greenhouse gas abatement cost estimates published by McKinsey&Company (2010) and Bloomberg (2010) show that the average total cost of CCS is about 50$ per ton of CO_2 avoided whereas other options for reducing CO_2 emissions can be achieved at no expense or with benefit, for instance by increasing the energy efficiency or by recycling wastes. Therefore, as long as CO_2 emissions will not be taxed, it is likely that CCS will not develop, except in very specific enhanced oil recovery projects, for which CCS can be profitable. Nevertheless, combining all solutions that are profitable under today regulation is not enough to mitigate climate change. Profitable solutions are limited to a total reduction of 12 Gt of CO_2 per year in 2030, which is three times as low as the reduction needed to limit the global warming to less than 2°C in 2100 (McKinsey&Company, 2010). As first attempt to regulate the CO_2 emissions, the European Union has established a system of CO_2 quotas for heavy industries which can exchange emission permits on a CO_2 market[5]. Today the emissions permits cost about 13$/t$CO_2$, which is too low to lead to a significant development of CCS projects. From 2013 to 2020, the allocated quotas should be reduced gradually, which could lead to an increase in the price of the emission permits.

1.2 Carbon dioxide storage in coal seams

1.2.1 Overview

The present work focuses on geological storage of carbon dioxide in unminable coal seams. Coal seams are natural deposits of methane and the injection of carbon dioxide is a technique that improves the production of natural gas from such reservoirs. Such a technique is known as enhanced coal bed methane recovery (ECBM). The concept of ECBM dates back to the 1970's: at that time the only purpose of injecting carbon dioxide was to increase the production of natural gas from unconventional deposits; the carbon dioxide was considered as an expense (White et al., 2005). Today, with increasing concerns regarding global warming, storing carbon dioxide has become as important as producing natural gas.

A coal seam is considered *unminable* if it is unlikely to be ever mined because of unfavorable quality, market prices, mining costs, location, and/or transportation infrastructure. Table 1.1 presents criteria in terms of site depth, bed thickness and coal rank which the US Energy Institute Agency uses to determine whether a coal resource is recoverable (EIA, 1996). Only a fraction of

[5]European Union Emissions Trading System - http://ec.europa.eu/clima/policies/ets/index_en.htm

the existing coal resources is recoverable. For instance it is estimated that only 15% of the coal in the United States can be recovered (WEC, 2010). Therefore a significant amount of coal reservoirs is available for ECBM. The worldwide storage capacity of CO_2 in coal is theoretically estimated to 360 Gt when assuming 6000 Gt of unminable coal in the world and a storage capacity of 0.06 tCO_2 per ton of coal (White et al., 2005). Practically however, the storage capacity of CO_2 in coal seams is estimated between 3 and 200 Gt (Metz et al., 2005). The discrepancy between those two estimates is due to high uncertainties regarding the technical and economical feasibility of ECBM: unlike enhanced oil recovery and injection in saline aquifers, for which carbon sequestration is already operational, the feasibility of ECBM at affordable prices is still uncertain. Gale and Freund (2001) quantified the economic potential of ECBM: *"5 to 15 Gt of carbon dioxide could conceivably be sequestered at a net profit, while about 60 Gt of sequestration capacity may be available at moderate costs of under \$50/t CO_2"*.

Rank and thickness (cm) →		Anthracite and bituminous coal			
		< 36	36 to 71	71 to 107	> 107
		subbituminous coal and lignite			
Mining method and depth (m) ↓		< 76	76 to 152	152 to 305	> 120
Surface	0 to 61	7%	20%	100%	100%
Underground	61 to 305	0%	0%	100%	100%
	305 to 609	0%	0%	3%	5%
	609 to 914	0%	0%	0%	2%

TABLE 1.1. *Recoverability of coal resources in function of the site depth, the bed thickness and the coal rank (adapted from EIA (1996)). Coal is likely to be recoverable if the site is shallow, the bed thick and the rank high.*

Twelve injection pilots over the world have experimented ECBM in situ (see Tab. 1.2), but only small quantities of CO_2 have been injected: the largest pilot, the Allison Unit, has injected less than 50 $ktCO_2$ per year, whereas an injection site at the industrial scale is expected to store 1000 $ktCO_2$ per year. ECBM is not yet a mature technology: all these in situ experiments aim at improving the scientific knowledge and at determining in what conditions ECBM is feasible. The number of pilots has dramatically increased in the last five years, demonstrating the interest for this type of storage.

Figure 1.3 sketches an injection of CO_2 in a coal seam. Usually, CO_2 is sequestered in geological sites deeper than 800 m because at those depths the bulk density of CO_2 is that of a liquid: thus a large amount of carbon dioxide can be stored in a small volume. For carbon sequestration in coal seams however, carbon dioxide is stored directly in the coal matrix and experiments show that the maximum storage capacity of CO_2 in this coal matrix is reached for bulk pressures of CO_2 as low as 3 MPa. For this reason the storage in coal is considered for sites as shallow as 300 m (White et al., 2005). Coal seams deeper than 1500 m are not considered for ECBM, because the permeability of such seams is very low, which impedes the fluid transfer for CCS applications.

Carbon dioxide and methane are both stored in the coal matrix, but the affinity of carbon dioxide for coal is greater than that of methane: when immersed in a fluid mixture made of equal amounts of carbon dioxide and methane, at least twice as many molecules of carbon dioxide as of methane are stored in the coal matrix (Ottiger et al., 2008). That is why the injection of carbon dioxide in coal seams improves the recovery of methane.

The affinity of carbon dioxide for coal is also greater than that of nitrogen. An option for CCS would be to use the coal seam as both a storage site and a separation system: the industrial flue

Project name	Location	Year of first injection	Total amount of injected CO_2 (t)
Allison Unit[a]	San Juan Basin, New Mexico, USA	1995	277000
Fenn[b]	Fenn/Big Valley, Alberta, Canada	1998	200
RECOPOL[c]	Kaniow, Poland	2004	760
Qinshui[d]	Qinshui Basin, China	2004	192
CSEMP[e]	Alberta, Canada	2005	10
Ybari	Ishikari Coal Basin, Hokkaido, Japan	2007	884
MGSC ECBM[f]	Wabash County, Illinois, USA	2007	91
SWP San Juan[g]	Navajo City, New Mexico, USA	2008	68000
PCOR Lignite[h]	Burke County, North Dakota, USA	2009	82
Black Warrior	Tuscaloosa County, Alabama, USA	2009	907
SECARB Central Appalachian[i]	Russell County, West Virginia, USA	2009	907
DOE West Virginia[j]	Marshall County, West Virginia, USA	2009	18000

Table 1.2. *ECBM injection pilots. Source: Cooperative Research Centre for Greenhouse Gas Technologies*[l].

[a] http://www.coal-seq.com/
[b] http://uregina.ca/ghgt7/PDF/papers/peer/039.pdf
[c] http://recopol.nitg.tno.nl/
[d] http://belfercenter.ksg.harvard.edu/files/21-jianping_ye.pdf
[e] http://www.co2storage.org//Overviews/Alberta{%}20ECBM{%}201996-2009{%}20summary.pdf
[f] http://www.sequestration.org/
[g] http://southwestcarbonpartnership.org/
[h] http://www.undeerc.org/PCOR/
[i] http://www.energy.vt.edu/secarb/index.asp
[j] http://fossil.energy.gov/news/techlines/2009/09063-First-of-a-Kind_Sequestration_Fiel.html
[k] http://www.co2crc.com.au
[l] http://www.co2crc.com.au

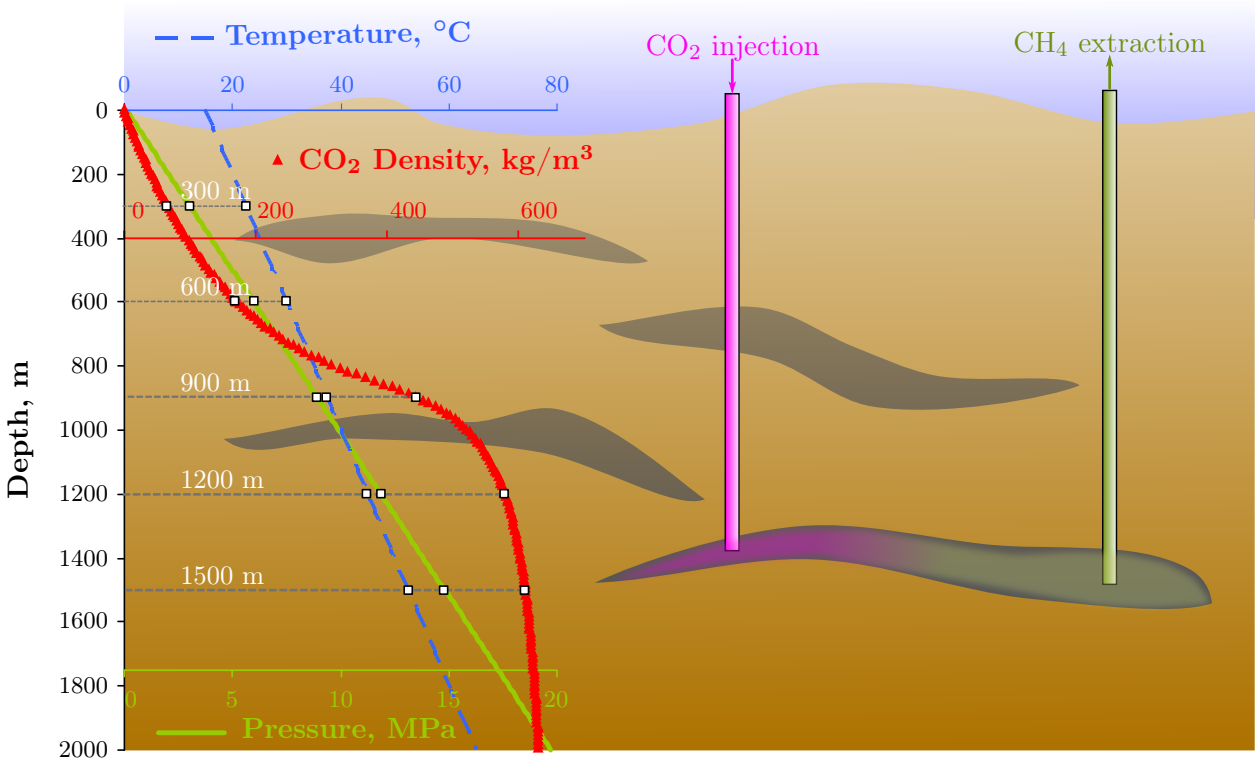

FIGURE 1.3. *Coal bed methane recovery enhanced by carbon dioxide injection. The temperature and pressure conditions are obtained by considering a geothermal gradient of* $25°C/km$ *with a surface temperature of* $15°C$ *and a hydrostatic pressure gradient with the water density* $\rho_{H_2O} = 1000\ kg/m^3$*, the Earth gravitation field* $g = 9.81\ m.s^{-2}$ *and a surface pressure of* $101325\ Pa$*. The density of carbon dioxide was computed with the experimental equation of state of Span and Wagner (2003b).*

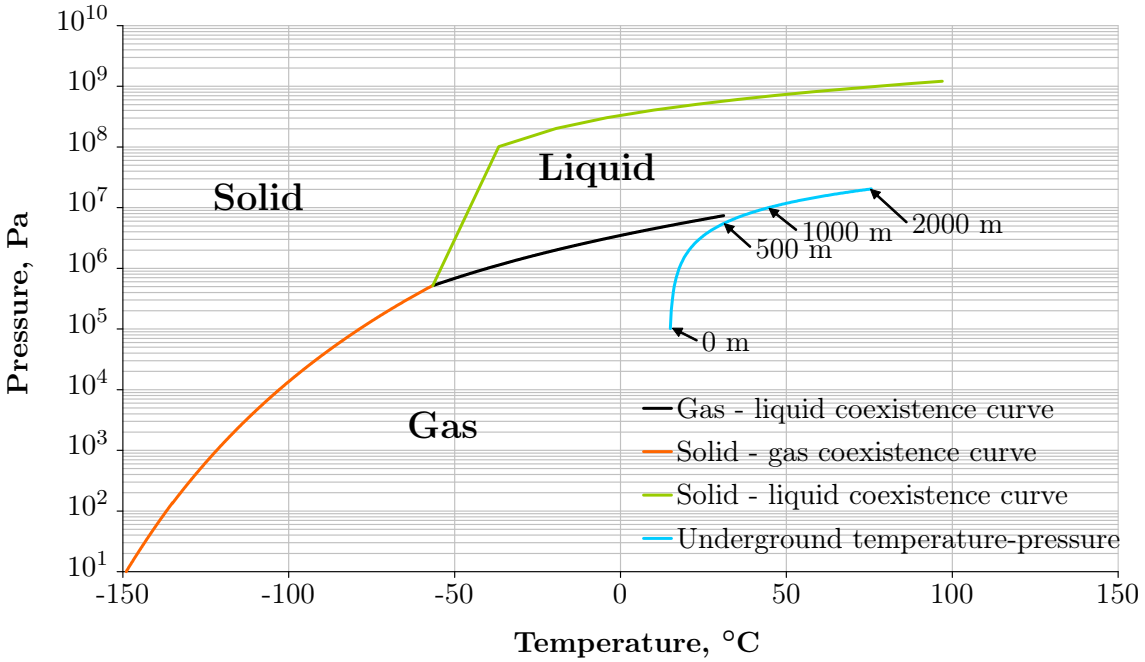

FIGURE 1.4. *Temperature-pressure phase diagram of carbon dioxide, and underground conditions. The coexistence curves are from Washburn (1933).*

gas, made of roughly 80% nitrogen and 20% carbon dioxide (in molar content) could be injected in the coal bed without prior separation. Because of its higher affinity for coal, carbon dioxide would remove the methane initially in place, which would be recovered along with nitrogen. This technique is called 'flue gas-ECBM', by opposition to 'CO_2-ECBM' in which only pure CO_2 is injected. The major interest of flue gas-ECBM is economical: the capture of CO_2 from the flue gas is the most expensive process in CCS (White et al., 2005, Mazzotti et al., 2009).

1.2.2 Issues

The feasibility of ECBM is uncertain because of several issues: the permeability of the reservoir, the evolutions of the permeability over the injection process, and the risks of leakage.

The most important issue is the permeability of the coal reservoirs. For the selection of a storage site, permeability is a critical parameter. According to Christensen and Holloway (2004), a permeability of 1 mD is necessary for ECBM to be affordable, which is only verified for a fraction of reservoirs. The permeability of coal reservoirs varies widely from site to site: it is on the order of 1 μD $= 10^{-18}$ m^2 to 1 mD and it generally decreases with increasing site depth (White et al., 2005)[6]. In order to mitigate the effect of the low permeability of a reservoir, one can increase the number of wellbores: in the case of the RECOPOL pilot project in Poland[7], the recovery wells were only 200 m away from the injection well. One can also increase the pressure of injection (Gaus, 2010). In the latter case it is necessary to make sure that the overpressure generated would not cause the surrounding rock to fracture and lead to a leakage (White et al., 2005).

Another issue for ECBM is the risk of leakage to the ground surface in regions where coal has been mined. In such coal fields large cavities are connected to the surface and the rocks are highly fractured because of the mining operations, which increases the risks of leakage. Moreover the sealing of abandoned coal mines is more complex than the sealing of depleted oil/gas field, since the pathways for leakage out of coal mines are not only well identified wellbores. Therefore abandoned coal mines are facing a high risk of leakage, which significantly reduces the potential of ECBM in regions where coal has been widely mined, for instance in Germany or in Great Britain (Christensen and Holloway, 2004).

In addition, other physical phenomena could impact the viability of ECBM, which occur while carbon dioxide is being injected in the seam:

- Carbon dioxide is a 'plasticizer' for coal: it causes coal to evolve from a glassy, brittle structure to a rubbery, plastic structure (Larsen et al., 1997, Özgen Karacan, 2003, Larsen, 2004, Mirzaeian and Hall, 2006). This phenomenon, called 'coal softening', usually occurs at temperatures greater than 400°C, but the injection of carbon dioxide might induce plasticization at temperatures prevailing in coal seams. Plasticization of coal may reduce the CO_2 storage capacity in coal and may reduce the permeability of coal. How plasticization may affect ECBM is not well understood yet.

- Experimental investigations show that carbon dioxide, mixed with water, can dissolve the mineral matter in coal and increase the porosity and permeability of the reservoir (Massarotto et al., 2010). Chemical reactions should be accounted for carefully when assessing the feasibility of ECBM.

[6] By comparison, the permeability of sand is around 100 D and that of an oil reservoir around 1 D

[7] http://recopol.nitg.tno.nl/index.shtml

A last physical phenomenon, that occurs while carbon dioxide is injected, is the loss of injectivity. During injection, the permeability decreases by about an order of magnitude (Harpalani and Schraufnagel, 1990). For field application of ECBM, the change of permeability causes problems of injectivity: the amount of carbon dioxide injected per unit of time reduces significantly over time while the pressure of injection remains constant. The feedback of the Allison unit injection pilot (Reeves, 2004) is a typical consequence in situ (see Fig. 1.5). After one and a half year of injection at constant pressure, the injectivity decreased by 60%. Well testing indicated that the coal permeability near the well had decreased by about two orders of magnitude. The injection, which was initially planned for three years, lasted six years. Interestingly the injectivity increased back slightly after this initial drop: we will refer to this phenomenon as to the injectivity rebound. For commercial applications of CCS, the rate of injection of carbon dioxide must be significantly larger than those experienced in the past and existing pilots. This particular problem is the focus of the thesis and is discussed in detail in the next section.

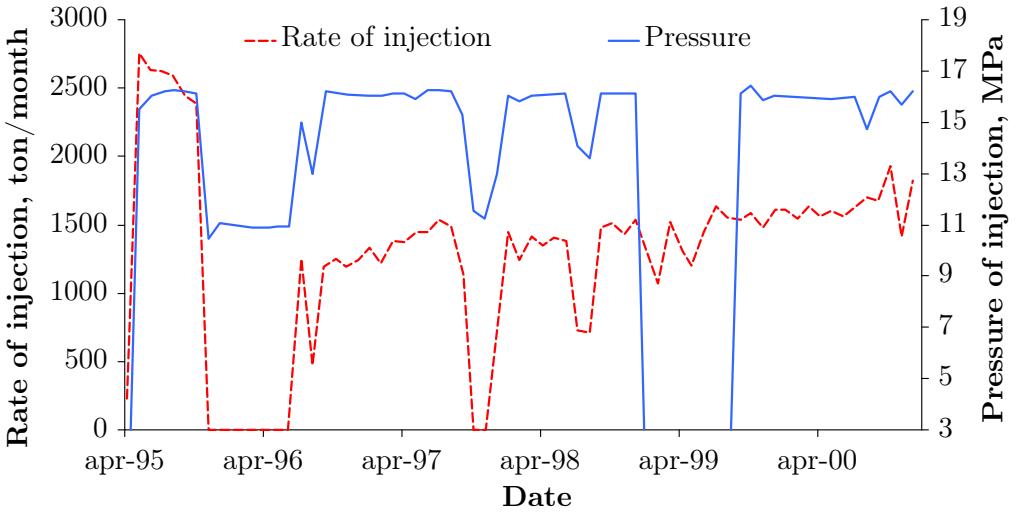

FIGURE 1.5. *Decrease of injectivity at the Allison unit injection pilot, adapted from Reeves (2004).*

1.2.3 Loss of injectivity during carbon dioxide injection in coal seams

In order to understand why the injectivity of the seam decreases when CO_2 is injected (see Sec. 1.2.2), several attempted to characterize the effect of the pore fluid on the permeability of coal. Harpalani and Schraufnagel (1990) (see Fig. 1.6) measured the permeability of a constrained coal sample saturated with methane. The permeability of the sample is divided by six when the pressure of methane increases from 0 to 3 MPa. At higher pressures of methane the permeability slightly increases back. This permeability rebound may be linked to the injectivity rebound observed on site (see Fig. 1.5). Mazumder and Wolf (2008) performed laboratory experiments in which the confining stress, the temperature, and the fluid pressures applied to the sample were representative of ECBM conditions. They injected with CO_2 cylindrical samples that were initially saturated with methane. For all cases they considered, the permeability decreased by more than one order of magnitude after five days of injection.

Coal reservoirs are made of fractured rocks in which the transport of fluid is governed by the network of fractures, also called cleats (Fig. 1.7). Cleats are connected macropores arranged in a network with a typical spacing of 1 cm. The coal matrix in between, where most of the fluid is stored, is a porous material of wide pore size distribution ranging from micropores (< 2 nm)

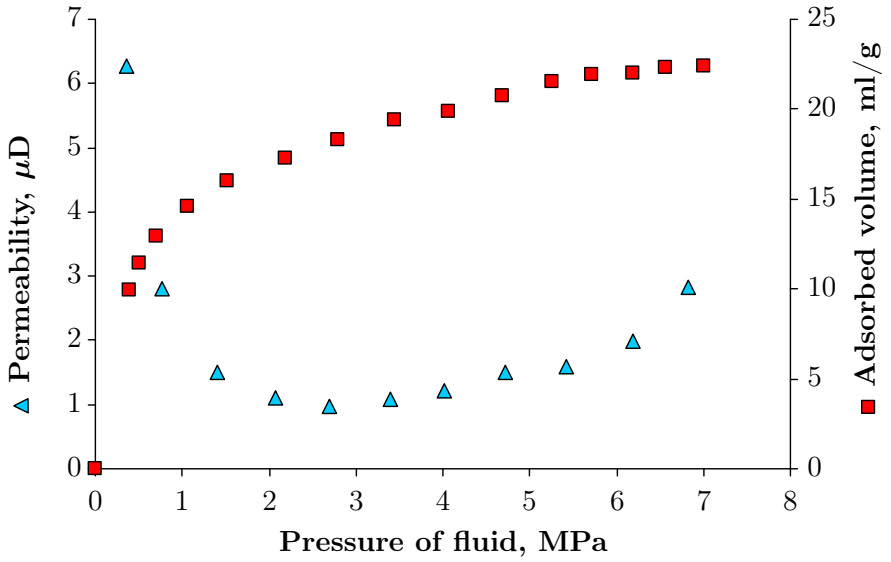

Figure 1.6. *Loss of permeability due to adsorption-induced swelling of coal. Adapted from Harpalani and Schraufnagel (1990).*

to mesopores ($>$ 2 nm and $<$ 50 nm) and to macropores ($>$ 50 nm). The coal matrix swells when carbon dioxide is injected and replaces methane. In situ, a coal seam is constrained by the surrounding geological layers and is not free to swell. The change of permeability is the result of a competition between the swelling of the matrix, which tends to close the cleats and the bulk pressure of the fluid which tends to reopen the cleats. Following the closure of the cleats network the permeability of the reservoir drops. At high fluid pressures, the matrix no more swells whereas the pressure tends to reopen the cleats network, which leads to a slight permeability rebound.

In contrast to confined conditions, other researchers observed coal samples that were merely immersed in pure fluids (Harpalani and Schraufnagel, 1990, Levine, 1996, Ottiger et al., 2008). When a coal sample is immersed in a fluid its volume varies, and this volume variation depends on the nature of the fluid (Fig. 1.8): for pure helium the coal sample slightly shrinks by less than 0.1% at a fluid pressure of 10 MPa; for pure methane the sample swells significantly, with volumetric strains ranging from 0.5% to 2% at a fluid pressure of 10 MPa; for pure carbon dioxide the sample swells two to three times as much as with methane. As a consequence, during the injection process, the progressive replacement of methane with carbon dioxide leads to a swelling of the coal which is called a 'differential swelling'.

At the scale of the coal matrix, the fluids are not in their bulk state but they are stored under an adsorbed form. Adsorption occurs when the molecules of a fluid are interacting with the atoms of a solid and tends to 'stick' to the surface of the pores. Both carbon dioxide and methane are adsorbed in the coal matrix, but the molecular interactions between carbon dioxide and coal are more significant than between methane and coal, which is the reason why the affinity of carbon dioxide for coal is greater than that of methane. Adsorption is known to govern the swelling of the coal matrix. Helium, which does not induce any swelling, is almost not adsorbed in coal whereas methane and carbon dioxide, which induce significant swellings, do adsorb (Ottiger et al., 2006). And the swelling is greater with carbon dioxide which has the higher affinity than with methane. Therefore the stronger the adsorption the greater the induced swelling.

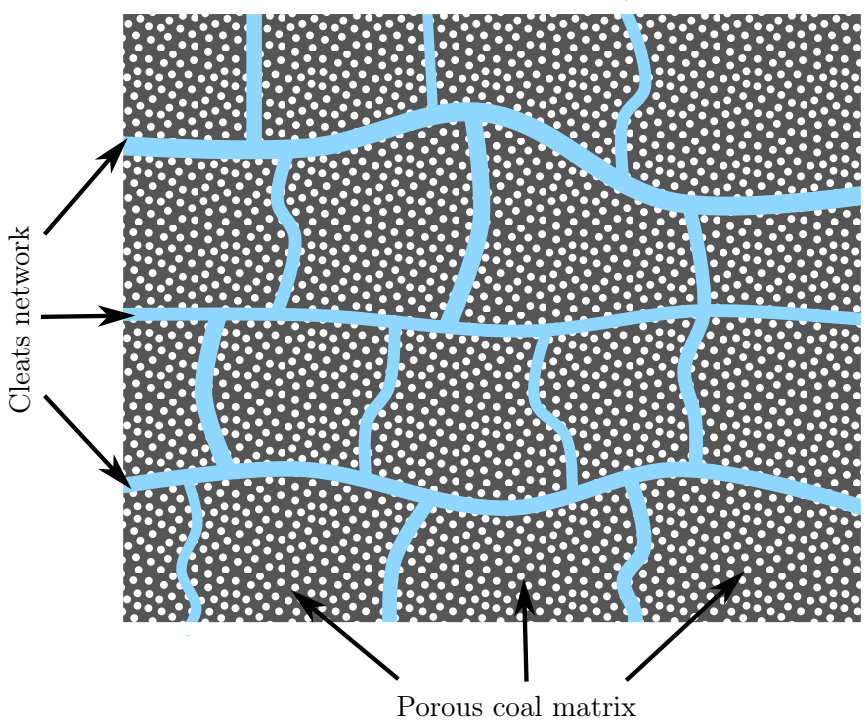

FIGURE 1.7. *Schematic representation of a coal seam (Adapted from Harpalani and Schraufnagel (1990)). Coal matrix is responsible for the differential swelling. The cleats network governs the transport properties of the seam.*

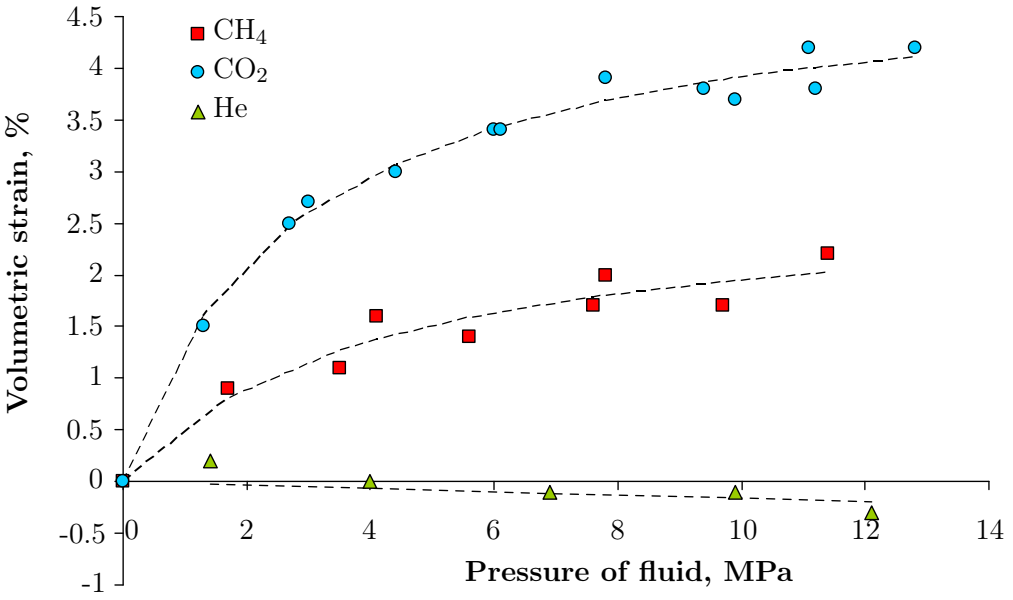

FIGURE 1.8. *Volumetric strain of coal sample immersed in a pure fluid. The results are adapted from Ottiger et al. (2008). The experiments are performed on dry coal samples from the Sulcis coal province (Italy).*

1.3 Research motivation and outline of the thesis

How adsorption impacts the mechanics of the coal matrix and eventually the permeability of a coal reservoir is important for field applications. Economic analysis of ECBM is based on predictions of rates of injection of CO_2 and of extraction of CH_4. To obtain relevant predictions, a relevant reservoir model must be available for the coal seam. Such a model must correctly capture the variation of injectivity observed in the field and must therefore explicitly take into account the adsorption-induced differential swelling observed in the laboratory. Empirical models were experimented in the case of the Allison Unit assuming that the matrix swelling is directly proportional to the amount of fluid adsorbed (Pekot and Reeves, 2002, Reeves et al., 2003, Shi and Durucan, 2004). Such models capture well the general behavior of the coal reservoir, even if significant discrepancies were obtained regarding the bottomhole pressures at the injection, recovery and observation wells. However, if one wants to explore or design innovative solutions for ECBM, one needs to move beyond empirical modeling, the predictive ability of which is limited to the range of conditions on which it has been experimentally verified.

As a first step toward this goal, we aim at obtaining the constitutive laws of a fluid-injected microporous solid, which would be suitable for a coal matrix saturated with methane and / or carbon dioxide. In order for such constitutive laws to be eventually usable in reservoir simulations, the model will be derived in the Biot-Coussy poromechanical framework.

Adsorption originates at the molecular scale from the interactions between the atoms of the coal solid skeleton and the molecules of the fluid. We will investigate the adsorption phenomenon at the molecular scale with molecular simulations. As a convenient alternative to experiments that would be very difficult to carry on, molecular simulations will be used in two ways: on model molecular systems to validate the theoretical derivations, and on a realistic molecular structure of coal to calibrate the derived constitutive laws. Molecular simulations will prove to be an invaluable tool to extend the realm of poromechanics to the effect of adsorption.

Chapter 2 recalls the basic notions of statistical physics and of numerical simulation of molecular systems, which we will use extensively in this work. In Chap. 3, we present the physics of the adsorption phenomenon and the current understanding of how adsorption leads to strain. In particular we introduce the notions of interface stress and disjoining pressure, which are used in most existing models for adsorption-induced strain. In Chap. 4 we extend the realm of poromechanics to adsorption phenomena for a generic porous solid whatever the size and shape of the pores. In Chap. 5 we perform molecular simulations of adsorption in model one-dimensional microporous solids to validate the extended poromechanical constitutive laws. Chapter 6 is dedicated to molecular simulations of adsorption of pure methane or carbon dioxide in the coal matrix. The results are validated by comparison with available experimental data. In Chap. 7 we use this molecular modeling of adsorption in coal to predict the differential swelling. We perform molecular simulation of adsorption of mixture of methane and carbon dioxide in the coal matrix at different temperatures and fluid pressures. The results obtained from the simulations, combined with the extended poromechanical constitutive laws, enable to estimate the adsorption-induced swelling of coal during the whole ECBM process for seams located at different depths.

Chapter 2

Molecular systems: physics and simulation

THIS CHAPTER*introduces the notions of statistical physics and molecular simulations which we use in this thesis to study adsorption. Classical thermodynamics provides a description of material bodies based on the notions of energy and entropy. The three laws of thermodynamics are the elementary physical principles that govern the evolutions of these two quantities. At the nanometer scale however, matter is made of atoms and molecules free to move according to the inter-atomic and inter-molecular interactions. Statistical physics provides a statistical description of molecular systems and enables to show the consistency between classical thermodynamics and the molecular description of matter. A molecular system explores the accessible molecular states according to the Boltzmann-Gibbs distribution. At the scale of atoms and molecules, the thermodynamic properties are not constant but fluctuate in time and space around their macroscopic values. The Monte Carlo methods, based on the Metropolis algorithm, make it possible to simulate molecular systems by sampling molecular configurations which follow the Boltzmann-Gibbs distribution. The inter-atomic and inter-molecular interactions govern the behavior at the molecular scale. The interactions that intervene for the adsorption of methane and carbon dioxide in coal are the steric repulsion, the chemical bonds, the electrostatic interactions, and the London dispersion forces. These interactions can be accounted for with effective potentials.*

Ce chapitre *présente les notions de physique statistique et les méthodes de simulations moléculaires que nous utilisons dans cette thèse pour l'étude de l'adsorption. La thermodynamique classique propose une description de la matière basée sur les notions d'énergie et d'entropie. Les trois principes de la thermodynamique sont les lois physiques élémentaires que vérifient ces deux grandeurs. À l'échelle nanométrique cependant, la matière est constituée d'atomes et de molécules libres de se déplacer en fonction des interactions inter-atomiques et inter-moléculaires. La physique statistique propose une description statistique des systèmes moléculaires et établit la cohérence entre une description moléculaire de la matière et la thermodynamique classique. Un système moléculaire explore les configurations moléculaires accessibles suivant la distribution de Boltzmann-Gibbs. À l'échelle des atomes et molécules, les propriétés thermodynamiques ne sont pas constantes mais fluctuent dans le temps et dans l'espace autour de leur valeur macroscopique. Les méthodes de Monte Carlo, basées sur l'algorithme de Metropolis, permettent de simuler numériquement des systèmes moléculaires en explorant les configurations moléculaires suivant la distribution de Boltzmann-Gibbs. Les intéractions inter-atomiques et inter-moléculaires déterminent le comportement à l'échelle moléculaire. Les interactions qui interviennent pour l'adsorption de dioxyde de carbone et de méthane dans le charbon sont la répulsion stérique, les liaisons chimiques, les interactions électrostatiques et les forces de dispersion de London. Ces interactions peuvent être prises en compte par des potentiels effectifs.*

Outline of Chapter 2

Adsorption, which is the main physical phenomenon studied in this thesis, originates from the molecular interactions of a fluid with a solid. In the following chapters adsorption will be studied at the molecular scale. This chapter introduces statistical physics and molecular simulations, which we will use extensively in the subsequent chapters.

2.1 Statistical physics

At the molecular scale, matter is made of atoms. Each atom evolves in the system according to its molecular interactions with the other atoms nearby. Any macroscopic system is made of a very large number of atoms, of the order of the Avogadro number $\mathcal{N}_A = 6.02 \times 10^{23}\text{mol}^{-1}$. The description of molecular systems is therefore very complex and can only be resolved for nanoscopic systems smaller than about 10 nm on very short time scales on the order of 1 ns. Statistical physics provides a statistical description of molecular systems. In particular, statistical physics enables to conciliate a molecular description of matter with thermodynamics. In this section, we recall the main concepts of classical thermodynamics (Kondepudi, 2008) and then we present the main notions of statistical physics (Chevoir, 2010).

2.1.1 Classical thermodynamics

Let us first recall the main concepts of thermodynamics, which was developed in the nineteenth century prior to statistical physics, at a time when the existence of atoms and molecules was not demonstrated. Thermodynamics provides a physical description of material bodies based on macroscopic variables only.

In thermodynamics, the state of a system is specified by a set of state variables such as the temperature, the pressure, or the volume, which entirely determines the equilibrium of the system. The laws of thermodynamics are the central principles that are verified by any system. The first law states that the internal energy E can be neither created nor destroyed, it can only be exchanged. An exchange of energy can be due to exchange of heat, volume, chemical composition, etc. When a system evolves from one state to the other, the energy change is independent of how is this evolution occur: this change only depends on the initial and final states. The internal energy is called a 'state function'.

The second law of thermodynamics asserts the existence of a state function, called entropy S, which never decreases for an isolated system. Thus the second law establishes an arrow of time for the evolution of systems. If the system is exchanging energy (heat, volume...) with its environment, the sum of the entropies of the system and of its environment can never decrease. At thermodynamic equilibrium, the entropy is a function of the state parameters only. An evolution is 'reversible' if the series of states the system goes through can be retraced in the exact opposite order. When a system exchanges only heat with its environment by mean of a 'reversible' evolution, the variation of entropy dS is proportional to the energy transferred δQ: $dS = \delta Q/T$, where T is the temperature of the system. In this case, the entropy in a generic state X can be related to the entropy of a reference state O by an integration through a reversible process:

$$S_X = S_O + \int_0^X \frac{\delta Q}{T} \tag{2.1}$$

For an irreversible evolution, entropy and heat transfer are related by: $dS \geq \delta Q/T$. The difference $dS - \delta Q/T$ is the energy dissipated in the process.

The third law of thermodynamics states that the entropy of any system approaches zero as the temperature approaches zero, thus providing a reference value to entropy.

All thermodynamic properties of a system can be derived from the internal energy and entropy. For instance, the temperature T, is defined by:

$$T = \left.\frac{\partial E}{\partial S}\right|_{N,V} \tag{2.2}$$

Likewise the mechanical pressure P is the force which opposes to a change of volume of the system. Equivalently, $-PdV$ is the energy which is transferred to the system consecutive to a variation dV of volume:

$$P = -\left.\frac{\partial E}{\partial V}\right|_{N,S} \tag{2.3}$$

We will use extensively in this thesis the chemical potential μ. The energy $\mu_k dN_k$ is the energy which is transferred to the system consecutive to a variation dN_k of amount of substance k:

$$\mu_k = \left.\frac{\partial E}{\partial N_k}\right|_{V,S} \tag{2.4}$$

The second law of thermodynamics states that any isolated system evolves spontaneously over time in order to maximize its entropy. Equivalently, non-isolated systems will evolve spontaneously over time in order to maximize or minimize other appropriate state functions. If we consider a system which can only exchange heat with its environment, this system is said to be in thermal equilibrium when its temperature is constant and equal to the temperature of the environment. For such a system, before reaching equilibrium, the only exchange of energy is the heat transfer δQ and according to the first and second laws, $dE = \delta Q \leq TdS \Rightarrow d(E - TS) \leq 0$. Therefore, such a system evolves spontaneously in order to minimize its Helmholtz free energy $F = E - TS$. The minimization of the Helmholtz free energy therefore drives the evolution of systems at constant temperature which can only exchange heat with their environment, as the maximization of the entropy drives the evolution of isolated systems. Likewise, for a system that can exchange heat and matter with its environment, the variation of energy of the system is the sum of the heat exchange δQ and of the energy $\sum_k \mu_k dN_k$ due to the exchange of matter. According to the first and second laws, at constant temperature and chemical potentials, $d(E - TS - \sum_k \mu_k N_k) \leq 0$. In other words, any system that can exchange heat and matter with a reservoir at constant temperature and chemical potential evolves spontaneously in order to minimize its grand potential $\Omega = E - TS - \sum_k \mu_k N_k$. Finally, for a system that can exchange heat and volume with a reservoir at constant temperature and pressure, the first and second laws imply that the Gibbs free energy $G = E - TS + PV$ is minimum at equilibrium.

For the different conditions presented above, we list in Tab. 2.1 the equations of state corresponding to the usual thermodynamic properties.

Property	Isolated system	Fixed temperature	Fixed temperature and chemical potential	Fixed temperature and pressure
Temperature	$T = \frac{\partial E}{\partial S}\big\vert_{N,V}$			
Entropy		$S = -\frac{\partial F}{\partial T}\big\vert_{N,V}$	$S = -\frac{\partial \Omega}{\partial T}\big\vert_{\mu,V}$	$S = -\frac{\partial G}{\partial T}\big\vert_{N,P}$
Pressure	$P = -\frac{\partial E}{\partial V}\big\vert_{S,N}$	$P = -\frac{\partial F}{\partial V}\big\vert_{T,N}$	$P = -\frac{\partial \Omega}{\partial V}\big\vert_{T,\mu}$	
Volume				$V = \frac{\partial G}{\partial P}\big\vert_{T,N}$
Chemical potential	$\mu = \frac{\partial E}{\partial N}\big\vert_{S,V}$	$\mu = \frac{\partial F}{\partial N}\big\vert_{T,V}$		$\mu = \frac{\partial G}{\partial N}\big\vert_{T,P}$
Amount of substance			$N = -\frac{\partial \Omega}{\partial \mu}\Big\vert_{T,V}$	

Table 2.1. *Equations of state for a system in different equilibrium conditions.*

2.1.2 Overview of statistical physics

The concepts of classical thermodynamics, which we recalled in the previous section, originate at the molecular scale. Statistical physics uses the theory of probability to relate the macroscopic properties of an assembly of particles to the underlying interactions that govern the motion of the particles at the microscopic scale. When the particles are molecules and atoms, statistical physics relates the thermodynamics properties such as the density, the pressure, and the temperature to the positions and impulsions of the molecules at the molecular scale.

At the molecular scale, any system is made of an assembly of atoms and molecules, which we call 'particles'. The particles are not at rest but are moving very rapidly under the effect of molecular interactions. All positions $(\mathbf{r}_i(t))_{i\in\{1,\dots,N\}}$ and impulsions $(\mathbf{p}_i(t))_{i\in\{1,\dots,N\}}$ of the particles form a 'micro-state' $(\mathbf{r}_i(t), \mathbf{p}_i(t))_{i\in\{1,\dots,N\}}$. The system is described by a succession of micro-states that are explored over time. A huge amount of information is needed to fully describe a system: 1 cm^3 of liquid water contains 3×10^{22} molecules which are moving at an average speed of 300 m/s at ambient temperature. At the macroscopic scale however, the same system is fully described by a finite number of thermodynamic properties that define the macro-state. At the end of the nineteenth century, Maxwell and Boltzmann first attempted to conciliate the well established thermodynamics with a molecular description of the matter. At equilibrium, the macro-scale temperature, pressure or density seem constant over time; but because of the thermal agitation at the micro-scale, each of these quantities is an average value which is fluctuating in space and time (see Fig. 2.1). The fluctuations are decreasing with the size of the system and are almost imperceptible for systems larger than one micrometer. The famous paper of Einstein (1905) on Brownian motion followed by the experiments of Perrin (1913) gave the first evidence that matter is made of atoms and molecules. Since then, statistical physics has been widely used to explain physical phenomena (such as adsorption) that originate from the molecular scale.

2.1.3 Microcanonical ensemble

Let us consider an isolated system with fixed number N of particles, energy E, and volume V: such a system is said to be in the microcanonical ensemble. The energy of a micro-state $(\mathbf{r}_i, \mathbf{p}_i)_{i\in\{1,\dots,N\}}$ is the sum of the molecular interactions $U(\mathbf{r}_1, ..., \mathbf{r}_N)$, which depends on the positions of the particles

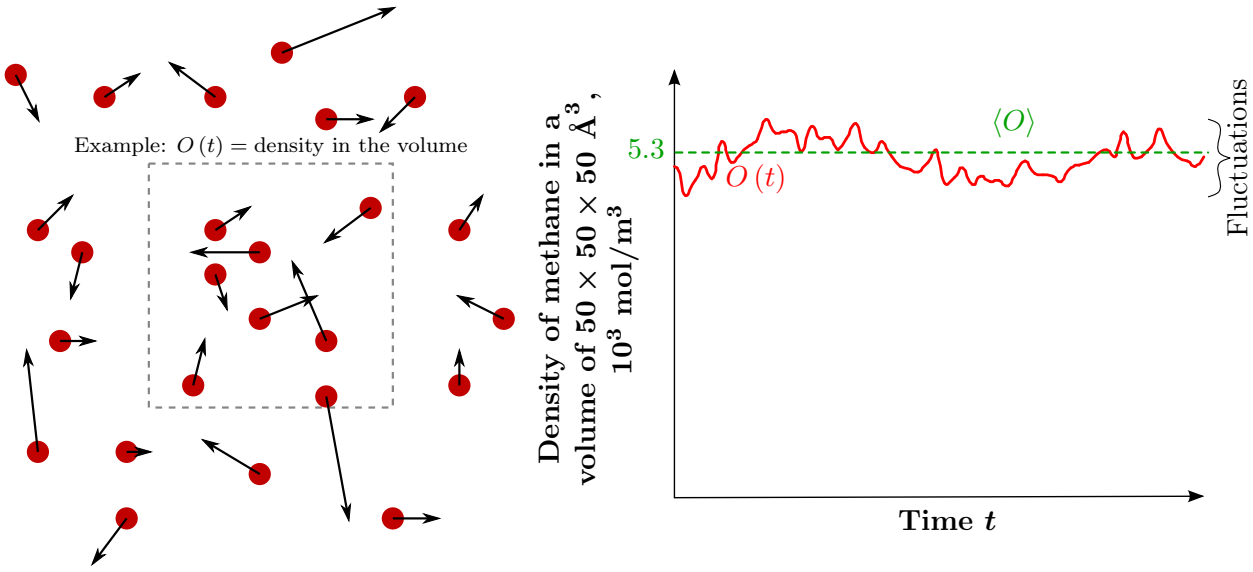

FIGURE 2.1. *Fluctuations of an observable at the molecular scale: case of the density of methane in a volume of* $50 \times 50 \times 50$ $\mathring{A}^3$ *at a temperature of* $310K$ *and at a pressure of* 12 *MPa. The volume contains an average of* 400 *molecules and the standard deviation is* 20 *molecules.*

only, and of the kinetic energy $\sum_i (\mathbf{p}_i)^2 \Big/ (2m_i)$, which depends on the impulsions of the particles only. We call $O(t) = O\left((\mathbf{r}_i(t), \mathbf{p}_i(t))_{i \in \{1,...,N\}}\right)$ an instantaneous global property of the system corresponding to the micro-state at time t. At equilibrium, the average $\langle O \rangle$ of $O(t)$ over time ($\langle O \rangle = \left(\int_{t_0}^{t} O(t)\, dt\right) \Big/ (t - t_0)$) is the macroscopic value of the property O. The accessible phase space $\Sigma(N, V, E)$ is the space in which all possible micro-states of the system are represented:

$$\Sigma(N, V, E) = \left\{ (\mathbf{r}_i, \mathbf{p}_i)_{i \in \{1,...,N\}} \in \mathbb{R}^{6N} \text{ with, } \forall i, \mathbf{r}_i \in V \text{ and } U(\mathbf{r}_1, ..., \mathbf{r}_N) + \sum_i \frac{(\mathbf{p}_i)^2}{2m_i} = E \right\} \tag{2.5}$$

Over long periods of time, the system is exploring much of the accessible phase space. Boltzmann formulated the ergodic hypothesis, which is the cornerstone of statistical physics: over long periods of time, the time spent by the system in some region of the phase space of micro-states with the same energy is proportional to the volume of this region. In other words, the average of O over time is equal to the average over all micro-states in the phase space, which, at a given energy, are all equiprobable:

$$\langle O \rangle = \frac{1}{t - t_0} \int_{t_0}^{t} O(t)\, dt \tag{2.6}$$

$$= \frac{1}{W(N, V, E)} \int_{\Sigma(N,V,E)} O\left((\mathbf{r}_i, \mathbf{p}_i)_{i \in \{1,...,N\}}\right) \frac{\mathbf{dr}_1 ... \mathbf{dr}_N \mathbf{dp}_1 ... \mathbf{dp}_N}{h^{3N}} \tag{2.7}$$

where $h \approx 6.626 \times 10^{-34}$ J.s is the Planck constant and $W(N, V, E) = \int_{\Sigma(N,V,E)} \frac{d\mathbf{r}_1 ... d\mathbf{r}_N d\mathbf{p}_1 d\mathbf{p}_N}{h^{3N}}$ is the volume of the phase space $\Sigma(N, V, E)$. The multiplicative constant $1/h^{3N}$ is introduced

because of the Heisenberg uncertainty principle, which states that the position and the impulsion of a particle cannot be known with an arbitrarily high precision. For a particle in a one-dimensional system, the product of the uncertainties $\Delta(\mathbf{r})_x$ in position and $\Delta(\mathbf{p})_x$ in impulsion is greater or equal to $\hbar = h/(2\pi)$: $\Delta(\mathbf{r})_x \cdot \Delta(\mathbf{p})_x \geq \hbar$. For N particles in a three-dimensional space, this leads to define the volume occupied by a micro-state in the phase space as $\Delta\mathbf{r}_1...\Delta\mathbf{r}_N\Delta\mathbf{p}_1...\Delta\mathbf{p}_N = h^{3N}$ (Diu et al., 1989). For systems with indistinguishable particles, the volume of a micro-state is divided by $N!$ (i.e., the number of possible permutation of the particles) and the multiplicative constant is $1/\left(h^{3N}N!\right)$. Therefore, the volume $W(N,V,E)$ of the phase space $\Sigma(N,V,E)$ is also the total number of micro-states in $\Sigma(N,V,E)$, so that integrations over the phase space Σ (as in Eq. (2.7)) can be considered equivalently as discrete sums over the micro-states:

$$\langle O \rangle = \frac{1}{t-t_0}\int_{t_0}^{t} O(t)\,dt = \sum_{u\in\Sigma(N,V,E)} O_u p_u \tag{2.8}$$

where 'u' represents a micro-state, p_u is the probability of occurrence of the micro-state u ($p_u = 1/W$ in the microcanonical ensemble), and O_u is the value of the property O for the micro-state u.

Boltzmann proposed that the entropy S used in thermodynamics is related to the logarithm of the number W of micro-states. Planck (1901) first wrote down the modern formulation:

$$S = k_B \ln(W) \tag{2.9}$$

where $k_B = 1.3806503 \cdot 10^{-23}$ J.K^{-1} is the Boltzmann constant. Gibbs (1902) proposed a more general definition based on the probabilities $(p_u)_{u\in\{1,...,W\}}$ of occurrence of the W micro-states:

$$S = -k_B \sum_u p_u \ln(p_u) \tag{2.10}$$

For an isolated system for which all micro-states are equiprobable ($p_u = 1/W(N,V,E)$), both definitions of entropy are equivalent. Interestingly, from Gibbs' definition of entropy one finds out that Boltzmann's entropy is obtained by maximizing the entropy of the system, as expected from the second law of thermodynamics. Indeed, in order to maximize Gibbs' entropy under the only constrain $\sum_u p_u = 1$ by mean of the method of Lagrange multipliers, we introduce the Lagrange multiplier λ in the Lagrange function $\widetilde{\Lambda}$ to be maximized:

$$\widetilde{\Lambda}\left((p_u)_{u\in\{1,..,W\}},\lambda\right) = -k_B\sum_u p_u \ln(p_u) - \lambda\left(\sum_u p_u - 1\right) \tag{2.11}$$

which, at the extremum, yields constant probabilities $p_u = e^{-1-\lambda/k_B}$. Therefore the entropy is maximum when all probabilities p_u of occurrence of the micro-state u are equal. So the equiprobable distribution corresponds to the maximum of entropy.

2.1.4 Canonical ensemble

Now, let us consider an isolated system made of two distinct sub-systems which can exchange only energy. The first sub-system is made of N particles in a volume V, the second sub-system is made of N_{th} particles in a volume V_{th}. The total energy E_T of the system is fixed, but the energies

E of the first sub-system and $E_{th} = E_T - E$ of the second sub-system can vary. The entropy of this system is $S_T = k_B \ln(W.W_{th})$ where $W(N,V,E)$ and $W_{th}(N_{th},V_{th},E_{th})$ are the total number of micro-states for each sub-system, respectively. Starting from an initial configuration, the two sub-systems will exchange energy in order to maximize the total entropy, that is the total number of micro-states $W_T = W.W_{th}$. At equilibrium, W and W_{th} verify:

$$\frac{\partial W}{\partial E}\Big|_{N,N_{th},V,V_{th}} W_{th} + \frac{\partial W_{th}}{\partial E}\Big|_{N,N_{th},V,V_{th}} W = 0 \tag{2.12}$$

$$\frac{\partial \ln(W)}{\partial E}\Big|_{N,V} = \frac{\partial \ln(W_{th})}{\partial E_{th}}\Big|_{N_{th},V_{th}} \tag{2.13}$$

$$\frac{\partial S}{\partial E}\Big|_{N,V} = \frac{\partial S_{th}}{\partial E_{th}}\Big|_{N_{th},V_{th}} \tag{2.14}$$

The derivative of the entropy with respect to the energy is the inverse of the temperature (see tab. 2.1): $\partial S/\partial E|_{N,V} = 1/T$. The temperatures of the two sub-systems are equal: the sub-systems are in thermal equilibrium. The energy and the temperature of each sub-system are fluctuating around their average values. The number of micro-states and the energy are linked by a relation $W \approx E^{Cst \cdot N}$, with Cst a dimensionless constant on the order of magnitude of one. Therefore, when energy $dE = -dE_{th}$ is exchanged between the sub-systems, the temperature T and T_{th} of the sub-systems verify: $dT/dT_{th} \approx N_{th}/N$. In other words, the larger the system, the lower the fluctuations of its temperature.

When one of the sub-systems is large compared to the other, e.g., $N \ll N_{th}$ and $V \ll V_{th}$, the large sub-system can be considered as a thermostat at fixed temperature. The temperature of this thermostat is imposed to the small sub-system. The small sub-system is in the so called canonical ensemble, in which the number of molecules, the volume and the temperature are fixed. The thermodynamical definition of the temperature of the thermostat $1/T_{th} = \partial S_{th}/\partial E_{th}|_{N_{th},V_{th}}$ can be integrated since $T_{th} = T$ is constant: $S_{th} = E_{th}/T + Cst$. Making use of Boltzmann's definition of entropy (Eq. 2.9), the number of micro-states of the thermostat of energy E_{th} is $W_{th} \propto \exp\left(\frac{E_{th}}{k_B T}\right) \propto \exp\left(-\frac{E}{k_B T}\right)$. The system made of the thermostat and of the small sub-system is isolated: all micro-states are equiprobable. A micro-state (u,v) of this system is the combination of the sub-micro-state u of the small sub-system of energy E_u, and of a sub-micro-state v of the thermostat of energy $E_{th} = E_T - E_u$. The probability of occurrence of the micro-state (u,v) is constant and equal to $1/W_T$. Therefore, the probability of occurrence of a micro-state u of energy E_u of the small sub-system is:

$$p_u = \frac{W_{th}(E_{th} = E_T - E_u)}{W_T} \propto \exp\left(-\frac{E_u}{k_B T}\right) \tag{2.15}$$

$$p_u = \frac{1}{Z}\exp\left(-\frac{E_u}{k_B T}\right) \tag{2.16}$$

Equation 2.16 is called the Boltzmann-Gibbs distribution. The normalization constant $Z = \sum_u \exp\left(-\frac{E_u}{k_B T}\right)$ is called the canonical partition function.

Since the whole system is isolated, its entropy $S_T = S + S_{th}$ is maximum at equilibrium. As we showed in the previous paragraph, the entropy S_{th} of the thermostat can be expressed as: $S_{th} = E_{th}/T + Cst = (E_T - E)/T + Cst$. Maximizing the entropy S_T of the whole system is

equivalent to maximizing $S+(E_T - E)/T$ or to minimizing $F = E-TS$, this latter thermodynamic potential being the Helmholtz free energy of the small sub-system. Accordingly, a system in the canonical ensemble minimizes its Helmholtz free energy at equilibrium. Combining the Boltzmann-Gibbs distribution (Eq. 2.16) with Gibbs' entropy (Eq. 2.10) we derive:

$$S = -k_B \sum_u p_u \ln(p_u) = \sum_u \frac{1}{Z} e^{-\frac{E_u}{k_B T}} \left(\frac{E_u}{T} + k_B \ln(Z) \right) = \frac{\langle E \rangle}{T} + k_B \ln(Z) \tag{2.17}$$

$$F = \langle E \rangle - TS = -k_B T \ln(Z) \tag{2.18}$$

which relates the free energy to the partition function and is analogous to Boltzmann's definition of entropy (Eq. 2.9) for systems in the canonical ensemble.

2.1.5 Other ensembles

The developments that we presented in the previous section for systems in the canonical ensemble can be adapted to treat other types of exchange. In our work, we use the grand canonical ensemble and the isobaric-isothermal ensemble in which, in addition to the exchange of energy, the system can exchange particles and volume with a large reservoir, respectively. At equilibrium, systems which can exchange particles have equal chemical potentials; systems which can exchange volume have equal pressures. Therefore a system is said to be in the grand canonical ensemble when its volume V, its temperature T, and the chemical potential μ of its particles are fixed. Likewise, a system is said in the isobaric-isothermal ensemble when its pressure P, its temperature T, and its number N of particles are fixed.

The Boltzmann-Gibbs distributions are the distributions of probability of occurrence of the micro-states. In the grand canonical ensemble, the probability of occurrence of a micro-state u of energy E_u and made of N_u particles is:

$$p_u = \frac{1}{Z_{GC}} \exp\left(-\frac{E_u - \mu N_u}{k_B T} \right) \tag{2.19}$$

where the normalization constant $Z_{GC} = \sum_u \exp(-(E_u - \mu N_u)/(k_B T))$ is called the grand canonical partition function.

In the isobaric-isothermal ensemble, the probability of occurrence of a micro-state u of energy E_u and of volume V_u is:

$$p_u = \frac{1}{Z_{NPT}} \exp\left(-\frac{E_u + PV_u}{k_B T} \right) \tag{2.20}$$

where the normalization constant $Z_{NPT} = \sum_u \exp(-(E_u + PV_u)/(k_B T))$ is the isobaric-isothermal partition function.

The grand potential $\Omega = \langle E \rangle - TS - \mu \langle N \rangle$ and the Gibbs free energy $G = \langle E \rangle - TS + P \langle V \rangle$ which are minimum for systems at equilibrium in the grand canonical and isobaric-isothermal ensembles, respectively, are related to the partition functions Z_{GC} and Z_{NPT} according to:

$$\Omega = \langle E \rangle - TS - \mu \langle N \rangle = -k_B T \ln (Z_{GC}) \quad (2.21)$$

$$G = \langle E \rangle - TS + P \langle V \rangle = -k_B T \ln (Z_{NPT}) \quad (2.22)$$

We summarize the main features of the different statistical ensembles in Tab. 2.2.

Statistical ensemble	Probability of occurrence of a micro-state	Partition function / Normalization constant	State function minimum/maximum at equilibrium
Microcanonical	$p_u = \frac{1}{W}$	W	$S = k_B \ln (W)$
Canonical	$p_u = \frac{1}{Z} \exp\left(-\frac{E_u}{k_B T}\right)$	$Z = \sum_u \exp\left(-\frac{E_u}{k_B T}\right)$	$F = -k_B T \ln (Z)$
Grand canonical	$p_u = \frac{1}{Z_{GC}} \exp\left(-\frac{E_u - \mu N_u}{k_B T}\right)$	$Z_{GC} = \sum_u \exp\left(-\frac{E_u - \mu N_u}{k_B T}\right)$	$\Omega = -k_B T \ln (Z_{GC})$
Isobaric-isothermal	$p_u = \frac{1}{Z_{NPT}} \exp\left(-\frac{E_u + PV_u}{k_B T}\right)$	$Z_{NPT} = \sum_u \exp\left(-\frac{E_u + PV_u}{k_B T}\right)$	$G = -k_B T \ln (Z_{NPT})$

TABLE 2.2. *Distributions of probability, partition functions and thermodynamic potentials minimum at equilibrium for the different statistical ensembles.*

2.2 Molecular simulations

A molecular simulation aims at sampling the possible configurations of a molecular system, in order to compute the statistical averages of macroscopic observables. The simulation explores the phase space of the possible positions and impulsions of the particles following the Boltzmann-Gibbs distribution. Many approaches exist to perform a molecular simulation, out of which the most common are the Molecular Dynamics and the Monte Carlo method. Molecular Dynamics consists in solving and integrating over time the equations of motion for each particle: thus the simulation predicts the evolution of a molecular system over time. Molecular Dynamics enables to estimate time-related properties, for instance transport properties. By contrast, the Monte Carlo method samples the phase space by following an evolution generated randomly according to the algorithm of Metropolis et al. (1953), which has no relationship with a physical evolution. Therefore, the Monte Carlo method cannot provide any information on the kinetics of a system. However, this method is more adapted to the simulation of systems for which non physical evolutions are needed to properly explore the phase space. In this work, we used the Monte Carlo method. In this section, we present the basics of the Monte Carlo method in the canonical, grand canonical, and isobaric-isothermal ensembles (Allen and Tildesley, 1989, Frenkel and Smit, 2001).

2.2.1 Metropolis algorithm in canonical ensemble

The purpose of the molecular simulation is to compute the average $\langle O \rangle$ of an observable O following the Boltzmann-Gibbs distribution. In the canonical ensemble (Sec. 2.1.4), the average $\langle O \rangle$ is:

$$\langle O \rangle = \frac{1}{Z} \sum_u O_u \exp\left(-\frac{E_u}{k_B T}\right) \tag{2.23}$$

$$= \frac{1}{Z} \frac{1}{h^{3N}} \int_{\Sigma(N,V,T)} O\left((\mathbf{r}_i, \mathbf{p}_i)_{i\in\{1,...,N\}}\right) \exp\left(-\frac{E\left((\mathbf{r}_i, \mathbf{p}_i)_{i\in\{1,...,N\}}\right)}{k_B T}\right) \mathbf{dr}_1 ... \mathbf{dr}_N \mathbf{dp}_1 ... \mathbf{dp}_N \tag{2.24}$$

with $Z = \sum_u \exp\left(-\frac{E_u}{k_B T}\right) = \frac{1}{h^{3N}} \int_{\Sigma(N,V,T)} \exp\left(-\frac{E\left((\mathbf{r}_i,\mathbf{p}_i)_{i\in\{1,...,N\}}\right)}{k_B T}\right) \mathbf{dr}_1 ... \mathbf{dr}_N \mathbf{dp}_1 ... \mathbf{dp}_N$. If an observable O is independent of the impulsions $\mathbf{p_i}$, the integration with respect to the impulsions in the above integral is a Gaussian integral: indeed, the energy $E\left((\mathbf{r}_i, \mathbf{p}_i)_{i\in\{1,...,N\}}\right)$ is the sum of the kinetic energy $\frac{1}{2}\sum_i \frac{(\mathbf{p}_i)^2}{m_i}$, which is a quadratic function of the impulsions of the particles, and of the interaction energy $U\left((\mathbf{r}_i)_{i\in\{1,...,N\}}\right)$, which depends on the positions of the particles only. Integrating Eq. (2.24) with respect to the impulsions, we obtain a simplified expression:

$$\langle O \rangle = \frac{1}{Z} \prod_i \frac{1}{\Lambda_i^3} \int_{V^N} O\left((\mathbf{r}_i)_{i\in\{1,...,N\}}\right) \exp\left(-\frac{U\left((\mathbf{r}_i)_{i\in\{1,...,N\}}\right)}{k_B T}\right) \mathbf{dr}_1 ... \mathbf{dr}_N \tag{2.25}$$

where $\Lambda_i = h/\sqrt{2\pi m_i k_B T}$ is the thermal de Broglie wavelength. If all particles are identical and indistinguishable, an additional factor $N!$ must be included, which accounts for all possible permutations of particles. In that case we have:

$$\langle O \rangle = \frac{1}{Z} \frac{1}{N! \Lambda^{3N}} \int_{V^N} O\left((\mathbf{r}_i)_{i\in\{1,...,N\}}\right) \exp\left(-\frac{U\left((\mathbf{r}_i)_{i\in\{1,...,N\}}\right)}{k_B T}\right) \mathbf{dr}_1 ... \mathbf{dr}_N \tag{2.26}$$

Equivalently, by noting $\mathbf{x}$ the molecular state $(\mathbf{r}_i)_{i\in\{1,...,N\}}$ and $\mathbb{P}(\mathbf{x})$ its probability of occurrence in the phase space V^N, the above equation can be rewritten as:

$$\langle O \rangle = \int_{\mathbf{x}\in\Sigma} O(\mathbf{x}) \mathbb{P}(\mathbf{x}) \mathbf{dx} \tag{2.27}$$

According to the law of large numbers, the average $\langle O \rangle$ is the asymptotic value of the empirical estimator $\widetilde{O}$ defined by:

$$\widetilde{O} = \frac{1}{n} \sum_{l=1}^{n} O(\mathbf{x}_l) \tag{2.28}$$

where $(\mathbf{x}_1, ..., \mathbf{x}_n)$ is a sample of values which follows the probability distribution $\mathbb{P}$.

There exists no direct random generator for the probability distribution $\mathbb{P}$. The simplest method to generate the sample of values $(\mathbf{x}_1, ..., \mathbf{x}_n)$ is the rejection sampling (Rubinstein and Kroese, 2008): if there is a probability distribution $\mathbb{Q}$, for which a random generator exists, and such that $\mathbb{P}(\mathbf{x})/\mathbb{Q}(\mathbf{x})$ is a bounded function of maximum M, then the rejection sampling algorithm consists

in generating a random value $\mathbf{x}$ following $\mathbb{Q}$ and a random value Y following a uniform distribution over $[0;1]$, and in accepting $\mathbf{x}$ as a realization of $\mathbb{P}$ only if $Y < \mathbb{P}(\mathbf{x}) / (M\mathbb{Q}(\mathbf{x}))$. An iteration of this algorithm will provide random values that follow the distribution $\mathbb{P}$.

The efficiency of the rejection sampling varies widely: if the distributions $\mathbb{P}$ and $\mathbb{Q}$ are very similar, most iterations are accepted; conversely, if the distributions differ significantly from each other, most iterations are rejected (Fig. 2.2). Molecular simulations correspond to this latter case: the energy of most molecular states in the accessible phase space is very high, from what follows that their probability of occurrence (according to the Boltzmann-Gibbs distribution) is very low. Since there exists no random generator able to generate a distribution close to the Boltzmann-Gibbs distribution, the rejection sampling algorithm is very inefficient to sample molecular states.

An alternative method of sampling was proposed by Metropolis et al. (1953), which consists in generating a Markov chain of molecular configurations:

■ Algorithm 2.1 (Metropolis)
Begin from an initial configuration $\mathbf{x}_0$. For $l \geq 0$,

1 - Propose a new configuration: From the configuration $\mathbf{x}_l$, propose a new configuration $\widetilde{\mathbf{x}}_{l+1}$ with a symmetric proposition function.

2 - Decide whether to accept a new configuration: The proposed configuration $\widetilde{\mathbf{x}}_{l+1}$ is accepted with probability:

$$p = \min\left(1, \frac{\mathbb{P}(\widetilde{\mathbf{x}}_{l+1})}{\mathbb{P}(\mathbf{x}_l)}\right) \tag{2.29}$$

If $\widetilde{\mathbf{x}}_{n+1}$ is rejected, then the configuration is not updated.

The probability of acceptation of a new configuration (Eq. 2.29) ensures that the sampled configurations follow the probability distribution $\mathbb{P}$. The proposition function must be symmetric, which means that the probability of generating the configuration $\widetilde{\mathbf{x}}_{l+1}$ from the configuration $\mathbf{x}_l$ must be equal to the probability of generating the configuration $\mathbf{x}_l$ from the configuration $\widetilde{\mathbf{x}}_{l+1}$. Since the Metropolis algorithm is a Markov chain, the sampled configurations are correlated, but the correlation between the configurations $\mathbf{x}_l$ and $\mathbf{x}_m$ vanishes when $|m-l|$ is large. This methodology of exploration of the phase space is much more efficient than the rejection sampling: once a configuration of high probability of occurrence has been reached, the Metropolis algorithm explores the 'neighborhood' of this configuration rather than generating configurations of low probability of occurrence. Since the configurations of high probability of occurrence are concentrated in a few regions of the phase space, the Metropolis algorithm focuses only on these regions and ignores much of the phase space in which the probability of occurrence is very low (Fig. 2.2).

The Metropolis algorithm is a particular case of the more general Metropolis-Hastings algorithm (Hastings, 1970), in which the proposition function is not necessarily symmetric. In this thesis, we used the original Metropolis algorithm only. The algorithm can be used in any statistical ensemble, such as the canonical, grand canonical, or isobaric-isothermal ensembles. From one ensemble to the other, the main steps of Alg. 2.1 remain identical, but the details of the Boltzmann-Gibbs distribution and of the proposition functions are specific to each ensemble. In the canonical ensemble, molecular states differ from each other through the positions $\mathbf{r}_i$ of the particles, from what follows that the proposition function is a random move of a particle. The explicit formulation of the Metropolis algorithm in the canonical ensemble is:

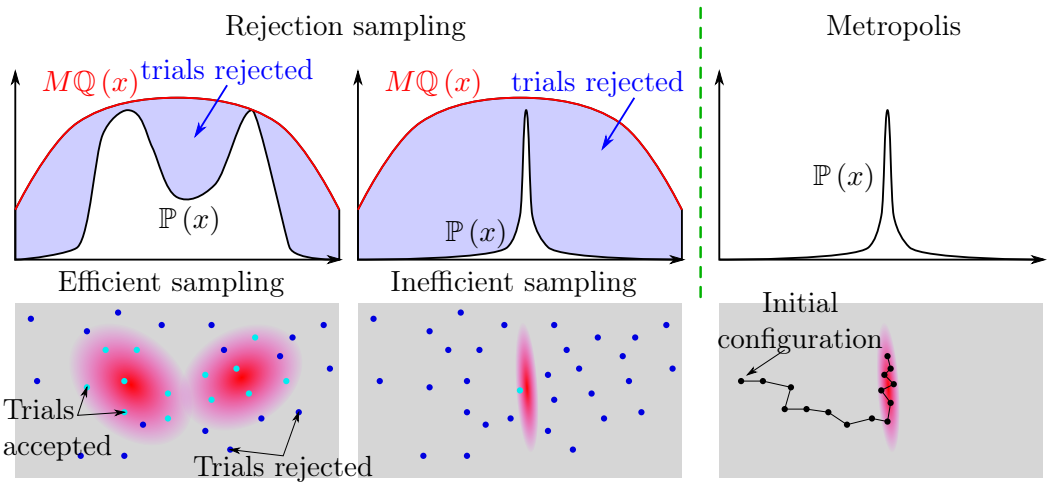

Figure 2.2. *Sketch of the rejection sampling method and of the Metropolis algorithm.*

■ Algorithm 2.2 (Canonical Monte Carlo)
Begin from a configuration $\mathbf{x}_0 = \left((\mathbf{r}_i)_{i\in\{1,\dots,N\}}\right)_0$,

1 - Propose a new configuration: From the configuration $\mathbf{x}_l$ propose a new configuration $\widetilde{\mathbf{x}}_{l+1}$ by performing a trial move:

Trial move: Choose randomly one of the particles and propose to displace it from its current position.

2 - Decide whether to accept a new configuration: The proposed configuration $\widetilde{\mathbf{x}}_{l+1}$ is accepted with probability:

Trial move:

$$p = \min\left(1, \exp\left(-\frac{U\left(\widetilde{\mathbf{x}}_{l+1}\right) - U\left(\mathbf{x}_l\right)}{k_B T}\right)\right) \tag{2.30}$$

If $\widetilde{\mathbf{x}}_{l+1}$ is rejected, then the configuration is not updated.

The amplitude of the trial move must be small enough to ensure that a significant proportion of the trial moves is accepted. But this amplitude must also be large enough to ensure a sufficient exploration of the phase space. In the present work, we adjusted the amplitude so that half of the trials were accepted: such a choice was arbitrary and may not be optimal.

2.2.2 Metropolis algorithm in other statistical ensembles

In the grand canonical and in the isobaric-isothermal ensembles, the proposition function of a new configuration and the probability of acceptation must be modified. In the grand canonical ensemble, the number of particles in the system varies. Therefore, the proposition function also includes the insertion and removal of particles. In the isobaric-isothermal ensemble, the volume of the system varies, from what follows that the proposition function includes changes of volume. The Boltzmann-Gibbs distributions differ also. The probability of acceptation (Eq. 2.29), which appears in the Metropolis algorithm, can be expressed by applying a change of variables to Eq. (2.26):

$$\langle O\rangle = \frac{1}{Z}\frac{V^N}{N!\Lambda^{3N}}\int_{[0;1]^{3N}} O\left(\left(\mathbf{r}'_i\right)_{i\in\{1,\dots,N\}}, V\right)\exp\left(-\frac{U\left(\left(\mathbf{r}'_i\right)_{i\in\{1,\dots,N\}}, V\right)}{k_B T}\right)\mathbf{dr}'_1\dots\mathbf{dr}'_N \tag{2.31}$$

The Boltzmann-Gibbs distributions $\mathbb{P}_{GC}$ in the grand canonical ensemble and $\mathbb{P}_{NPT}$ in the isobaric-isothermal ensemble can therefore be rewritten:

$$\mathbb{P}_{GC} = \frac{1}{Z_{GC}} \frac{V^N}{N!\Lambda^N} \exp\left(-\frac{U\left((\mathbf{r}'_i)_{i\in\{1,\dots,N\}}, V \right) - \mu N}{k_B T} \right) \tag{2.32}$$

$$\mathbb{P}_{NPT} = \frac{1}{Z_{NPT}} \frac{V^N}{N!\Lambda^N} \exp\left(-\frac{U\left((\mathbf{r}'_i)_{i\in\{1,\dots,N\}}, V \right) + PV}{k_B T} \right) \tag{2.33}$$

The explicit formulations of the Metropolis algorithm in the grand canonical and isobaric-isothermal ensembles are:

■ Algorithm 2.3 (Grand canonical Monte Carlo)
Begin from a configuration $\mathbf{x}_0 = \left((\mathbf{r}'_i)_{i\in\{1,\dots,N\}} \right)_0$ of volume V

1 - Propose a new configuration: From a configuration $\mathbf{x}_l$ propose a new configuration $\widetilde{\mathbf{x}}_{l+1}$ following one of these trials:

- **a - Trial move:** Choose randomly one of the particles and propose to displace it from its current position.
- **b - Trial insertion:** Choose randomly a location in the system and propose to insert a new particle at this location.
- **c - Trial removal:** Choose randomly one of the particles and propose to remove it from the system.

2 - Decide whether to accept a new configuration: The proposed configuration $\widetilde{\mathbf{x}}_{l+1}$ is accepted with probability:

a - Trial move:

$$p = \min\left(1, \exp\left(-\frac{U\left(\widetilde{\mathbf{x}}_{l+1}, V\right) - U\left(\mathbf{x}_l, V\right)}{k_B T} \right) \right) \tag{2.34}$$

b - Trial insertion:

$$p = \min\left(1, \frac{V}{\Lambda^3 (N+1)} \exp\left(-\frac{\left(U\left(\widetilde{\mathbf{x}}_{l+1}, V\right) - U\left(\mathbf{x}_l, V\right) - \mu\right)}{k_B T} \right) \right) \tag{2.35}$$

c - Trial removal:

$$p = \min\left(1, \frac{\Lambda^3 N}{V} \exp\left(-\frac{\left(U\left(\widetilde{\mathbf{x}}_{l+1}, V\right) - U\left(\mathbf{x}_l, V\right)\right) + \mu}{k_B T} \right) \right) \tag{2.36}$$

If $\widetilde{\mathbf{x}}_{l+1}$ is rejected, the configuration is not updated.

■ Algorithm 2.4 (NPT Monte Carlo)
Begin from a configuration $\mathbf{x}_0 = \left((\mathbf{r}'_i)_{i\in\{1,\dots,N\}} \right)_0$ of volume V_0

1 - Propose a new configuration: From the configuration $(\mathbf{x}_l, V_l)$ propose a new configuration $\left(\widetilde{\mathbf{x}}_{l+1}, \widetilde{V}_{l+1}\right)$ following one of these trials:

- **a - Trial move:** Choose randomly one of the particles and propose to displace it from its current position.
- **b - Trial volume change:** Propose a variation of the volume of the system.

2 - Decide a new configuration: The proposed configuration $\left(\widetilde{\mathbf{x}}_{l+1}, \widetilde{V}_{l+1}\right)$ is accepted with probability:

a - Trial move:

$$p = \min\left(1, \exp\left(-\frac{U\left(\widetilde{\mathbf{x}}_{l+1}, V_l\right) - U\left(\mathbf{x}_l, V_l\right)}{k_B T}\right)\right) \tag{2.37}$$

b - Trial volume change:

$$p = \min\left(1, \left(\frac{\widetilde{V}_{l+1}}{V_l}\right)^{N+1} \exp\left(-\frac{U\left(\mathbf{x}_l, \widetilde{V}_{l+1}\right) - U\left(\mathbf{x}_l, V_l\right) + P\left(\widetilde{V}_{l+1} - V_l\right)}{k_B T}\right)\right) \tag{2.38}$$

If $\left(\widetilde{\mathbf{x}}_{l+1}, \widetilde{V}_{l+1}\right)$ is rejected, then the configuration is not updated.

For Monte Carlo simulations in the grand canonical ensemble or in the isobaric-isothermal ensemble, the proposition function involves different types of trials; a repartition between these different types of trials must be chosen. In the grand canonical ensemble, the computational cost of an insertion or of a removal is similar to the computational cost of a displacement. We gave equal weight to the insertion / removal trials and to the move trials: a quarter of the Monte Carlo steps were insertions, a quarter of the Monte Carlo steps were removals, and half of the Monte Carlo steps were displacements. In isobaric-isothermal ensemble, the computational cost of a trial volume change is much larger than the computational cost of a trial move, since for a trial volume change the total energy of interaction of the system must be computed, whereas for a trial move only the energy related to the displaced particle has to be assessed. The ratio of the computational cost between a trial volume change and a trial move is about the number of particles in the system. Therefore, we chose to perform one trial volume change every N trial moves, where N is the number of particles in the system.

In the isobaric-isothermal ensemble, we performed logarithmic trial volume changes: $\ln\left(\widetilde{V}_{l+1}\right) = \ln\left(V_l\right) + \Delta V$, where ΔV was chosen randomly following a uniform distribution. By doing so, the probability of acceptation of the trials is identical whatever the volume of the system. Indeed, a logarithmic volume variation corresponds to a change of density that is independent of the size of the system. And, since the energy of interaction of a system is often a function of the distance between particles, this energy depends primarily on the density of the system. Therefore, a Monte Carlo simulation should be more efficient at sampling with logarithmic trial volume changes than with uniform trial volume changes.

In the grand canonical ensemble, for sake of convenience, we imposed the fugacity fug instead of the chemical potential μ. The fugacity is defined with respect to the chemical potential according to the relation:

$$\mu = \mu^0_{IdG} + k_B T \ln\left(\frac{fug}{k_B T}\right) \tag{2.39}$$

where $\mu^0_{IdG} = k_B T \ln\left(\Lambda^3\right)$ is the reference chemical potential of an ideal gas at a density of 1 particle per cubic meter. For an ideal gas, the fugacity is equal to the bulk pressure. For any other fluid, the fugacity represents the bulk pressure of an ideal gas at the chemical potential considered. The use of the fugacity simplifies the probability of acceptation of a trial insertion or a trial removal in the grand canonical ensemble:

- Trial insertion:

$$p = \min\left(1, \frac{V \cdot fug}{k_B T\,(N+1)} \exp\left(-\frac{(U\,(\widetilde{\mathbf{x}}_{l+1}, V) - U\,(\mathbf{x}_l, V))}{k_B T}\right)\right) \tag{2.40}$$

- Trial removal:

$$p = \min\left(1, \frac{k_B T N}{V \cdot fug} \exp\left(-\frac{(U\,(\widetilde{\mathbf{x}}_{l+1}, V) - U\,(\mathbf{x}_l, V))}{k_B T}\right)\right) \tag{2.41}$$

For simulating mixtures, the Boltzmann-Gibbs distribution is slightly modified: particles of different types are distinguishable and their thermal wavelengths are different. For canonical and NPT Monte Carlo simulations, the probability acceptation remain unchanged, but, in grand canonical Monte Carlo, the probabilities of acceptation of the trial insertions and trial removals are modified as follows:

- Trial insertion (particle of type k)

$$p = \min\left(1, \frac{V}{\Lambda_k^3\,(N_k+1)} \exp\left(-\frac{(U\,(\widetilde{\mathbf{x}}_{l+1}, V) - U\,(\mathbf{x}_l, V) - \mu_k)}{k_B T}\right)\right) \tag{2.42}$$

- Trial removal (particle of type k)

$$p = \min\left(1, \frac{\Lambda_k^3 N_k}{V} \exp\left(-\frac{(U\,(\widetilde{\mathbf{x}}_{l+1}, V) - U\,(\mathbf{x}_l, V)) + \mu_k}{k_B T}\right)\right) \tag{2.43}$$

where Λ_k is the thermal De Broglie wavelength for the particles of type k, and N_k is the number of particles of type k.

2.2.3 Calculation of observables

Observables are computed frequently during the simulations. Observables that have a negligible computational cost (e.g., the density or the energy of interaction) can be computed at every Monte Carlo step. By contrast, the computational cost of the mechanical stress or of the chemical potential is high: indeed, it is comparable to computing the total energy of interaction of the system. Computing such observables at every Monte Carlo step would increase dramatically the computation time. Moreover, because of the correlation between molecular configurations, a computation of observables at every Monte Carlo step is far from optimal: two successive configurations during the sampling would give almost the same value of the observable. A reasonable alternative is to compute the observables periodically. In the present work, in order to equilibrate the computation time allocated to the computation of the observables and the computation time allocated to the sampling of the molecular configurations, the mechanical stress and the chemical potentials were computed every 1000 Monte Carlo steps.

We considered in this work three observables: the mechanical stress, the density and the chemical potential. The mechanical stress was calculated with the so-called virial estimate, which we introduce in Chap. 3. The density is readily available at every step of the simulation. We used the Widom insertion method to compute the chemical potential (Widom, 1963). The Widom insertion method consists in performing virtual insertions of particles in order to determine the variation of free energy consecutive to a variation of number of particles.

Let us recall the demonstration of the Widom formula for a pure component system in the canonical ensemble. This demonstration can be extended to mixtures and to other statistical ensembles. In the canonical ensemble, the Helmholtz free energy is related to the partition function according to Eq. (2.18), which after integration with respect to the impulsions yields:

$$\begin{aligned} F\left(N,V,T\right) &= -k_B T \ln\left(Z\right) \\ &= -k_B T \ln\left(\frac{1}{N!h^{3N}} \int_{\Sigma(N,V,T)} \exp\left(-\frac{\frac{1}{2m}\sum_i \left(\mathbf{p}_i\right)^2 + U\left(\left(\mathbf{r}_i\right)_{i\in\{1,\ldots,N\}}\right)}{k_B T}\right) \mathbf{dr}_1 ... \mathbf{dr}_N \mathbf{dp}_1 ... \mathbf{dp}_N\right) \\ &= -k_B T \ln\left(\frac{V^N}{N!\Lambda^{3N}} \int_{[0;1]^{3N}} \exp\left(-\frac{U\left(\left(\mathbf{r}_i\right)_{i\in\{1,\ldots,N\}}\right)}{k_B T}\right) \mathbf{dr}_1 ... \mathbf{dr}_N\right) \end{aligned} \tag{2.44}$$

The chemical potential is the derivative of the Helmholtz free energy with respect to the number of particles. It can be approximated by the difference of free energy between the current system and the system with one particle added to it:

$$\begin{aligned} \mu &= \left.\frac{\partial F}{\partial N}\right|_{V,T} \approx F\left(N+1,V,T\right) - F\left(N,V,T\right) \\ &= -k_B T \ln\left(\frac{V}{\left(N+1\right)\Lambda^3} \frac{\int_{[0;1]^{3N}} \left(\int_{[0;1]^3} \exp\left(-\frac{U^{Supp}(\mathbf{r}_{N+1})}{k_B T}\right) \mathbf{dr}_{N+1}\right) \exp\left(-\frac{U\left(\left(\mathbf{r}_i\right)_{i\in\{1,\ldots,N\}}\right)}{k_B T}\right) \mathbf{dr}_1 ... \mathbf{dr}_N}{\int_{[0;1]^{3N}} \exp\left(-\frac{U\left(\left(\mathbf{r}_i\right)_{i\in\{1,\ldots,N\}}\right)}{k_B T}\right) \mathbf{dr}_1 ... \mathbf{dr}_N}\right) \end{aligned} \tag{2.45}$$

where $U^{Supp}\left(\mathbf{r}_{N+1}\right)$ is the supplementary energy of interaction due to the addition of a particle in the initial system: $U\left(\left(\mathbf{r}_i\right)_{i\in\{1,\ldots,N+1\}}\right) = U\left(\left(\mathbf{r}_i\right)_{i\in\{1,\ldots,N\}}\right) + U^{Supp}\left(\mathbf{r}_{N+1}\right)$. The above equation can be rewritten as an average:

$$\mu = -k_B T \ln\left(\frac{V}{\left(N+1\right)\Lambda^3}\right) - k_B T \ln\left(\left\langle \int_{[0;1]^3} \exp\left(-\frac{U^{Supp}\left(\mathbf{r}_{N+1}\right)}{k_B T}\right) \mathbf{dr}_{N+1} \right\rangle\right) \tag{2.46}$$

We approximate the integral term in the above expression with its empirical estimator, by choosing randomly a large number $\mathcal{V}$ of positions $\left(\mathbf{r}^v_{N+1}\right)_{v\in\{1,\ldots,\mathcal{V}\}}$ and performing virtual insertions at these locations:

$$\int_{[0;1]^3} \exp\left(-\frac{U^{Supp}\left(\mathbf{r}_{N+1}\right)}{k_B T}\right) \mathbf{dr}_{N+1} \approx \frac{1}{\mathcal{V}} \sum_{v=1}^{\mathcal{V}} \exp\left(-\frac{U^{Supp}\left(\mathbf{r}^v_{N+1}\right)}{k_B T}\right) \tag{2.47}$$

Therefore, the Widom insertion method approximates the instantaneous value of the chemical potential by virtually inserting particles. This operation is repeated throughout the molecular simulation in order to compute the average value of the observable (Eq. 2.46).

The Widom insertion method can also be used to compute the fugacity instead of the chemical potential:

$$fug = \frac{k_B T \left(N+1\right)}{V \left\langle \int_{[0;1]^3} \exp\left(-\frac{U^{Supp}(\mathbf{r}_{N+1})}{k_B T}\right) \mathbf{dr}_{N+1} \right\rangle} \tag{2.48}$$

Before computing the observables, one has to make sure that the simulation is equilibrated. Indeed, if the initial configuration is unphysical, i.e., its probability of occurrence is very low, the first configurations sampled with the Metropolis algorithm are not representative of the Boltzmann-Gibbs distribution. In theory, the metropolis algorithm samples the Boltzmann-Gibbs distribution after an infinite number of Monte Carlo steps. Even if the initial configuration has a very low probability, the Markov chain reaches a region of high probability of occurrence after a finite number of steps. During the equilibration, the value of an observable evolves continuously and converges toward its equilibrium value (Fig. 2.3). In practice, if the energy barriers ΔE that must be overcome to move from the initial configuration to the region of high probability is high compared to $k_B T$, the 'sufficient number of Monte Carlo steps' may be too large for reasonable computational costs. Such is the case for solid states, for which the initial configuration must be a configuration of high probability. In the present work, the initial configuration for solids was the atomic structure of the solid. For fluids, the initial configuration was chosen randomly.

2.2.4 Estimation of uncertainty

According to the central limit theorem (Rubinstein and Kroese, 2008), the empirical estimator $\widetilde{O}$ of the observable O (Eq. 2.28) follows a normal distribution $\mathcal{N}\left(\langle O\rangle, \left(\overline{SD}_O\right)^2 \Big/ n\right)$ of mean value $\langle O\rangle$ and variance $\left(\overline{SD}_O\right)^2 \Big/ n$, provided the random sample $(\mathbf{x}_l)_{l\leq n}$ is *independent and identically distributed*. The quantity $\overline{SD}_O$ is the standard deviation of O: $\left(\overline{SD}_O\right)^2 = \int_{\mathbf{x}\in\Sigma} \left(O\left(\mathbf{x}\right) - \langle O\rangle\right)^2 \mathbb{P}\left(\mathbf{x}\right) \mathbf{dx}$. The central limit theorem can be converted into a confidence interval. For instance, since 1.96 is the quantile of the standard normal distribution at 5%, $\langle O\rangle \in \left[\widetilde{O} - 1.96\overline{SD}_O / \sqrt{n}\,; \widetilde{O} - 1.96\overline{SD}_O / \sqrt{n}\right]$ with a probability of 95%.

The central limit theorem is not valid for configurations $\mathbf{x}_l$ sampled with the Metropolis algorithm, because configurations are strongly correlated when they are separated by a small number of Monte Carlo steps. This correlation vanishes after a large number of Monte Carlo steps. The central limit theorem no more applies, but an equivalent theorem does (Frenkel and Smit, 2001): the empirical estimator $\widetilde{O}$ follows a normal distribution of mean $\langle O\rangle$ and variance $\left(\overline{SD}_{\widetilde{O}}\right)^2 \Big/ n$ with:

$$\left(\overline{SD}_{\widetilde{O}}\right)^2 = \left(\overline{SD}_O\right)^2 + 2\sum_{l=1}^{+\infty} \left\langle \left(O\left(\mathbf{x}_l\right) - \langle O\rangle\right)\left(O\left(\mathbf{x}_0\right) - \langle O\rangle\right)\right\rangle \tag{2.49}$$

The summation term accounts for the correlation between the configurations. If the configurations are independent, this summation term is equal to zero.

In order to estimate $\overline{SD}_{\widetilde{O}}$ and thus the uncertainty of the empirical estimator $\widetilde{O}$, there exists the block averaging method (Frenkel and Smit, 2001). This method starts with dividing the Monte Carlo simulation into $\mathcal{B}$ blocks of length n_{bl}. The total number n of Monte Carlo steps in the simulation verifies $\mathcal{B} \times n_{bl} = n$. For each block we compute the empirical estimator $\widetilde{O}_b$ of O over this block: $\widetilde{O}_b = \frac{1}{n_{bl}} \sum_{l=(b-1)n_{bl}+1}^{b\cdot n_{bl}} O\left(\mathbf{x}_l\right)$. We call $\left(\widetilde{SD}_{\widetilde{O}}\right)^2$ the empirical variance of the series $\left(\widetilde{O}_b\right)_{b\in\{1,\ldots,\mathcal{B}\}}$:

$$\left(\widetilde{SD}_{\widetilde{O}}\right)^2 = \frac{1}{\mathcal{B}} \sum_{b=1}^{\mathcal{B}} \left(\widetilde{O}_b - \langle O \rangle\right)^2 \tag{2.50}$$

We know that after a large number $\overline{n}$ of Monte Carlo steps, the configurations $(\mathbf{x}_l)_{l \geq \overline{n}}$ sampled are not correlated with the first configuration $\mathbf{x}_0$ anymore:

$$\sum_{l=\overline{n}}^{+\infty} \langle (O(\mathbf{x}_l) - \langle O \rangle)(O(\mathbf{x}_0) - \langle O \rangle) \rangle \approx 0 \tag{2.51}$$

If $n_{bl} > \overline{n}$, the series $\left(\widetilde{O}_b\right)_{b \in \{1,\ldots,\mathcal{B}\}}$ follows a normal distribution of mean value $\langle O \rangle$ and variance $\left(\overline{SD}_{\widetilde{O}}\right)^2 \Big/ n_{bl}$. If $n_{bl} < \overline{n}$, the variance of the series $\left(\widetilde{O}_b\right)_{b \in \{1,\ldots,\mathcal{B}\}}$ is lower than $\left(\overline{SD}_{\widetilde{O}}\right)^2 \Big/ n_{bl}$ because of the correlation. Therefore, $n_{bl} \cdot \left(\widetilde{SD}_{\widetilde{O}}\right)^2$ is an increasing function of n_{bl} which converges toward the asymptotic value $\left(\overline{SD}_{\widetilde{O}}\right)^2$ for $n_{bl} > \overline{n}$. As an example, we display in Fig. 2.3 the density of a Lennard-Jones fluid simulated in the grand canonical ensemble. The system is made of about 400 particles. The decorrelation threshold $\overline{n}$ is 65000 Monte Carlo steps. In this thesis, we used the block averaging method to estimate the uncertainty of the molecular simulations. The size n_{bl} of the blocks was adapted to each system with a minimum size of 100000 Monte Carlo steps.

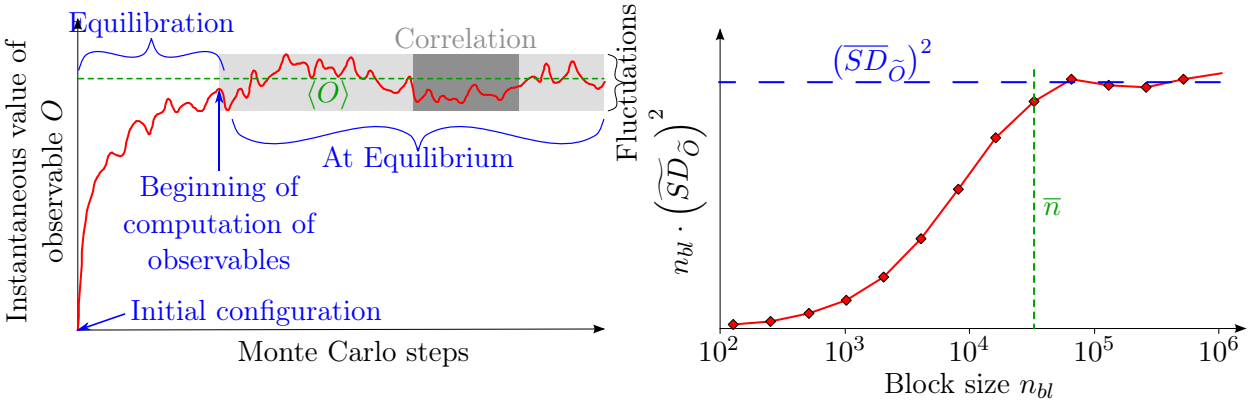

Figure 2.3. *Uncertainty estimation in a molecular simulation by the block averaging method.*

2.2.5 Boundary conditions

The choice of the boundary conditions is a technical issue that must be handled before practical implementation. In the present work, we considered periodic boundary conditions which mimic an infinite volume of material. Molecules were interacting according to the minimum image convention (Fig. 2.4): if the distance between two particles i and j was larger than half the length of the system, particle i would interact with the nearest replica of particle j in the periodic replica of the system. Moreover if a trial move proposed to move a particle outside the boundaries of the system, this particle would reenter into the system through the opposite side. The range of interactions between particles had to be handled carefully due to the finite size of the system. Indeed, if the range of the interaction is larger than half the length of the system, interactions are not limited to the minimum image and a non negligible part of the interaction energy would be ignored by applying the minimum image convention (this is for instance the case for electrostatic interactions).

Specific methods exist to deal with long range interactions. In this work we used the Ewald sum for electrostatic interactions between point charges (Allen and Tildesley, 1989, Frenkel and Smit, 2001).

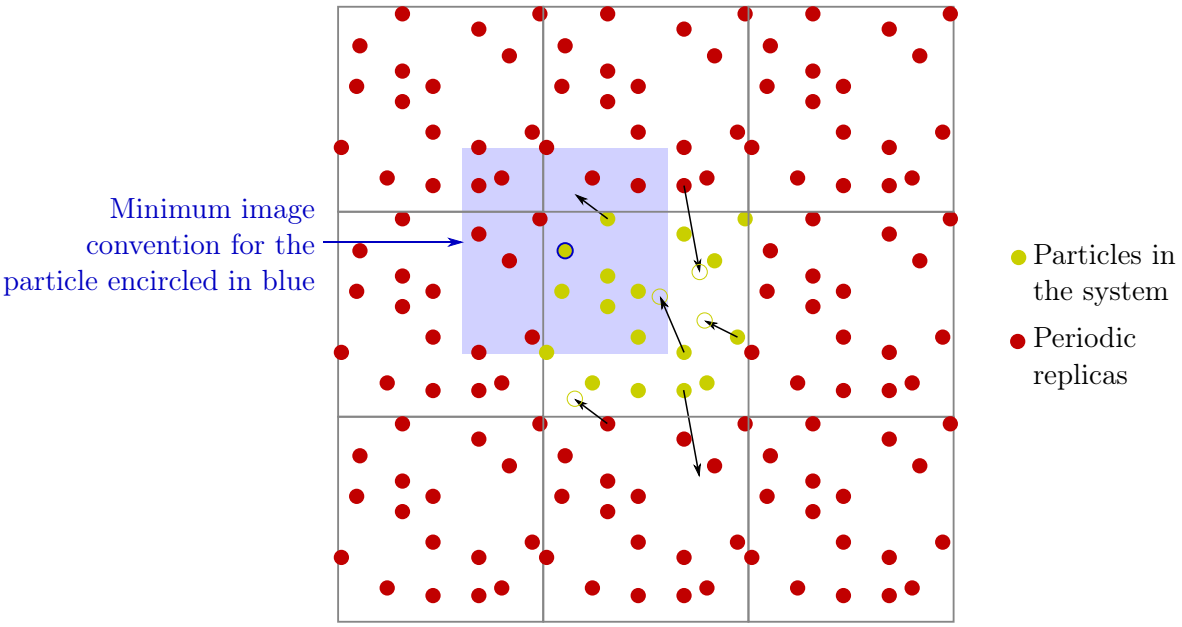

FIGURE 2.4. *Periodic boundary conditions and minimum image convention.*

2.3 Molecular interactions

A molecular simulation can be performed by following the theory and methods presented in Secs. 2.1 and 2.2. The behavior of a molecular system depends entirely on the energy of interaction between the atoms and molecules. In this section, we present the different interactions encountered in the present work and the effective potentials used to approximate these interactions.

2.3.1 Quantum mechanics and molecular mechanics

Quantum mechanics describes matter at the atomic and sub-atomic scales. A particle is described by its wave function $\Psi(\mathbf{r}, t)$, which gives the probability of presence of the particle at time t at the location $\mathbf{r}$. The exact position and impulsion of a particle are not known. The Schrödinger equation is the central equation of quantum mechanics. This equation is a differential equation which predicts how the wave function $\Psi(\mathbf{r}, t)$ evolves in an external energy potential U (Schrödinger, 1926):

$$\left(-\frac{\hbar^2}{2m}\left(\frac{\partial}{\partial x^2}+\frac{\partial}{\partial y^2}+\frac{\partial}{\partial z^2}\right)+U\right)\Psi(\mathbf{r}, t)=i\hbar\frac{\partial\Psi(\mathbf{r}, t)}{\partial t} \tag{2.52}$$

Quantum theory reduces to classical mechanics when the uncertainties on the position and impulsion are negligible. At temperature T, the average impulsion is $|\mathbf{p}| = \sqrt{3mk_BT}$. Following the Heisenberg uncertainty principle (Heisenberg (1927), English translation by Wheeler and Zurek (1983)), the thermal de Broglie wavelength $\Lambda = h/\sqrt{2\pi mk_BT}$ is the length scale above which the quantum effects can be neglected. At ambient temperature, quantum effects cannot be neglected for electrons ($\Lambda \approx 10$ nm) but the classical approximation is valid for atoms ($\Lambda \approx 1$ Å). Except for very

specific systems (like the hydrogen atom for instance), the Schrödinger equation cannot be solved exactly. Numerical methods exist which yield approximate solutions, but these methods are unable to compute systems larger than a few dozens of atoms. Molecular mechanics is an alternative approach based on classical mechanics, which can handle much larger systems up to thousands of atoms. Molecular mechanics ignores the motion of the electrons; the energy of the system is described by effective potentials, which depend on the nuclear positions only. The reliability of molecular mechanics relies on the representativity of the effective inter-atomic and inter-molecular potentials.

2.3.2 Inter-atomic and inter-molecular interactions

The inter-atomic and inter-molecular interactions we encountered in this work are presented in this section (Israelachvili, 1992).

Steric repulsion: At small inter-atomic distances, a strong repulsive force appears between molecules, which determines how close two molecules can be. This repulsion arises from the overlap of the electronic cloud of nearby molecules. Since electrons are fermions, they follow the Pauli exclusion principle (Pauli, 1925). According to this principle, the electrons of an atom cannot occupy the same quantum state, from what follows that they are organized in shells. This shell structure of the atoms defines a 'volume' occupied by the atoms. When the electron shells of two distinct molecules overlap, a strong repulsion arises since Pauli exclusion principle prevents the electrons of the external shell from moving toward the inner shells. This interaction is called the steric repulsion. The repulsion originates from quantum effects. No general equation describes how this repulsion depends on the distance between particles. The most common empirical potentials used to describe the steric repulsion are the hard sphere potential, the inverse power law potential and the exponential potential (Fig. 2.5).

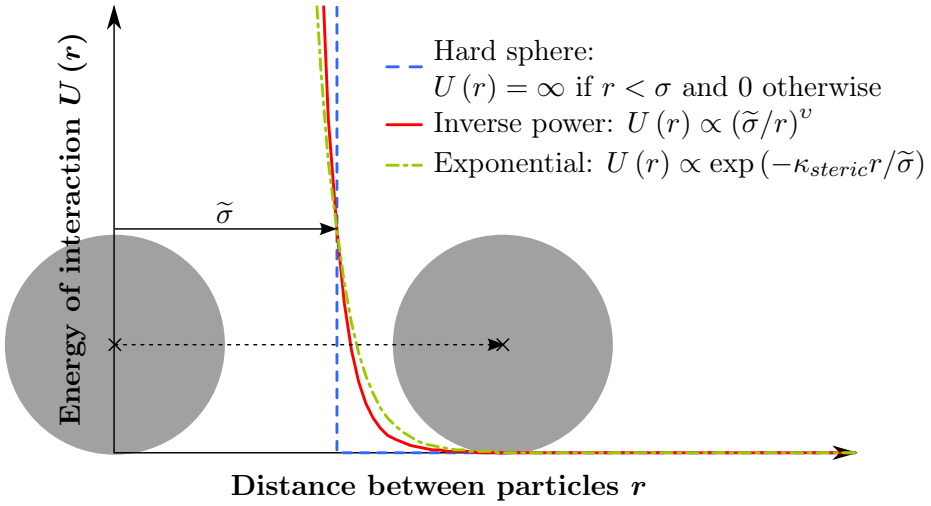

Figure 2.5. *Empirical potentials for the steric repulsion. $\widetilde{\sigma}$ represents the diameter of the particles.*

Chemical bond: When two or more atoms form a molecule, the force that tightly binds the atoms within the molecules are chemical bonds. The distance between chemically bonded nuclei is much smaller than the minimum inter-atomic distance involved in the steric repulsion, because the atoms are sharing electrons. Covalent bonds and metallic bonds are the most usual forms

of chemical bond. Chemical bonds are quantum mechanical in nature. Each atom is able to share a limited number of electrons depending on its valence, an intrinsic propriety of the electronic structure of the atom. Moreover, chemical bonds have preferential orientations. A set of atoms in a molecule is organized in a specific atomic structure: the energy of interaction of each chemical bond cannot be considered independently from the other chemical bonds. Therefore, there is no simple analytical formulation of the energy of interaction between chemically bonded atoms. However, effective potentials exist, which approximately describe the energy of interaction of chemical bonds. The simplest effective representation of chemical bonding (Leach, 2001) includes bond stretching (with Morse or harmonic potentials), angle bending and torsional terms (Fig. 2.6). This simple representation is valid if the sampled atomic configurations are near the equilibrium structure of the molecule. In contrast, reactive potentials are able to account for fundamental changes in the atomic structure of the molecule. Such potentials are more versatile but also more complex to implement. In this work, we considered the REBO reactive potential for carbonaceous materials (Brenner, 1990, Stuart et al., 2000).

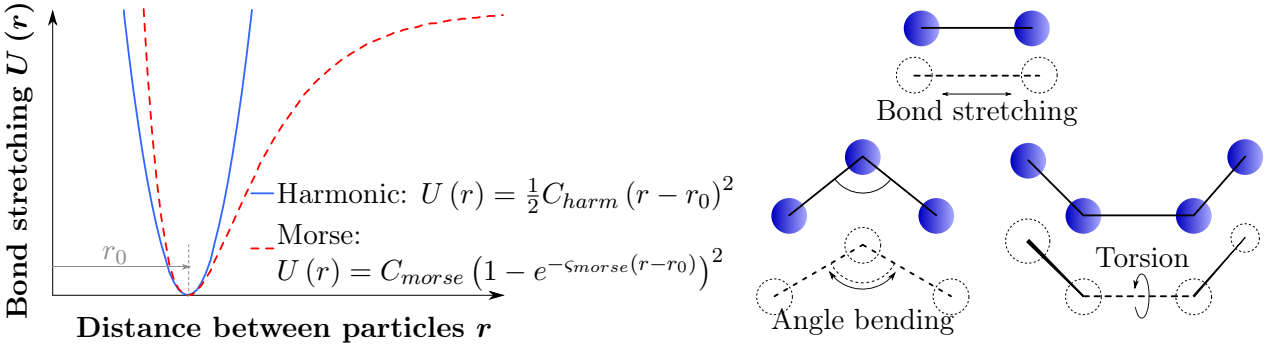

FIGURE 2.6. *Simple representation for the interaction energy of chemical bonds.*

Electrostatic interactions: Since all atoms are made of charged particles, namely the electrons and the protons, interactions between molecules always involve electrostatic interactions. The most elementary electrostatic interaction is the interaction between two point charges of electric charges q_i and q_j located at locations $\mathbf{r}_i$ and $\mathbf{r}_j$ in vacuum, for which the energy of interaction U is:

$$U = \frac{1}{4\pi\varepsilon_0}\frac{q_i q_j}{r} \tag{2.53}$$

where ε_0 is the vacuum permittivity and $r = |\mathbf{r}_i - \mathbf{r}_j|$ is the distance between the point charges. The electrostatic interaction between molecules with a permanent charge, i.e., ionic species, can be assimilated to an interaction between point charges located at the center of charge of each molecule. If the charge of the electronic cloud is equal to the charge of the nucleus, the total charge is zero, but the molecule can be polar, i.e., the center of charge of the negative charges is not located at the same position than the center of charge of the positive charges. A polar molecule can be assimilated to a dipole, i.e., two opposite point charges separated by a finite distance. The energy of interaction between a dipole and a point charge is the sum of two point charges interaction (Eq. 2.53) which are nearly opposite. A first order expansion shows that the energy between a dipole and a point charge is proportional to r^{-2} and is much smaller than the energy of interaction between two point charges (Israelachvili, 1992). Similarly, the interaction between two polar molecules can be approximated by the

interaction between two dipoles, which is proportional to r^{-3} in a first order approximation. The same logic applies to nonpolar molecules which have a multipole of higher order. Carbon dioxide, for instance, is quadrupolar and can be assimilated to three point charges (Fig. 2.9). In a first order expansion, the energy of interaction between two molecules of carbon dioxide is proportional to r^{-5}.

Induced electrostatic interactions: Any nonpolar molecule can be polarized when submitted to an external electric field. This polarization arises from the displacement of the negatively charged electronic cloud relatively to the positively charged nucleus under the influence of the external electric field. A simple representation of the polarization is displayed in Fig. 2.7, in which an electron which circles around the nucleus is sketched. The polarizability α characterizes the dependence of the induced dipole moment $\mathbf{u}_{ind}$ to the external electric field E: $\mathbf{u}_{ind} = \alpha\mathbf{E}$. The energy of interaction between a point charge q and a molecule polarized by the electric field of the point charge is:

$$U = -\frac{1}{2\left(4\pi\varepsilon_0\right)^2}\frac{\alpha q^2}{r^4} \tag{2.54}$$

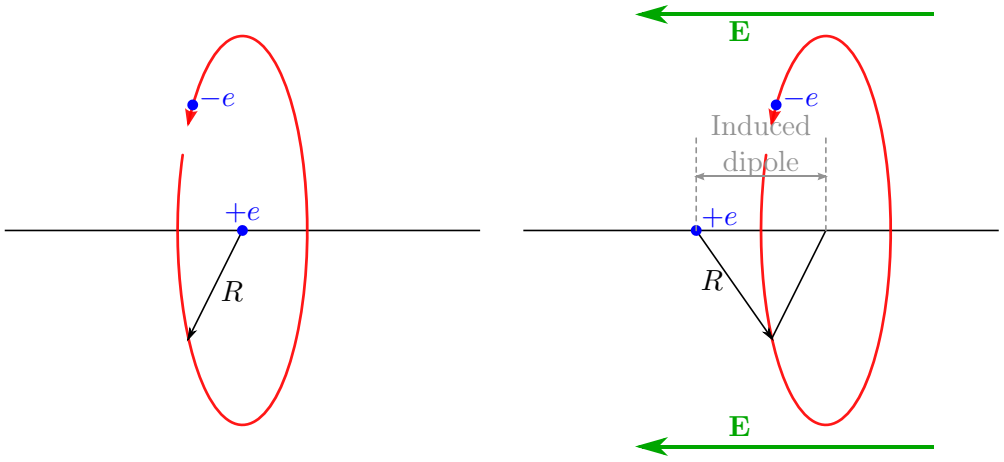

Figure 2.7. *Sketch of an induced dipole in a one electron atom. Adapted from Israelachvili (1992).*

London dispersion force: The London dispersion force exists between all molecules and corresponds to a specific interaction distinct from the electrostatic or induced electrostatic interactions. Dispersion forces are quantum mechanical in origin but can be interpreted as the interaction between the instantaneous dipoles of the molecules. Indeed, even if a molecule is nonpolar, at any time there exists a finite dipole moment given by the instantaneous position of the electrons in the electronic cloud. This instantaneous dipole generates an electric field which polarizes the nearby molecules. Thus, even two nonpolar molecules interact. The London dispersion force is an attractive force, and was derived by London (1937) using quantum mechanical perturbation theory. The energy U of interaction due to London dispersion forces is:

$$U = -\frac{C_{disp}}{r^6} \tag{2.55}$$

where the coefficient C_{disp} can be related to the polarizability of the atoms considered and to the orbiting frequencies of the electrons around the atoms.

2.3.3 Simplified models

In a molecular simulation, the calculation of the energy of interaction is by far the most expensive step in terms of computational cost. Therefore, simplified models of the inter-atomic and inter-molecular interactions are used. Chemical bonds can be modeled with bond stretching, angle bending, and torsional terms (see Sec. 2.3.2). This representation is very efficient since the computation of the energy of interaction scales in $O(N)$, where N is the number of atoms.

The energy of interaction between fluid molecules is commonly modeled with the Lennard-Jones potential U_{LJ}, which takes into account the steric repulsion and the London dispersion force:

$$U_{LJ} = 4\widetilde{\varepsilon}\left(\left(\frac{\widetilde{\sigma}}{r}\right)^{12} - \left(\frac{\widetilde{\sigma}}{r}\right)^{6}\right) \tag{2.56}$$

where $\widetilde{\sigma}$ and $\widetilde{\varepsilon}$ are the Lennard-Jones parameters. $\widetilde{\sigma}$ is characteristic of the size of the molecule and $\widetilde{\varepsilon}$ is the minimum of the energy.

Special care should be dedicated to the induced electrostatic interactions and to the London dispersion forces, which are not pairwise additive: indeed, the energy of interaction between two molecules is influenced by the presence of molecules nearby and the total energy of interaction due to induced electrostatic interactions and to London dispersion forces cannot be obtained by addition of pair potentials. Analytical expressions were derived to account for many body interactions (Leach, 2001). Alternatively, a significant proportion of the many body effects can be captured with properly parametrized effective pair potentials. These effective potentials are not the actual energy of interaction between two isolated molecules. The relative difference between the energy of interaction of isolated molecules and the effective potential is usually less than 20% (Israelachvili, 1992). The use of effective pair potentials limits the computational cost to that of two body interactions, i.e., $O\left(N^2\right)$, which is significantly better than that of three body interactions which scale in $O\left(N^3\right)$.

Simplified potentials can also be used to avoid considering unnecessary degrees of freedom, i.e., degrees of freedom for which all configurations are nearly equiprobable. This is the case for the orientation of polar molecules in a medium of high permittivity, in which the molecules can rotate almost freely. This is also the case for the methane molecule, for which the steric repulsion, the dispersion forces, and the polarizability depend on the orientation because of the tetrahedral atomic structure, but which is almost free to rotate at ambient temperature. The criterion to determine whether a degree of freedom needs to be taken into account explicitly is to compare the maximum energy change associated with this degree of freedom to $k_B T$. If the energy change is small with respect to $k_B T$, the Boltzmann-Gibbs distribution (Eq. 2.16) yields an almost equal probability of occurrence for all configurations which only differ by this degree of freedom. A simplified potential of energy can be used which no more depends on the degrees of freedom deemed unnecessary. Integrating the Boltzmann-Gibbs distribution over the unnecessary degrees of freedom $\mathbf{x}_{un}$, we have:

$$\exp\left(-\frac{U(\mathbf{x})}{k_B T}\right) = \int_{\mathbf{x}_{un}} \exp\left(-\frac{U(\mathbf{x}, \mathbf{x}_{un})}{k_B T}\right) \mathbf{dx}_{un} \tag{2.57}$$

where $\mathbf{x}_{un}$ is the set of degrees of freedom that we do not need to take into account explicitly and where $\mathbf{x}$ stands for the remaining degrees of freedom. A series expansion gives (Israelachvili, 1992):

$$U(\mathbf{x}) = \left\langle U(\mathbf{x}, \mathbf{x}_{un}) - \frac{(U(\mathbf{x}, \mathbf{x}_{un}))^2}{2k_B T} \right\rangle \tag{2.58}$$

For methane molecules for instance, quantum calculations show that the energy of interaction between molecules depends on the relative orientation of the molecules (see Fig. 2.8). In the present work, we used a simplified pairwise Lennard-Jones potential which does not model the dependence of the energy of interaction on the orientation of the molecules.

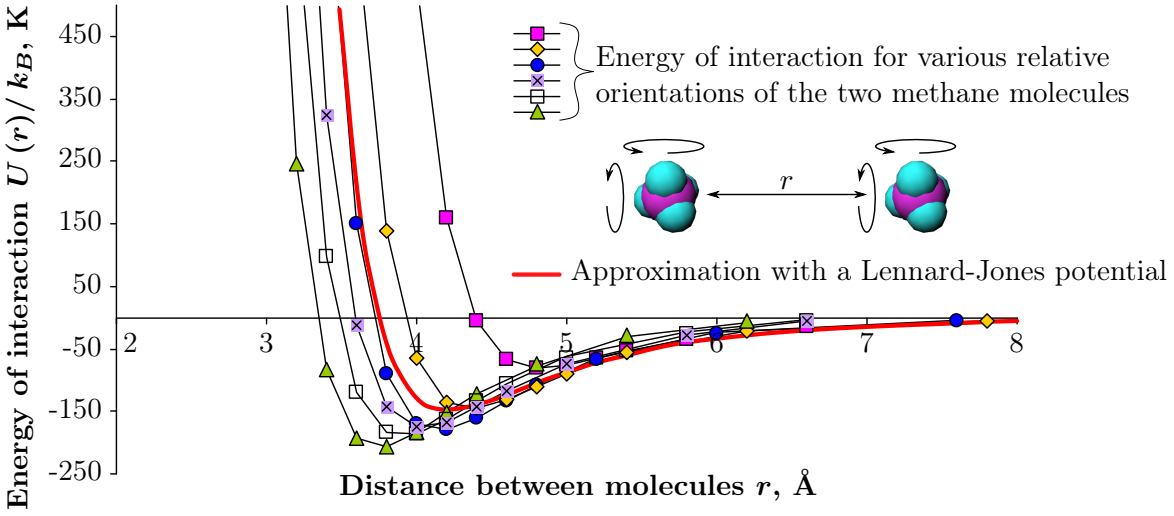

Figure 2.8. *Dependency of the energy of interaction between two methane molecules on the relative orientation of the molecules and average Lennard-Jones potential. The energy of interaction for the various orientations is estimated by Tsuzuki et al. (1998) with ab initio methods. The Lennard-Jones potential is the potential used in the present work and was proposed by Kurniawan et al. (2006) for supercritical methane.*

We also simplified the electrostatic interaction between electronic clouds. The electronic cloud is a charge distributed in space and the calculation of the electrostatic energy between continuous charge distributions is computationally expensive. An approximation consists in replacing the electronic cloud with an effective set of point charges. The set of point charges must generate an electric field near the molecule that is as similar as possible to the electric field generated by the actual continuous distribution of charges. A common practice consists in positioning point charges on the atomic nuclei. We display in Fig. 2.9 the example of the carbon dioxide molecule. The electronic cloud obtained by quantum calculation can be assimilated to three point charges at the centers of the carbon and oxygen atoms. For large atomic structures however, the electronic cloud cannot be computed by quantum calculations; other methods were developed to derive effective sets of point charges for such large structures (Leach, 2001). In the present work, we considered two methods to derive the set of charges in the coal matrix: the 'partial equalization of orbital electronegativity' (PEOE) (Gasteiger and Marsili, 1980) and the 'charge equilibration method' (QEq) (Rappe and Goddard, 1991).

2.4 Summary

At the microscopic scale, matter is made of atoms and molecules, whose motion is governed by the inter-atomic and inter-molecular interactions. At this scale, a system is fully determined by the

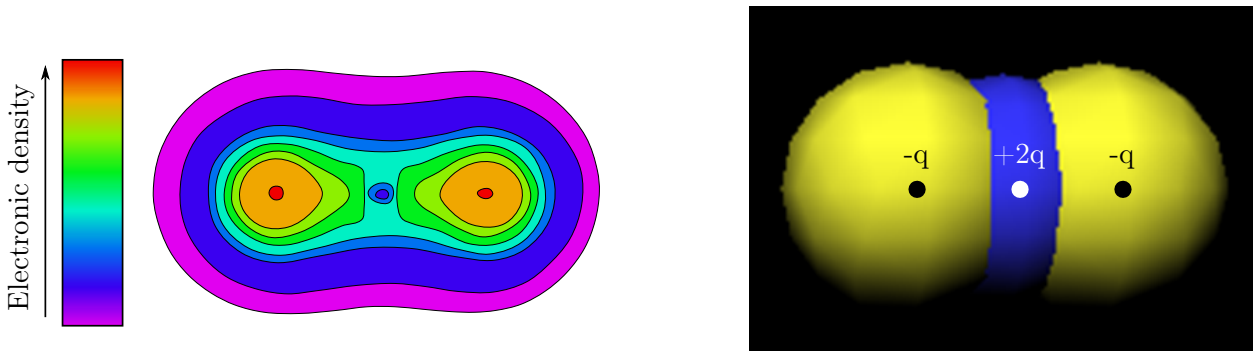

FIGURE 2.9. *Set of point charges (right) equivalent to the continuous charge distribution (left) in the CO_2 molecule.*

location and impulsion of these particles. By contrast, at the macroscopic scale, thermodynamics provides a description of the same system based on a few macroscopic properties (temperature, pressure, chemical potential...). Statistical physics aims at relating these macroscopic properties to the motion of the particles that make up this system at the microscopic scale. Statistical physics shows that the evolution of a molecular system with time leads to the Boltzmann-Gibbs probability distribution of the molecular configurations. At the microscopic scale, a thermodynamic property is not constant but its instantaneous value varies from one molecular configuration to the other. The macroscopic value of a thermodynamic property is the average of the instantaneous value over time (time-average) or, equivalently, over a sampling of molecular configurations following the Boltzmann-Gibbs distribution (ensemble-average).

In this thesis, we use Monte Carlo molecular simulations to study adsorption. Monte Carlo simulations, based on the Metropolis algorithm, consist in sampling the molecular configurations according to the Boltzmann-Gibbs distribution. The macroscopic properties are computed as ensemble-averages. Molecular interactions, which govern the evolution of a system at the molecular scale, are accounted for with effective potentials representing the various interactions between atoms and molecules: steric repulsion, chemical bonding, electrostatic and induced-electrostatic interactions, and London dispersion forces.

Chapter 3

Adsorption and mechanical behavior

THIS CHAPTER *presents the scientific context of this thesis. Adsorption of fluid in a solid corresponds to a variation of the fluid concentration in the vicinity of the solid. The adsorption phenomenon originates from the molecular interactions between the molecules of the fluid and the atoms of the solid. How adsorption depends on the pressure of the fluid is the focus of most classical models for adsorption. However, these models disregard the coupling between adsorption and deformation, while many materials (among which coal) exhibit adsorption-induced deformations. The mechanical effect of surface adsorption is captured with the notion of surface stress which acts in the plane of the fluid-solid interface. When the size of the pores is of the order of the range of the molecular interactions, a mechanical pressure also arises orthogonal to the interface: for slit pores, such a pressure is the disjoining pressure. At the molecular scale, the virial equation relates the mechanical stress, the surface stress, and the disjoining pressure to the interactions between particles. However, the notions of surface stress and disjoining pressure can not be easily applied to pores with complex morphology, such as micropores in coal, for which the notions of pore size, pore volume and interface are ambiguous. In the literature, most models of adsorption-induced strain are valid for mesoporous solids or for flat micropores. There exist also models which are valid for micropores with complex geometry, but these models are limited to the study of samples immersed in the fluid. The objective of this thesis is to develop a model which couples mechanics and adsorption and is valid for a generic microporous solid, and to apply this model to carbon sequestration in coal.*

Ce chapitre *présente le contexte scientifique de cette thèse. L'adsorption d'un fluide dans un solide correspond à un changement de la concentration de fluide près du solide. Le phénomène d'adsorption a pour origine les interactions moléculaires entre les molécules du fluide et les atomes du solide. Comment l'adsorption dépend de la pression du fluide est l'objet de la plupart des modèles classiques d'adsorption. En revanche, ces modèles négligent le couplage entre adsorption et déformation, alors que de nombreux matériaux, dont le charbon, présentent des déformations induites par l'adsorption. L'effet mécanique de l'adsorption sur une surface s'explique par la notion de contrainte de surface, qui s'exerce dans le plan de l'interface fluide-solide. Lorsque la taille des pores est de l'ordre de la portée des interactions moléculaires, une pression mécanique orthogonale aux interfaces s'ajoute. Pour les pores plans, il s'agit de la pression de disjonction. A l'échelle moléculaire, l'équation du viriel permet de relier la contrainte mécanique, la contrainte de surface et la pression de disjonction aux interactions entre particules. Cependant, les notions de contraintes de surface et de pression de disjonction ne s'appliquent pas au cas de micropores de morphologie complexe, présents dans le charbon, pour lesquels les notions de taille de pore, de volume de pore et d'interface sont ambigües. Dans la littérature, la plupart des modèles de déformation induite par l'adsorption sont valides pour des solides mésoporeux ou bien pour des micropores plans. Des modèles valides pour des micropores de géométrie complexe existent également, mais restent limités à l'étude d'échantillons immergés dans le fluide. L'objectif de cette thèse est de développer un modèle couplant mécanique et adsorption valide pour des solides microporeux quelconques et de l'appliquer à la séquestration de carbone dans le charbon.*

Outline of Chapter 3

The International Union of Pure and Applied Chemistry[1] defines the adsorption phenomenon as *"an increase in the concentration of a dissolved substance at the interface of a condensed and a liquid phase due to the operation of surface forces. Adsorption can also occur at the interface of a condensed and a gaseous phase."* The adsorption phenomenon originates from the molecular interactions between a solid and a fluid, which modify the state of the fluid in the vicinity of the solid. The adsorption phenomenon occurs whatever the solid and the fluid, but becomes significant when the interactions between the molecules of the fluid and the molecules of the solid are strong. Figure 3.1 sketches adsorption on a solid surface.

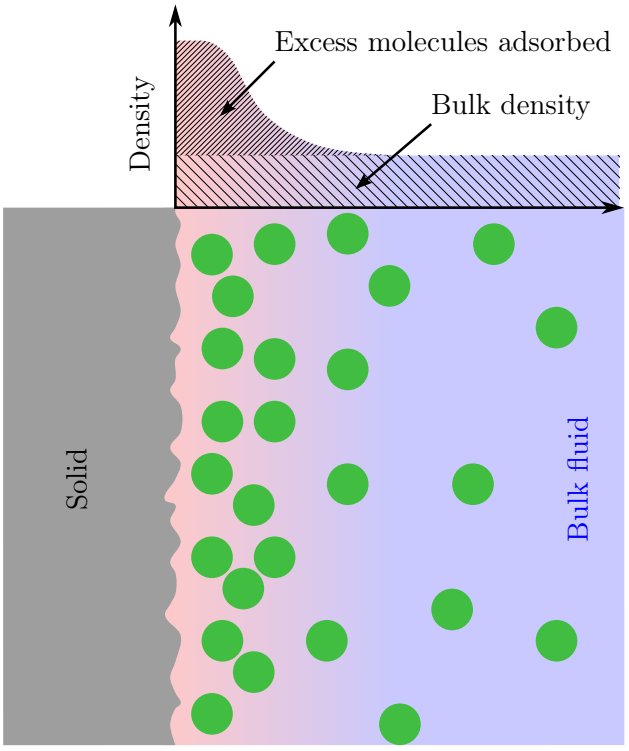

Figure 3.1. *Sketch of the adsorption phenomenon.*

By contrast with *"an increase in the concentration of a dissolved substance"*, we would more generally define adsorption as a 'variation in the concentration of a fluid component at the interface of a condensed and a fluid phase due to the operation of surface forces': indeed, the presence of an interface can lead to a lack of fluid in the vicinity of this interface, if the energy of interaction of a fluid molecule with another fluid molecule is lower than with an atom of the condensed phase. The adsorbed fluid can be a gas, a liquid, or a supercritical fluid; it can be a pure component fluid or a mixture. The adsorption takes place 'near the solid', i.e., at a distance to the solid that is comparable to the range of the molecular interactions. Fluid molecules can be adsorbed at the surface of a solid, but also inside a solid if this solid is porous. Regarding the sequestration of carbon in coal, a supercritical mixture of carbon dioxide and methane is adsorbed in the coal matrix.

The adsorption phenomenon can be quantified with laboratory experiments, the most common of which being the gravimetric method and the volumetric method. These experiments aim at determining the amount of fluid adsorbed as a function of the bulk pressure of the fluid. The gravimetric method is based on the measurement of the increase of mass of the solid when immersed

[1]IUPAC - http://www.iupac.org/

in the fluid. The adsorbent, usually in the form of a powder, is placed on a high precision balance and is immersed in the fluid, whose pressure is controlled. The increase in mass of the solid is measured. Because of the buoyancy, the mass which is measured is not the total mass of fluid in the solid but the mass of fluid adsorbed in excess of the mass of bulk fluid (Fig. 3.1). In the volumetric experiment, the bulk volume of the fluid in the pores of the solid is measured. The volume of the porous space is determined first by using a weakly adsorbing gas such as helium. The excess volume adsorbed is the difference between the total bulk volume of fluid in the pores and the volume of pores determined with helium. Alternatively, one can measure the bulk pressure of the fluid while imposing the bulk volume injected in the solid. This alternative method is called the manometric method. How the amount of adsorbed fluid depends on the bulk pressure of the fluid at a fixed temperature is called an adsorption isotherm. According to the International Union of Pure and Applied Chemistry, adsorption isotherms can be gathered into six categories (Sing et al., 1985). Adsorptions of methane and carbon dioxide in coal are type I isotherms. Adsorption is said to be a chemical adsorption if the adsorbed fluid molecules form a chemical bond with the solid skeleton. Otherwise, adsorption is said to be a physical adsorption. The energy of interaction between an adsorbed fluid molecule and the solid is generally much lower in the case of chemical adsorption than in the case of physical adsorption. Moreover, like most chemical reactions, chemical adsorption often involves an energy of activation, thus being an irreversible process.

In this chapter, we focus on the scientific understanding of the adsorption-induced swelling. First, we introduce the fundamentals of adsorption starting from the basics of statistical physics. In addition to coal, several examples of adsorption-induced deformations are presented. Then, we recall the thermodynamics of interface stress and disjoining pressure, which can explain the mechanical effect of adsorption at the macroscopic scale. We also present a more detailed vision of these mechanical effects at the molecular scale. Finally, the existing models for adsorption-induced strain are presented and discussed.

3.1 Adsorption phenomenon

In this section we present the most common analytical models used to describe adsorption. These models disregard the coupling between adsorption and strain. Then we give a few examples in which adsorption induces strain.

3.1.1 Models for adsorption

We consider a system made of a solid surface in contact with a fluid phase. The system extends far enough in the fluid phase so that some fluid molecules do not interact with atoms of the solid. The molecules of the fluid are free to enter or exit the system. At equilibrium, the chemical potential of the molecules of the fluid is the same everywhere in the system, far from as well as near the interface. But the molecular interactions near the atoms of the solid differ from the molecular interactions inside the bulk fluid. According to the the Boltzmann-Gibbs distribution in the grand canonical ensemble (Eq. 2.19), the density of fluid molecules increases in the vicinity of the solid surface if the energy of interaction per fluid molecule is lower near the solid than in the bulk fluid. Conversely, if the energy of interaction per fluid molecule is larger near the solid than in the bulk fluid, the density of fluid molecules decreases near the interface (Fig. 3.2). In the case of fluid mixtures, depending on specific chemical affinities, the presence of the solid surface can modify the density of the different species in different manners.

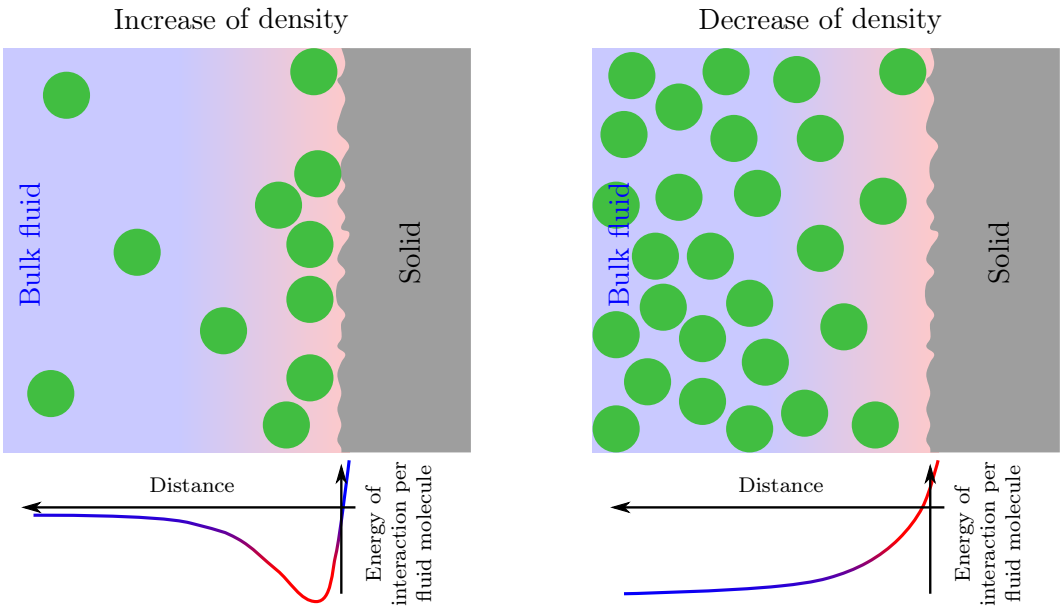

Figure 3.2. *Influence of the fluid-fluid and fluid-solid energies of interaction on the fluid density near the solid.*

The adsorbed densities can be estimated precisely by molecular simulation. But, for some simple situations, the adsorption isotherm can be derived analytically. For instance, let us consider that the fluid can only be adsorbed on N_{site} specific adsorption sites, at the location of which the energy of an adsorbed molecule is equal to U_{ads} (see Fig. 3.3). This situation corresponds, for instance, to the adsorption of one layer of gas on a solid surface at small temperature. The energy of interaction of a fluid molecule with an atom of the solid is assumed to be much lower than with another fluid molecule.

A micro-state u is made of N_u adsorbed molecules of fluid. Neglecting the kinetic energy at small temperature, the total energy of the system is the interaction energy $N_u U_{ads}$. According to the Boltzmann-Gibbs distribution (Eq. 2.19), the probability of occurrence of a micro-state is:

$$p_u = \frac{1}{Z_{GC}} \exp\left(-N_u \frac{U_{ads} - \mu}{k_B T}\right) \tag{3.1}$$

where the partition function $Z_{GC} = \sum_u \exp\left(-N_u \frac{U_{ads}-\mu}{k_B T}\right)$ is a sum over all micro-states. There are $N_{site}!/(N!\,(N_{site}-N)!)$ micro-states for which N molecules are adsorbed on N_{site} sites. Making use of the binomial formula, the partition function is:

$$Z_{GC} = \sum_{N=0}^{N_{site}} \frac{N_{site}!}{N!\,(N_{site}-N)!} \exp\left(-N \frac{U_{ads} - \mu}{k_B T}\right) = \left(1 + \exp\left(-\frac{U_{ads} - \mu}{k_B T}\right)\right)^{N_{site}} \tag{3.2}$$

The average proportion of occupied adsorption sites $\langle N \rangle / N_{site}$ can be determined:

$$\begin{aligned}\frac{\langle N\rangle}{N_{site}} &= \frac{1}{Z_{GC}}\sum_{N=0}^{N_{site}}\frac{N}{N_{site}}\frac{N_{site}!}{N!\,(N_{site}-N)!}\exp\left(-N\frac{U_{ads}-\mu}{k_BT}\right)\\ \frac{\langle N\rangle}{N_{site}} &= \frac{1}{1+\exp\left(\frac{U_{ads}-\mu}{k_BT}\right)}\end{aligned} \tag{3.3}$$

Assuming the fluid is an ideal gas, its chemical potential μ can be related to its bulk pressure P: $\mu = \mu_0 + k_BT\ln(P)$, where μ_0 is the chemical potential at a pressure of 1 Pa and is a function of the temperature only. The proportion of occupied sites can then be rewritten:

$$\frac{\langle N\rangle}{N_{site}} = \frac{P}{P+P_0} \text{ with } P_0 = \exp\left(\frac{U_{ads}-\mu_0}{k_BT}\right) \tag{3.4}$$

Equation (3.4), also known as the Langmuir isotherm (Langmuir, 1916), relates the adsorbed amount to the pressure of the fluid at a given temperature. The Langmuir isotherm is displayed in Fig. 3.4. The shape of this isotherm is often observed in adsorption experiments, especially at low pressures. Such a shape corresponds to the first category of isotherms in the classification of the International Union of Pure and Applied Chemistry and is characteristic of physical adsorption (Sing et al., 1985). The main assumptions of the Langmuir model are that the adsorption of a molecule is not influenced by the fluid molecules nearby and that adsorption occurs on equivalent sites only (see Fig. 3.3).

Other analytical models have been derived to account for more complex situations. The BET isotherm extends Langmuir-type adsorption to multilayer adsorption (Brunauer et al., 1938). The BET adsorption is based on the assumption that each adsorbate molecule in the closest layer to the solid surface can be used to form a second adsorbed layer. This second layer is an adsorption site for a third layer, and so on. The adsorption in second and subsequent layers is assumed to be equivalent to a condensation of gas molecules on a liquid surface, so that the energy U^1_{ads} of adsorption in these layers differs from the energy U^0_{ads} of adsorption in the first layer. The BET isotherm can be derived from statistical physics (Hill, 1946, Bae et al., 2008). The relation between the adsorbed amount and the bulk pressure of the fluid is:

$$\frac{\langle N\rangle}{N_{site}} = \frac{B\,(P/P_{sat})}{(1-(P/P_{sat}))\,(1+(B-1)\,(P/P_{sat}))} \tag{3.5}$$

where P_{sat} is the saturation pressure at the temperature considered and the coefficient B is proportional to $\exp\left(\left(U^0_{ads}-U^1_{ads}\right)/\left(k_BT\right)\right)$. An example of BET isotherm is displayed in Fig. 3.4. The difference between the Langmuir and BET isotherms becomes significant at medium and high pressures, at which multilayer adsorption occurs in the BET model.

The Langmuir and BET models are applied to the adsorption in macro- or meso-porous solids, for which the size of the pores is large compared to the range of molecular interactions ($\approx 1-2$ nm), and are used to investigate the porous structure of such solids. For instance, in the case of Langmuir-type adsorption, assuming that each adsorption site corresponds to a given interfacial area between the solid surface and the pores, the maximum adsorbed amount can be related to the specific surface of the porous solid. However, the Langmuir and BET models are not appropriate to describe adsorption in microporous solids, for which the size of the pores is smaller than the range of inter-molecular interactions. In such microporous solids, adsorption cannot be explained by

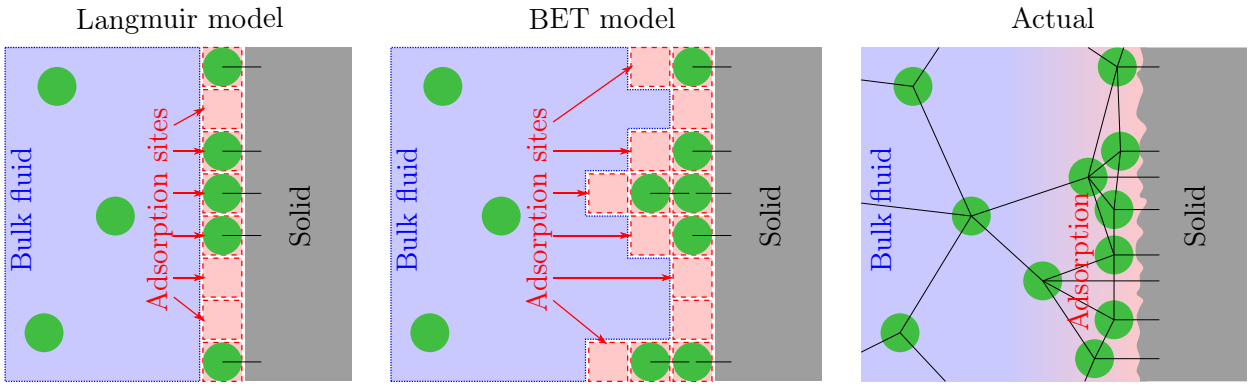

Figure 3.3. *Sketch of the Lamgmuir and BET models for adsorption on surfaces and sketch of an actual adsorption. The black lines represent the energies of interaction taken into account.*

surface covering, but rather by a pore filling mechanism. The Dubinin-Radushkevich (D-R) model is an analytical model of adsorption adapted to the case of microporous solids (Dubinin, 1967). This model assumes that the filling of micropores depends only on the energy U_{ads} of adsorption and on the ratio between the variation $\Delta\mu$ of chemical potential from the saturation pressure P_{sat} to the current pressure P. For an ideal gas, $\Delta\mu = k_B T \ln(P_{sat}/P)$. The energy U_{ads} of adsorption is related to the energy U^0_{ads} of adsorption of a reference species through $U_{ads} = \beta U^0_{ads}$, where β is called the affinity coefficient. In the case of carbonaceous adsorbent, the proportion of filled micropores is:

$$\frac{\langle N\rangle}{N_{site}} = \exp\left(-\left(D\ln(P_{sat}/P)\right)^2\right) \text{ with } D = \frac{k_B T}{\beta U^0_{ads}} \tag{3.6}$$

An extension of the Dubinin-Radushkevich isotherm is the Dubinin-Astakhov isotherm (Dubinin and Astakhov, 1971): $\langle N\rangle/N_{site} = \exp\left(-\left(D\ln(P_{sat}/P)\right)^{\nu}\right)$, where ν is a supplementary parameter. The Dubinin-Astakhov isotherm can be applied to a wider range of adsorbent. The Dubinin-Radushkevich model is an empirical model and is not perfectly consistent with the underlying physics. In particular, it does not reduce to Henry's law at low pressures and its validity is limited to $\langle N\rangle/N_{site} > 0.15$. As such, the D-R isotherm cannot be derived from statistical physics. Many extensions and modifications of the initial D-R isotherm have been proposed (Hutson and Yang, 1997), some of which were derived from statistical physics: Chen and Yang (1994) derived an isotherm equation from statistical physics which reduces to the D-R isotherm for pore filling $\langle N\rangle/N_{site}$ larger than 0.1. For $\langle N\rangle/N_{site} \to 0$ their equation is consistent with Henry's law.

We display in Fig. 3.4 an example of a Dubinin-Radushkevich isotherm. The general shape of the D-R isotherm is similar to that of the Langmuir isotherm. Adsorption in coal has been studied within the framework of these analytical models. White et al. (2005) reviewed adsorption experiments, focusing on CO_2 and CH_4 adsorption for ECBM. The D-R isotherm, its derivatives, and the Langmuir isotherm all fit reasonably well the experimental data in the range of pressures and temperatures of interest for ECBM. The D-R isotherm, based on pore filling theory, is more representative of the adsorption phenomenon in the microporous coal matrix, but is not for adsorption in larger pores. Experimental data of adsorption do not allow to distinguish in detail the adsorption mechanisms in coal: is the adsorption of carbon dioxide a multilayer adsorption? How does the competitive adsorption of fluid mixtures occur? What is the impact of the heterogeneity of the adsorption energy from one site or micropore to another? Molecular simulations, which we

use in this thesis, are an alternative to laboratory experiments, that make it possible to investigate these questions.

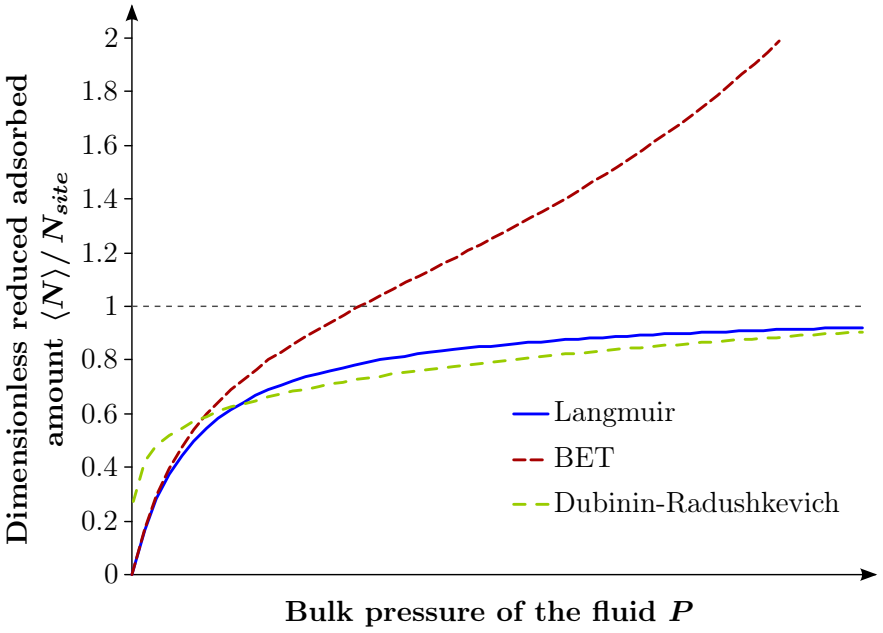

FIGURE 3.4. *Examples of Langmuir, BET and Dubinin-Radushkevich isotherms.*

3.1.2 Examples of adsorption-induced deformation

The models for adsorption described in the previous section do not take into account the deformability of the solid. However, we know that adsorption can induce deformations. Coal is an example of such a phenomenon: coal swells in presence of carbon dioxide. But there are many other materials, for which the mechanical behavior is influenced by adsorption. In this section, we present a few other examples of adsorption-induced deformation.

Wood shrinks and swells depending on its moisture content (see Fig. 3.5). At the micrometer scale, wood is a heterogeneous anisotropic material made of stacked tubular cells (Derome et al., 2011). The walls of these cells are composed primarily of cellulose and lignin, which are microporous solids in which water molecules can adsorb. When wood is exposed to humidity, water molecules adsorb in the walls of the cell and induce a swelling. Conversely, when wood is dried, water molecules desorb and desorption induces a shrinkage. Derome et al. (2011) observed the swelling of the cells by X-ray tomography and reported a total volumetric swelling larger than 10% upon full imbibition. In practice, the adsorption-induced deformation of wood leads to a degradation of the material over time: the uneven exposure of wood elements to humidity generates differential strains inside the material, which can generate high stresses and eventually cracking.

The swelling of clay is also a well known example of adsorption-induced deformation. Clay is a mineral made of fine platelets covered with electric charges (see Fig. 3.6b). The platelets are self-aligned and the interstitial space between two platelets is a slit pore in which adsorption can occur. In saturated conditions, when the slit pore is filled with water, the concentration in ions inside the pore is highly influenced by the electrostatic charges covering the platelets. The difference in ions concentration between the external environment and the pore generates a mechanical stress which makes the slit pore deform. Analytical calculations on the slit pore geometry explain why

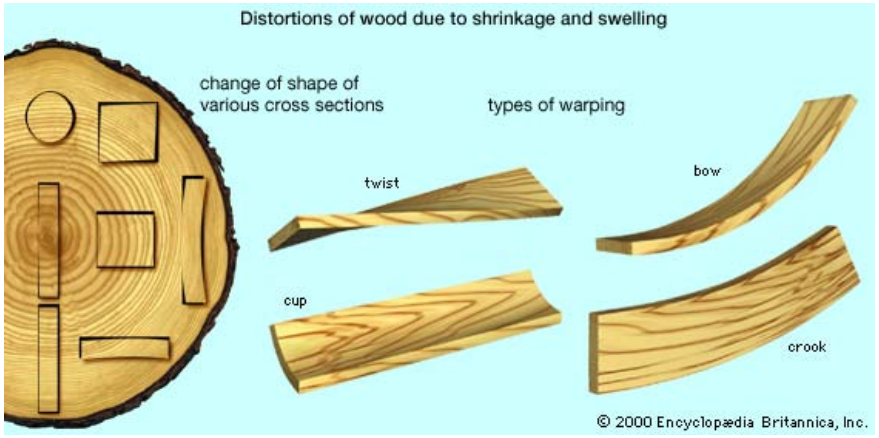

Figure 3.5. *Wood: shrinkage and swelling. Credit: Encyclopædia Britannica Online*[a].

[a]Art. Encyclopædia Britannica Online. Web. 11 May. 2011. http://www.britannica.com/EBchecked/media/55254/Distortions-in-sawn-wood-due-to-shrinkage-and-swelling-At

clay shrinks when moved from a freshwater environment to a seawater environment (Coussy, 2010). Apart from the effect of a solute, the adsorption of water itself can affect the mechanical behavior of clay. Excessive or insufficient water exposure causes the clay to swell or shrink, respectively. In practice, such a phenomenon has many consequences: desiccation cracks (see Fig. 3.6a), soil movements, risks for building foundations, degradation of constructions made of mudbricks (Anger and Fontaine, 2009).

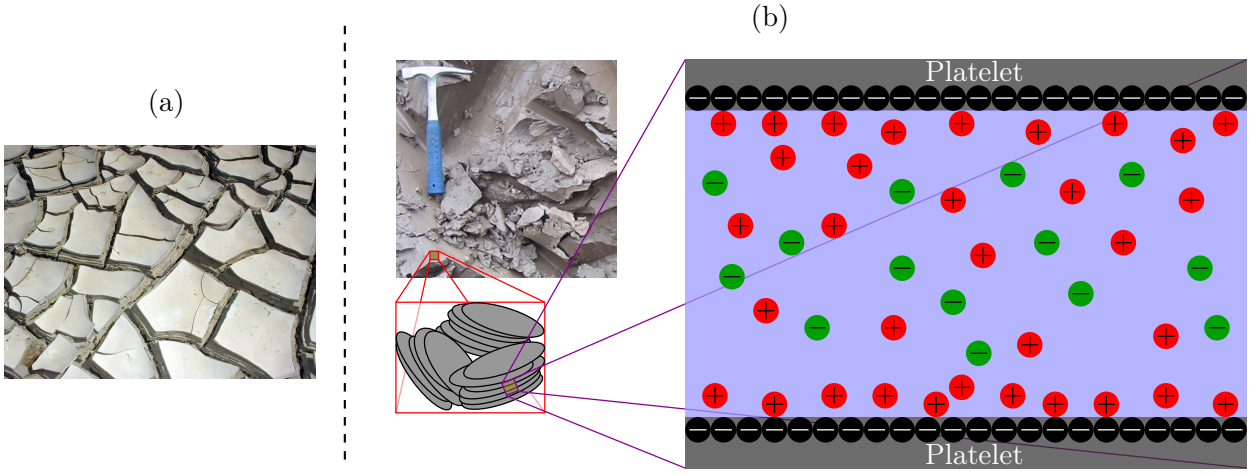

Figure 3.6. *Desiccation cracks resulting from the drying of a flood deposit (a) and sketch of the micro-structure of clays (b). Credit for Fig. (a): Joe Capesius, United States Geological Survey - from Wikipedia may* 10^{th}*, 2011. Fig. (b) is adapted from Coussy (2010).*

Hybrid organic-inorganic frameworks are microporous crystalline materials made of inorganic particles connected with organic molecules. These materials are very good adsorbent and are very promising in the fields of gas separation, energy storage, drug delivery, or catalysis. Such hybrid frameworks exhibit a variety of guest-induced structural phase transitions upon gas adsorption and desorption. The case of MIL-53 (see Fig. 3.7) is typical of an adsorption-induced deformation: the molecular structure is bistable and changes from a 'narrow pore' configuration to a 'large pore' configuration when the pressure of the fluid is increased. Coudert et al. (2008) proposed a stability

analysis to determine which configuration is stable in function of the pressure of the fluid. The capacity of adsorption of MIL-53 is enhanced significantly by this adsorption-deformation coupling.

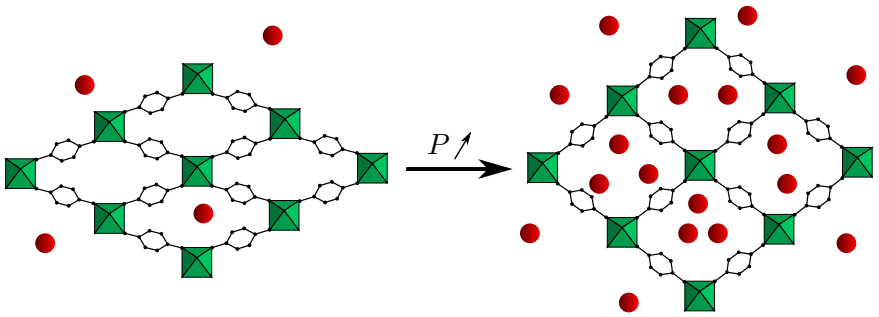

FIGURE 3.7. *Breathing of MIL-53 metal organic framework upon adsorption. P is the bulk pressure of the fluid.*

Edmiston and Underwood (2009) studied swellable organically modified silica that swell up to eight times their initial volume upon adsorption of organic compounds. These materials are interesting because they are hydrophobic and do not adsorb water at all. Therefore, organic compound can be effectively separated from water, which is promising for water treatment. The mechanism proposed to explain this adsorption-induced deformation is the opening of nanometer-scale pores consecutive to an initial adsorption (see Fig. 3.8).

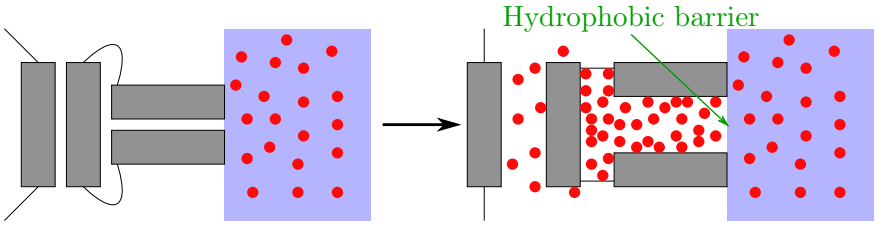

FIGURE 3.8. *Micropore opening of swellable organically modified silica. Adapted from Edmiston and Underwood (2009).*

All these examples show that adsorption and mechanical behavior are coupled phenomena. How adsorption induces a deformation and how a deformation affects adsorption are scientific questions of interest. In the following sections, we present the physical origin of adsorption-induced strain and we discuss the existing models that describe this coupling.

3.2 Adsorption-induced strain at the macroscopic scale

At the macroscopic scale, in the case of surface adsorption, the thermodynamics of interfaces is an appropriate tool to study how adsorption causes strain. The adsorption of a fluid on a fluid-solid interface modifies the interface stress, which is a two-dimensional mechanical stress acting parallel to the interface. A mechanical stress orthogonal to the interface appears when two parallel fluid-solid interfaces are separated by a distance which is smaller than the range of molecular interactions. This latter effect is called the disjoining pressure. We introduce in this paragraph the notions of interface stress and disjoining pressure, and explain how they are modified by adsorption.

3.2.1 Interface stress

Let us consider a system made of two immiscible phases I and J, which are in contact at an interface. This system is composed of two homogeneous regions on each side of the interface, in which the properties are substantially uniform, separated by a thin layer of physical inhomogeneity in-between them, around which the properties are varying (see Fig. 3.9). The inhomogeneous layer has a thickness of the order of magnitude of the range of molecular interactions. Gibbs (1928) proposed a thermodynamical representation of such interfacial systems: the inhomogeneous layer is replaced by an infinitely thin geometrical surface, called the dividing surface, surrounded by two perfectly homogeneous phases. The energy, the entropy, and the number of molecules of the system are the sum of the energies, entropies, and numbers of molecules which the two phases would have if they remained strictly homogeneous and of an additional term which is the necessary correction arising from the presence of the transition layer. In a thermodynamic representation, the excess amounts E^s of energy, S^s of entropy and N_k^s of number of molecules of chemical species k are concentrated in the dividing surface (see Fig. 3.9).

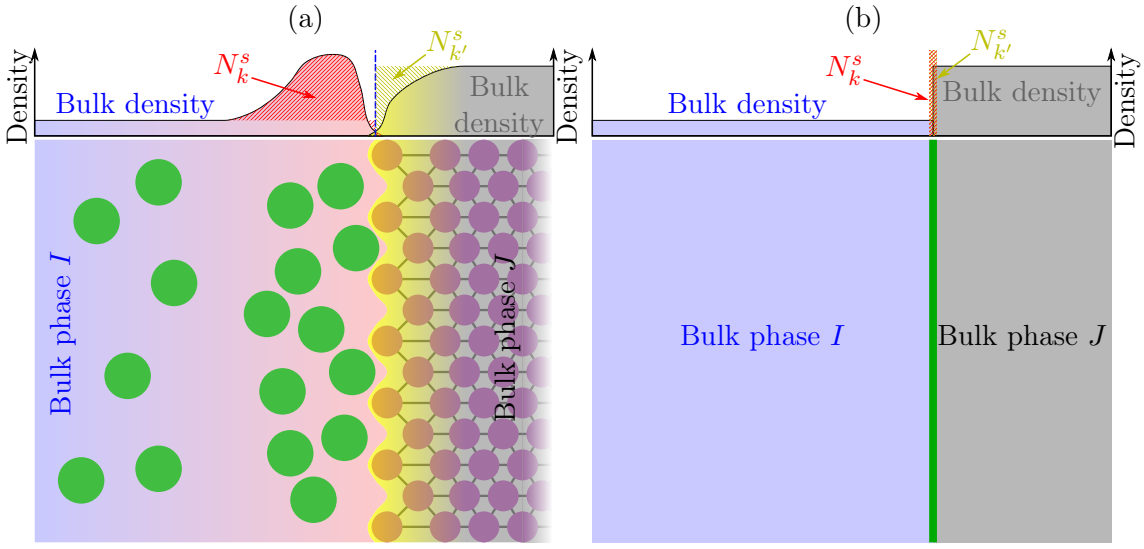

Figure 3.9. *Sketch of the inhomogeneous layer at the interface between two immiscible phases (a) and thermodynamical representation of the dividing surface (b).*

For fluid-fluid interfaces, Gibbs assumed that three state parameters are sufficient for a thermodynamic description of the interface, i.e., the area A and the two principal curvatures of the dividing surface. Gibbs showed that it is possible to choose the location of the dividing surface such that the mean curvature of this surface is zero: he proposed to use such a criterion (zero mean curvature) in order to locate this dividing surface. If a solid is involved, as is the case for adsorption, an additional state parameter must be considered, i.e., the surface strain $\epsilon^s = \ln(A/A_0)$, where A_0 is the area of the undeformed surface. The dividing surface is exchanging energy and molecules with the two homogeneous phases and, therefore, at equilibrium the temperature T and chemical potentials μ_k in the interface are the same as in the surrounding phases:

$$\left.\frac{\partial E^s}{\partial S^s}\right|_{A,N_k^s} = T \text{ and } \left.\frac{\partial E^s}{\partial N_k^s}\right|_{A,S^s,N_{k'\neq k}^s} = \mu_k \tag{3.7}$$

We define the interface stress σ^s as the intensive parameter conjugated to the area:

$$\left.\frac{\partial E^s}{\partial A}\right|_{S^s,N_k^s} = \sigma^s \tag{3.8}$$

The interface being in contact with a reservoir of fixed temperature T and fixed chemical potentials μ_k of the chemical species k, its grand potential $\Omega^s = E^s - TS^s - \sum_k \mu_k N_k^s$ must be minimum at equilibrium. Combining Eq. (3.7) and Eq. (3.8), the variation $d\Omega^s$ of grand potential consecutive to a change of temperature, chemical potentials, and area can be derived:

$$d\Omega^s = d\left(E^s - TS^s - \sum_k \mu_k N_k^s\right) = -S^s dT - \sum_k N_k^s d\mu_k + \sigma^s dA \tag{3.9}$$

At fixed chemical potential and temperature, the interface stress is the energy required to increase the surface per unit area created. The interface stress has the dimension of a force per unit length. It is analogous to a mechanical stress, but in two dimensions.

We also define the interface energy γ as the grand potential of the interface per unit area:

$$\Omega^s = \gamma A \tag{3.10}$$

Up to now, we did not precise what the physical mechanisms are, by which the area of the interface can increase by a small amount dA. Actually, two mechanisms are possible (see Fig. 3.10): straining the interface or adding new molecules to the interface. Straining the surface is characteristic of solid surfaces, for which $dA = Ad\epsilon^s$, whereas increasing a surface by addition of new molecules is characteristic of fluid surfaces. For a fluid-solid interface, both mechanisms can occur. Therefore, when no solid is involved, the grand potential Ω^s is a linear function of the area. According to the definition of interface energy (Eq. 3.10), the interface energy γ depends only on the temperature T and on the chemical potentials μ_k, and is independent of the area. By contrast when a solid is involved, the grand potential is not a linear function of the area and the interface energy depends on the surface strain ϵ^s.

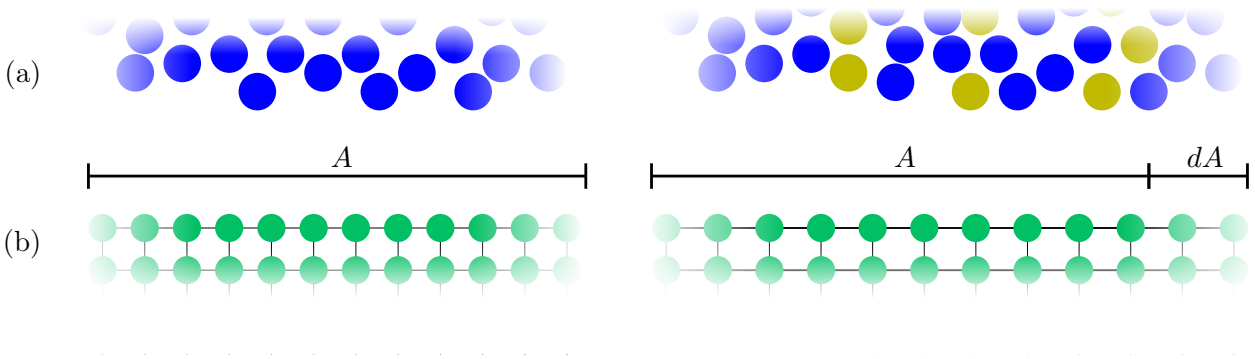

FIGURE 3.10. *The two mechanisms of surface creation: adding new molecules (a) and straining the surface (b). In Fig. (a), the particles in yellow are the new molecules that are brought to the surface when the area is increased.*

The relation between interface energy and interface stress is obtained by differentiating the definition of interface energy (Eq. 3.10) with respect to the area:

$$\sigma^s = \left.\frac{\partial \Omega^s}{\partial A}\right|_{T,\mu_k} = \gamma \text{ for a fluid-fluid interface} \tag{3.11}$$

$$\sigma^s = \left.\frac{\partial \Omega^s}{\partial A}\right|_{T,\mu_k} = \gamma + \left.\frac{\partial \gamma}{\partial \epsilon^s}\right|_{T,\mu_k} \text{ for a fluid-solid or solid-solid interface} \tag{3.12}$$

Accordingly, interface stress and interface energy are equal for fluid-fluid interfaces, but are different for interfaces involving a solid. Equation (3.12) is known as the Shuttleworth equation (Shuttleworth, 1950). In the literature (Kramer and Weissmüller, 2007), the interface stress for fluid-fluid interfaces is often referred to as the 'surface tension', which represents *"the work per area of forming new surface reversibly at constant structure"*. Whereas the terminology 'interface stress', often restricted to interfaces involving a solid, represents *"the force which opposes an elastic deformation of the surface, changing the inter-atomic distance at constant number of atoms"*.

How interface energy depends on the temperature and on the chemical potentials is also derived by combining the definition of interface energy (Eq. 3.10) with the expression of the change of grand potential (Eq. 3.9):

$$S^s dT + \sum_k N_k^s d\mu_k + A\, d\gamma|_{\epsilon^s} = 0 \tag{3.13}$$

where $|_{\epsilon^s}$ means that the small increment of interface energy is performed at constant surface strain. Equation (3.13) is called the Gibbs adsorption equation. It shows that an excess amount adsorbed N_k^s at a fluid-solid interface modifies the interface energy when the chemical potential μ_k varies:

$$\left.\frac{\partial \gamma}{\partial \mu_k}\right|_{T,\mu_{k'\neq k},\epsilon^s} = \frac{N_k^s}{A} = \Gamma_k \tag{3.14}$$

The quantity Γ_k is the excess amount adsorbed per unit area of interface for the component k of the fluid. Combining the Shuttleworth equation (Eq. 3.12) and the Gibbs' adsorption equation (Eq. 3.13), the variation of interface stress consecutive to a change of chemical potential is:

$$\left.\frac{\partial \sigma^s}{\partial \mu_k}\right|_{T,\mu_{k'\neq k},\epsilon^s} = \Gamma_k + \left.\frac{\partial \Gamma_k}{\partial \epsilon^s}\right|_{T,\mu_k} \tag{3.15}$$

Accordingly, the interface stress depends on the excess amount adsorbed in function of both the chemical potential and the surface strain. Therefore, site adsorption, which verifies $\partial \Gamma_k / \partial \epsilon^s|_{T,\mu_k} = -\Gamma_k$, does not make the interface stress vary. By contrast, if adsorption occurs by covering with $\partial \Gamma_k / \partial \epsilon^s|_{T,\mu_k} = 0$, the variations of interfaces stress are equal to the variations of interface energy: $\partial \sigma^s / \partial \mu_k|_{T,\mu_{k'\neq k},\epsilon^s} = \partial \gamma / \partial \mu_k|_{T,\mu_{k'\neq k},\epsilon^s} = \Gamma_k$.

Interface stress, which is positive except for very specific situations, acts like a stretched membrane. A well-known consequence of the existence of interface stresses is the fact that the pressures inside and outside a liquid bubble differ from each other. In order to show where this difference stems from, let us consider the system sketched in Fig. 3.11a: a fluid phase I of volume V_I at pressure P_I is separated from a fluid phase J of volume V_J at pressure P_J by a spherical interface of interface energy γ. At equilibrium, the grand potential $\Omega = -P_I V_I - P_J V_J + \gamma A$ of this system must be minimum. Due to the specific geometry of the system, the changes in area A and volumes

V_I and V_J are related by: $dV_I = -dV_J = RdA/2$, where R is the radius of the bubble of phase I. The minimization of the grand potential yields the Young-Laplace equation (Young, 1805, Laplace, 1808):

$$P_I - P_J = \frac{2\gamma}{R} \tag{3.16}$$

Another well-known effect of interface stress is the capillary rise of water in a tube (Fig. 3.11b): The stretched interface between the liquid water and the air is a curved meniscus which generates a drop of pressure between the two phases. The liquid pressure in the vicinity of the meniscus is lower than the ambient pressure in the air, which leads to the capillary rise. The smaller the radius of the tube, the higher the capillary rise, because the curvature of the meniscus increases and so does the difference of pressures between the liquid and the air.

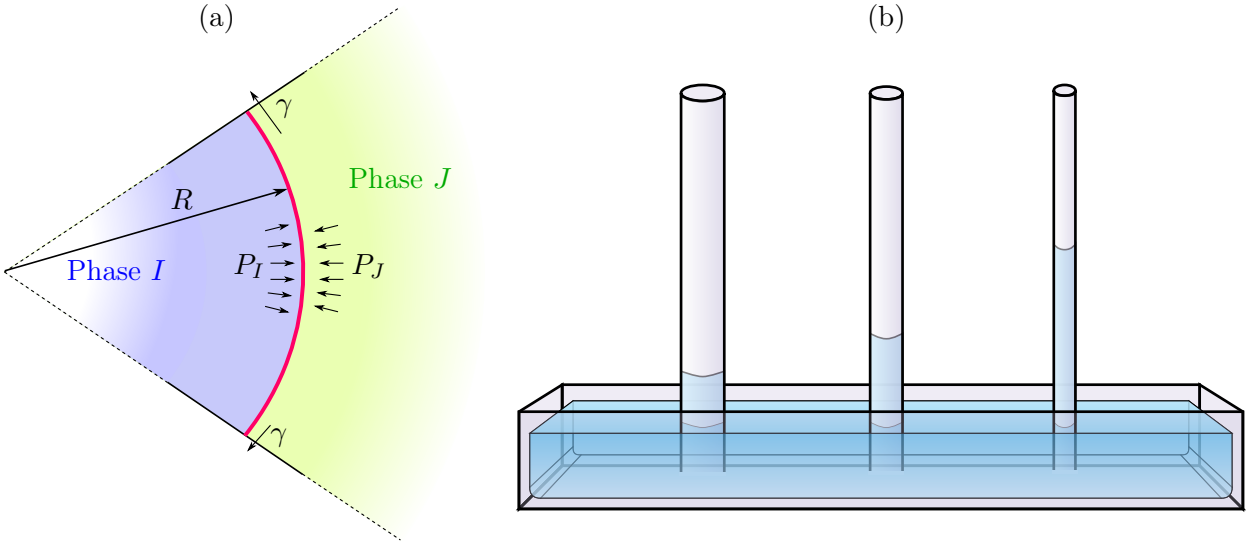

FIGURE 3.11. *Examples of the mechanical effect of interface stress: difference in pressures inside and outside a bubble (a) and capillary rise (b).*

Regarding fluid-solid interfaces, the mechanical effect of interface stress is difficult to observe experimentally because of the stiffness of solids. A possible experiment consists in measuring the curvature of a thin plate exposed to adsorption on one of its side and to vacuum on its other side (Fig. 3.12). At zero gas pressure, no molecule is adsorbed and the interface stress on both sides of the plate is equal. When the gas pressure is increased, the adsorption of gas molecules makes the interface energy decrease according to Gibbs adsorption equation (3.13). Therefore, the side exposed to the gas is less stretched than the side exposed to vacuum and a curvature of the plate arises. This phenomenon is used to measure interface stresses (Martinez et al., 1990).

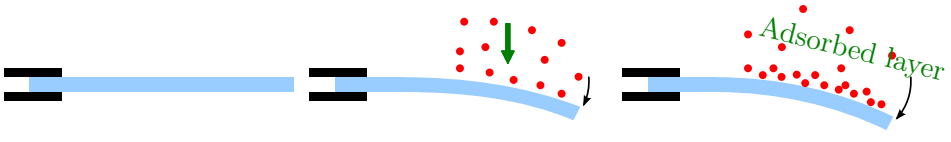

FIGURE 3.12. *Sketch of the mechanical effect of adsorption on a thin plate.*

3.2.2 Disjoining pressure

The thermodynamics of interfaces is a relevant tool to study surface adsorption. In a porous material, this theory can be used if the size of the pores is greater than the thickness of the inhomogeneous layer (Fig. 3.9). For smaller pores, however, this approach is no more relevant, since the inhomogeneous fluid layers induced by the opposite pore walls overlap. The notion of disjoining pressure, introduced by Derjaguin and Obuchov (1936), accounts for this overlap in the case of flat thin films.

Let us consider a thin film of fluid F confined between two other phases, as displayed in Fig. 3.13. The thermodynamical representation of this system is composed of two dividing surfaces which separate three phases. The dividing surfaces are flat: therefore, the mechanical stress acting normal to the film should be the same in the three phases and equal to the bulk pressure P of the fluid in the film. However, the experiments of Derjaguin and Obuchov (1936) with thin liquid films between flat mica surfaces showed that the opposite of the stress normal to the film differs from the bulk pressure P of the fluid when the film is thin. The difference between the actual mechanical stress acting normally on the film and the bulk pressure P of the fluid is called the disjoining pressure Π, or solvation pressure. This disjoining pressure originates from the overlap of the inhomogeneous fluid layers.

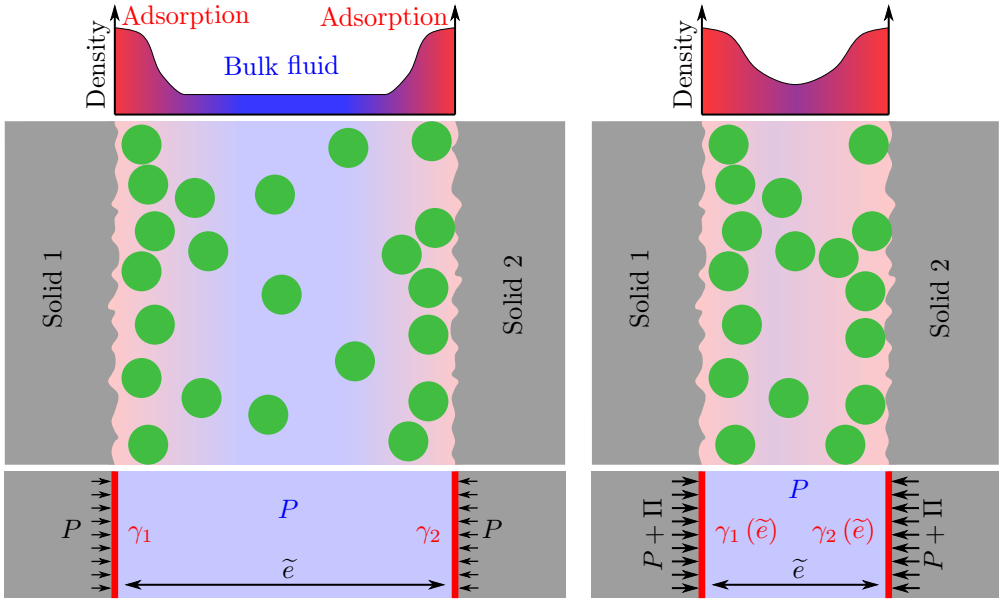

Figure 3.13. *Sketch of the overlap of the inhomogeneous layer for thin film and of the disjoining pressure effect.*

Let us interpret the disjoining pressure with thermodynamics. The grand potential Ω of the system made of the thin fluid film and of the two interfaces is $\Omega = -PA\widetilde{e} + (\gamma_1 + \gamma_2)\, A$, where $\widetilde{e}$ is the thickness of the film, A is the area of the film and γ_1 and γ_2 are the interface energies of each interface. The opposite P_{mech} of the stress normal to the film is the opposite of the derivative of the grand potential with respect to the thickness $\widetilde{e}$, per unit area: $P_{mech} = -\left(\partial\Omega / \partial\widetilde{e}\right)|_{T,A,\mu_k} \Big/ A$. As long as the inhomogeneous layers do not overlap, the interface energies γ_1 and γ_2 do not depend on the thickness $\widetilde{e}$ and the mechanical pressure is equal to the bulk pressure: $P_{mech} = P$. For thin films however, the interface energies do depend on the thickness $\widetilde{e}$, because the inhomogeneous layers overlap. The mechanical pressure orthogonal to the film is the sum of the bulk pressure and of the disjoining pressure $P_{mech} = P + \Pi$, where the disjoining pressure is given by:

$$\Pi = P_{mech} - P = -\frac{1}{A}\left.\frac{\partial \Omega}{\partial \widetilde{e}}\right|_{T,A,\mu_k} - P = -\left.\frac{\partial\left(\gamma_1+\gamma_2\right)}{\partial \widetilde{e}}\right|_{T,A,\mu_k} \tag{3.17}$$

The disjoining pressure characterizes the 'repulsion' between the two dividing surfaces. A positive disjoining pressure means that the total interface energy $(\gamma_1 + \gamma_2)$ is a decreasing function of the thickness of the film. In such case, the disjoining pressure is truly 'disjoining', in the sense that the two interfaces tend to separate in order to minimize the total interface energy. Conversely, a negative disjoining pressure means that the interface energy is an increasing function of the thickness. In this latter case, the disjoining pressure becomes 'joining', in the sense that the two interfaces tend to come closer to each other. Experimentally, both effects can be observed (Israelachvili, 1992). When the stress normal to the film is controlled instead of the thickness of the film, an increasing disjoining pressure isotherm corresponds to an instability (Fig. 3.14). The disjoining pressure is a function of the thickness of the film, the temperature, the chemical potentials, and the surface strain. The disjoining pressure can be measured experimentally with highly calibrated devices (Churaev, 2003).

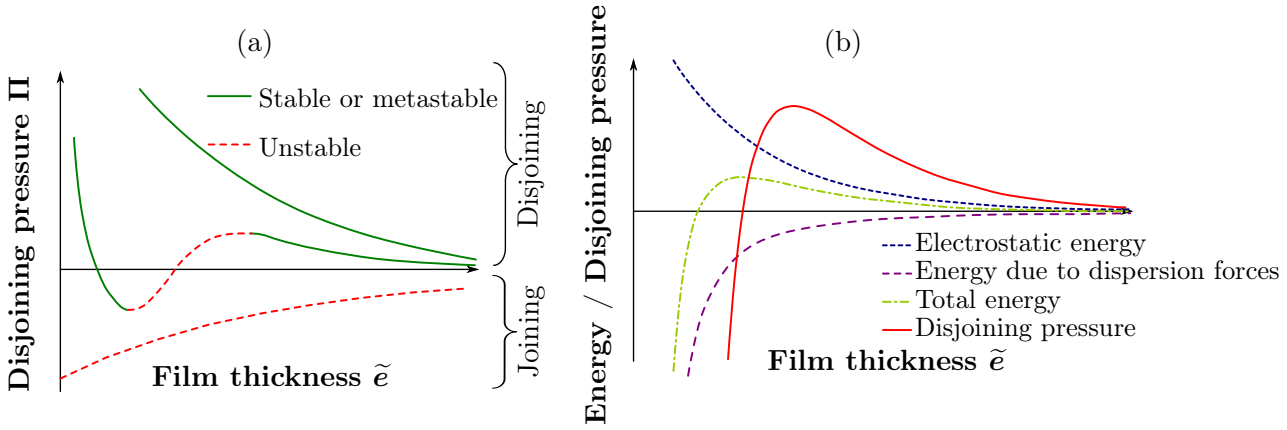

FIGURE 3.14. *Typology of disjoining pressure isotherms (a) and DLVO theory (b).*

In addition to experiments, theories were developed to explain the measured disjoining pressure isotherms. Derjaguin and Landau (1941) and Verwey and Overbeek (1948) proposed the DLVO theory which consists in an analytical integration of the dispersion forces and electrostatic interactions between surfaces separated by a thin liquid film. This theory predicts an attraction at short distances (i.e., a negative disjoining pressure) and a repulsion at large distances (i.e., a positive disjoining pressure). At short distances the dispersion forces prevail, whereas at large distances the electrostatic interactions do (Fig. 3.14). The DLVO theory corresponds to solid surfaces separated by a liquid film containing dilute ionic species and is relevant for films whose thickness is larger than a few nanometers. Such a theory is suitable to predict the stability of colloidal suspensions or the behavior of clay platelets (Fig. 3.6).

However, ECBM deals with non ionic fluids in micropores. For films of nanometric thickness, the disjoining pressure is dominated by physical effects that are not taken into account by the DLVO theory, such as the ordering of molecules within the film and the affinity of the solid for the fluid molecules (Israelachvili, 1992). The effect of molecular ordering is displayed in Fig. 3.15: such an ordering leads to a disjoining pressure that oscillates with the thickness of the film. For non ionic fluids, in a first approximation, the disjoining pressure can be described as an exponentially decaying sinusoidal function (Israelachvili, 1992):

$$\Pi = -k_B T \rho_{bulk} \cos\left(\frac{2\pi\widetilde{e}}{\widetilde{\sigma}}\right) \exp\left(-\frac{\widetilde{e}}{\widetilde{\sigma}}\right) \tag{3.18}$$

where $\widetilde{\sigma}$ stands for the diameter of a fluid molecule and ρ_{bulk} is the bulk density of the fluid. In addition to molecular ordering, the affinity of the solid for the fluid also modifies the disjoining pressure (Fig. 3.15). A strongly attractive energy between the solid and the fluid molecules leads to a large amount of fluid adsorbed in excess in the film and thus to a high positive disjoining pressure. Conversely, a repulsive energy leads to negative disjoining pressures.

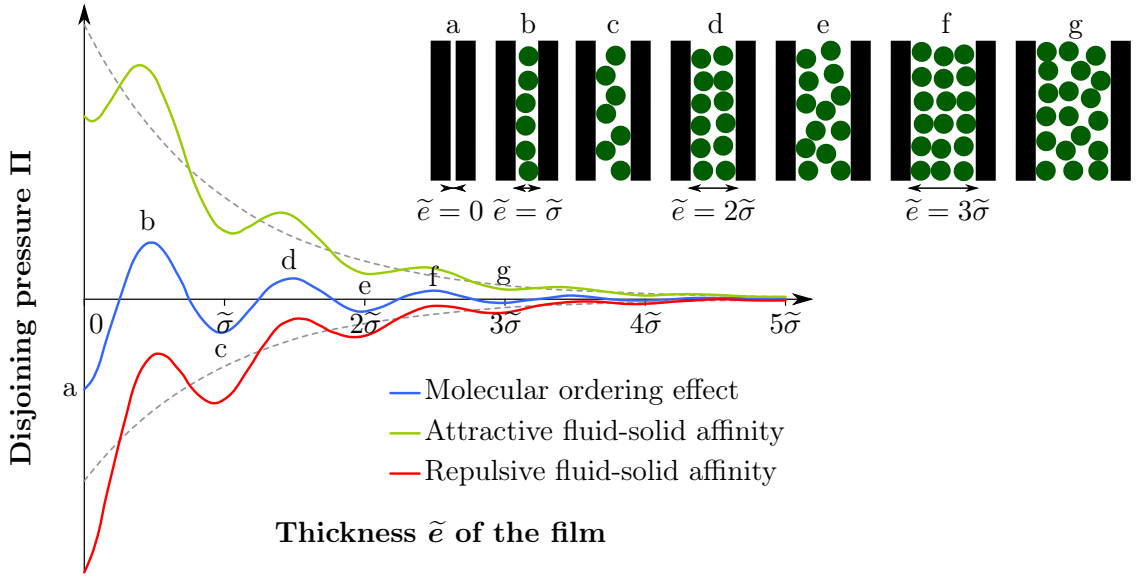

Figure 3.15. *Non DLVO effects: Molecular ordering and fluid-solid affinity. Adapted from Israelachvili (1992).*

To sum up, adsorption on surfaces acts like a stretched membrane parallel to the interface. This mechanical effect is captured in thermodynamics by the notion of interface stress. When adsorption occurs in small pores, the inhomogeneous layers of adsorbed fluid may overlap, which generates an additional stress normal to the interfaces. In the case of slit pores, this normal stress is the disjoining pressure. Regarding coal, the situation is more complex since micropores are not planar. Moreover, in such pores the notions of interface and dividing surface no more hold.

3.3 Adsorption-induced strain at the molecular scale

In this section, we present how mechanical stress originates from the molecular scale and we revisit the notions of interface stress and disjoining pressure at this scale.

3.3.1 Mechanical stress at the molecular scale

At the molecular scale, the mechanical pressure P_{mech} is related to the inter-particle energy according to the so called virial formula (Allen and Tildesley, 1989). Let us recall the demonstration of the virial equation in the canonical ensemble. We consider an assembly of N particles in the canonical ensemble at temperature T. The mechanical pressure exerted on the system is defined in thermodynamics as the opposite of the derivative of the Helmholtz free energy $F = E - TS$

with respect to the volume of the system. Using the relation between the free energy and the canonical partition function (Eq. 2.18), we can relate the mechanical pressure to a summation over all micro-states u.

$$P_{mech} = -\left.\frac{\partial F}{\partial V}\right|_{N,T} = k_B T \left.\frac{\partial \left(\ln\left(Z\right)\right)}{\partial V}\right|_{N,T} \tag{3.19}$$

$$P_{mech} = k_B T \frac{1}{Z}\frac{\partial}{\partial V}\left[\sum_u \exp\left(-\frac{E_u}{k_B T}\right)\right]_{N,T} \tag{3.20}$$

A micro-state is defined by the positions $(\mathbf{r}_i)_{i\in\{1,...,N\}}$ and impulsions $(\mathbf{p}_i)_{i\in\{1,...,N\}}$ of all particles in the system. The sum over all micro-states is an integral over all accessible states in the phase space[2] $\Sigma\left(N,V,T\right) = \left\{(\mathbf{r}_i,\mathbf{p}_i)_{i\in\{1,...,N\}} \in \mathbb{R}^{6N} \text{ with } \forall i, \mathbf{r}_i \in V\right\}$:

$$P_{mech} = k_B T \frac{1}{Z}\frac{\partial}{\partial V}\left[\int_{V^N,\mathbb{R}^{3N}} \exp\left(-\frac{E\left((\mathbf{r}_i,\mathbf{p}_i)_{i\in\{1,...,N\}}\right)}{k_B T}\right)\mathbf{dr}_1...\mathbf{dr}_N\mathbf{dp}_1...\mathbf{dp}_N\right]_{N,T} \tag{3.21}$$

In order to differentiate the integral, a change of variables $(\mathbf{r}_i)_x = V^{1/3}\left(\mathbf{r}'_i\right)_x$, $(\mathbf{r}_i)_y = V^{1/3}\left(\mathbf{r}'_i\right)_y$ and $(\mathbf{r}_i)_z = V^{1/3}\left(\mathbf{r}'_i\right)_z$ is performed, so that the volume $V = L_x L_y L_z$ in the integration boundary is replaced by $V' = \left[0; L_x/V^{1/3}\right] \times \left[0; L_y/V^{1/3}\right] \times \left[0; L_z/V^{1/3}\right]$, where L_x, L_y and L_z are the lengths of the system in the x, y and z directions, respectively. Thus, the differentiation can be applied directly to the integrand:

$$P_{mech} = k_B T \frac{1}{Z}\int_{(V')^N,\mathbb{R}^{3N}} \frac{\partial}{\partial V}\left[\exp\left(-\frac{E\left(\left(V^{1/3}\left(\mathbf{r}'_i\right)_x, V^{1/3}\left(\mathbf{r}'_i\right)_y, V^{1/3}\left(\mathbf{r}'_i\right)_z, \mathbf{p}_i\right)_{i\in\{1,...,N\}}\right)}{k_B T}\right) V^N\right]_{N,T} \mathbf{dr}'_1...\mathbf{dr}'_N\mathbf{dp}_1...\mathbf{dp}_N \tag{3.22}$$

The energy of a micro-state is the sum of the molecular interactions U and of the kinetic energy: $E\left((\mathbf{r}_i,\mathbf{p}_i)_{i\in\{1,...,N\}}\right) = U\left(\mathbf{r}_1,...,\mathbf{r}_N\right) + \sum_i \left(\mathbf{p}_i\right)^2 \Big/ \left(2m_i\right)$. The kinetic energy does not depend on the volume of the system and, accordingly:

$$\left.\frac{\partial E}{\partial V}\right|_{T,N} = \left.\frac{\partial U}{\partial V}\right|_{T,N} \Rightarrow \left.\frac{\partial E}{\partial V}\left(\left(V^{1/3}\left(\mathbf{r}'_i\right)_x, V^{1/3}\left(\mathbf{r}'_i\right)_y, V^{1/3}\left(\mathbf{r}'_i\right)_z, \mathbf{p}_i\right)_{i\in\{1,...,N\}}\right)\right|_{T,N} = \frac{1}{3}\sum_{i=1}^{N}\mathbf{r}_i{\cdot}\nabla_{\mathbf{r}_i}U \tag{3.23}$$

By changing again the variables, we finally obtain the virial equation:

[2] For the sake of simplicity, we do not mention here the volume h^3 of a micro-state and disregard the role of indiscernability, which do not intervene in the derivation.

$$P_{mech} = \frac{1}{Z}\int_{V^N,R^{3N}}\left(\frac{k_BT}{V}-\frac{\sum_{i=1}^{N}\mathbf{r}_i\cdot\nabla_{\mathbf{r}_i}U}{3V}\right)\exp\left(-\frac{E\left((\mathbf{r}_i,\mathbf{p}_i)_{i\in\{1,\ldots,N\}}\right)}{k_BT}\right)\mathbf{dr}_1\ldots\mathbf{dr}_N\mathbf{dp}_1\ldots\mathbf{dp}_N$$

$$P_{mech} = \left\langle\frac{Nk_BT}{V}-\frac{1}{3V}\sum_{i=1}^{N}\mathbf{r}_i\cdot\nabla_{\mathbf{r}_i}U\right\rangle \tag{3.24}$$

The first term in Eq. (3.24) is the kinetic pressure and is independent of the molecular interactions. The summation term arises from the molecular interactions. For ideal gases, for which the molecules do not interact at all with each other, the kinetic pressure is the only contribution to the pressure. This is the well known ideal gas law. For systems with weak molecular interactions, i.e., gases, the kinetic pressure is dominating. Conversely, for systems with strong molecular interactions, e.g., condensed matter, the second term is comparable to or larger than the kinetic pressure.

The interaction energy U is often approximated by a sum of pair potentials between molecules: $U=\sum_{i<j}U_{ij}\left(\mathbf{r}_{ij}\right)$ where $\mathbf{r}_{ij}=\mathbf{r}_j-\mathbf{r}_i$ is the vector from particle i to particle j. Such approximation is often too simplistic, since actual interactions may involve three or more bodies and are not additive. Nevertheless, for additive pair potentials, the virial equation (3.24) becomes:

$$\mathbf{r}_i\cdot\nabla_{\mathbf{r}_i}U_{ij}+\mathbf{r}_j\cdot\nabla_{\mathbf{r}_j}U_{ij}=\mathbf{r}_{ij}\cdot\nabla_{\mathbf{r}_{ij}}U_{ij}=-\mathbf{r}_{ij}\cdot\mathbf{F}_{ij} \tag{3.25}$$

$$P_{mech}=\left\langle\frac{Nk_BT}{V}+\frac{1}{3V}\sum_{i<j}\mathbf{r}_{ij}\cdot\mathbf{F}_{ij}\right\rangle \tag{3.26}$$

where $\mathbf{F}_{ij}=-\nabla_{\mathbf{r}_{ij}}U_{ij}$ is the force exerted by particle i on particle j. This formulation of the virial equation is easier to interpret: each interaction between particles contributes to the overall pressure through what is called the internal virial: $w_{ij}=\frac{1}{3}\mathbf{r}_{ij}\cdot\mathbf{F}_{ij}$. If two particles attract each other, the internal virial is negative and the contribution to the overall pressure is negative. If two particles repulse each other, the contribution to the overall pressure is positive. These observations are consistent with a macroscopic interpretation: a negative pressure corresponds to matter in tension, whereas a positive pressure corresponds to matter in compression. We display in Fig. 3.16 the molecular interpretation of the Van der Waals equation of state, assuming a Lennard-Jones potential U_{ij} of interaction between fluid molecules:

$$U_{ij}\left(\mathbf{r}_{ij}\right)=4\widetilde{\varepsilon}\left(\left(\frac{\widetilde{\sigma}}{|\mathbf{r}_{ij}|}\right)^{12}-\left(\frac{\widetilde{\sigma}}{|\mathbf{r}_{ij}|}\right)^{6}\right) \tag{3.27}$$

Such a potential of interaction is relevant for a nonpolar fluid with spherical molecules.

The virial equation (3.26) can be generalized to interpret the stress tensor from the molecular scale (Jouanna and Brocas, 2001):

$$\underline{\underline{\sigma}}=\left\langle-\frac{1}{V}\sum_i\frac{\mathbf{p}_i\otimes\mathbf{p}_i}{m_i}-\frac{1}{V}\sum_{i<j}\mathbf{r}_{ij}\otimes\mathbf{F}_{ij}\right\rangle \tag{3.28}$$

where $\underline{\underline{\sigma}}$ is the stress tensor, whose components σ_{ab} are conjugate to the components ϵ_{ab} of the strain tensor $\underline{\underline{\epsilon}}$, $(a,b)\in\{x,y,z\}^2$, $(\cdot\otimes\cdot)$ is the tensor product, and m_i is the mass of particle i. The

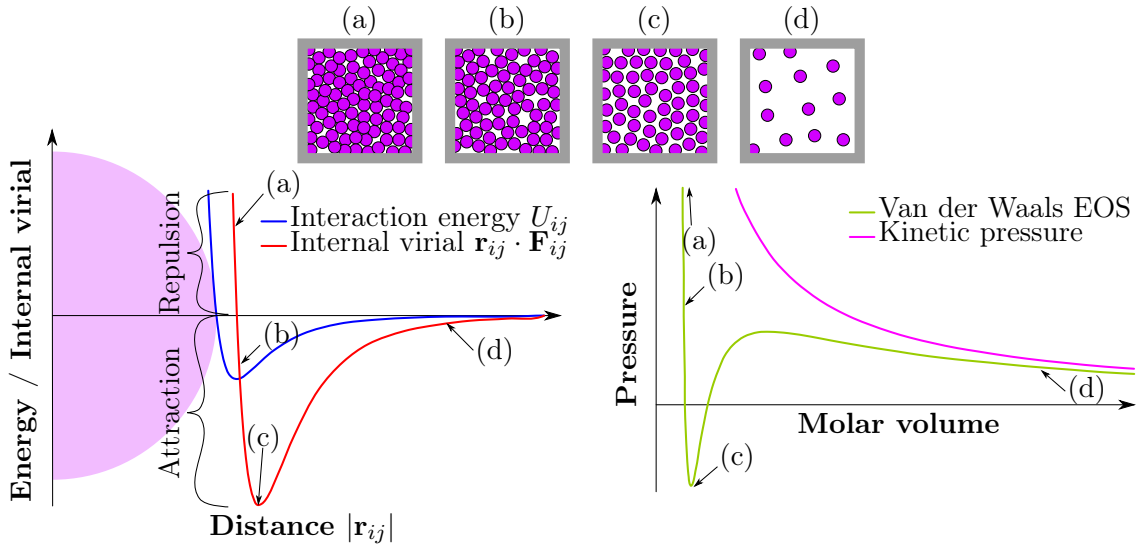

FIGURE 3.16. *Interpretation of the Van der Waals equation of state at the molecular scale. EOS holds for 'equation of state', U_{ij} is the energy of interaction between particle i and particle j, $\mathbf{r}_{ij}$ is the vector from particle i to particle j, and $\mathbf{F}_{ij}$ is the force exerted by particle i on particle j.*

kinetic term reduces to the kinetic pressure for the diagonal contributions thanks to the equipartition theorem (Chevoir, 2010): $\sigma_{aa}^{kin} = -\left\langle \frac{1}{V}\sum_i \left((\mathbf{p}_i)_a\right)^2 \Big/ m_i \right\rangle = -Nk_BT/V$ with $a \in \{x, y, z\}$. Indeed, the equipartition theorem states[3] that the statistical average of the kinetic energy $\left((\mathbf{p}_i)_a\right)^2 \Big/ (2m_i)$ of any particle i in direction a is equal to $k_BT/2$. Therefore, the generalized virial equation for the stress tensor (Eq. 3.28) is consistent with the virial equation for the pressure (Eq. 3.26): $P_{mech} = -\left(\sigma_{xx} + \sigma_{yy} + \sigma_{zz}\right)/3$.

3.3.2 Surface stress at the molecular scale

An equivalent of the virial equation exists for the surface stress that acts at fluid-fluid interfaces[4] (Gloor et al., 2005, Kirkwood and Buff, 1949). We consider a system in the canonical ensemble, which is made of two fluid phases separated by a flat interface orthogonal to the z-direction. Starting with the definition of the interface stress σ^s (Eq. 3.8), we obtain:

$$\sigma^s = \left.\frac{\partial \Omega}{\partial A}\right|_{\mu_k,V,T} = \left.\frac{\partial F}{\partial A}\right|_{N,V,T} = -\frac{k_BT}{Z}\left.\frac{\partial Z}{\partial A}\right|_{N,V,T}$$

$$\sigma^s = -\frac{k_BT}{Z}\int_{[0;1]^{3N},\mathbb{R}^{3N}} \frac{\partial}{\partial A}\left[\exp\left(-\frac{E\left(\left(L_x\left(\mathbf{r}'_i\right)_x, L_y\left(\mathbf{r}'_i\right)_y, L_z\left(\mathbf{r}'_i\right)_z, \mathbf{p}_i\right)_{i\in\{1,\ldots,N\}}\right)}{k_BT}\right) V^N\right]_{N,V,T} \mathbf{dr}'_1\ldots\mathbf{dr}'_N\mathbf{dp}_1\ldots\mathbf{dp}_N \quad (3.29)$$

A fluid-fluid interface is isotropic and its change in area $dA = L_x dL_y + L_y dL_x$ is evenly distributed in the x- and y-directions: $dL_x = dA/2L_y$ and $dL_y = dA/2L_x$. Moreover, the differ-

[3] The demonstration of the equipartition theorem is straightforward by integrating the Boltzmann-Gibbs distribution over the impulsion component $\mathbf{p}_k$ and making use of a Gaussian integral.

[4] The case of interfaces with solids is discussed later in this paragraph.

entiation is performed at constant volume ($dV = 0 = L_z dA + A dL_z$), which implies a constraint in the z-direction: $dL_z = -L_z dA/A$. This differentiation 'at constant volume' is valid for fluids, for which the volume is the only geometrical property that has to be considered in addition to the area A in order to characterize the deformation of the system. In contrast, for a solid, the proper thermodynamic representation includes the whole strain tensor, i.e., six independent geometrical properties. The differentiation in Eq. (3.29) can be written explicitly:

$$\sigma^s = \frac{1}{Z}\int_{V^N,\mathbb{R}^{3N}} \sum_i \left(\frac{(\mathbf{r}_i)_x}{2L_xL_y}\frac{\partial U}{\partial (\mathbf{r}_i)_x} + \frac{(\mathbf{r}_i)_y}{2L_xL_y}\frac{\partial U}{\partial (\mathbf{r}_i)_y} - \frac{(\mathbf{r}_i)_z}{A}\frac{\partial U}{\partial (\mathbf{r}_i)_z} \right) \exp\left(-\frac{E\left((\mathbf{r}_i,\mathbf{p}_i)_{i\in\{1,\ldots,N\}}\right)}{k_BT} \right) \mathbf{dr}_1 \ldots \mathbf{dr}_N \mathbf{dp}_1 \ldots \mathbf{dp}_N \tag{3.30}$$

$$\sigma^s = \left\langle \frac{1}{A}\sum_i \begin{pmatrix} (\mathbf{r}_i)_x/2 \\ (\mathbf{r}_i)_y/2 \\ -(\mathbf{r}_i)_z \end{pmatrix} \cdot \nabla_{\mathbf{r}_i} U \right\rangle \tag{3.31}$$

Equation (3.31) is the equivalent for the surface stress of the virial equation (3.24). In the case of additive pair interactions, the above equation can be rewritten:

$$\sigma^s = \left\langle \frac{1}{A}\sum_{i<j} (\mathbf{r}_{ij})_z (\mathbf{F}_{ij})_z - \frac{(\mathbf{r}_{ij})_x (\mathbf{F}_{ij})_x + (\mathbf{r}_{ij})_y (\mathbf{F}_{ij})_y}{2} \right\rangle \tag{3.32}$$

Therefore, the interface stress originates from an anisotropy of the internal virial at the interface. To account for such localized effects at the molecular scale, the notion of local mechanical stress needs to be defined.

3.3.3 Local mechanical stress at the molecular scale

Defining a local mechanical stress is difficult since there exists no unique definition but a variety of definitions. All these definitions are consistent with the macroscopic mechanical stress acting on the volume and defined by the virial equation (Eqs. (3.24) and (3.28)).

Let us first present the definition proposed by Irving and Kirkwood (1950): the local kinetic stress $\underline{\underline{\sigma}}^{kin}(\mathbf{r})$ is related to the local density at position $\mathbf{r}$, while the stress $\underline{\underline{\sigma}}^{int}(\mathbf{r})$ due to interaction energies is defined through its projections $\underline{\underline{\sigma}}^{int}(\mathbf{r}) \cdot \mathbf{dS}$ on a unit vector $\mathbf{dS}$ perpendicular to an imaginary surface at point $\mathbf{r}$. The term $\underline{\underline{\sigma}}^{int}(\mathbf{r}) \cdot \mathbf{dS}$ is interpreted as *"the force acting across* $\mathbf{dS}$*"*. According to Irving and Kirkwood (1950), the force between a pair of particles 'acts across $\mathbf{dS}$' if the line segment between the two particles intersects $\mathbf{dS}$. Defining the stress from a force acting on a surface is the conventional definition of continuum mechanics. Following this definition, we have:

$$\underline{\underline{\sigma}}(\mathbf{r}) = \underline{\underline{\sigma}}^{kin}(\mathbf{r}) + \underline{\underline{\sigma}}^{int}(\mathbf{r}) = -\left\langle \sum_i \frac{\mathbf{p}_i \otimes \mathbf{p}_i}{m_i}\delta(\mathbf{r}_i - \mathbf{r}) \right\rangle - \left\langle \sum_{i<j} \left(\frac{\mathbf{r}_{ij} \otimes \mathbf{F}_{ij}}{|\mathbf{r}_{ij}|} \int_0^1 \delta(\mathbf{r}_i + \eta\mathbf{r}_{ij} - \mathbf{r})\, d\eta \right) \right\rangle \tag{3.33}$$

where $\delta(\cdot)$ is the Dirac delta function. The definition of Irving and Kirkwood (1950) is consistent with the virial equation (3.28): the average of the local stress over the volume is equal to the mechanical stress acting on the volume. In this definition, the contribution to the stress of an inter-particle interaction is distributed uniformly on the line segment between the two particles. This choice of distribution is not unique and a more general definition of local stresses is:

$$\underline{\underline{\sigma}}(\mathbf{r}) = -\left\langle \sum_i \frac{\mathbf{p}_i \otimes \mathbf{p}_i}{m_i} \delta(\mathbf{r}_i - \mathbf{r}) \right\rangle - \left\langle \sum_{i<j} (\mathbf{r}_{ij} \otimes \mathbf{F}_{ij}) f(\mathbf{r}_i, \mathbf{r}_j, \mathbf{r}) \right\rangle \tag{3.34}$$

where the function $f(\mathbf{r}_i, \mathbf{r}_j, \mathbf{r})$ distributes the contribution of the inter-particle interaction in space and must verify $\int_V f(\mathbf{r}_i, \mathbf{r}_j, \mathbf{r})\, \mathbf{dr} = 1$ to ensure the consistency with the virial equation (3.28). In practice, the function $f(\mathbf{r}_i, \mathbf{r}_j, \mathbf{r})$ is expected to be nonzero only near the particles i and j. Therefore the choice of Irving and Kirkwood (1950) is valid. Another definition commonly used is $f(\mathbf{r}_i, \mathbf{r}_j, \mathbf{r}) = (\delta(\mathbf{r}_i - \mathbf{r}) + \delta(\mathbf{r}_j - \mathbf{r}))/2$, which means that the total contribution of an interaction between particles is concentrated at the position of the particles (Walton et al., 1983, Gloor et al., 2005).

The surface stress estimate (Eq. 3.32) can be interpreted in terms of local stresses. We define the local stress $\sigma_{aa}(z)$ in a plane normal to the z-direction as the average of the local stress $\sigma_{aa}(\mathbf{r})$ in this plane:

$$\sigma_{aa}(z) = \frac{1}{A} \int_0^{L_x} \int_0^{L_y} \sigma_{aa}(\mathbf{r})\, dxdy \tag{3.35}$$

$$= -\rho(z)\, k_B T - \frac{1}{A} \left\langle \sum_{i<j} (\mathbf{r}_{ij})_a (\mathbf{F}_{ij})_a \int_0^{L_x} \int_0^{L_y} f(\mathbf{r}_i, \mathbf{r}_j, \mathbf{r})\, dxdy \right\rangle \tag{3.36}$$

where $\rho(z) = \frac{1}{A} \left\langle \int_0^{L_x} \int_0^{L_y} \sum_i \delta(\mathbf{r}_i - \mathbf{r})\, dxdy \right\rangle$ is the planar density. The comparison with the surface stress estimate yields:

$$\sigma^s = \int_0^{L_z} \left(\frac{\sigma_{xx}(z) + \sigma_{yy}(z)}{2} - \sigma_{zz}(z) \right) dz \tag{3.37}$$

Accordingly, the surface stress can be interpreted as the difference between the local mechanical stresses parallel to the interface and the local mechanical stress orthogonal to the interface. Interestingly, Eq. (3.37) does not depend on the distribution function $f(\mathbf{r}_i, \mathbf{r}_j, \mathbf{r})$.

Tolman (1949) performed analytical calculations for liquid-vapor interfaces of Lennard-Jones fluids and concludes to an overall drop of pressure in the inhomogeneous layer. According to his calculation, the drop of pressure is due to the particular state of matter in the inhomogeneous layer: the inhomogeneous layer is made of nearly cavitated liquid at very low pressure and of regions with nearly condensed states at high pressure. Nevertheless, at the scale of the inhomogeneous layer, Tolman (1949) predicts an overall drop of pressure. However, the calculation of Tolman (1949) is only approximate, since it does not treat separately each component of the stress tensor and the density does not vary continuously within the inhomogeneous layer. Molecular simulations (Walton et al., 1983) provide a more precise picture of liquid-vapor interfaces: the component of the mechanical stress σ_{zz} orthogonal to the interface varies slightly within the inhomogeneous layer, but its average value in the inhomogeneous layer is equal to its value outside the layer:

they also find out that the mechanical stresses σ_{xx} and σ_{yy} tangent to the interface are larger in the inhomogeneous layer than in the bulk phases. We display in Fig. 3.17 the results of a molecular simulation of a liquid-vapor interface for methane at $T = 130$ K. Such a local anisotropy of the stress tensor is surprising for a fluid: according to the balance of momentum in continuum mechanics, such an anisotropy means that shear stresses exist in the inhomogeneous layer, while fluids at rest cannot sustain shear. This inconsistency comes from the fact that the local stresses (Eq. 3.34) are not a measure of the mechanical force between material points and therefore do not respect the balance of momentum of continuum mechanics (Zhou, 2003).

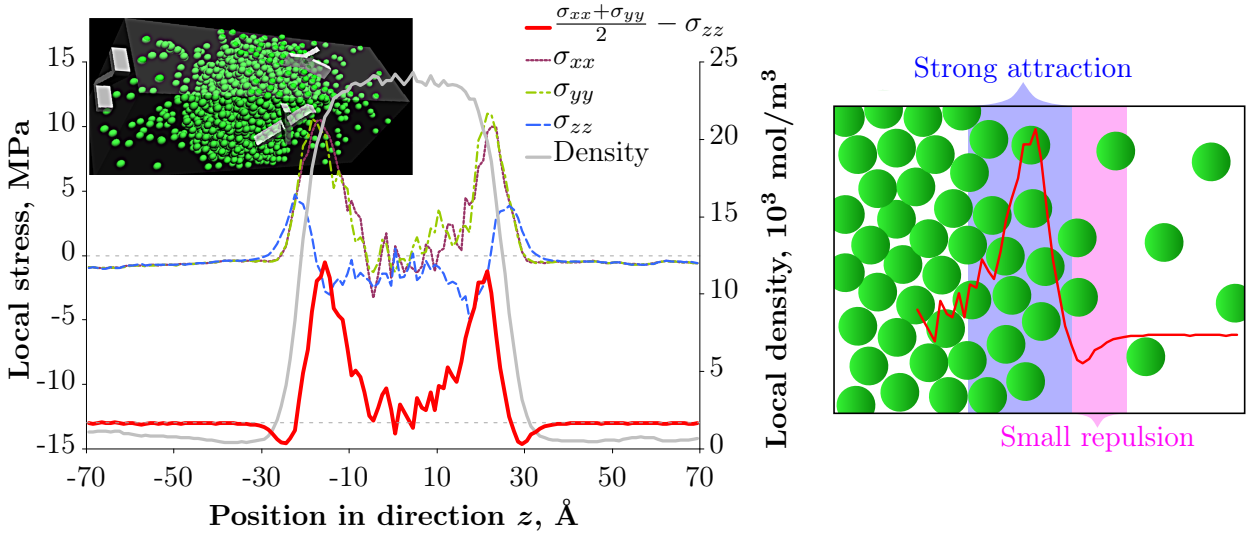

Figure 3.17. *Local stresses in a liquid-vapor interface at the molecular scale. The curve for* $(\sigma_{xx} + \sigma_{yy})/2 - \sigma_{zz}$ *has been shifted for clarity.*

The molecular interpretations presented in Secs. 3.3.2 and 3.3.3 only hold for fluid-fluid interfaces. The interface stress for interfaces involving a solid cannot be estimated from the sole interfacial system, but must be interpreted as the difference between the local stress acting in the interfacial system and the macroscopic mechanical stress acting in the bulk phases (see Fig. 3.18). Nevertheless, as was the case for fluid-fluid interfaces, the interface stress remains due to inhomogeneous local stresses within the interfacial region:

$$\sigma_x^s = \int_0^{L_z} \left(\sigma_{xx}(z) - \sigma_{xx}^{\text{bulk}}(z)\right) dz \tag{3.38}$$

$$\sigma_y^s = \int_0^{L_z} \left(\sigma_{yy}(z) - \sigma_{yy}^{\text{bulk}}(z)\right) dz \tag{3.39}$$

where σ_a^s is the component of the interface stress in direction $a \in \{x, y\}$ and $\sigma_{aa}^{\text{bulk}}(z)$ are the local stresses in the bulk phases extrapolated to the dividing surface (Fig. 3.18). Equations (3.38) and (3.39) are consistent with Eq. (3.37) for fluid-fluid interfaces. Indeed, the mechanical stress in a bulk fluid is isotropic ($\sigma_{xx}^{\text{bulk}}(z) = \sigma_{yy}^{\text{bulk}}(z) = \sigma_{zz}^{\text{bulk}}(z)$), the local stress parallel to the interface is isotropic as well ($\sigma_{xx}(z) = \sigma_{yy}(z)$), and the average stress orthogonal to the interface is equal to the bulk stress $\sigma_{zz}^{\text{bulk}}(z) = \frac{1}{L_z}\int_0^{L_z} \sigma_{zz}(z)\, dz$.

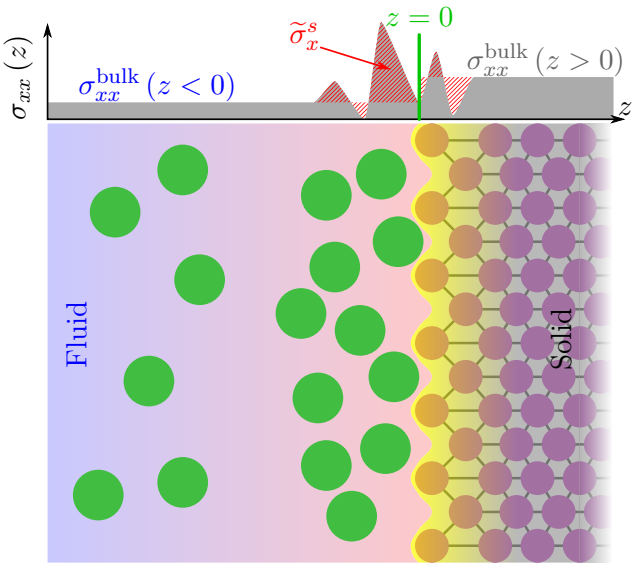

FIGURE 3.18. *Estimation of the interface stress at the molecular scale.*

3.3.4 Disjoining pressure and effect of adsorption in micropores

The disjoining pressure also can be interpreted at the molecular scale. When two interfaces are very close to each other, the mechanical pressure orthogonal to the interface differs from the bulk pressure P of the fluid: the difference is the disjoining pressure Π. The expression of the disjoining pressure at the molecular scale is:

$$\Pi = -\sigma_{zz} - P = \left\langle \frac{Nk_BT}{V} + \frac{1}{V}\sum_{i<j}(\mathbf{r}_{ij})_z(\mathbf{F}_{ij})_z \right\rangle - P = -\int_0^{L_z}\sigma_{zz}(z)\,dz - P \tag{3.40}$$

Interestingly, only the total pressure $P+\Pi$ is defined at the molecular scale and at the macroscopic scale. This is logical since a thin film may exist even if the bulk phase is not stable, as is the case for a liquid film below cavitation pressure. In such case, the bulk pressure P of the fluid could not be defined.

Equation (3.40) can be used in molecular simulation to compute the disjoining pressure and compare simulated results with theory. Balbuena et al. (1993) computed the disjoining pressure for model Lennard-Jones fluids between solid surfaces. They computed a disjoining pressure which oscillated with the size of the film, similar to what is displayed in Fig. 3.15. The underlying physics of this oscillating function is the stepwise filling of the pore due to the commensurability of the size of the pore to the size of the fluid molecules. The amplitude and position of the oscillations are very sensitive to various parameters of the system, such as roughness of the solid walls, interaction energies, temperature, and so on. Malani et al. (2009) considered the more realistic case of water confined between mica surfaces and hydroxylated silica surfaces. Both surfaces are hydrophilic, but the computed disjoining pressures differs significantly from each other: the disjoining pressure oscillates with the distance between hydroxylated silica surfaces, but decreases monotonically with the distance between mica surfaces. Such a difference is explained by the structural arrangement of water molecules near the surface, which strongly depends on the chemical composition of the surfaces. According to these two examples, the disjoining pressure is very system-dependent and no general theory is for now able to capture all its specificities.

In microporous solids, the disjoining pressure will also induce a strain. We sketch in Fig. 3.19 what deformation would be induced qualitatively by adsorption of a fluid in a micropore of complex morphology. Depending on the size and shape of the adsorbed molecules and of the micropore, adsorption can induce a contraction or a swelling, isotropically or anisotropically, etc. The fact that coal swells upon adsorption is not easily explained with these simple sketches.

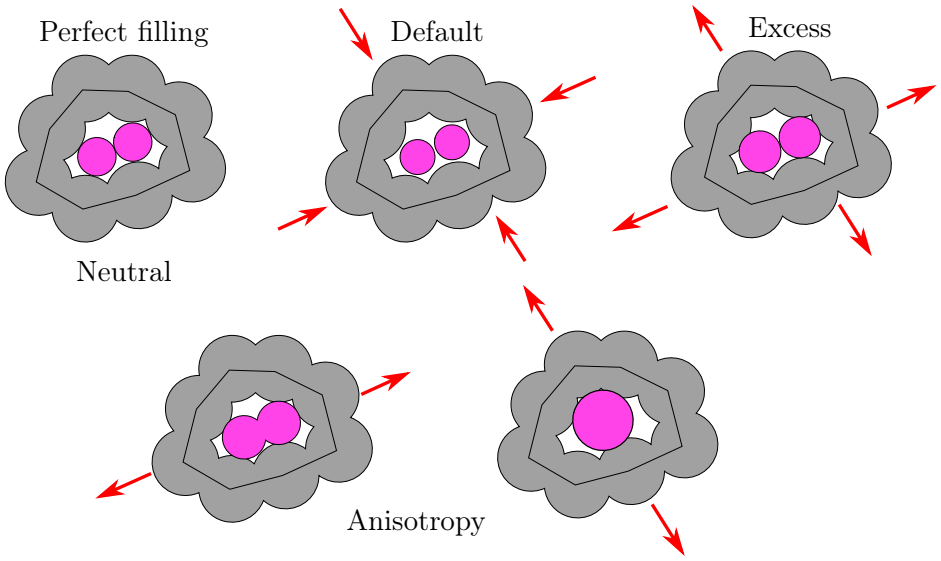

Figure 3.19. *Sketch of the deformations induced by adsorption in a micropore of complex geometry.*

3.4 Existing models for adsorption-induced strain

We discuss in this section the existing models of adsorption-induced deformation in coal and other porous solids. We distinguish three categories: the models based on interface effects, the models based on disjoining pressure, and the models for non-planar micropores.

3.4.1 Models based on interface effects

Pan and Connell (2007) proposed a model for coal swelling based on variations of interface energy. They estimated the variation of interface energy due to adsorption by integrating the Gibbs adsorption equation (Eq. 3.13) from zero pressure to the current bulk pressure. They used a Langmuir model (Eq. 3.4) to relate the bulk pressure of fluid to the adsorbed amount. They eventually related the strain of the solid to the variation of interface energy with the model of Scherer (1986) developed for the swelling of porous glass and assumed valid for coal.

The model of Scherer (1986) is valid for a mesoporous glass. Likewise, the model of Pan and Connell (2007) is well adapted to mesoporous solids. Seven parameters need to be set in this model. Once those parameters are calibrated, the model captures very well the experimental data of coal swelling consecutively to an immersion in CO_2. In addition to the model of Pan and Connell (2007), let us also mention the work of Grosman and Ortega (2008), which relates adsorption to interface stress and to mechanical strain for mesoporous glass.

Variations of interface energy can explain adsorption-induced strain in mesoporous solids such as porous silicon (Dolino et al., 1996) and silica aerogels (Reichenauer and Scherer, 2000, Herman

et al., 2006), but cannot explain adsorption-induced swelling for microporous solids (Dolino et al., 1996, Günther et al., 2008), since in such solids with such small pores, the notion of surface of a pore no more holds. Therefore, models based on variations of interface energy are not adapted to model the CO_2-induced swelling of coal, since coal is microporous.

3.4.2 Models based on disjoining pressure

How disjoining pressure leads to the deformation of a slit pore has been studied at the scale of the pore by several. Ustinov and Do (2006) studied the case of slit pores that deform elastically: the contraction or the dilatation of the pore modifies the free energy of the system and the energy is assumed to be a quadratic function of the strain of the pore. At equilibrium, the sum of the grand potential of the fluid and of the free energy stored in the system by elastic deformation is minimum. Such a minimization leads to a deformation of the pore such that the elastic force induced by the deformation compensates exactly the mechanical pressure of the fluid, which itself is equal to the sum of the disjoining pressure and the bulk pressure of the fluid. Ustinov and Do (2006) computed the particular case of nitrogen adsorption in graphitic slit pores, for which the disjoining pressure depends in a complex manner on the thickness of the pore: in such case, the deformation of the pore upon adsorption depends in a complex manner on the thickness of the pore in the state of reference. A similar study was performed by Do et al. (2008), who considered walls constrained by the surrounding solid.

At the scale of the material, Kowalczyk et al. (2008) developed a model for microporous carbons. They represented the microporous matrix of these carbons by a series of slit pores with various thicknesses in which the mechanical pressure exerted by the fluid is the sum of the bulk pressure of the fluid and of the disjoining pressure. Like Ustinov and Do (2006), Kowalczyk et al. (2008) include an additional elastic energy to account for the increase of free energy stored in the solid matrix during expansion or contraction of the pores. They consider an incompressible solid. Each pore is at equilibrium when the total mechanical stress exerted by the fluid equals the elastic stress exerted by the solid, thus leading to a specific strain for each pore. The total strain of the solid depends on the pore size distribution.

Kowalczyk et al. (2008) considered the case of argon adsorption between graphite walls. They computed the disjoining pressure by molecular simulation and studied the effect of the size of the pore on the adsorption-induced strain. This strain depends significantly on the size of the pore. Such a result is not surprising since the disjoining pressure isotherm for Lennard-Jones fluids depends significantly on the size of the pore (Fig. 3.15). From their results for pores with a variety of sizes, they predicted the pore size distribution of a carbide-derived activated carbon, for which adsorption-induced strain was measured experimentally. The model of Kowalczyk et al. (2008) is applicable to microporous solids with slit-like micropores and an incompressible solid matrix. These conditions are nearly verified for the elementary constituents of activated carbons. However, the molecular structure of coal is amorphous and is not well represented by slit pores. Despite this lack of representativity, Yang et al. (2010) modeled the swelling of coal with an approach equivalent to that of Kowalczyk et al. (2008), but based on grand potential minimization. They obtain a good fit of swelling experiments by calibrating the pore size distribution of the coal matrix.

In constrast, Gor and Neimark (2010) used the concept of disjoining pressure for mesoporous solids. Their model aims at predicting the adsorption-induced deformation of cylindrical mesopores by considering the adsorbed molecules as a thin liquid film between the solid matrix and the vapor phase. The thermodynamical representation of the thin film requires the introduction of the

disjoining pressure. Because of the cylindrical geometry, the adsorbed film is curved: the mechanical effect induced by the adsorbed film is due to interface energy and disjoining pressure effects. When the liquid is condensed in the pore, the deformation of the solid is due to the capillary pressure. Their approach is valid for pores whose diameter is larger than 8 nm (Gor and Neimark, 2011).

3.4.3 Models for non planar micropores

Ravikovitch and Neimark (2006) adapted the notion of disjoining pressure to spheroidal geometries: the characteristic size of a pore is its radius R instead of its thickness. The mechanical pressure P_{mech} exerted by the fluid on the pore walls is the derivative of the grand potential Ω of the fluid (including the interface) with respect to the volume $V = 4\pi R^3/3$ of the spherical pore. The disjoining pressure Π of the adsorbed fluid inside the pore is the difference between the mechanical pressure P_{mech} and the bulk pressure P:

$$\Pi = P_{mech} - P = -\left.\frac{\partial \Omega}{\partial V}\right|_{T,\mu_k} - P = -\frac{1}{4\pi R^2}\left.\frac{\partial \Omega}{\partial R}\right|_{T,\mu_k} - P \tag{3.41}$$

Ravikovitch and Neimark (2006) applied this expression to the case of Xenon and Krypton adsorption in zeolites, for which the approximation of spheroidal pores is mostly valid. Such an approach cannot be easily transposed to coal however, since, in the coal matrix, the size of a pore cannot be defined unambiguously.

Coudert et al. (2008) used a different approach to study the breathing of MIL-53, a bi-stable crystalline microporous metal organic framework which evolves from a narrow pore configuration to a large pore configuration upon adsorption (Fig. 3.7). The approach of Coudert et al. (2008) consists in determining the most stable state by minimizing the so-called osmotic potential. The osmotic ensemble is a hybrid statistical ensemble in which the solid is in the isothermal-isobaric ensemble and the fluid is in the grand canonical ensemble. In such an ensemble, the quantities which are imposed by the environment are the temperature T, the volumetric mechanical stress σ exerted on the solid, and the chemical potentials μ_k of the components of the fluid. These conditions are suitable for the study of MIL-53 for which the adsorption experiments are performed by immersion: in such experiments, MIL-53 is immersed in fluids at controlled chemical potentials. In that case, the volumetric mechanical stress exerted on the solid is the bulk pressure of the fluid: $\sigma = -P$. Their model was used to predict the temperature-pressure phase diagram of MIL-53 (Boutin et al., 2011) and is consistent with the notion of disjoining pressure introduced by Neimark et al. (2011). However, the case of coal differs from that of MIL-53: coal is not bi-stable but can adopt an infinity of strains upon adsorption and the mechanical stress exerted on coal in underground conditions is not the bulk pressure of the fluid but the stress applied by surrounding rocks and resulting from the geological history of the site.

Mushrif and Rey (2009) proposed a procedure to relate the amount adsorbed in micropores to the change of porosity and to the induced strain. They assume that the adsorbed molecules are filling the microporosity at an adsorbed density. Making use of the constitutive equation of classical poroelasticity (Coussy, 2004), they estimate the variation of microporosity during adsorption from the adsorption-induced strain measured experimentally. Then, they use statistical physics to relate this adsorbed amount to the chemical potential of the adsorbed phase. Comparing the solid deformed upon adsorption with the solid in its state of reference, they develop an iterative procedure which leads to a relation between the adsorbed amount and the induced strain.

The procedure developed by Mushrif and Rey (2009) is validated by verifying that the predicted adsorption-induced strain compares well with the experimental adsorption-induced strain used as an input in the procedure.

Jakubov and Mainwaring (2002) used the so-called theory of vacancy solutions to develop a model of adsorption-induced strain, which captures well the dimensional change of zeolites under adsorption. In the theory of vacancy solution, the system adsorbent-adsorbate is considered as a thermodynamic solution made of adsorbate molecules and vacancies. A change of volume at fixed amount of adsorbed molecules is modeled as being equivalent to compressing the solution with a membrane permeable to the vacancies and impermeable to the adsorbed molecules. Jakubov and Mainwaring (2002) used this representation to relate the adsorption-induced strain to the difference of fluid chemical potential between a configuration in which the solid is immersed in the fluid, and a configuration at zero strain with the same amount of fluid adsorbed. In this model, the variation of interface stress is introduced but is eventually neglected and the Helmholtz free energy per unit volume of the adsorbate-vacancy solution (i.e., the mechanical stress of the adsorbate-vacancy solution) is assumed equal to the mechanical stress of the adsorbent-adsorbate system, which is questionable.

3.5 Conclusion

Most existing models for adsorption-induced deformation are not suitable for amorphous microporous solids: the notion of interface stress is only valid for mesoporous solids with clearly defined interfaces, the notion of disjoining pressure is only applied to micropores with specific geometries, such as slit pores or spheroidal pores. Only the approach of Coudert et al. (2008) in the osmotic ensemble introduces no notion of interface, porosity or pore size. Therefore this approach could theoretically be adapted to the study of coal. However, MIL-53 differs significantly from coal: MIL-53 is bi-stable, its structure is crystalline, and, in the case studied by Coudert et al. (2008), the external confining stress is equal to the bulk pressure of the adsorbed fluid. The objective of our work is to develop a physical model of adsorption-induced deformation valid for amorphous microporous solids and in particular for coal subject to an adsorption of carbon dioxide and methane. The model must relate the strain of the solid to the bulk pressure of the adsorbed fluid and to the confining stress exerted on the solid. The derivation of such a model is the focus of the next chapter.

Chapter 4

Poromechanics of adsorption phenomena

THIS CHAPTER *presents classical poromechanics and its extension to adsorption on surfaces and in micropores. The constitutive equations of classical poromechanics are derived assuming that the fluid in the pores remains in its bulk state. According to those equations, the poromechanical behavior of a medium does not depend on the composition of the pore fluid, but on its bulk pressure only. When the fluid is adsorbed at the surface of the pores, an additional term intervenes in the energy balance of the system, which accounts for the energy stored at the fluid-solid interface. In that case, the constitutive equations of poromechanics account explicitly for the effect of the interface stresses and the poromechanical behavior of the medium depends explicitly on the nature of the fluid. How interface stresses lead to a macroscopic deformation significantly depends on the microstructure. An analysis of orders of magnitude shows that surface effects are significant only for mediums whose specific surface is large and stiffness is low. In order to account for adsorption in micropores, more general poromechanical constitutive equations are derived, which do not refer to the notions of porosity or specific surface. These equations are valid for a generic fluid and a generic porous structure, and in particular for a fluid adsorbed in micropores with complex morphology. The mechanical effect of adsorption can be determined if the amount of adsorbed fluid in the medium is known in function of both the chemical potentials of the components of the fluid and the volumetric strain of the porous medium. These poromechanical equations are consistent with the notion of disjoining pressure and with the existing models for adsorption-induced strain.*

Ce chapitre *présente la poromécanique classique et son extension à l'adsorption de surface puis à l'adsorption dans des micropores. Les équations constitutives de la poromécanique classique sont obtenues en supposant que le fluide dans les pores est dans son état bulk. D'après ces équations, le comportement mécanique d'un milieu poreux ne dépend pas de la composition du fluide dans les pores, mais seulement de la pression du réservoir de fluide. Lorsque le fluide est adsorbé à la surface des pores, un nouveau terme apparaît dans le bilan d'énergie du système, qui représente l'énergie à l'interface fluide-solide. Dans ce cas, les équations constitutives poromechaniques tiennent compte explicitement de l'effet de la contrainte d'interface et le comportement mécanique du solide poreux dépend de la nature du fluide. Pour une contrainte d'interface donnée, l'effet mécanique des interfaces est très sensible à la microstructure. Quelques calculs d'ordres de grandeurs montrent que les effets de surface ne sont significatifs que pour des solides de grande surface spécifique et suffisamment souples. Pour traiter l'adsorption dans des micropores, une version plus générale des équations constitutives est développée, ne faisant intervenir ni la notion de porosité ni la notion de surface spécifique. Ces équations sont valides quelque soit la forme du fluide et quelque soit la structure poreuse, en particulier pour un fluide adsorbé dans des micropores de morphologie complexe. L'effet mécanique de l'adsorption peut être estimé à condition de connaître comment la quantité de fluide adsorbée dépend à la fois des potentiels chimiques des composants du fluide et de la déformation volumique du solide. Ces équations poromécaniques sont cohérentes avec la notion de pression de disjonction et avec les modèles existants de déformation induite par l'adsorption.*

Outline of Chapter 4

The purpose of this chapter is to develop a physical model that captures the mechanical effect of adsorption in porous solids. In the perspective of applying this model to coal during ECBM, the model must be valid for adsorption in microporous solids, for which the notions of specific surface, pore volume or pore size are ambiguous. The model must also take into account the fact that external confining stress and bulk pressure of the fluid are independent parameters.

The model will rely on poromechanics, which is a field of physics defined as *"the study of porous materials whose mechanical behavior is significantly influenced by the pore fluid"* (Coussy, 2004). Poromechanics aims at predicting the relationship between confining stress, strain and fluid bulk pressure. Therefore, the framework of poromechanics is an appropriate framework in which to derive our model. In the first section, we recall the fundamentals of classical poromechanics, which applies to macroporous solids only, for which all pore fluid is in its bulk state. In the second section, we extend classical poromechanics to mesoporous solids for which adsorption on the pore walls cannot be neglected. In the third section, we extend poromechanics to microporous solids. The derived constitutive equations prove to be valid whatever the state of the fluid in the porous solid is: bulk, adsorbed on surfaces, or adsorbed in micropores. We show the consistency of those latter constitutive equations, with the models existing in the literature and we discuss how those equations can be used in practice.

4.1 Classical poromechanics

In this section we recall how the constitutive equations of classical poromechanics (Coussy, 2004, 2010) are derived.

4.1.1 Derivation

The system considered is a porous solid in which all fluid is in its bulk state: therefore, the derivation performed in this section is only valid for a macroporous solid. The volume fraction filled by the fluid is called the porosity. The solid part is called the solid skeleton. We consider that the whole system can exchange heat and fluid molecules with a large reservoir. The fluid is in the grand canonical ensemble; the solid is in the canonical ensemble.

In the grand canonical ensemble, the fluid can exchange particle and energy with a large reservoir, so that the chemical potentials μ_k of its components and its temperature T are fixed. In this ensemble, the thermodynamic potential which is minimum is the grand potential $\Omega_f = E_f - TS_f - \sum_k \mu_k N_k$, where E_f is the internal energy of the fluid, S_f is its entropy, and N_k is the number of fluid molecules of chemical species k. Molecules in a fluid are free to move and rearrange. A fluid is isotropic and cannot sustain shear at equilibrium. In the grand canonical ensemble, the macroscopic parameters that fully determine the state of a fluid are the chemical potentials μ_k of its components, its volume V_f, and its temperature T. Using the equations of state with respect to these parameters (Tab. 2.1), we derive the grand potential energy balance:

$$d\Omega_f = -S_f dT - P dV_f - \sum_k N_k d\mu_k \tag{4.1}$$

where $P = -\partial\Omega_f / \partial V_f|_{T,\mu_k}$ is the pressure.

The temperature T and the chemical potentials μ_k are intensive parameters. Moreover, provided the fluid is in its bulk state, the volume V_f is an extensive parameter. Therefore, the grand

potential Ω_f of a fluid in its bulk state is of the form $\Omega_f = \chi \cdot V_f$, where $\chi(T, \mu_k)$ is a function of the temperature and chemical potentials only. According to the definition of pressure ($P = -\partial\Omega_f / \partial V_f|_{T,\mu_k}$), χ can be interpreted as the opposite of the bulk pressure P. For a bulk fluid, the grand potential Ω_f is:

$$\Omega_f = -PV_f \tag{4.2}$$

Combining the energy balance (Eq. 4.1) and the expression of the grand potential (Eq. 4.2) we obtain the Gibbs-Duhem equation:

$$-S_f dT + V_f dP - \sum_k N_k d\mu_k = 0 \tag{4.3}$$

or, equivalently:

$$\left.\frac{\partial P}{\partial \mu_k}\right|_{T,\mu_{k'\neq k}} = (\rho_k)_{bulk} = \frac{1}{(\overline{V}_k)_{bulk}} \;;\; \left.\frac{\partial P}{\partial T}\right|_{\mu_k} = \left(\frac{S_f}{V_f}\right)_{bulk} \;;\; \left.\frac{\partial \mu_k}{\partial T}\right|_{P,\mu_{k'}} = -\left(\frac{S_f}{N_k}\right)_{bulk} \tag{4.4}$$

where $\rho_k = N_k/V_f$ is the density of the component k of the fluid, $\overline{V}_k = 1/\rho_k$ is its volume per molecule, and the subscript $\square_{bulk}$ indicates that the quantities considered are those of a bulk fluid.

In contrast to a fluid, a solid does not exchange molecules with its environment, provided we disregard chemical reactions and phase changes. In the canonical ensemble, the number of atoms, the volume, and the temperature are fixed. For a non porous solid in the canonical ensemble, the thermodynamic potential which is minimum at equilibrium is the Helmholtz free energy $F_s = E_s - TS_s$, where E_s is the internal energy of the solid, T is its temperature, and S_s is its entropy. In a solid, the atoms are not free to move but are tightly bonded to their position in the atomic structure: a solid can sustain shear. Therefore, the macroscopic parameters that determine the physical state of an elastic solid in the canonical ensemble are its strain tensor $\underline{\underline{\epsilon}}$, its undeformed volume V_0, and its temperature T. The Helmholtz free energy F_s is an extensive function of the undeformed volume V_0. The Helmholtz free energy per unit undeformed volume $f_s = F_s/V_0$ depends on the strain $\underline{\underline{\epsilon}}$ and on the temperature T only. The components σ_{ab} of the stress tensor of the solid are defined as the derivative of the Helmholtz free energy with respect to the components ϵ_{ab} of the strain tensor:

$$\sigma_{ab} = \left.\frac{\partial f_s}{\partial \epsilon_{ab}}\right|_{T,\epsilon_{a'b'\neq ab}} \quad \text{with} \;\; (a,b) \in \{x,y,z\}^2 \tag{4.5}$$

Accordingly, the Helmholtz free energy balance for a non porous solid is:

$$df_s = -\widetilde{s}_s dT + \sum_{a,b} \sigma_{ab} d\epsilon_{ab} \tag{4.6}$$

where $\widetilde{s}_s = S_s/V_0$ is the entropy per unit undeformed volume. The stress tensor $\underline{\underline{\sigma}}$ and the strain tensor $\underline{\underline{\epsilon}}$ can be decomposed into their spherical (σ, ϵ) and deviatoric $(\underline{\underline{s}}, \underline{\underline{e}})$ parts, respectively (Fig 4.1):

$$\underline{\underline{\sigma}} = \sigma \underline{\underline{1}} + \underline{\underline{s}} \text{ with } \sigma = \tfrac{1}{3}\left(\sigma_{xx} + \sigma_{yy} + \sigma_{zz}\right) \tag{4.7}$$

$$\underline{\underline{\epsilon}} = \tfrac{1}{3}\epsilon \underline{\underline{1}} + \underline{\underline{e}} \text{ with } \epsilon = \epsilon_{xx} + \epsilon_{yy} + \epsilon_{zz} \tag{4.8}$$

where $\left(\underline{\underline{1}}\right)_{ab} = \delta_{ab}$. An equivalent formulation of the free energy balance (Eq. 4.6) is:

$$df_s = -\widetilde{s}_s dT + \sigma d\epsilon + \sum_{a,b} s_{ab} de_{ab} \tag{4.9}$$

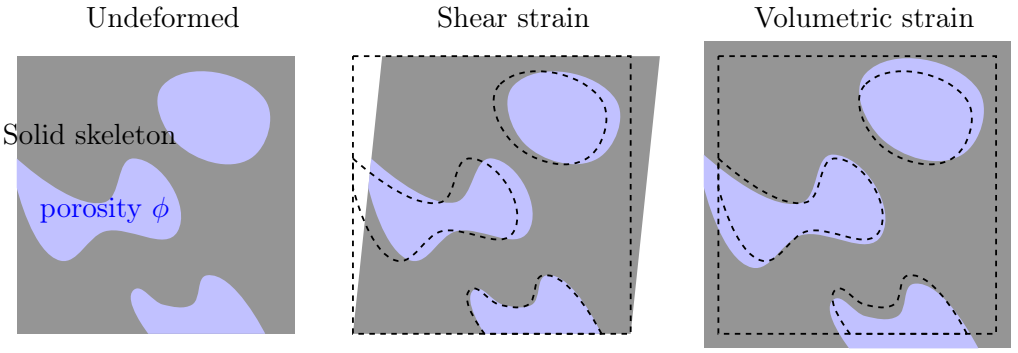

FIGURE 4.1. *Types of strain that can be applied to a porous medium.*

Let us consider that the solid is porous and a fluid, in its bulk state, can fill the pores. We consider the system made of the solid skeleton and the fluid in the pores. We call this system the 'porous medium'. The undeformed volume of the porous medium is V_0. The porous medium can exchange heat and fluid molecules with a large reservoir. Therefore the temperature T of the system, the chemical potentials μ_k of the components of the fluid, and the strain $\underline{\underline{\epsilon}}$ are imposed. At equilibrium, the thermodynamic potential which is minimum is an hybrid potential ω_{hyb} per unit undeformed volume defined as:

$$\omega_{hyb} = \Omega_{hyb}/V_0 = \left(E - TS - \sum_k \mu_k N_k\right) \Big/ V_0 \tag{4.10}$$

where E is the internal energy of the system, S is its entropy and N_k is the number of molecules of the component k of the fluid. The summation to be performed is over the components of the fluid only. This potential is 'hybrid' because it is the sum of the Helmholtz free energy f_s per unit undeformed volume of the porous medium in the absence of any fluid and of the grand potential ω_f of the fluid in the pores: $\omega_f = \Omega_f/V_0 = -P\phi$, where the Lagrangian porosity $\phi = V_f/V_0$ is the volume occupied by the fluid per unit undeformed volume of the porous solid. The energy balance associated to the whole system is:

$$d\omega_{hyb} = \sigma d\epsilon + \sum_{a,b} s_{ab} de_{ab} - \widetilde{s} dT - \sum_k \widetilde{n}_k d\mu_k \tag{4.11}$$

where $\widetilde{s} = S/V_0$ is the entropy and $\widetilde{n}_k = N_k/V_0$ is the number of molecules of the component k of the fluid. f_s, ω_f, $\widetilde{s}$, and $\widetilde{n}_k$ are all expressed per unit undeformed volume of the porous medium.

The porosity ϕ is an additional parameter that governs the exchange of volume between the fluid and the solid matrix: therefore, the fluid and the solid matrix can exchange energy through

mechanical work. The small amount $d\omega_f = -Pd\phi$ of grand potential lost by the fluid consecutively to an increase of porosity $d\phi$ is transferred to the solid, whose free energy f_s increases by a small amount $df_s = Pd\phi$. Porosity is a state variable for the solid matrix and for the fluid considered separately, but not for the system made of the porous medium as a whole: the porosity evolves toward its equilibrium value for which the hybrid potential ω_{hyb} is minimum. The energy balance (4.11) can be rewritten as the sum of the energy balance of the solid matrix and of the fluid considered separately:

$$\begin{array}{rcllll} df_s & = & \sigma d\epsilon & +\sum_{a,b} s_{ab} de_{ab} & -\widetilde{s}_s dT & +Pd\phi \\ d\omega_f & = & & & -\widetilde{s}_f dT & -Pd\phi & -\sum_k \widetilde{n}_k d\mu_k \\ d\omega_{hyb} = df_s + d\omega_f & = & \sigma d\epsilon & +\sum_{a,b} s_{ab} de_{ab} & -\widetilde{s} dT & & -\sum_k \widetilde{n}_k d\mu_k \end{array} \tag{4.12}$$

where $\widetilde{s}_s = S_s / V_0$, $\widetilde{s}_f = S_f / V_0$ and $\widetilde{s} = \widetilde{s}_s + \widetilde{s}_f$.

Since fluid in macropores is in its bulk state, $\widetilde{n}_k = \phi (\rho_k)_{bulk}$ and $\widetilde{s}_f = \phi (S_f / V_f)_{bulk}$. Making use of the Gibbs-Duhem equation (4.3), we rewrite the energy balance (4.11) of the porous medium:

$$d\omega_{hyb} = \sigma d\epsilon + \sum_{a,b} s_{ab} de_{ab} - \widetilde{s}_s dT - \phi dP \tag{4.13}$$

In that energy balance, the composition of the fluid no more intervenes: only the bulk pressure P of the fluid matters. Equation (4.13) shows that the hybrid potential ω_{hyb} is fully determined by the set of state variables (ϵ, e_{ab}, T, P). Likewise, the volumetric stress σ, the deviatoric stresses s_{ab}, the entropy $\widetilde{s}_s$ of the solid, and the porosity ϕ depend on the same set of state variables. The constitutive equations of poromechanics are the equations that relate σ, s_{ij} and ϕ to ϵ, e_{ij}, T and P:

$$\begin{array}{rcl} \sigma & = & \left.\dfrac{\partial \omega_{hyb}}{\partial \epsilon}\right|_{e_{ab},T,P} = \sigma (\epsilon, e_{ab}, T, P) \\ \phi & = & -\left.\dfrac{\partial \omega_{hyb}}{\partial P}\right|_{\epsilon,e_{ab},T} = \phi (\epsilon, e_{ab}, T, P) \\ s_{ab} & = & \left.\dfrac{\partial \omega_{hyb}}{\partial e_{ab}}\right|_{\epsilon,e_{a'b'\neq ab},T,P} = s_{ab} (\epsilon, e_{a'b'}, T, P) \end{array} \tag{4.14}$$

Under the assumption of linear poroelasticity, σ, ϕ and s_{ab} depend linearly on the state variables. Under the assumption of isotropy, only the shear stresses depend on the shear strains. Therefore, for a linear isotropic poroelastic solid in isothermal conditions, the constitutive equations are:

$$\begin{array}{rcl} \sigma & = & K\epsilon - bP \\ \varphi & = & b\epsilon + P/\overline{N} \\ s_{ab} & = & 2\overline{G} e_{ab} \end{array} \tag{4.15}$$

where $\varphi = \phi - \phi_0$ is the variation of Lagrangian porosity with respect to the porosity ϕ_0 at zero strain ($\epsilon = 0$) and zero pressure ($P = 0$). K is called the bulk modulus, b the Biot coefficient, $\overline{N}$

the Biot modulus, and $\overline{G}$ the shear modulus.

4.1.2 Detailed analysis

An important assumption used in order to derive the constitutive equations (4.15) of classical poromechanics is that the fluid in the pores is in its bulk state. This assumption implies that the fluid molecules in the pores are at their bulk density, thus providing a clear definition of the porosity: the pore volume is the volume occupied by the fluid molecules at their bulk density. Moreover, the energy balance (Eq. 4.13) shows that the fluid (potentially multi-component) only intervene through its bulk pressure P. In other words, the mechanical behavior of the porous medium only depends on the bulk pressure of the fluid and not on its detailed composition. Two fluids of different compositions but at the same bulk pressure lead to the same deformation of the medium. But, during an immersion of coal in a fluid, experiments show that the deformation of the coal sample depends on the nature of the fluid (Fig. 1.8). Such experimental observation cannot be explained by the classical constitutive equations (4.15). The fact that two fluids at the same bulk pressure but with different composition induce different deformations is an evidence that at least one of the two fluids is not in its bulk state in the porous medium.

Another important assumption used in order to derive the constitutive equations (4.15) of classical poromechanics is that the system is fully determined by the strains ϵ and e_{ab} in addition to the fluid pressure P and the temperature T. Such an assumption is only valid for poroelasticity. More complex behaviors require the introduction of additional parameters: time for viscoelasticity, irreversible deformations for plasticity... Moreover, the dependence of the free energy $f_s\left(\epsilon, e_{ab}, \phi, T\right)$ of the solid skeleton on its arguments is assumed unchanged in presence of the fluid. Such assumption implies that there is no modification of the atomic structure of the solid, e.g., by fracturation or through chemical reactions.

The constitutive equations (4.15) for an isotropic linear poroelastic solid are common in poromechanics. Several refinements of these equations exist (Coussy, 2010) for non-linear poroelasticity, thermoporoelasticity, poroviscoelasticity, poroplasticity. The poroelastic properties K, b, $\overline{N}$, and $\overline{G}$ characterize the poromechanical behavior of the material. These properties only depend on the solid skeleton, but not on the nature of the fluid. The bulk modulus K and the shear modulus $\overline{G}$ characterize the mechanical behavior of the porous solid in the absence of any fluid. Those moduli are positive quantities: such a positivity is required for the solid to be mechanically stable. The Biot coefficient b is a coupling coefficient between the fluid and the solid skeleton, which represents the fraction of the volumetric strain ϵ which comes from a variation of porosity $\phi - \phi_0$, and which represents also the fraction of the fluid pressure P that contributes to the overall volumetric stress σ.

When the solid matrix is incompressible, any volumetric strain of the porous medium is due to a variation of porosity, and any change of porosity is due to a volumetric strain of the porous medium. Therefore, the Biot coefficient and Biot modulus of a porous medium with an incompressible solid matrix are $b = 1$ and $\overline{N} \to +\infty$, respectively. When the solid matrix is compressible, part of the volumetric strain is due to the strain of the solid matrix and a pore pressure can induce a change of porosity: $b < 1$ and $\overline{N}$ is finite. Moreover, a positive strain increases the porosity and so does a positive pressure of the fluid: $b > 0$ and $\overline{N} > 0$. Therefore the ranges of possible values for the Biot coefficient b and Biot modulus $\overline{N}$ are $[0; 1]$ and $[0; +\infty[$, respectively.

Micromechanical approaches were developed to relate the poroelastic properties K, $\overline{G}$, b, and $\overline{N}$

to the elastic properties of the solid skeleton. Two relations hold irrespective of the pore morphology, provided the solid skeleton is a homogeneous linear elastic solid with bulk modulus K_s:

$$b = 1 - \frac{K}{K_s} \text{ and } \frac{1}{\overline{\overline{N}}} = \frac{b - \phi_0}{K_s} \tag{4.16}$$

The immersion experiment is an experiment in which the porous solid is immersed in the fluid. The stress which is exerted on the boundaries of the sample is the bulk pressure of the fluid: $\underline{\underline{\sigma}} \cdot \mathbf{n} = -P\mathbf{n}$ for any unit vector $\mathbf{n}$ orthogonal to the boundary. For a fluid at rest, neglecting any body force such as gravitation, the balance of momentum is: $\nabla \cdot \underline{\underline{\sigma}} = \mathbf{0}$. The solution of this problem is a uniform spherical stress:

$$\underline{\underline{\sigma}} = -P\underline{\underline{1}} \Leftrightarrow \sigma = -P \text{ and } s_{ab} = 0 \tag{4.17}$$

which does not depend on the constitutive equations of the solid. For an isotropic linear poroelastic solid immersed in a fluid, making use of the first constitutive equation of linear poroelasticity (Eqs. 4.15), we obtain the volumetric strain ϵ during an immersion experiment:

$$\epsilon = \frac{b-1}{K}P = -\frac{P}{K_s} < 0 \tag{4.18}$$

Classical poromechanics predicts a shrinkage of the porous medium during an immersion experiment (Fig. 4.2). The more rigid the solid matrix, the smaller the shrinkage. The total volumetric strain ϵ is equal to the volumetric strain of the solid matrix ϵ_s.

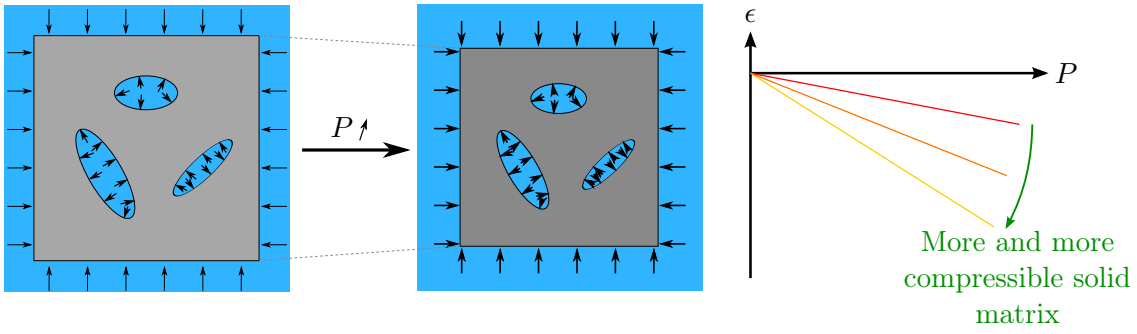

FIGURE 4.2. *Shrinkage during an immersion experiment as predicted by the constitutive equations (4.15) of classical poromechanics.*

For coal, a small shrinkage proportional to the pressure of the fluid is indeed observed when coal is immersed in pure helium (Fig. 1.8). However, only with helium is this shrinkage observed: other fluids, such as carbon dioxide and methane, lead to a swelling of the coal sample. Helium is almost not adsorbed in coal and therefore the assumption of pores filled with a bulk fluid is respected. Coal filled with helium behaves as expected by classical poromechanics, which suggests that, apart from the effect of adsorption, coal is satisfactorily described by a linear elastic behavior.

In order to model the immersion of coal in another fluid, poromechanics must be extended to cases in which some of the pore fluid is not in its bulk state, i.e., is in an adsorbed state. The next section is dedicated to the extension of poromechanics to surface adsorption.

4.2 Extension of poromechanics to surface adsorption

4.2.1 Derivation

In this section, we aim at extending poromechanics to porous media for which adsorption of fluid at the surface of the pores occurs. We consider a porous medium in which a fraction of the fluid molecules in the pores are not in their bulk state, but are adsorbed on the pore walls. According to the Gibbs adsorption equation (3.13), the adsorbed molecules modify the energy of the interface between the fluid and the solid skeleton. In order to extend poromechanics to case in which adsorption occurs on surfaces, interface energy must be taken into account in the derivation of the constitutive equations. The specific surface a is the area of pore walls per unit volume of undeformed porous medium. The interface energy per unit volume of undeformed porous medium is therefore γa.

As in classical poromechanics, when the strain $\underline{\underline{\epsilon}}$, the temperature T, and the chemical potentials μ_k of the components of the pore fluid are imposed, at equilibrium, the hybrid potential $\omega_{hyb} = (E - TS - \sum_k \mu_k N_k)/V_0$ is minimum. The energy balance is:

$$d\omega_{hyb} = \sigma d\epsilon + \sum_{a,b} s_{ab} de_{ab} - \widetilde{s} dT - \sum_k \widetilde{n}_k d\mu_k \tag{4.19}$$

The summation term in the energy balance (4.19) cannot be simplified with the Gibbs-Duhem equation (4.3) as in the previous derivation because the fluid molecules, which are in amount $\widetilde{n}_k = N_k/V_0$, are not in their bulk state. We distinguish the number of fluid molecules $(\rho_k)_{bulk}\,\phi$ that fill the pores at the bulk density, and the number of fluid molecules $\Gamma_k a$ adsorbed in excess on the pore walls, so that: $\widetilde{n}_k = (\rho_k)_{bulk}\,\phi + \Gamma_k a$. Using the Gibbs-Duhem equation (4.3) and the Gibbs adsorption equation (3.13), we obtain:

$$d\omega_{hyb} = \sigma d\epsilon + \sum_{a,b} s_{ab} de_{ab} - \widetilde{s}_s dT - \phi dP + a\, d\gamma|_{\epsilon^s} \tag{4.20}$$

where $\widetilde{s}_s = (S - S_f - S^s)/V_0$ is the entropy of the solid skeleton, to which the excess entropy S^s at the fluid-solid interface is substracted. The specific area a is not a state parameter of the porous medium, but evolves toward its equilibrium value for which the hybrid potential ω_{hyb} is minimum. Indeed, in the hybrid ensemble here considered, a is a function of the volumetric strain ϵ, of the deviatoric strains e_{ab}, of the temperature T, and of the chemical potentials μ_k of the components of the fluid. For small strains of an isotropic medium, a does not depend on the deviatoric strains e_{ab}. The interface energy γ is a function of the fluid chemical potentials μ_k and of the surface strain[1] $\epsilon^s = \ln(a/a_0)$, where a_0 is the specific surface in the undeformed configuration. Therefore, the variation $d\gamma|_{\epsilon^s}$ of interface energy in the energy balance (4.20) depends on the variation $d\mu_k$ of the chemical potentials: $d\gamma|_{\epsilon^s} = \sum_k \left.\frac{\partial \gamma}{\partial \mu_k}\right|_{\epsilon^s} d\mu_k$. Unlike the energy balance (4.13) of classical poromechanics, the composition of the fluid intervenes in the energy balance (4.20). Therefore, when interface energy is taken into account, the mechanical behavior of the porous medium depends on the nature of the fluid. The energy balance (4.20) can be rearranged by using Shuttleworth equation (3.12), thus introducing the interface stress σ^s:

[1] Here we assume that the interface is isotropic and there is no need to distinguish the orientation of the surface strain.

$$d\left(\omega_{hyb} - \gamma a\right) = \sigma d\epsilon + \sum_{a,b} s_{ab} de_{ab} - \widetilde{s}_s dT - \phi dP - \sigma^s da \tag{4.21}$$

We call ω^r_{hyb} the energy $\omega_{hyb} - \gamma a$. The constitutive equations of poromechanics (Eqs. 4.14) are modified as follows:

$$\begin{aligned} \sigma &= \left.\frac{\partial \omega^r_{hyb}}{\partial \epsilon}\right|_{e_{ab},T,P} + \sigma^s \alpha^\mu_\epsilon \\ \phi &= -\left.\frac{\partial \omega^r_{hyb}}{\partial P}\right|_{\epsilon,e_{ab},T} - \alpha^\epsilon_P \sigma^s \\ s_{ab} &= \left.\frac{\partial \omega^r_{hyb}}{\partial e_{ab}}\right|_{\epsilon,e_{a'b'\neq ab},T,P} \end{aligned} \tag{4.22}$$

where $\alpha^\mu_\epsilon = \left.\frac{\partial a}{\partial \epsilon}\right|_{T,\mu_k}$ and $\alpha^\epsilon_P = \sum_k \left(\overline{V}_k\right)_{bulk} \left.\frac{\partial a}{\partial \mu_k}\right|_{\epsilon,T,\mu_{k'\neq k}}$.

ω^r_{hyb} is the hybrid potential of the porous medium with no interface energy, i.e., which can be described by classical poromechanics. Therefore, the derivatives of ω^r_{hyb} in Eqs. (4.22) are the constitutive equations of classical poromechanics. For an isotropic linear poroelastic material in isothermal conditions, the constitutive equations of poromechanics extended to surface effects are:

$$\begin{aligned} \sigma &= K\epsilon - bP + \alpha^\mu_\epsilon \sigma^s \\ \varphi &= b\epsilon + \frac{P}{\overline{N}} - \alpha^\epsilon_P \sigma^s \\ s_{ab} &= 2\overline{G} e_{ab} \end{aligned} \tag{4.23}$$

Since the specific surface a is a geometrical feature, it is more intuitive to consider its dependency on the other geometrical characteristics, i.e., the volumetric strain ϵ and the porosity ϕ. By considering the set of control variables ϵ, e_{ab}, ϕ and T, the constitutive equations (4.23) can be rewritten as follows:

$$\begin{aligned} \sigma - \alpha^\phi_\epsilon \sigma^s &= K\epsilon - b\left(P - \alpha^\epsilon_\phi \sigma^s\right) \\ \varphi &= b\epsilon + \frac{P - \alpha^\epsilon_\phi \sigma^s}{\overline{N}} \\ s_{ab} &= 2\overline{G} e_{ab} \end{aligned} \tag{4.24}$$

where $\alpha^\phi_\epsilon = \left.\frac{\partial a}{\partial \epsilon}\right|_\phi$ and $\alpha^\epsilon_\phi = \left.\frac{\partial a}{\partial \phi}\right|_\epsilon$ are material properties of the porous medium. These derivatives depend on the morphology of the pores and on the mechanical properties of the matrix.

The interface stress σ^s, which acts as a stretched membrane at the surface of all pores, generates a pre-stress $\sigma_{ini} = \alpha^\phi_\epsilon \sigma^s$ and an initial pore pressure $P_{ini} = \alpha^\epsilon_\phi \sigma^s$. Therefore, the interface stress induces a permanent strain ϵ_{ini} and a permanent change of porosity φ_{ini}:

$$\epsilon_{ini} = -\frac{1}{K}\left(\alpha_\epsilon^\phi + b\alpha_\phi^\epsilon\right)\sigma^s = -\frac{1}{K}\alpha_\epsilon^\mu\sigma^s \tag{4.25}$$

$$\varphi_{ini} = b\epsilon_{ini} - \frac{\alpha_\phi^\epsilon}{\overline{N}}\sigma^s \tag{4.26}$$

The expression of the change of porosity φ_{ini} can be simplified by considering the volumetric stress σ instead of the volumetric strain ϵ as control variable:

$$\varphi_{ini} = -\left(\frac{b^2}{K} + \frac{1}{\overline{N}}\right)\left.\frac{\partial a}{\partial\phi}\right|_\sigma \sigma^s = -\left(\frac{b^2}{K} + \frac{1}{\overline{N}}\right)\alpha_\phi^\sigma\sigma^s \tag{4.27}$$

4.2.2 Role of the microstructure

Even in the absence of any fluid, the interface stress σ^s that prevails at the surface of the pores generates a strain ϵ_{ini} and a change of porosity φ_{ini} (see Sec. 4.2.1). When the fluid fills the pores and adsorption occurs, the interface stress varies according to the Gibbs adsorption equation (3.13). This additional strain is an adsorption-induced strain. In contrast to what is observed with classical poromechanics, poromechanics extended to surface adsorption depends on the composition of the fluid since the change of interface energy depends on the excess adsorbed amount, which is specific to a fluid.

The parameters $\alpha_\epsilon^\phi = \left.\frac{\partial a}{\partial\epsilon}\right|_\phi$ and $\alpha_\phi^\epsilon = \left.\frac{\partial a}{\partial\phi}\right|_\epsilon$ determine how an interface stress leads to a strain. α_ϵ^ϕ is the derivative of the specific surface with respect to the strain at fixed porosity. α_ϕ^ϵ is the derivative of the specific surface with respect to the porosity at fixed strain. How the specific surface depends on the strain and on the porosity is specific to a microstucture. To illustrate this specificity, we consider two model microstructures sketched in Fig. 4.3.

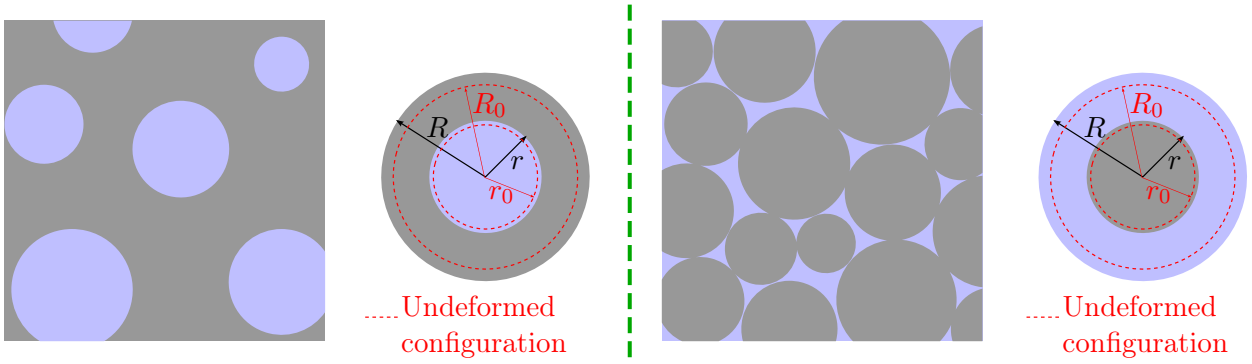

FIGURE 4.3. *Model microstructures for porous media made of spherical pores or spherical grains.*

The first microstructure considered is a spherical pore at the center of a spherical solid matrix. This model microstructure is an idealized geometry for a porous medium with spherical voids. With the notation of Fig. 4.3, the Lagrangian porosity is $\phi = (r/R_0)^3$, the strain is $\epsilon = (R/R_0)^3 - 1$ and the specific surface is $a = 3r^2/R_0^3 = 3\phi^{2/3}/R_0$. From these expressions we derive the parameters α_ϵ^ϕ and α_ϕ^ϵ:

$$\alpha_\epsilon^\phi = 0 \text{ and } \alpha_\phi^\epsilon = \frac{2}{R_0}\phi^{-1/3} = \frac{2}{r} \tag{4.28}$$

Therefore the permanent strain ϵ_{ini} and permanent change of porosity φ_{ini} induced by the surface stress for this microstructure are:

$$\epsilon_{ini} = -\frac{2b}{Kr}\widetilde{\sigma}^s \text{ and } \varphi_{ini} = -\frac{2}{r}\left(\frac{b^2}{K} + \frac{1}{\overline{\overline{N}}}\right)\widetilde{\sigma}^s \tag{4.29}$$

The second microstructure considered is a spherical solid grain surrounded by a spherical void. This second microstructure is an idealized geometry for a granular material. The porosity is $\phi = \left(R^3 - r^3\right)/R_0^3$, the strain $\epsilon = \left(R/R_0\right)^3 - 1$ and the specific surface $a = 3r^2/R_0^3 = 3\left(1+\epsilon-\phi\right)^{2/3}\Big/R_0$. From what follows:

$$\alpha_\epsilon^\phi = \frac{2}{r} \; ; \; \alpha_\phi^\epsilon = -\frac{2}{r} \tag{4.30}$$

and

$$\epsilon_{ini} = -\frac{1-b}{K}\frac{2}{r}\widetilde{\sigma}^s = -\frac{1}{K_s}\frac{2\widetilde{\sigma}^s}{r} \; ; \; \varphi_{ini} = \frac{2}{r}\left(\frac{1}{\overline{\overline{N}}} - \frac{b}{K_s}\right)\widetilde{\sigma}^s = -\frac{\phi_0}{K_s}\frac{2\widetilde{\sigma}^s}{r} \tag{4.31}$$

The strain of the medium is due to the fact that the pressure inside the grain is greater than the bulk fluid pressure by an amount $2\,\sigma^s/r$. Such an amount is reminiscent of Laplace equation (3.16).

For both microstructures considered in this section, the strain induced by surface effects is proportional to the interface stress. But the order of magnitude of the variation of volume induced by an interface stress significantly depends on the microstructure: if the porous medium is much softer than its solid phase (i.e., $K \ll K_s$), the variation of volume can be much greater if the porous medium is made of spherical voids than if the porous medium is made of spherical grains.

For a porous solid with a generic microstructure, the material parameters α_ϵ^ϕ and α_ϕ^ϵ, or equivalently α_ϵ^μ and α_P^ϵ can be determined, in theory, as soon as the microstructure of the porous medium and the mechanical properties of the solid skeleton are known.

4.2.3 Immersion experiment

When immersing a sample in a fluid, the variation $\Delta\epsilon$ of volumetric strain predicted by the first constitutive equation (4.23) is:

$$\Delta\epsilon = -\frac{\alpha_\epsilon^\mu}{K}\Delta\sigma^s - \frac{P}{K_s} \tag{4.32}$$

where the variation $\Delta\sigma^s$ of interface stress is obtained by integrating the Gibbs adsorption equation (3.13) and using Shuttleworth equation (3.12):

$$\Delta\sigma^s = \Delta\gamma + \left.\frac{\partial\Delta\gamma}{\partial\epsilon^s}\right|_{\mu_k} \text{ with } \Delta\gamma = -\int_{(-\infty,\ldots,-\infty)}^{(\mu_1,\ldots,\mu_K)} \sum_k \Gamma_k d\mu_k \tag{4.33}$$

where Γ_k is the excess adsorbed amount per unit area of interface for the component k of the fluid. According to Eq. (4.32), the strain in an immersion experiment can be positive or negative. The term '$-\Delta\sigma^s\alpha_\epsilon^\mu/K$' in Eq. (4.32) arises from the adsorption phenomenon. The term '$-P/K_s$' in Eq.

(4.32) arises from the compressibility of the solid skeleton and corresponds to the strain predicted by classical poromechanics.

For adsorption isotherms of type I, such as the commonly used Langmuir isotherm (Eq. 3.4), the interface energy γ decreases mostly at small pressure of the fluid. For an ideal gas whose adsorption isotherm is governed by the Langmuir isotherm, the integration of Eq. (4.33) yields:

$$\left\{\begin{array}{l}\Gamma = \Gamma_{\max} P/(P+P_0) \\ \mu = \mu_0(T) + k_B T \ln(P)\end{array}\right. \Longrightarrow \Delta\gamma = -k_B T \Gamma_{\max} \int_0^P \frac{1}{P+P_0} dP = -k_B T \Gamma_{\max} \ln\left(1+\frac{P}{P_0}\right) \tag{4.34}$$

Assuming that the excess amount Γ per unit area does not depend on the surface strain (i.e., assuming $\frac{\partial \Delta\Gamma}{\partial \epsilon^s}\big|_{T,\mu_k} = 0$), the variation $\Delta\sigma^s$ of interface stress is equal to the variation $\Delta\gamma$ of interface energy. Under this assumption, the variation of volumetric strain is:

$$\Delta\epsilon = \frac{\alpha_\epsilon^\mu}{K} k_B T \Gamma_{\max} \ln\left(1+\frac{P}{P_0}\right) - \frac{P}{K_s} \tag{4.35}$$

The strain $\Delta\epsilon$ depends on the material properties α_ϵ^μ, K, K_s, and on the parameters $\Gamma_{\max}$ and P_0 that govern the adsorption. For weak adsorption, i.e., $\alpha_\epsilon^\mu k_B T \Gamma_{\max} \ll K P_0/K_s$, the swelling induced by adsorption can be neglected with respect to the contraction due to the compressibility of the solid matrix. By contrast, for strong adsorption, i.e., $\alpha_\epsilon^\mu k_B T \Gamma_{\max} \gg k_B T K P_0/K_s$, the contraction due to the compressibility of the solid matrix can be neglected with respect to the swelling induced by adsorption. We display in Fig. 4.4 the different situations.

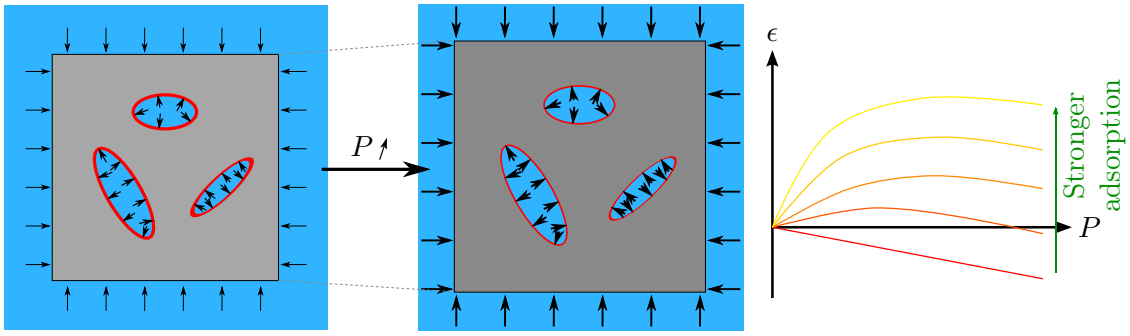

Figure 4.4. *Effect of surface adsorption on strain during an immersion experiment.*

4.2.4 Range of validity

The thermodynamics of interface is valid as long as the inhomogeneous layers of two opposite pore walls do not overlap. We distinguish mesopores and micropores according to this criterion: if the inhomogeneous layers on opposite walls of the pore overlap, the pore is a micropore; conversely, if part of the fluid in the pore is in its bulk state, the pore is a mesopore. Poromechanics extended to surface effects applies to mesoporous materials only. The pore size below which a pore is a micropore depends on the range of molecular interactions. For London dispersion forces, the range of interaction is as small as a few molecular diameters: a threshold of 2 nm for the diameter of the pore is generally used to distinguish micropores from mesopores. By contrast, for dipolar or ionic fluids, the range of interactions can be as large as a few hundred nanometers: the threshold

of 2 nm is not valid. For instance, in the DLVO theory introduced in Sec. 3.2.2, the characteristic length to which the size of the pore must be compared is the Debye length of the electrical double layer and is about 700 nm for water at room temperature.

On the other hand, one can wonder what the pore size is above which surface effects can be neglected. In order to do so, we introduce a distinction between mesopores (in which surface effects must be taken into account) and macropores (in which surface effects can be neglected). In a macroporous material, the specific surface is small enough to neglect the effects of interface energy, i.e., $|\epsilon_{ini}| \ll 1$, which implies $\alpha_\epsilon^\mu \sigma^s \ll K$. The values of interface stress for fluid-solid interface do not exceed 1 N/m in most cases (Andrieu and Müller, 2005). Considering a material made of mono-sized spherical pores of radius r, the material parameter α_ϵ^μ is given by Eq. (4.29): $\alpha_\epsilon^\mu = 2b/r$. Interface effects can be neglected when $2/r \ll K/b$, i.e., when $r/2 \gg 1/K - 1/K_s$. For most porous solids, for which K and K_s are on the order of or larger than 1 GPa, this estimate gives a very small pore radius: $r \gg 2$ nm. Therefore for most solids, only adsorption in micropores can significantly affect the mechanical behavior of the porous solid. Nevertheless, there exist some very compliant solids for which interface effects must be taken into account, e.g., silica aerogels (Reichenauer and Scherer, 2000, Herman et al., 2006) and porous silicons (Dolino et al., 1996). The bulk modulus K of these materials is comprised between 1 and 100 MPa, so that the interface effects must be taken into account for pore sizes up to 1 μm and 10 nm, respectively.

The bulk modulus K of coal is about 1 to 5 GPa (Pan and Connell, 2007, Wang et al., 2009). Therefore only adsorption in micropores can have a significant effect on the mechanical behavior of coal.

4.3 Extension of poromechanics to adsorption in micropores

In this section we derive a general formulation of the constitutive equations of poromechanics that is valid whatever the state of the fluid in the pores is. Such a formulation is in particular valid for microporous media.

For micropores, the notion of pore volume may not be defined unambiguously. Therefore, the notion of solid skeleton and porosity are unclear. From now on, we use the following terminology: 'porous medium' represents the whole system made of the solid and the fluid, 'solid skeleton' represents the atoms of the solid, and 'solid matrix' represents the solid skeleton and the fluid in the micropores.

4.3.1 Derivation

In order to extend poromechanics to adsorption in micropores, the notions of porosity or specific surface must be avoided, since no unambiguous definition of those notions exists for micropores (Fig. 4.5).

We consider a porous solid in thermal equilibrium filled with a fluid for which the chemical potentials of the different components are imposed by an external reservoir. The solid is in the canonical ensemble, the fluid in the grand canonical ensemble; the parameters of control are the strain $\underline{\underline{\epsilon}}$, the chemical potentials μ_k of the components of the fluid, and the temperature T. The hybrid potential $\omega_{hyb} = (E - TS - \sum_k \mu_k N_k)/V_0$ is minimum at equilibrium. The fluid and the solid can exchange energy through mechanical work, but we cannot determine a parameter that

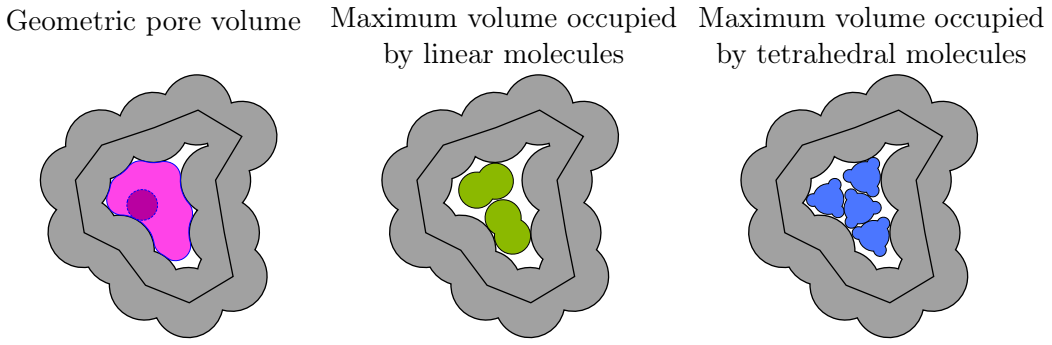

FIGURE 4.5. *Ambiguity in defining the pore volume in a microporous medium. The three methods here presented to measure the pore volume will lead different estimates.*

characterizes this exchange of energy, such as the porosity in classical poromechanics (Sec. 4.1). The energy balance of the system remains the same as for classical poromechanics (Eq. 4.11):

$$d\omega_{hyb} = \sigma d\epsilon + \sum_{a,b} s_{ab} de_{ab} - \widetilde{s} dT - \sum_{k} \widetilde{n}_k d\mu_k \tag{4.36}$$

We cannot further simplify this energy balance as we did for classical poromechanics (Eq. 4.13) by using the Gibbs-Duhem equation. The general form of the constitutive equations of poromechanics is:

$$\begin{aligned}
\sigma &= \left.\frac{\partial \omega_{hyb}}{\partial \epsilon}\right|_{e_{ab},T,\mu_k} = \sigma\left(\epsilon, e_{ab}, T, \mu_k\right) \\
\widetilde{n}_k &= -\left.\frac{\partial \omega_{hyb}}{\partial \mu_k}\right|_{\epsilon,e_{ab},T,\mu_{k'\neq k}} = \widetilde{n}_k\left(\epsilon, e_{ab}, T, \mu_{k'}\right) \\
s_{ab} &= \left.\frac{\partial \omega_{hyb}}{\partial e_{ab}}\right|_{\epsilon,e_{a'b'\neq ab},T,\mu_k} = s_{ab}\left(\epsilon, e_{a'b'}, T, \mu_k\right)
\end{aligned} \tag{4.37}$$

A more explicit formulation of these constitutive equations is obtained from the following two Maxwell relations:

$$\left.\frac{\partial^2 \omega_{hyb}}{\partial \mu_k \partial \epsilon}\right|_{e_{ab},T,\mu_{k'\neq k}} = \left.\frac{\partial^2 \omega_{hyb}}{\partial \epsilon \partial \mu_k}\right|_{e_{ab},T,\mu_{k'\neq k}} \tag{4.38}$$

$$\left.\frac{\partial^2 \omega_{hyb}}{\partial \mu_k \partial e_{ab}}\right|_{\epsilon,e_{a'b'\neq ab},T,\mu_{k'\neq k}} = \left.\frac{\partial^2 \omega_{hyb}}{\partial e_{ab} \partial \mu_k}\right|_{\epsilon,e_{a'b'\neq ab},T,\mu_{k'\neq k}} \tag{4.39}$$

These Maxwell relations can be expressed in function of the first order derivatives σ, $\widetilde{n}_k$, and s_{ab} of ω_{hyb}. The fluid molecules are not in their bulk state and the amounts $\widetilde{n}_k$ may depend on the parameters ϵ, e_{ab}, T and $\mu_{k'}$. In our work, we consider an isotropic medium that undergoes small strains, for which the amounts $\widetilde{n}_k$ do not depend on the deviatoric strains e_{ab}. Therefore the Maxwell relations become:

$$\left.\frac{\partial \sigma}{\partial \mu_k}\right|_{\epsilon,e_{ab},T,\mu_{k'\neq k}} = -\left.\frac{\partial \widetilde{n}_k}{\partial \epsilon}\right|_{e_{ab},T,\mu_{k'}} \tag{4.40}$$

$$\left.\frac{\partial s_{ab}}{\partial \mu_k}\right|_{\epsilon,e_{a'b'},T,\mu_{k'\neq k}} = -\left.\frac{\partial \widetilde{n}_k}{\partial e_{ab}}\right|_{\epsilon,e_{a'b'\neq ab},T,\mu_{k'}} = 0 \tag{4.41}$$

Integration with respect to all the chemical potentials yields:

$$\begin{aligned} \sigma &= \sigma_0 - \frac{\partial}{\partial \epsilon}\left[\int_{(-\infty,\ldots,-\infty)}^{(\mu_1,\ldots,\mu_{\mathcal{K}})} \sum_k \widetilde{n}_k d\mu_k\right]_{e_{ab},T,\mu_k} \\ \widetilde{n}_k &= \widetilde{n}_k\left(\epsilon,\mu_k\right) \\ s_{ab} &= \left(s_{ab}\right)_0 \end{aligned} \tag{4.42}$$

where $\sigma_0 = \sigma\left(\{\mu_1,...,\mu_{\mathcal{K}}\} \rightarrow \{-\infty,..,-\infty\}\right)$ and $\left(s_{ab}\right)_0 = s_{ab}\left(\{\mu_1,...,\mu_{\mathcal{K}}\} \rightarrow \{-\infty,..,-\infty\}\right)$ are the volumetric and deviatoric stresses that prevail when there is no fluid in the pores, respectively. The integration in the first constitutive equation does not depend on the path of integration. According to this formulation of the constitutive equations, the stress of the porous solid can be fully determined as long as the amount of fluid in the porous medium is known in function of both the chemical potentials μ_k of the components of the fluid and the volumetric strain ϵ. Conversely, integrating the first Maxwell equation (4.40) with respect to the volumetric strain, we obtain an alternative formulation of the constitutive equation:

$$\begin{aligned} \sigma &= \sigma\left(\epsilon,\mu_k\right) \\ \widetilde{n}_k &= \widetilde{n}_k^0 - \frac{\partial}{\partial \mu_k}\left[\int_0^{\epsilon} \sigma d\epsilon\right]_{\epsilon,e_{ab},T,\mu_{k'\neq k}} \\ s_{ab} &= \left(s_{ab}\right)_0 \end{aligned} \tag{4.43}$$

where $\widetilde{n}_k^0 = \widetilde{n}_k\left(\epsilon = 0\right)$ is the number of molecules per unit undeformed volume at zero volumetric strain. Accordingly, the amount of fluid in the porous medium can be fully determined if the volumetric stress σ is known in function of both the volumetric strain ϵ and the chemical potentials μ_k of the components of the fluid.

The two sets of constitutive equations (Eqs. (4.42) and (4.43)) are strictly equivalent to each other. In the present work we focus on the impact of adsorption on the mechanical behavior of the porous medium. Therefore we considered the first set of constitutive equations (Eqs. 4.42), for which the amount of adsorbed fluid is an input.

For a linear elastic solid: $\sigma_0 = K\epsilon$ and $\left(s_{ab}\right)_0 = 2\overline{G}e_{ab}$. Moreover, if the fluid is a pure component fluid, according to the Gibbs-Duhem equation (4.3) in isothermal conditions $d\mu = \overline{V}_{bulk}dP$, so that the constitutive equations (4.42) can be rewritten in an alternative form in which the bulk pressure P of the fluid explicitly appears as a state variable:

$$\begin{aligned} \sigma &= K\epsilon - \frac{\partial}{\partial \epsilon}\left[\int_0^P \widetilde{n}\overline{V}_{bulk} dP\right]_{e_{ab},T,P} \\ \widetilde{n}\overline{V}_{bulk} &= \widetilde{n}\left(\epsilon, P\right)\overline{V}_{bulk}\left(P\right) \\ s_{ab} &= 2\overline{G}e_{ab} \end{aligned} \tag{4.44}$$

The notion of porosity used in classical poroelasticity (see Eq. (4.15)) is here replaced by the quantity $\widetilde{n}\overline{V}_{bulk}$, which is the volume occupied by the fluid when fluid molecules are in their bulk state. The integral term in Eq. (4.44) captures the coupling between the pressure of the fluid and the mechanical behavior of the solid: such coupling is captured by the Biot coefficient in classical poromechanics.

According to the first constitutive equation in Eqs. (4.44), how fluid affects the mechanical behavior of the porous medium can be determined if the amount of fluid $\widetilde{n}$ in the porous medium is known in function of both the bulk pressure of the fluid and the deformation of the solid. For adsorption in micropores, many models exist to predict the amount adsorbed in function of the fluid pressure: we presented a few models in Sec. 3.1.1. However, how adsorption depends on the strain is often not considered. In the subsequent chapters, we study in detail how adsorption depends on strain by using molecular simulation.

4.3.2 Consistency with classical poromechanics and with poromechanics extended to surface effects

The general poroelastic constitutive equations (4.44) are valid for porous media with a generic pore size distribution. In this section, we aim at verifying that these new equations are consistent with both classical poromechanical equations (4.15) and poromechanical equations (4.24) extended to surface effect.

In a macroporous medium, since all fluid molecules are in their bulk state, the Gibbs-Duhem equation in isothermal conditions relates the porosity, the amounts of fluid molecules, the change of chemical potentials and the change of pressure: $\sum_k \widetilde{n}_k d\mu_k = \phi dP$. The first constitutive equation in Eqs. (4.42) and the second constitutive equation in Eqs. (4.43) can be rewritten:

$$\sigma = \sigma_0 - \frac{\partial}{\partial \epsilon}\left[\int_0^P \phi dP\right]_{e_{ab},T,P} \tag{4.45}$$

$$\phi = \phi^0 - \frac{\partial}{\partial P}\left[\int_0^\epsilon \sigma d\epsilon\right]_{\epsilon,e_{ab},T} \tag{4.46}$$

where the superscript $\square^0$ stand for 'at zero volumetric deformation' and the subscript $\square_0$ stands for 'in the absence of any fluid'. These constitutive equations are readily obtained by integrating the following Maxwell relation corresponding to the hybrid potential ω_{hyb} considered in Sec. 4.1:

$$\left.\frac{\partial^2 \omega_{hyb}}{\partial P \partial \epsilon}\right|_{e_{ab},T} = \left.\frac{\partial^2 \omega_{hyb}}{\partial \epsilon \partial P}\right|_{e_{ab},T} \Rightarrow \left.\frac{\partial \sigma}{\partial P}\right|_{\epsilon,e_{ab},T} = -\left.\frac{\partial \phi}{\partial \epsilon}\right|_{e_{ab},T,P} \tag{4.47}$$

where the equality $\phi = -\partial\omega_{hyb}/\partial P|_{\epsilon,e_{ab},T}$ comes from the energy balance (Eq. 4.13). This verification shows that the general constitutive equations derived in this section are consistent with classical poromechanics, this latter being valid for macroporous media only.

In a mesoporous medium, the amount $\widetilde{n}_k$ of fluid molecules per unit undeformed volume is the sum of the amount $(\rho_k)_{bulk}\,\phi$ of fluid molecules in their bulk state in the mesopores and the amount $\Gamma_k a$ of fluid molecules adsorbed in excess at the surface of the mesopores: $\widetilde{n}_k = (\rho_k)_{bulk}\,\phi + \Gamma_k a$. According to the Gibbs-Duhem equation (4.3):

$$\sum_k \widetilde{n}_k d\mu_k = \phi dP + a\sum_k \Gamma_k d\mu_k \tag{4.48}$$

For a mesoporous medium, the first constitutive equation in Eqs. (4.42) and the second constitutive equation in Eqs. (4.43) are:

$$\sigma = \sigma_0 - \frac{\partial}{\partial\epsilon}\left[\int_0^P \phi dP\right]_{e_{ab},T,P} - \frac{\partial}{\partial\epsilon}\left[\int_{(-\infty,\ldots,-\infty)}^{(\mu_1,\ldots,\mu_K)} a\sum_k \Gamma_k d\mu_k\right]_{e_{ab},T,\mu_k} \tag{4.49}$$

$$\phi = \phi^0 - \frac{\partial}{\partial P}\left[\int_0^\epsilon \sigma d\epsilon\right]_{\epsilon,e_{ab},T} - \sum_k \left(a\Gamma_k - a^0\Gamma_k^0\right)\left(\overline{V}_k\right)_{bulk} \tag{4.50}$$

These equations can be obtained by integrating the following Maxwell relation corresponding to the hybrid potential ω_{hyb} considered in Sec. 4.2:

$$\left.\frac{\partial^2\omega_{hyb}}{\partial\mu_k\partial\epsilon}\right|_{e_{ab},T,\mu_{k'\neq k}} = \left.\frac{\partial^2\omega_{hyb}}{\partial\epsilon\partial\mu_k}\right|_{e_{ab},T,\mu_{k'\neq k}} \tag{4.51}$$

The explicit formulation of this Maxwell relation is derived from the energy balance (Eq. 4.20) with the help of the Gibbs adsorption equation (3.13):

$$\left.\frac{\partial\sigma}{\partial\mu_k}\right|_{\epsilon,e_{ab},T,\mu_{k'\neq k}} = -\left(\rho_k\right)_{bulk}\left.\frac{\partial\phi}{\partial\epsilon}\right|_{e_{ab},T,\mu_{k'}} - \left.\frac{\partial\left(a\Gamma_k\right)}{\partial\epsilon}\right|_{e_{ab},T,\mu_{k'}} \tag{4.52}$$

Integrating Eq. (4.52) over all chemical potentials μ_k, we readily obtain Eq. (4.49). Integrating Eq. (4.52) over the strain ϵ, we readily obtain Eq. (4.50). Therefore, the generalized constitutive equations (4.42) and (4.43) are consistent with poromechanics extended to surface effects.

4.3.3 Apparent poroelastic properties

The general constitutive equations here derived can be used to calculate apparent poroelastic properties. The apparent tangent drained bulk modulus K^{tan}, secant drained bulk modulus K^{sec}, tangent drained Biot coefficient b^{tan}, and secant drained Biot coefficient b^{sec} are defined as follows:

$$K^{tan} = \left.\frac{\partial \sigma}{\partial \epsilon}\right|_{\mu_k} \quad ; \quad K^{sec} = \frac{\sigma - \sigma\left(\epsilon = 0\right)}{\epsilon} \quad ; \quad b^{tan} = -\left.\frac{\partial \sigma}{\partial P}\right|_{\epsilon} \quad ; \quad b^{sec} = -\frac{\sigma - \sigma\left(P = 0\right)}{P} \tag{4.53}$$

With the help of the first constitutive equation (4.42), we derive the following expressions for these apparent poroelastic properties:

$$K^{tan} = K_0^{tan} - \frac{\partial^2}{\partial \epsilon^2}\left[\int_{(-\infty,\ldots,-\infty)}^{(\mu_1,\ldots,\mu_{\mathcal{K}})} \sum_k \widetilde{n}_k d\mu_k\right]_{e_{ab},T,\mu_k} \tag{4.54}$$

$$K^{sec} = K_0^{sec} - \frac{1}{\epsilon}\int_0^{\epsilon} \frac{\partial^2}{\partial \epsilon^2}\left[\int_{(-\infty,\ldots,-\infty)}^{(\mu_1,\ldots,\mu_{\mathcal{K}})} \sum_k \widetilde{n}_k d\mu_k\right]_{e_{ab},T,\mu_k} d\epsilon \tag{4.55}$$

$$b^{tan} = \sum_k \left.\frac{\partial \widetilde{n}_k}{\partial \epsilon}\right|_{T,\mu_l} \left(\overline{V}_k\right)_{bulk} \tag{4.56}$$

$$b^{sec} = \frac{1}{P}\frac{\partial}{\partial \epsilon}\left[\int_{(-\infty,\ldots,-\infty)}^{(\mu_1,\ldots,\mu_{\mathcal{K}})} \sum_k \widetilde{n}_k d\mu_k\right]_{e_{ab},T,\mu_k} \tag{4.57}$$

where $K_0^{tan} = \left.\frac{\partial \sigma_0}{\partial \epsilon}\right|_P$ and $K_0^{sec} = \frac{\sigma_0 - \sigma_0(\epsilon=0)}{\epsilon}$ are the tangent and secant bulk modulus of the porous solid in the absence of any fluid. For a linear elastic solid of bulk modulus (for which $K = K_0^{tan} = K_0^{sec}$) filled with a one-component fluid, the expressions of the apparent poroelastic properties become:

$$K^{tan} = K - \frac{\partial^2}{\partial \epsilon^2}\left[\int_0^P \widetilde{n}\overline{V}_{bulk} dP\right]_{e_{ab},T,P} \tag{4.58}$$

$$K^{sec} = K - \frac{1}{\epsilon}\int_0^{\epsilon} \frac{\partial^2}{\partial \epsilon^2}\left[\int_0^P \widetilde{n}\overline{V}_{bulk} dP\right]_{e_{ab},T,P} d\epsilon \tag{4.59}$$

$$b^{tan} = \left.\frac{\partial \widetilde{n}}{\partial \epsilon}\right|_{T,P} \overline{V}_{bulk} \tag{4.60}$$

$$b^{sec} = \frac{1}{P}\frac{\partial}{\partial \epsilon}\left[\int_0^P \widetilde{n}\overline{V}_{bulk} dP\right]_{e_{ab},T,P} \tag{4.61}$$

These equations show that, if the adsorption isotherm $\widetilde{n}\left(\epsilon, \mu_1, ..., \mu_{\mathcal{K}}\right)$ depends on the deformation in a complex manner, the apparent bulk moduli K^{tan} and K^{sec} of the porous medium may differ from the bulk modulus K of the solid in the absence of any fluid: the coupling between adsorption and deformation can lead to apparent non-linearities of the porous medium, even when the porous medium behaves linearly in the absence of any fluid. Likewise, the apparent Biot coefficients may depend on the fluid pressure in a complex manner.

For a microporous solid, it is not possible to define the bulk modulus K_s of the solid skeleton and the relation $b = 1 - K/K_s$ between the bulk modulus of the porous medium and the Biot coefficient is no more valid. Nevertheless, combining Eqs. (4.54) and (4.56), one can readily derive the following relation between the tangent drained bulk modulus K^{tan} and the tangent Biot coefficient b^{tan}:

$$K^{tan} = K_0^{tan} - \frac{\partial}{\partial \epsilon}\left[\int_0^P b^{tan} dP\right]_{e_{ab},T,\mu_k} \tag{4.62}$$

A relation also exists between the apparent secant bulk modulus and the apparent secant Biot coefficient. Indeed, combining Eqs. (4.55) and (4.57) we derive:

$$K^{sec} = K_0^{sec} - \frac{P}{\epsilon}\left(b^{sec} - b^{sec}\left(\epsilon = 0\right)\right) \tag{4.63}$$

4.3.4 First order approximation at small strains

Under the hypothesis of small deformations ($\epsilon \ll 1$), we can perform a first-order expansion of the amount of fluid molecules in the solid:

$$\widetilde{n}_k \approx \widetilde{n}_k^0 \left(1 + \widetilde{C}_k \epsilon\right) \tag{4.64}$$

where $\widetilde{n}_k^0 = \widetilde{n}_k\left(\epsilon = 0\right)$ is the amount of fluid per unit undeformed volume when the medium is kept at zero deformation. In the general case, the coupling coefficient $\widetilde{C}_k = \widetilde{C}_k\left(\mu_k\right)$ depends on the chemical potentials μ_k of the components of the fluid[2]. If the approximation (Eq. 4.64) holds, the first constitutive equation (4.42) can be rewritten as:

$$\sigma = \sigma_0 - \int_{(-\infty,\ldots,-\infty)}^{(\mu_1,\ldots,\mu_K)} \sum_k \widetilde{C}_k \widetilde{n}_k^0 d\mu_k \tag{4.65}$$

which, when the solid is linear elastic and is filled with a one-component fluid, reduces to:

$$\sigma = K\epsilon - \int_0^P \widetilde{C}\left(P\right) n^0 \overline{V}_{bulk} dP \tag{4.66}$$

For specific porous media, it may well be that the coupling coefficient $\widetilde{C}$ does not depend on the bulk pressure P of the fluid. In such a case, the poroelastic constitutive equation would further simplify:

$$\sigma = K\epsilon - \widetilde{C}\int_0^P \widetilde{n}^0 \overline{V}_{bulk} dP \tag{4.67}$$

A constant coupling coefficient $\widetilde{C}$ could be interpreted as the inverse of a porosity. Indeed, assuming that the molecules in the micropores are at an adsorbed density ρ_{ads} and that the solid matrix is incompressible, the amount of fluid $\widetilde{n}$ in the porous medium can be expressed as $\widetilde{n} = \rho_{ads}\phi^0 + \rho_{ads}\epsilon = \rho_{ads}\phi^0\left(1 + \epsilon/\phi^0\right)$, from which the coupling coefficient $\widetilde{C}$ is identified as $\widetilde{C} = 1/\phi^0$.

4.4 Discussion

In this work, we used the framework of poromechanics and extended this framework to adsorption at the surface of mesopores and in micropores. The stress induced by the adsorbed fluid is related

[2]In the general case, the coupling coeffcient $\widetilde{C}_k\left(\mu_k, T\right)$ also depends on the temperature. In this work, this dependence is not explicitly written in the notation

to the amount of fluid adsorbed according to the constitutive equations (4.42). How adsorption depends on the strain governs the fluid-induced stress. In the literature, Ravikovitch and Neimark (2006) and Kowalczyk et al. (2008) already came to that conclusion by considering adsorption in spheroidal and slit pores, respectively. Ravikovitch and Neimark (2006) and Kowalczyk et al. (2008) relate the adsorption stress σ_{ads}, i.e., the stress exerted by the fluid molecules on the pore walls, to the grand potential Ω_f of the fluid in the pore according to:

$$\sigma_{ads} = \left.\frac{\partial \Omega_f}{\partial V_{pore}}\right|_{T,\mu} \tag{4.68}$$

The adsorption stress is the stress induced by the adsorbed fluid. The adsorption stress is analogous to $\sigma - \sigma_0$ when the solid is incompressible (by using the notation notations of Sec. 4.3). Kowalczyk et al. (2008) relate explicitly the adsorption stress to the amount of fluid N in a slit pore of area A and thickness $\widetilde{e}$:

$$\sigma_{ads} = \int_{-\infty}^{\mu} \frac{1}{A}\frac{\partial N}{\partial \widetilde{e}} d\mu \tag{4.69}$$

where we set the reference chemical potential of Kowalczyk et al. (2008) to $-\infty$. Equation (4.69) corresponds to the first constitutive equation (4.42) in the case of an anisotropic medium made of slit pores and of an incompressible solid skeleton. In such a medium, the adsorption stress is also related to the disjoining pressure: $\Pi = \sigma_{ads} - P$. Therefore, the constitutive equations derived in Sec. 4.3 are also consistent with adsorption-induced strain models based on disjoining pressure (Ustinov and Do, 2006, Kowalczyk et al., 2008, Do et al., 2008, Yang et al., 2010). The balance of grand potential Ω per unit area of the system composed of a thin film and its two interfaces (Fig. 3.13) is:

$$\frac{1}{A}d\Omega = -\frac{S}{A}dT - \frac{P+\Pi}{A}d\widetilde{e} - \sum_k \frac{N_k}{A}d\mu_k \tag{4.70}$$

Integration at fixed temperature T and fixed thickness $\widetilde{e}$ yields:

$$\frac{\Omega}{A} = -\int_{(-\infty,\ldots,-\infty)}^{(\mu_1,\ldots,\mu_K)} \sum_k \frac{N_k}{A} d\mu_k \tag{4.71}$$

Following the definition of the disjoining pressure (Eq. 3.17) we obtain:

$$P + \Pi = -\frac{\partial}{\partial \widetilde{e}}\left[\int_{(-\infty,\ldots,-\infty)}^{(\mu_1,\ldots,\mu_K)} \sum_k \frac{N_k}{A} d\mu_k\right]_{\mu_k,T} \tag{4.72}$$

Equation (4.72) is equivalent to the formulation of Kowalczyk et al. (2008) (Eq. (4.69)), but for a multicomponent fluid.

The constitutive equations (4.42) also are consistent with the work of Coudert et al. (2008), which consisted in minimizing the osmotic potential $\omega_{os} = (E - TS - \sum_k N_k\mu_k)/V_0 - \sigma\epsilon$. This potential is minimum at equilibrium for a system in the 'osmotic ensemble', for which the control variables are the number of atoms of the solid skeleton, the chemical potentials of the components of the fluid, the volumetric stress σ and the temperature T. In their work, the volumetric stress is equal to the opposite of the fluid pressure since they study an immersed sample. By using the

formalism introduced in Sec. 4.3, we can derive constitutive equations that are relevant to the osmotic ensemble:

$$\begin{aligned} \epsilon &= \epsilon_0 + \frac{\partial}{\partial \sigma}\left[\int_{(-\infty,\ldots,-\infty)}^{(\mu_1,\ldots,\mu_{\mathcal{K}})} \sum_k \widetilde{n}_k d\mu_k\right]_{s_{ab},T,\mu_k} \\ \widetilde{n}_k &= \widetilde{n}_k\left(\sigma,\mu_k\right) \\ e_{ab} &= \left(e_{ab}\right)_0 \end{aligned} \tag{4.73}$$

or

$$\begin{aligned} \epsilon &= \epsilon\left(\sigma,\mu_k\right) \\ \widetilde{n}_k &= {}^0\widetilde{n}_k + \frac{\partial}{\partial \mu_k}\left[\int_0^{\sigma} \epsilon d\sigma\right]_{\sigma,s_{ab},T,\mu_{k'\neq k}} \\ e_{ab} &= \left(e_{ab}\right)_0 \end{aligned} \tag{4.74}$$

where ϵ_0 and $\left(e_{ab}\right)_0$ are the volumetric and deviatoric strains in the absence of any fluid, respectively, and where ${}^0\widetilde{n}_k$ is the amount of fluid molecules when the volumetric stress is zero. For an isotropic linear elastic solid, $\epsilon_0 = \sigma/K$ and $\left(e_{ab}\right)_0 = s_{ab}\,/\left(2\overline{G}\right)$. In order to describe the mechanical behavior with this alternative formulation, the amounts of fluid $\widetilde{n}_k$ in the porous medium in function of both the chemical potentials μ_k and the volumetric stress σ must be known. Conversely, the adsorption behavior can be described if the volumetric strain ϵ is known in function of both the volumetric stress σ and the chemical potentials μ_k.

In addition to existing works, in the present work we take into account the compressibility of the solid skeleton and we consider generic pore morphologies. Nevertheless, a few assumptions remain:

- We assumed that the amount of fluid does not depend on the shear strain. Even for an isotropic medium, such an assumption is only valid for small strains.
- We did not consider irreversibilities of the adsorption process: to model hysteresis of the adsorption isotherm, it would be necessary to distinguish adsorption from desorption and to take into account dissipation.
- We considered no modification of the atomic structure of the solid (such modifications could be induced by chemical adsorption, fracturation, plasticization of coal...).

In order to use the poromechanical constitutive equations (4.42) practically, it is necessary to know the adsorption isotherm $\widetilde{n}$ in function of both the volumetric strain ϵ and the chemical potentials μ_k of the components of the fluids, or, equivalently, in function of both the volumetric stress σ and the chemical potentials μ_k of the components of the fluid. In practice, controlling those two parameters independently in a laboratory experiment is not easy. We display in Fig. 4.6 three ways to measure the adsorption isotherm. The most common experiment is an immersion experiment (see Fig. 4.6a) in which the confining stress exerted on the solid is the opposite of the bulk fluid pressure. An immersion experiment gives access to a specific series of strain-pressure conditions. The isotherm obtained with an immersion experiment is not sufficient to apply the

poromechanical equations (4.42) in the general case since bulk fluid pressure and confining stress are not varied independently. An alternative experiment (see Fig. 4.6b) is an experiment at fixed strain in which the size of the sample is imposed by an external device. In practice, an experimental set-up made of a rigid box can only prevent swelling, not shrinkage. Therefore such an experiment only gives access to a specific strain (generally zero strain). The third experiment (see Fig. 4.6c) is known as a triaxial experiment in geotechnical engineering. This experimental set up enables to control independently confining stress and fluid pressure, provided the opposite of the stress is higher than the pressure. In this thesis we perform molecular simulations in order to measure the adsorption isotherm. Although Molecular simulation is not an experiment, it is very easy to control independently strain and fluid pressure by molecular simulation.

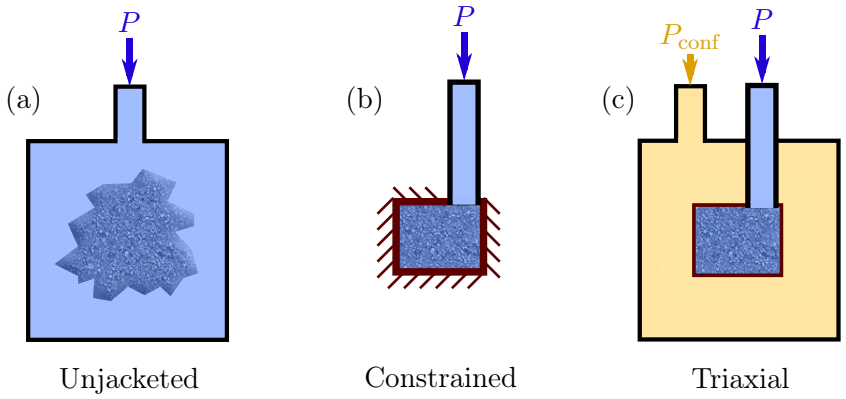

Figure 4.6. *Examples of experimental set-ups to measure adsorbed amounts of fluid. In the second set-up, the strain is fixed. In the third set-up the confining stress σ is controlled independently from the fluid bulk pressure P. The confining pressure P_{conf} is the opposite of the confining stress σ and must be larger than the fluid bulk pressure P.*

Chapter 5

Study of adsorption in one-dimensional microporous solids

THIS CHAPTER *aims at validating the poromechanical equations derived for microporous solids. Numerical experiments of molecular simulations of one-dimensional microporous solids are performed and the constitutive equations derived in Chap. 4 are verified for these model systems. The first case considered is a crystalline chain, in which the size of all micropores is unique. Adsorption depends on the strain of the chain in a complex manner and the poromechanical behavior of the chain differs significantly from that of a macroporous solid. Adsorption can make the medium shrink or swell. The constitutive equations derived in Chap. 4 capture the poromechanical behavior of the crystalline chain very well. This behavior can be explained qualitatively by the commensurability of the size of the micropores to the size of a fluid molecule. In order to investigate the effect of pore size disorder, a one-dimensional amorphous solid is studied, in which the sizes of the micropores are chosen randomly. In this amorphous chain, adsorption depends linearly on the strain. As a consequence, adsorption always makes the medium swell. By taking into account the linear dependence of adsorption on the strain of the medium, the constitutive equations derived in Chap. 4 can be simplified. These simplified equations predict satisfactorily the adsorption-induced stress in the amorphous solid. Assuming that adsorption in a micropore depends only on the size of the pore, a detailed analysis makes it possible to relate the fluid-induced stress to the pore size distribution of the chain. This approach shows that the smallest micropores play a significant role in the poromechanical behavior of the medium. An interesting perspective is to use the adsorption-induced strain to characterize the pore size distribution of microporous solids.*

Ce chapitre *a pour but de vérifier la validité des équations poromécaniques étendues aux solides microporeux. Des expériences numériques de simulation moléculaires de solides microporeux unidimensionnels sont réalisées et les équations constitutives développées au Chap. 4 sont vérifiées pour ces systèmes modèles. Le premier cas considéré est une chaîne cristalline où tous les micropores sont de taille identique. L'adsorption évolue en fonction de la déformation de façon complexe et le comportement mécanique de la chaine est très différent du cas d'un solide macroporeux. L'adsorption peut induire aussi bien une contraction qu'un gonflement. Les équations constitutives développées au Chap. 4 sont parfaitement vérifiées par cette chaîne cristalline. Le comportement observé peut être expliqué qualitativement par la commensurabilité de la taille des micropores à la taille d'une molécule de fluide. Afin de juger l'effet d'une distribution de tailles de pores étendue, le cas d'un solide unidimensionnel amorphe est considéré, dans lequel les micropores sont de tailles aléatoires. L'adsorption dans ce solide amorphe est linéaire en fonction de la déformation. Par conséquent, le fluide induit toujours un gonflement. Les équations constitutives développées au Chap. 4 peuvent être simplifiées en considérant une relation linéaire entre adsorption et déformation. Ces équations simplifiées prédisent de façon satisfaisante les contraintes induites par l'adsorption dans le solide amorphe. En supposant que l'adsorption dans un micropore ne dépend que de la taille du pore, une analyse détaillée permet de relier la distribution de tailles de pores à la contrainte induite par le fluide. Cette approche met en évidence le rôle important des plus petits micropores pour le comportement mécanique. Une perspective est d'utiliser la déformation induite par l'adsorption pour caractériser la distribution de taille de pore des solides microporeux.*

Outline of Chapter 5

The constitutive equations (4.42) we derived for microporous solids can be tested by molecular simulation. According to Frenkel and Smit (2001), a computer simulation designed to test a theory is a computer experiment. The objective of such a computer experiment is to compare the results of a simulation on a given model system with the predictions of a theory. A computer experiment is a first step toward applying the theory to a real system. The constitutive equations for microporous solids can be tested by simulating the adsorption of a fluid in a model microporous solid. Indeed, the volumetric stress and the amount of fluid computed must satisfy the first two constitutive equations (4.42) independently of the fluid and of the microporous solid considered. The model systems we consider in the present chapter are one-dimensional linear elastic microporous chains, in which a Lennard-Jones fluid is adsorbed. Because of the low computational cost, the simulation of a one-dimensional system provides very accurate results and therefore enables to precisely verify the validity of the constitutive equations (4.42) for microporous solids.

5.1 Model crystalline one-dimensional chain

In order to illustrate the effect of adsorption on the poromechanical behavior of a microporous solid and validate the general constitutive equations (4.42), we modeled a one-dimensional microporous molecular chain on which we performed Monte Carlo simulations of adsorption of a fluid.

5.1.1 Description of the system

We consider a one-dimensional crystalline chain made of equally distributed atoms separated by an equilibrium distance r_0. Each atom interacts with its two closest neighbors. The energy U_s of interaction between two neighbors is harmonic: $U_s\left(\mathbf{r}_i, \mathbf{r}_j\right) = \frac{1}{2} C_{harm}\left(r_{ij} - r_0\right)^2$, where $r_{ij} = \left|\mathbf{r}_j - \mathbf{r}_i\right|$ is the distance between the two neighbors. Thus, this one-dimensional chain is linear elastic. The space between two atoms of the solid skeleton is large enough to accommodate a few adsorbed fluid molecules (Fig. 5.1). The fluid considered for the simulation is a Lennard-Jones fluid. The energy U_f of interaction between two fluid molecules is $U_f\left(\mathbf{r}_i, \mathbf{r}_j\right) = 4\widetilde{\varepsilon}_f \left(\left(\widetilde{\sigma}_f / r_{ij}\right)^{12} - \left(\widetilde{\sigma}_f / r_{ij}\right)^{6}\right)$ where $\widetilde{\varepsilon}_f$ and $\widetilde{\sigma}_f$ are the Lennard-Jones parameters of the fluid. The energy U_{fs} of interaction between a fluid molecule and an atom of the solid skeleton is a Lennard-Jones potential as well, but with different parameters $\widetilde{\varepsilon}_{fs}$ and $\widetilde{\sigma}_{fs}$. The Lennard-Jones potential is suited to represent physical adsorption for systems involving dispersion forces and steric repulsion. The total interaction energy U of the system is:

$$U = \sum_{\substack{i,j\in \text{ skeleton} \\ i<j \text{ closest neighbors}}} U_s\left(\mathbf{r}_i, \mathbf{r}_j\right) + \sum_{\substack{i,j\in \text{ fluid} \\ i<j}} U_f\left(\mathbf{r}_i, \mathbf{r}_j\right) + \sum_{\substack{i\in \text{ fluid} \\ j\in \text{ skeleton}}} U_{fs}\left(\mathbf{r}_i, \mathbf{r}_j\right) \tag{5.1}$$

We performed Monte Carlo molecular simulations of such a system. The solid was simulated in the canonical ensemble, in which the number N_s of atoms in the solid skeleton, the volume (i.e., the length L of the chain), and the temperature T are fixed. The fluid was simulated in the grand canonical ensemble: the temperature and the volume are the same as for the solid, while the fluid chemical potential μ is imposed by an external reservoir. We varied the fluid chemical potential μ and the length L, in order to assess the evolution of the adsorption in function of both the fluid chemical potential and the volumetric strain $\epsilon = \left(L - L_0\right)/L_0$, where $L_0 = N_s r_0$ is the undeformed length of the system. During the simulations, we computed the volumetric stress (i.e.,

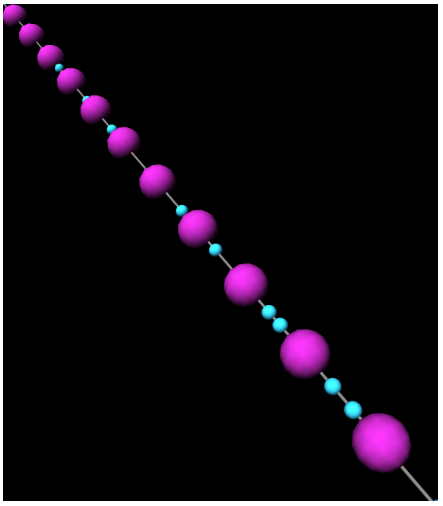

FIGURE 5.1. *Example of molecular configuration of fluid adsorbed in the one-dimensional crystalline chain. The fluid molecules can enter or leave the interstitial space between solid atoms. The atoms of the solid are the large pink balls, the fluid molecules are the small blue balls, the line represents the one-dimensional space.*

for the one-dimensional system, the force acting on the chain) with the virial estimate and we also computed the number N_f of fluid molecules in the system. Since we considered a one-dimensional system, the virial estimate is slightly different from Eq. (3.26):

$$P_{mech} = \left\langle \frac{Nk_BT}{L} + \frac{1}{L}\sum_{i<j} \mathbf{r}_{ij} \cdot \mathbf{F}_{ij} \right\rangle \tag{5.2}$$

The values of the different parameters used for this numerical experiment were chosen such that adsorption was significant: $C_{harm} = 4 \times 10^{-20}$ J.Å^{-2}, $r_0 = 6$ Å, $\widetilde{\varepsilon}_f = 2 \times 10^{-21}$ J, $\widetilde{\sigma}_f = 1$ Å, $\widetilde{\varepsilon}_{fs} = 5 \times 10^{-21}$ J, $\widetilde{\sigma}_{fs} = 2$ Å. The simulated chain was made of 50 atoms and was 300 Å long in the undeformed configuration. The temperature T of the system was fixed at 100 K.

In the following sections, we refer to the dimensionless bulk pressure of the fluid $P^* = P/K$ and to the dimensionless volumetric stress $\sigma^* = \sigma/K$, where $K = C_{harm}r_0 = 2.4 \times 10^{-9}$ N is the bulk modulus of the chain at zero fluid pressure. Molecular simulations of the bulk fluid were performed to obtain the equation of state $P^*(\mu)$ of the bulk fluid.

5.1.2 Mechanical behavior of the chain under adsorption

We display in Fig. 5.2 the dimensionless stress σ^* in function of the strain ϵ at different fluid pressures P. At zero pressure of the fluid ($\mu \to -\infty$), there was no fluid molecule in the system and the elastic behavior of the medium was linear: $\sigma = \sigma_0(\epsilon) = K\epsilon$. When the pressure of the fluid was non zero, fluid molecules adsorbed and the mechanical behavior was no more linear. Adsorption of fluid led to an increase of the mechanical stress around zero strain and to a decrease near $\epsilon = \pm 0.1$. By contrast, for a macroporous medium, the poroelastic constitutive equation (4.15) predicts that at fixed strain ϵ the volumetric stress should increase by $-bP$, where b is the Biot coefficient.

We display in Fig. 5.3 the apparent tangent drained bulk modulus K^{tan} defined by Eq. (4.53). As is expected for a linear elastic medium, $K^{tan} = K$ in the absence of any fluid. By contrast, under adsorption K^{tan} was no more constant: the adsorption of fluid modified its value by up to

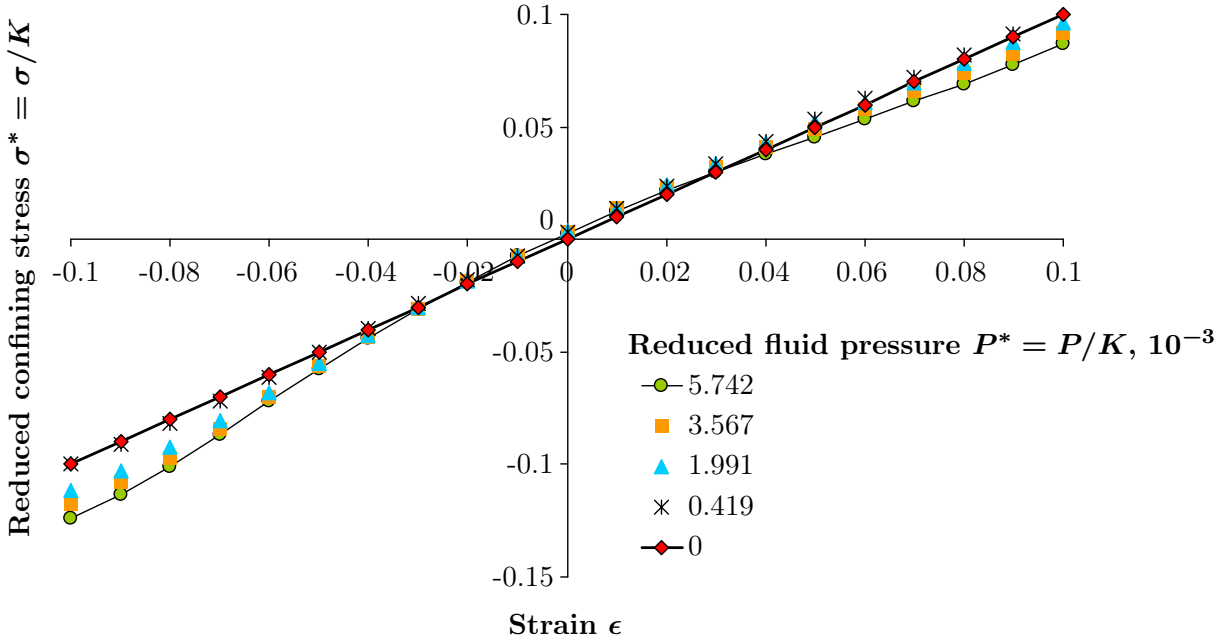

Figure 5.2. *Mechanical stress in the crystalline chain in function of the strain at different fluid pressures.*

−24% and +45% in this example. The apparent tangent and secant Biot coefficients are displayed in Fig. 5.4 and in Fig. 5.5, respectively. To a large extent, the values obtained for those Biot coefficients were out of the conventional range $[0; 1]$, reaching values as high as 10 and as low as -10. In other words, the mechanical pressure exerted by the adsorbed fluid can be up to 10 times as important as the bulk pressure of the fluid.

5.1.3 Verification of the constitutive equations derived for microporous solids

The constitutive equations (4.44) were derived for a generic linear elastic porous solid and are expected to be able to capture the poromechanical behavior of the one-dimensional chain here simulated. The first constitutive equation (4.44) relates the mechanical stress to the amount $\widetilde{n} = N_f/L_0$ of fluid molecules per unit length of the undeformed chain. This adsorbed amount must be known in function of both the bulk pressure of the fluid and the strain of the solid. Figure 5.6 displays the amount $\widetilde{n}(\epsilon, P)$ in function of the strain ϵ of the chain for various dimensionless bulk fluid pressures P^*. At large pressures, the greater the strain was, the more fluid molecules there were in the pores. At low pressures, interestingly, the amount of fluid molecules in the pores decreased with the strain of the medium. No simple analytical expression could capture the observed adsorption behavior.

The fluid-induced stress $\sigma_{f-i} = \sigma(\epsilon, P) - \sigma_0(\epsilon) = \sigma(\epsilon, P) - K\epsilon$ characterizes the confining stress that must be additionally exerted on the system to keep it at a given strain ϵ when the pressure of the fluid is increased from 0 to P. We display in Fig. 5.7 the dimensionless fluid-induced stress $\sigma^*(\epsilon, P) - \sigma_0^*(\epsilon) = (\sigma(\epsilon, P) - K\epsilon)/K$ in function of the bulk fluid pressure for different strains. We display both the fluid-induced stress computed directly from the molecular simulations by using the virial estimate and the fluid-induced stress calculated with the first constitutive equation (4.44) in which the simulated adsorption isotherm $\widetilde{n}(\epsilon, P)$ displayed in Fig. 5.6 was used. The match between those two ways of estimating the fluid-induced stress was very satisfactory, proving therefore that the derivations performed in Chap. 4 enable to capture accurately the poromechanical behavior of

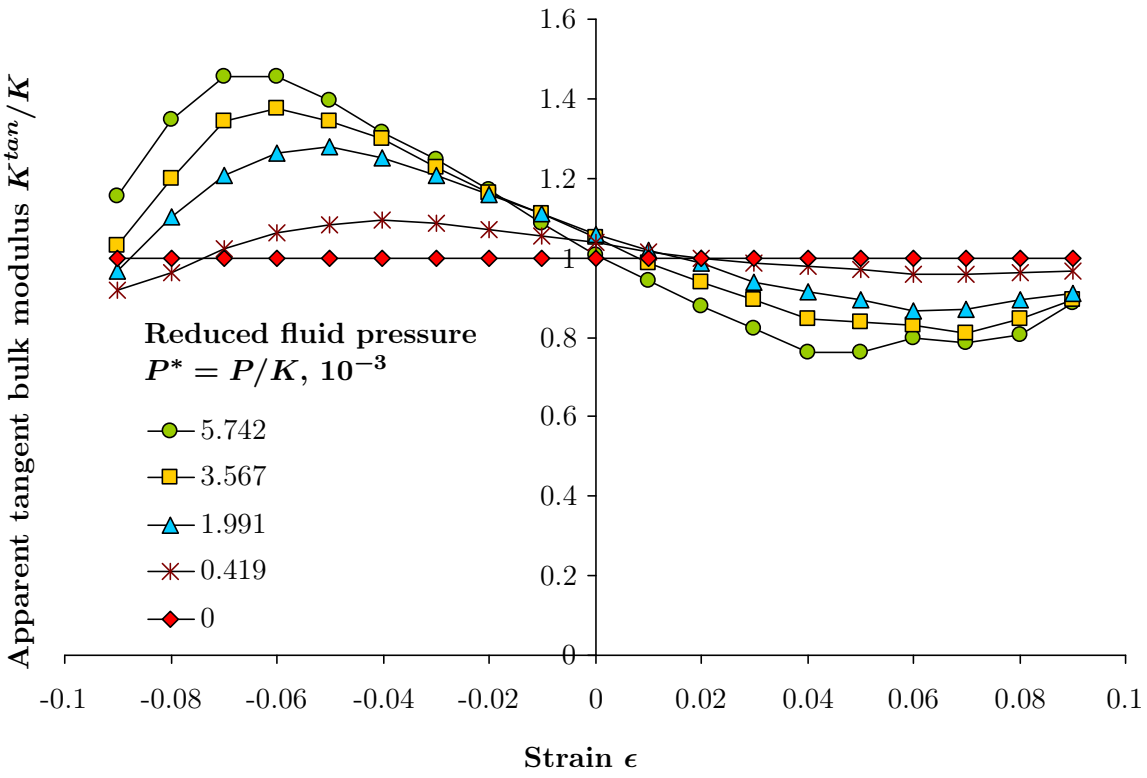

FIGURE 5.3. *Apparent tangent drained bulk modulus K^{tan} of the crystalline chain.*

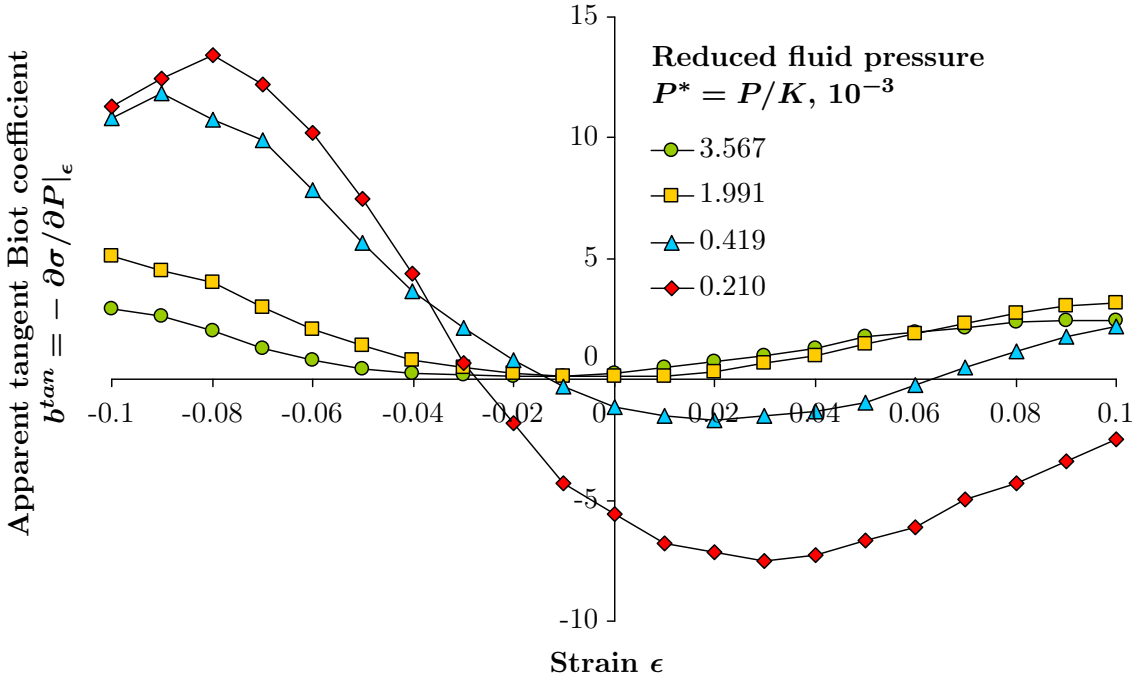

FIGURE 5.4. *Apparent tangent Biot coefficient b^{tan} of the crystalline chain.*

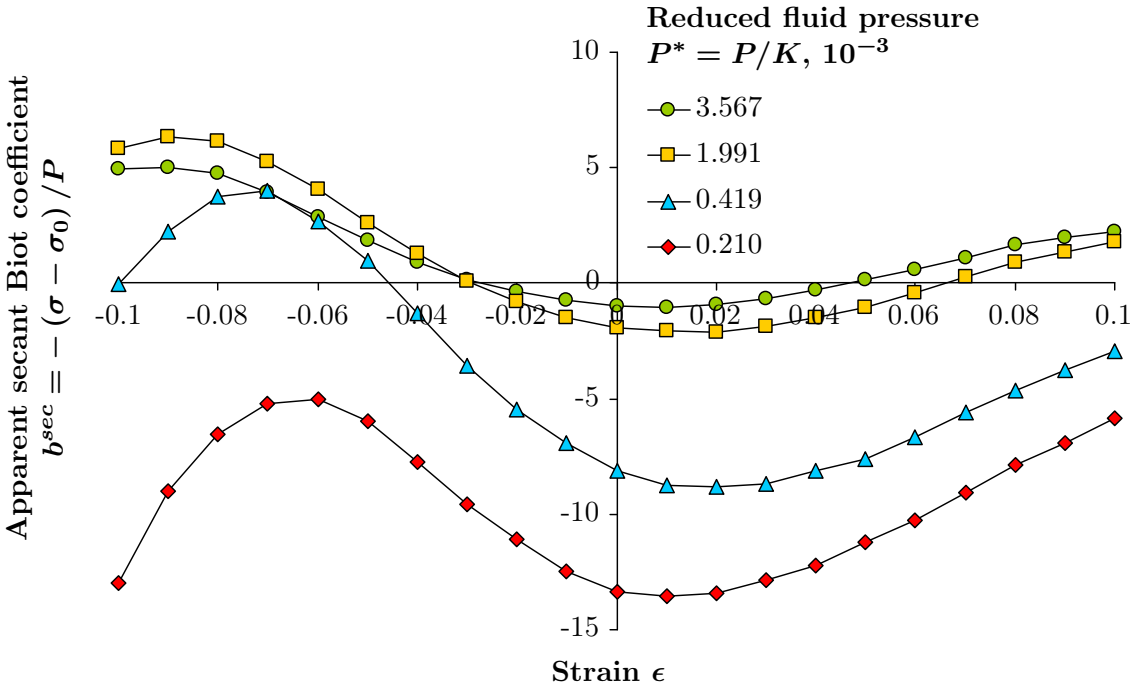

Figure 5.5. *Apparent secant Biot coefficient b^{sec} of the crystalline chain.*

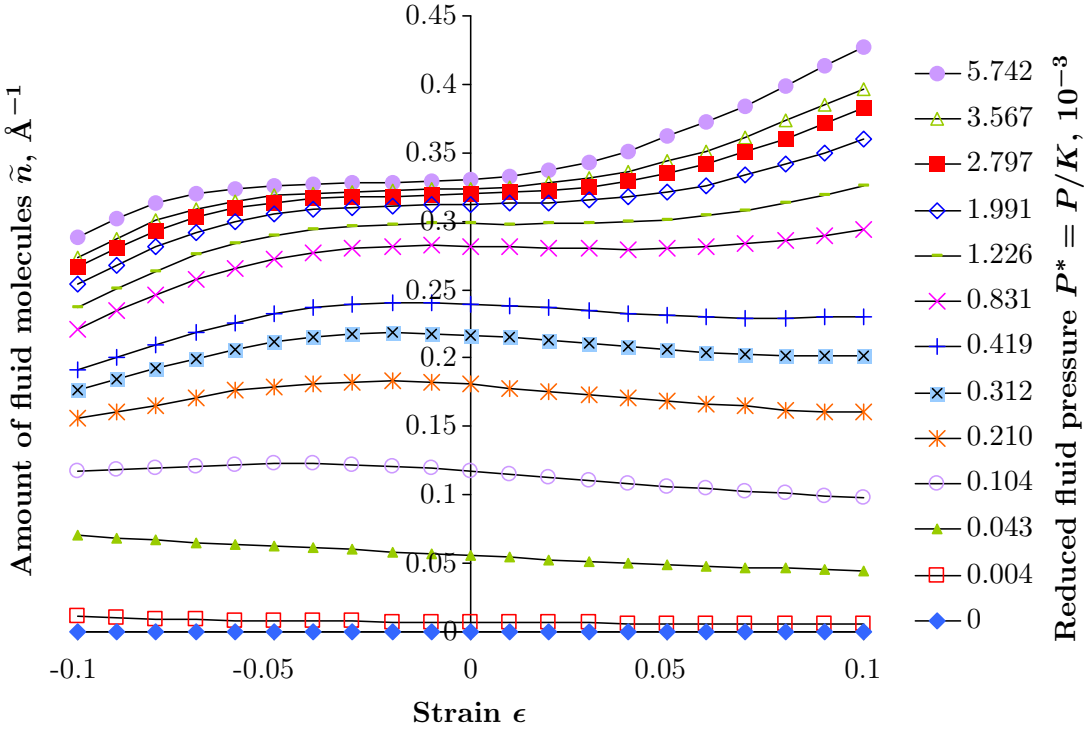

Figure 5.6. *Amount of fluid molecules adsorbed per unit length of the undeformed chain in function of the strain of the solid for various bulk pressures of the fluid.*

the microporous chain here considered, although the adsorption isotherms strongly depended on the strain of the medium (Fig. 5.6).

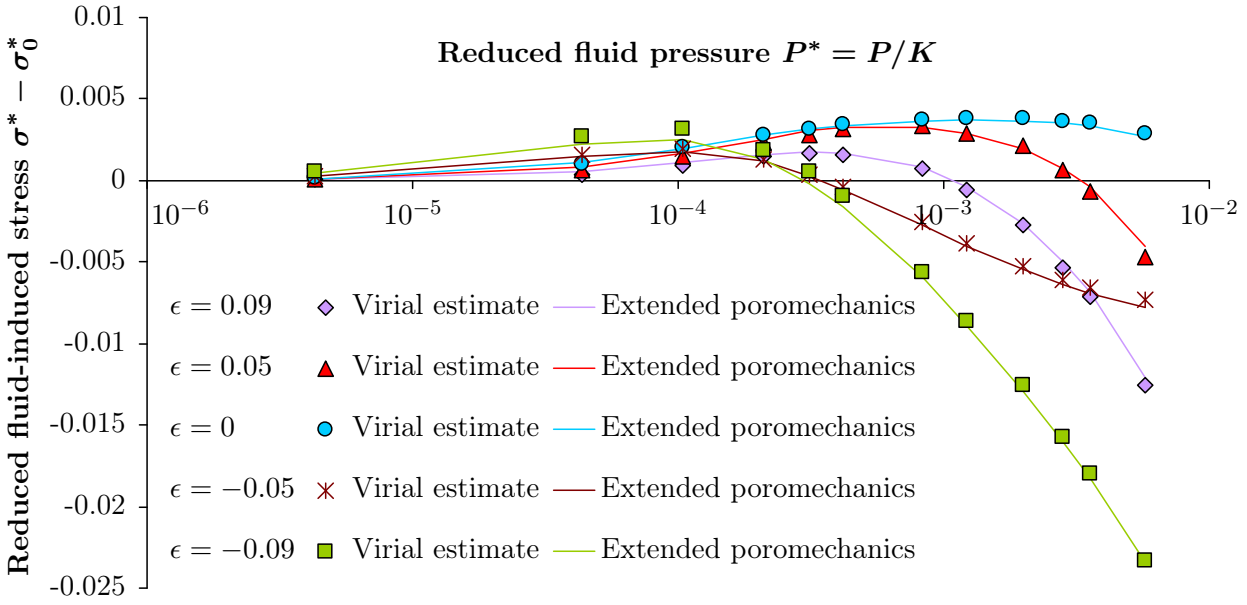

FIGURE 5.7. *Dimensionless fluid-induced stress for the crystalline chain under adsorption computed from the molecular simulations with the virial estimate (symbols) and computed with the simulated adsorption isotherms $\widetilde{n}(\epsilon, P)$ (displayed in Fig. 5.6) combined with the constitutive equation (4.44) (lines).*

5.1.4 Interpretation

The fluid-induced stress $\sigma_{f-i} = \sigma(\epsilon, P) - \sigma_0(\epsilon)$ sometimes was positive or 'joining' (in the sense that the fluid makes the porous medium shrink) and sometimes was negative or 'disjoining' (in the sense that the fluid makes the porous medium expand). In fact, the fluid had a joining effect at low bulk pressure of the fluid and mostly a disjoining effect at the highest bulk pressures considered. The complex effect of adsorption in this crystalline chain is closely related to the number of fluid molecules that micropores can accommodate. Indeed, by deforming the medium from $\epsilon = -0.1$ to $\epsilon = 0.1$, the average distance between neighboring atoms of the solid changes by 1.2 Å, which is approximately the size of one fluid molecule. We display in Fig. 5.8 the fluid-induced stress $\sigma_{f-i} = \sigma(\epsilon, P) - \sigma_0(\epsilon)$ and the number of fluid molecules per pore versus the size of the pores (considered as the distance between two atoms of the solid) for a dimensionless fluid pressure $P^* = 5.742 \times 10^{-3}$. We also sketch the filling of a slit pore in order to understand the different situations at stake:

- For pore sizes between 5.6 and 6.1 Å, the pore could accommodate two fluid molecules. The (Lagrangian) density of fluid remained almost constant and the fluid-induced stress mostly increased with the strain in this range, reaching a maximum at a pore size of about 6 Å. The fluid had a disjoining effect up to a pore size of 5.8 Å and a joining effect in larger pores.

- For pore sizes between 6.1 and 6.6 Å, a third molecule of fluid may enter the pore. The density of fluid increased with the strain and the fluid-induced stress decreased with the strain. The fluid had a joining effect in pores smaller than 6.2 Å. For larger pores, the larger the pore was, the more disjoining the effect of the fluid was.

- Finally, for pore sizes between 5.4 and 5.6 Å, the second fluid molecule could be excluded from the pore. The density was an increasing function of the pore size and the fluid had a strongly disjoining effect.

The mechanical effect of adsorption can be interpreted in terms of the commensurability of the size of the micropores to the size of the fluid molecules. The size of the pores for which the fluid-induced stress was maximal (5.4 Å) did not correspond to completely filled pores. Indeed, Eq. (4.44) shows that the fluid-induced stress depends on the derivative of the adsorbed amount of fluid with respect to the strain at the current and at lower chemical potentials. Therefore, the mechanical effect of adsorption in a crystalline microporous medium can not be simply related to the pore filling, but to the capacity of the pores to accommodate additional molecules of fluid with strain.

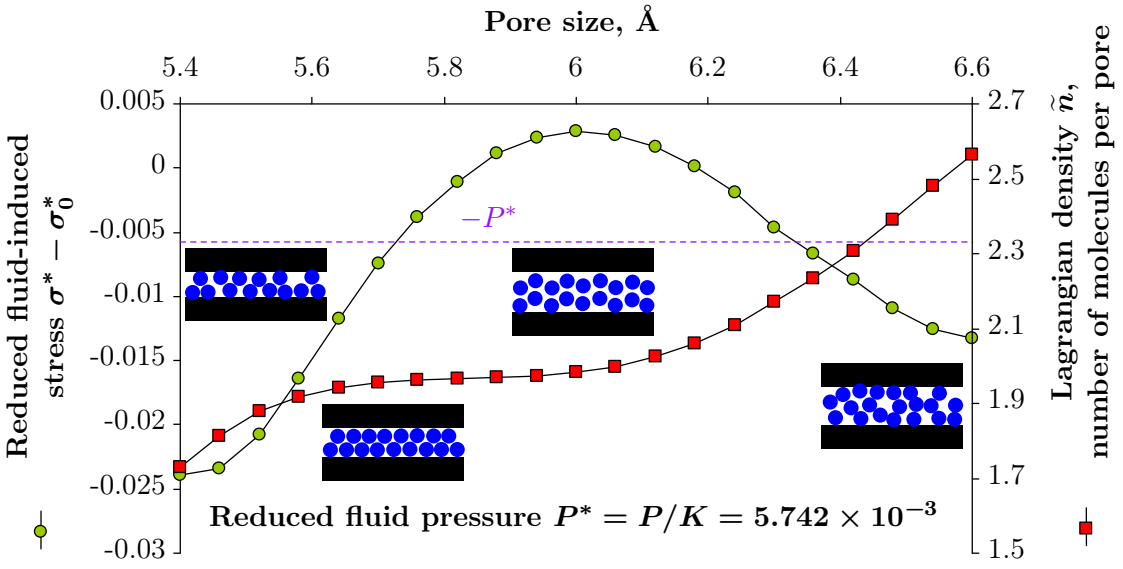

Figure 5.8. *Fluid-induced stress and number of fluid molecules per pore as a function of the average distance between two solid atoms of the crystalline chain.*

The fluid-induced stress displayed in Fig. 5.8 is analogous to the disjoining pressure in thin films. The oscillation we observed by simulation, due to molecular ordering effects, recalls the oscillations of Fig. 3.15 for non-DLVO effects in nanometric films (Israelachvili, 1992, Balbuena et al., 1993, Kowalczyk et al., 2008, Yang et al., 2010).

5.2 Effect of pore size disorder: model one-dimensional amorphous chain

The effect of molecular ordering observed in the crystalline chain was closely related to the fact that the microporous solid we considered is a crystalline solid, in which all micropores were of the exact same size. In this section, we consider a one-dimensional microporous medium with a variety of micropore sizes chosen randomly. We will refer to this medium as to the 'amorphous' chain.

5.2.1 Description of the system and results

The molecular interactions considered were the same as in Sec. 5.1, except for the equilibrium length r_0 which was specific to each pair of neighboring atoms of the solid. The equilibrium lengths were generated randomly between 3 and 11 Å following a uniform law (Fig. 5.9). The chain was made of 139 atoms and its total length in the undeformed configuration was 1000 Å. We performed Monte Carlo simulations of adsorption of fluid on this chain, by using the same potentials of interaction as in Sec. 5.1.

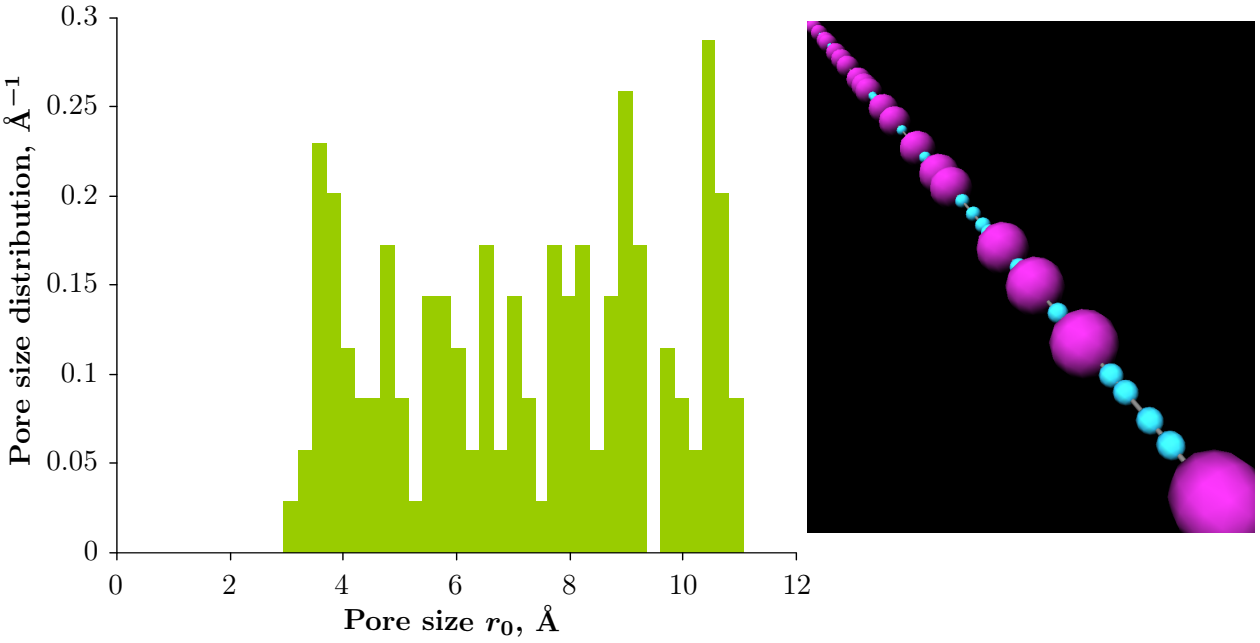

FIGURE 5.9. *(Left) Pore size distribution for the amorphous chain; (Right) Example of molecular configuration.*

For various bulk pressures of the fluid and strains of the medium, we computed the number of adsorbed molecules and the confining stress by using the virial estimate. We display in Fig. 5.10 and in Fig. 5.11 the adsorbed amount $\widetilde{n}(\epsilon, P)$ per unit volume of the undeformed chain and the fluid-induced stress $\sigma_{f-i} = \sigma(\epsilon, P) - \sigma(\epsilon, P = 0)$ due to the adsorption of fluid, respectively. The behavior of the amorphous chain differed significantly from that of the crystalline chain (Fig. 5.6 and Fig. 5.7). Indeed, for the amorphous chain, the adsorbed amounts of fluid depended linearly on the strain of the medium and the fluid-induced stress did almost not depend on the strain of the medium. Moreover, in contrast to what was observed for the crystalline chain (Fig. 5.3), the apparent tangent bulk modulus K^{tan} remained mostly constant ($K^{tan} = K \pm 3.15\%$) for strains ϵ ranging from -0.1 to $+0.1$ and for dimensionless fluid pressures $P^* = P/K$ ranging from 0 to 4.789×10^{-3}.

We display in Fig. 5.11 both the fluid-induced stress computed directly from the molecular simulation by using the virial estimate and the fluid-induced stress calculated with the constitutive equation (4.44) in which the simulated adsorption isotherm $\widetilde{n}(\epsilon, P)$ displayed in Fig. 5.10 was used. As was the case for the crystalline chain (see Fig. 5.7), both ways of estimating the fluid-induced stress compared very well with each other, which further confirms that the constitutive equations derived in Chap. 4 enable to capture accurately the poromechanical behavior of a microporous medium.

We display in Fig. 5.12 the apparent secant Biot coefficient b^{sec}. At low bulk fluid pressures

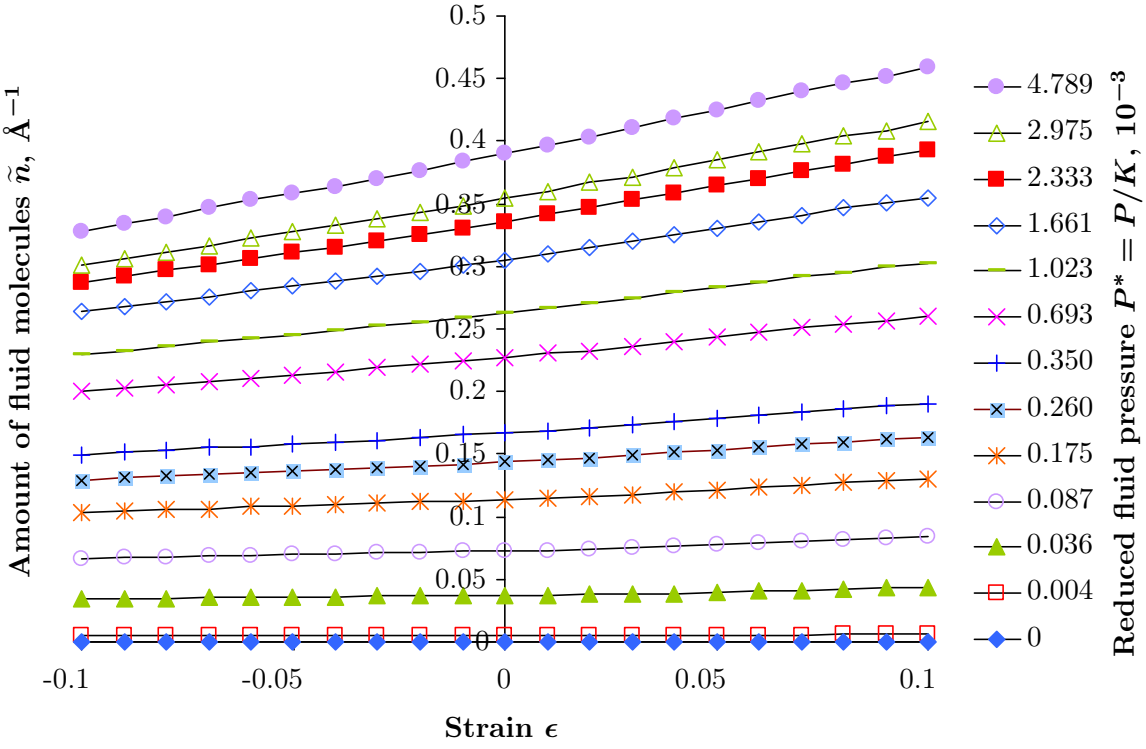

Figure 5.10. *Adsorbed amount of fluid molecules in the amorphous chain per unit length of the undeformed chain.*

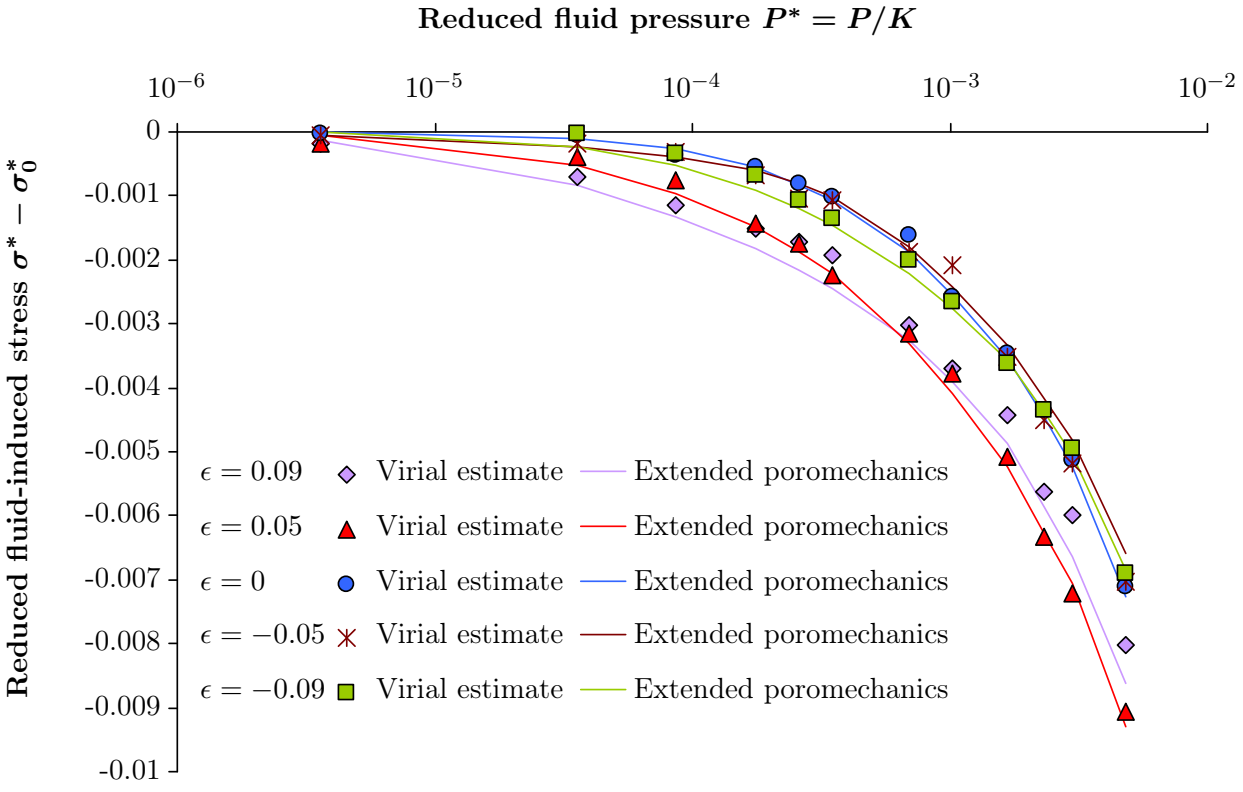

Figure 5.11. *Dimensionless fluid-induced stress computed from the molecular simulations with the virial estimate (symbols) and computed with the simulated adsorption isotherms* $\widetilde{n}(\epsilon, P)$ *(displayed in Fig. 5.10) combined with the constitutive equation (4.44) (lines).*

($P^* < 10^{-3}$), this coefficient significantly depended on the strain. The greater the bulk pressure of the fluid was, the less this coefficient depended on the strain, and the smaller its average value over strains from -0.1 to $+0.1$ was. At the largest bulk fluid pressure considered ($P^* = 2.97 \times 10^{-3}$), the apparent secant Biot coefficient was mostly insensitive to the strain ($b^{sec} = 1.91 \pm 15\%$). In any case, for all pressures here considered, the secant Biot coefficient remained greater than unity, i.e., greater than the value observed in macroporous media.

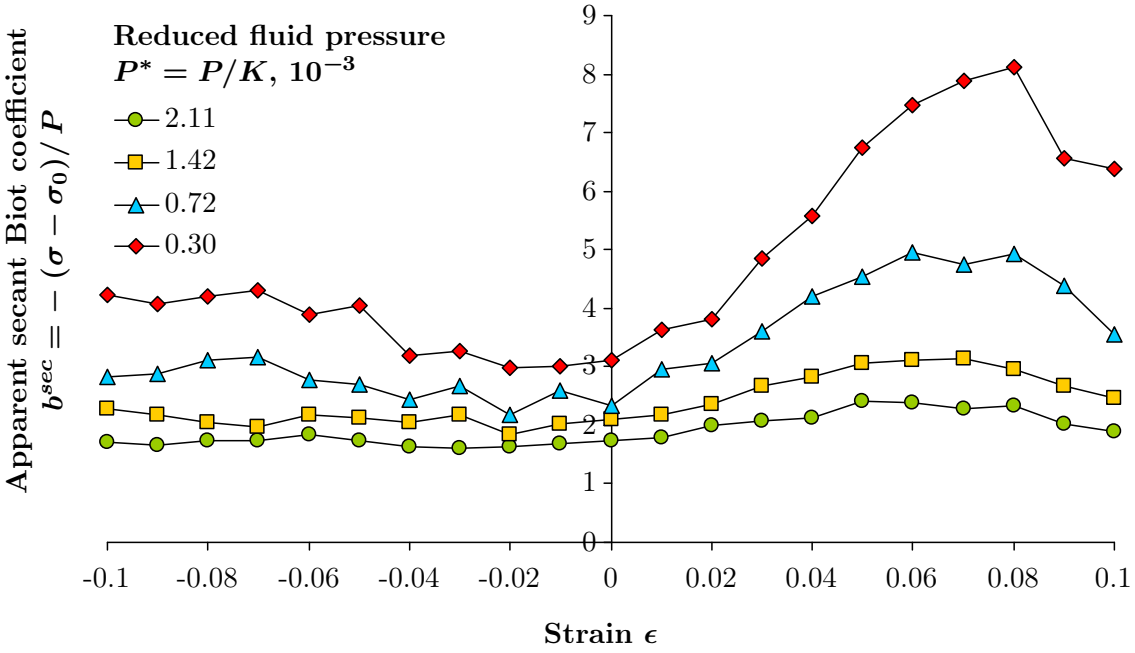

FIGURE 5.12. *Apparent secant Biot coefficient b^{sec} of the amorphous chain.*

The linear dependence of the adsorbed amount on the strain is in fact a consequence of the complex response of each pore present in the amorphous chain. At a given bulk fluid pressure, some pores contract while others expand, which eventually leads, at the scale of the porous medium, to an overall disjoining action of the fluid (i.e., adsorption always makes the solid expand), for any strain of the medium. Interestingly, even at low fluid pressure, we observed no joining effect of the fluid for the amorphous chain whereas, for the crystalline chain, a joining effect was observed at the lowest pressures for all strains considered. Such a discrepancy is due to the fact that the range of pore sizes explored in the crystalline chain (see Fig. 5.8) is too narrow to account for all pore sizes of the amorphous chain, which extend from 3 Å up to 11 Å. Balbuena et al. (1993) showed that pores that are a few-Angstrom large (i.e., that are about the size of one fluid molecule) exhibit a very strong disjoining behavior upon adsorption, even at low fluid pressure. Moreover, for pores that are larger than five fluid molecules, i.e., larger than 9 Å in our case, they found out that the fluid-induced stress is always negative.

5.2.2 Simplified poromechanical model for the amorphous chain

Since, for the amorphous chain, the adsorbed amount depended almost linearly on the strain of the medium, a first-order approximation of the adsorption isotherm should be valid for this chain in the range of strains here considered, i.e., for $-0.1 \leq \epsilon \leq 0.1$:

$$\widetilde{n} \approx \widetilde{n}^0 \left(1 + \widetilde{C}\,(P)\,\epsilon\right) \text{ where } \widetilde{n}^0 = \widetilde{n}\,(\epsilon = 0, P) \tag{5.3}$$

Based on the simulation results, we calculated the coupling coefficient $\widetilde{C}(P) = (\partial\widetilde{n}/\partial\epsilon|_P)/\widetilde{n}^0$ for the whole range of pressures considered in this study. The results of the calculations are displayed in Fig. 5.13. The coupling coefficient $\widetilde{C}(P)$ did almost not depend on the pressure P of the fluid. We derived in Sec. 4.3.4 a simplified formulation of the constitutive equations assuming that the first order expansion (Eq. 5.3) is valid and that the coupling coefficient $\widetilde{C}$ is constant:

$$\sigma = K\epsilon - \widetilde{C}\int_0^P \widetilde{n}^0 \overline{V}_{bulk} dP \tag{5.4}$$

This simplified poromechanical model is expected to hold for the amorphous chain. We display in Fig. 5.14 the fluid-induced stress calculated with the simplified constitutive equation (5.4) together with the fluid-induced stresses estimated directly from the molecular simulations with the virial estimate: the simplified model and the simulation results compared well. Such a good agreement proves that the simplified poroelastic constitutive equations derived in Sec. 4.3.4 enable to describe satisfactorily the poromechanical behavior of the amorphous chain.

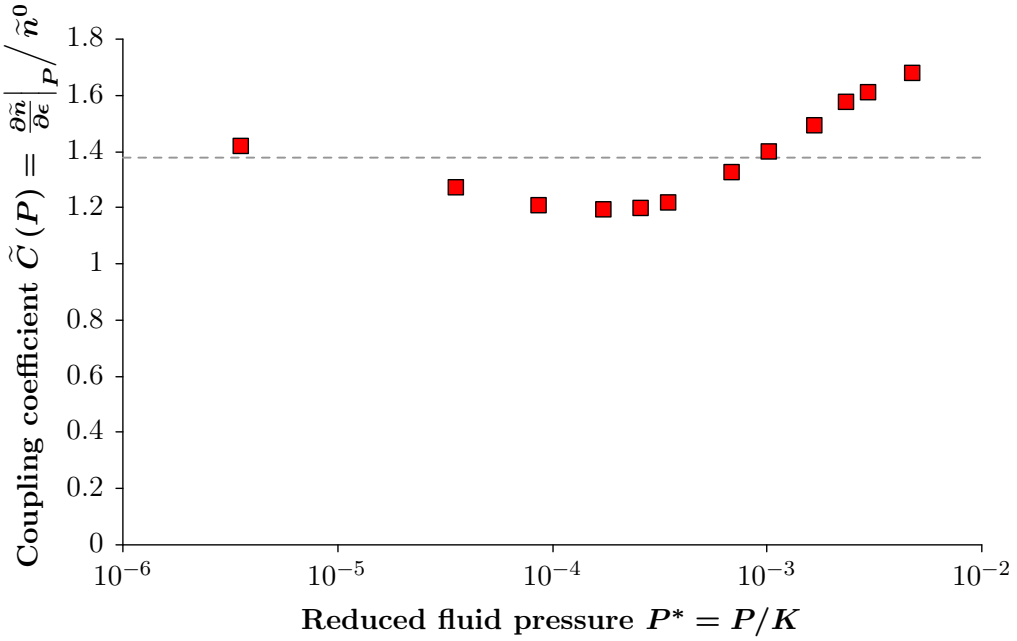

Figure 5.13. *Coupling coefficient $\widetilde{C}(P)$ for the amorphous chain.*

5.3 Detailed analysis

The poromechanical behavior obtained for the amorphous chains is simple at the macroscopic scale, but is complex at the nanometer scale: the behavior of each pore is specific and depends on the commensurability of the size of the pore to the size of the fluid molecules. In this section, we propose a way to infer the behavior of the whole chain from the behavior of each pore. We illustrate this approach on the amorphous chain. We show that, for a wide uniform pore size distribution, the mechanical effect of the fluid is disjoining and is nearly insensitive to the strain. Finally, we consider the inverse problem and show that the poromechanical behavior of the medium and the adsorption isotherms are complementary information for the characterization of the pore size distribution.

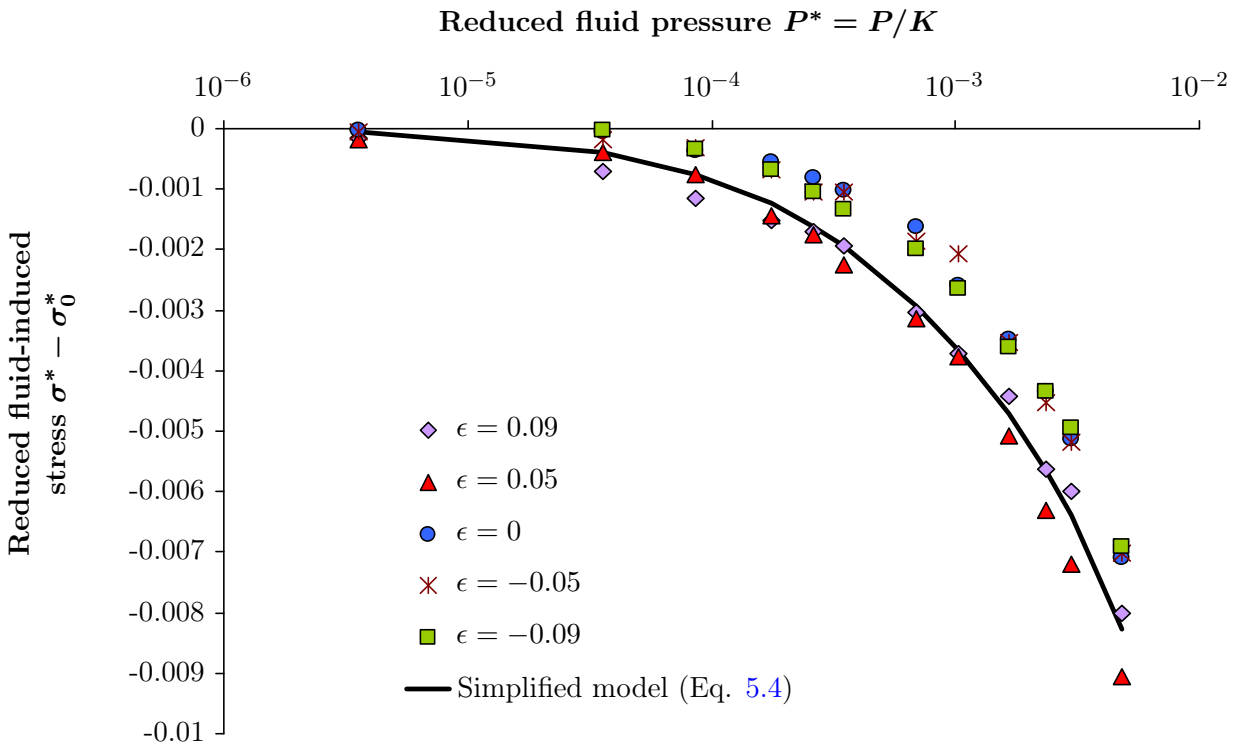

FIGURE 5.14. *Comparison between the fluid-induced stress predicted by the simplified poromechanical model (Eq. 5.4) and the fluid-induced stress calculated from the molecular simulations for the amorphous chain.*

5.3.1 Combination of pore self-contribution

The approach we propose in order to infer the poromechanical behavior of the medium from the behavior of each individual pore is based on the following assumption: the state of the fluid in a micropore only depends on the size l of the pore in the deformed configuration and on the bulk pressure P of the fluid. The amount adsorbed in a pore is assumed independent of any other parameter. The state of a fluid molecule in a pore only depends on the molecular interactions with other fluid molecules in this pore and with the atoms of the solid skeleton adjacent to this pore. This assumption makes it possible to consider each micropore independently. Such an assumption does not hold for two- or three-dimensional systems.

The adsorbed amount and the fluid-induced stress in a micropore are functions of the size l of the pore and of the fluid pressure P, and can be estimated by simulating adsorption in a crystalline chain of undeformed pore size $r_0 = l$. We considered crystalline chains made of pores with a given equilibrium size r_0. From chain to chain, the equilibrium size of the pores varied from 3 Å to 12 Å. We performed Monte Carlo simulations of adsorption of fluid in those chains at zero strain, for which the deformed pore size l was therefore equal to the equilibrium size r_0. We display in Fig. 5.15 the fluid-induced stress in function of the actual size l of the pore and for various fluid bulk pressures. Figure 5.15 extends the results displayed in Fig. 5.8 to a wider range of pore sizes.

Now we come back to the case of an amorphous chain with pores of various equilibrium sizes. The pore size distribution $p(r_0)\,dr_0$ is defined as the proportion of the Lagrangian porosity ϕ for which the size r_0 of the pore in the undeformed configuration is comprised between r_0 and r_0+dr_0. We call $\epsilon_p(r_0)$ the strain of the pores of undeformed size r_0, so that the actual size l in the deformed configuration is related to the size r_0 in the undeformed configuration: $l = r_0(1+\epsilon_p(r_0))$. The elastic

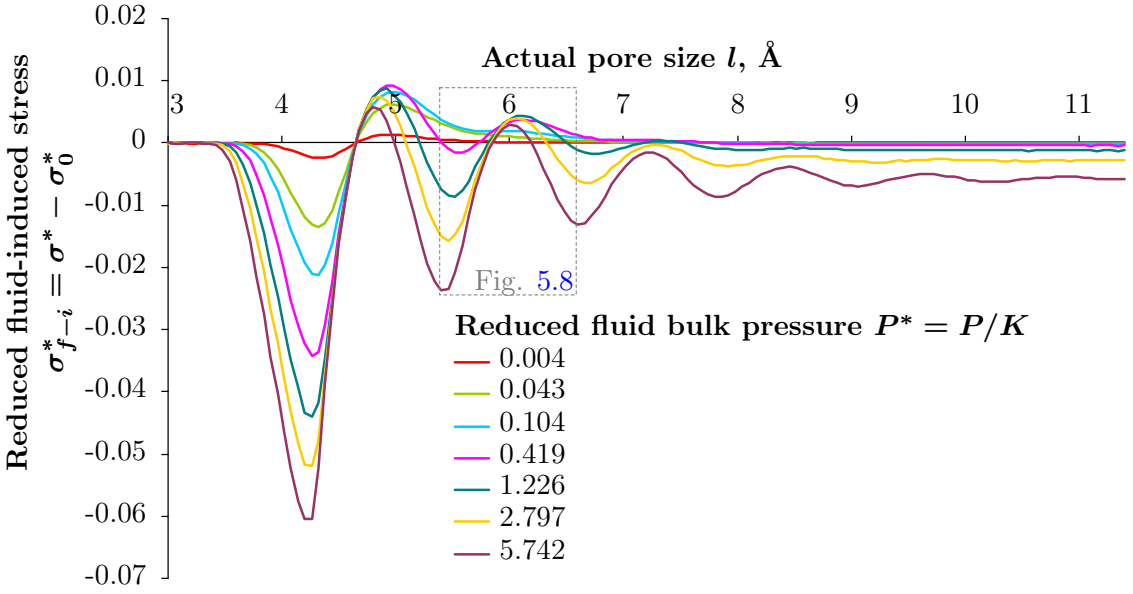

Figure 5.15. *Fluid-induced stress σ_{f-i} due to the fluid in a pore in function of the actual size l of the pore. The bulk modulus K, used to make parameters dimensionless, is the bulk modulus of the crystalline chain studied in Sec. 5.1.*

behavior of each micropore is linear, characterized by an elastic modulus $k(r_0) = C_{harm} \cdot r_0$ such that $\frac{1}{2}k(r_0)(\epsilon_p(r_0))^2 = \frac{1}{2}C_{harm}(l - r_0)^2/r_0$ is the energy of deformation per unit undeformed length of a micropore in absence of any fluid. When fluid is adsorbed in the micropore, the hybrid potential ω_{hyb} (see Sec. 4.3) includes an additional energy $\int_0^P \widetilde{n}\overline{V}_{bulk}dP$ which accounts for the adsorption of the fluid. Alternatively, this additional energy can be rewritten as an integration of the fluid-induced stress $\sigma_{f-i}(l, P)$ defined in the previous paragraph: $\int_0^{\epsilon_p(r_0)} \sigma_{f-i}(r_0(1 + \epsilon_p(r_0)), P)\, d\epsilon_p$. The complete expression of the hybrid potential ω_{hyb} is obtained by integrating the energy for each pore size over the total pore size distribution:

$$\omega_{hyb} = \int_{r_0^{min}}^{r_0^{max}} \frac{1}{2}k(r_0)(\epsilon_p(r_0))^2 p(r_0)\, dr_0 + \int_{r_0^{min}}^{r_0^{max}} \left(\int_0^{\epsilon_p(r_0)} \sigma_{f-i}(r_0(1 + \epsilon_p), P)\, d\epsilon_p \right) p(r_0)\, dr_0 \tag{5.5}$$

where r_0^{min} and r_0^{max} are the minimum size and maximum size of the pores. At equilibrium, the hybrid potential ω_{hyb} is minimum. σ_{f-i}, $k(r_0)$ and $p(r_0)$ are known quantities. The local strain $\epsilon_p(r_0)$ is obtained by minimizing the potential ω_{hyb} under the constraint that the total deformation ϵ is fixed:

$$\int_{r_0^{min}}^{r_0^{max}} \epsilon_p(r_0)\, p(r_0)\, dr_0 = \epsilon \tag{5.6}$$

This constrained minimization can be solved by using the method of Lagrange multipliers. The constrained minimization of ω_{hyb} is equivalent to the minimization of:

$$\widetilde{\Lambda} = \int_{r_0^{min}}^{r_0^{max}} \frac{1}{2} k\left(r_0\right)\left(\epsilon_p\left(r_0\right)\right)^2 p\left(r_0\right) dr_0 + \int_{r_0^{min}}^{r_0^{max}} \left(\int_0^{\epsilon_p(r_0)} \sigma_{f-i}\left(r_0\left(1+\epsilon_p\right), P\right) d\epsilon_p \right) p\left(r_0\right) dr_0 + \lambda \left(\epsilon - \int_{r_0^{min}}^{r_0^{max}} \epsilon_p\left(r_0\right) p\left(r_0\right) dr_0 \right) \tag{5.7}$$

where λ is the Lagrange multiplier. According to the Euler-Lagrange equation, $\widetilde{\Lambda}$ is minimum for:

$$\forall r_0, \frac{\partial}{\partial \epsilon_p\left(r_0\right)} \left(\frac{1}{2} k\left(r_0\right)\left(\epsilon_p\left(r_0\right)\right)^2 p\left(r_0\right) + p\left(r_0\right) \int_0^{\epsilon_p(r_0)} \sigma_{f-i}\left(r_0\left(1+\epsilon_p\right), P\right) d\epsilon_p - \lambda \epsilon_p\left(r_0\right) p\left(r_0\right) \right) \Bigg|_{k,\sigma_{f-i},p,\lambda} = 0 \tag{5.8}$$

which implies that in each micropore:

$$k\left(r_0\right)\epsilon_p\left(r_0\right) + \sigma_{f-i}\left(r_0\left(1+\epsilon_p\left(r_0\right)\right), P\right) = \lambda \tag{5.9}$$

The Lagrange multiplier λ can be interpreted as the macroscopic stress σ prevailing in the chain. Indeed, the macroscopic stress is related to the potential ω_{hyb} according to $\sigma = \partial \omega_{hyb} / \partial \epsilon|_{T,P}$. In the explicit expression (5.5) of ω_{hyb}, the local deformation ϵ_p is the only parameter which depends on the strain ϵ. Differentiating ω_{hyb} with respect to ϵ, we obtain:

$$\sigma = \int_{r_0^{min}}^{r_0^{max}} \left(k\left(r_0\right)\epsilon_p\left(r_0\right) + \sigma_{f-i}\left(r_0\left(1+\epsilon_p\left(r_0\right)\right), P\right) \right) \frac{\partial \epsilon_p\left(r_0\right)}{\partial \epsilon} \Bigg|_{T,P} p\left(r_0\right) dr_0 \tag{5.10}$$

$$\sigma = \lambda \frac{\partial}{\partial \epsilon} \left(\underbrace{\int_{r_0^{min}}^{r_0^{max}} \epsilon_p\left(r_0\right) p\left(r_0\right) dr_0}_{\epsilon} \right) \Bigg|_{T,P} = \lambda \tag{5.11}$$

Therefore, at equilibrium, the stress $k\left(r_0\right)\epsilon_p\left(r_0\right) + \sigma_{f-i}\left(r_0\left(1+\epsilon_p\left(r_0\right)\right), P\right)$ in each pore is equal to the macroscopic stress σ that prevails in the porous medium. The stress σ can be determined through the minimization of ω_{hyb}.

Therefore, for a generic microporous one-dimensional solid, we can determine the stress σ in function of the strain ϵ and of the fluid bulk pressure P by using the fluid-induced stress isotherms displayed in Fig. 5.15.

We applied this approach on the amorphous chain studied in Sec. 5.2. We considered the pore size distribution of the amorphous chain, for which we solved numerically the minimization problem presented in the previous section. In Fig. 5.16 we display the macroscopic fluid-induced stress $\sigma - \sigma_0$ estimated from the minimization problem together with that measured directly with the virial estimate. The approach we proposed captures very well the mechanical behavior of the amorphous chain: the match is as good as in Fig. 5.11. It proves that the assumption that micropores do not interact with each other is valid and that it is theoretically possible to estimate the mechanical behavior of any one-dimensional microporous solid from the knowledge of its pore size distribution and of the fluid-induced stress isotherms displayed in Fig. 5.15.

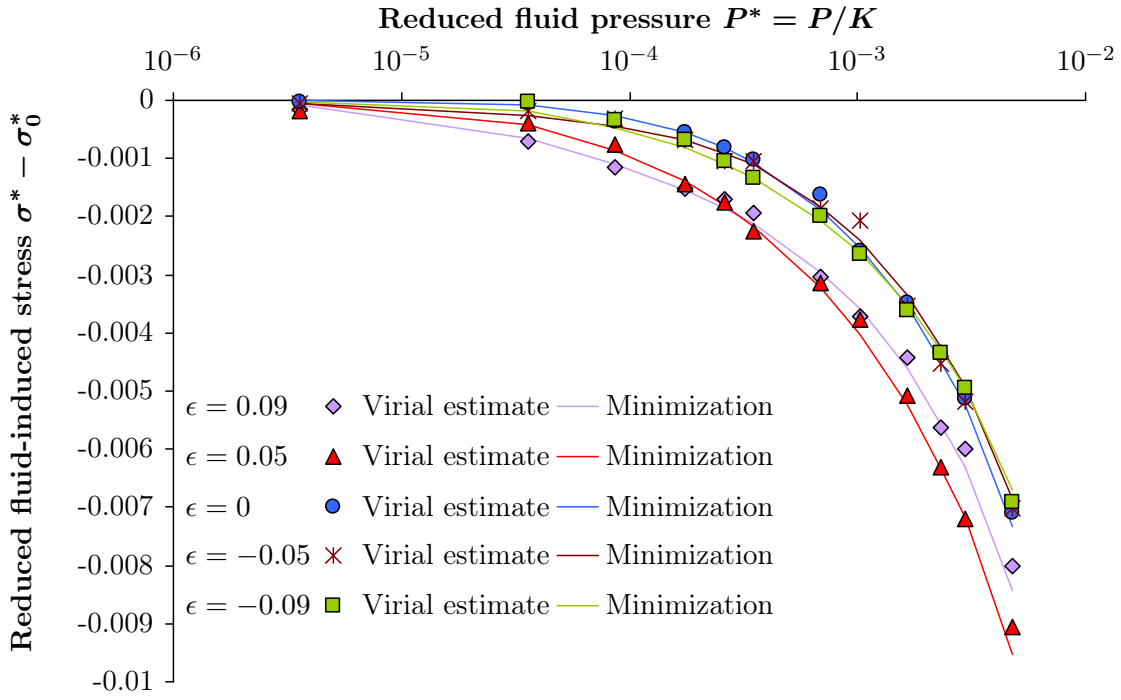

Figure 5.16. *Fluid-induced stress of the amorphous chain estimated from the minimization problem and estimated directly with the virial estimate.*

The proposed approach gives access to the local deformation ϵ_p for each pore. We display in Fig. 5.17 the local deformation in the amorphous chain at the largest fluid pressure considered here when the total strain ϵ is zero. We also display the opposite of the fluid-induced stress. The local strain is clearly governed by the fluid-induced stress. The higher the opposite of the fluid-induced stress was, the higher the local strain was.

5.3.2 Origin of the poromechanical behavior of an amorphous chain

As we shall see in this section, the approach we developed in Sec. 5.3.1 makes it possible to explain why a microporous solid with a wide pore size distribution swells even at low fluid pressure and why the fluid-induced stress is almost independent of the strain. Indeed, combining the stress equilibrium condition (Eq. 5.9) and the strain constraint (Eq. 5.6), we obtain a relation between the macroscopic stress σ and strain ϵ:

$$\epsilon = \sigma \int_{r_0^{min}}^{r_0^{max}} \frac{p\left(r_0\right)}{k\left(r_0\right)} dr_0 - \int_{r_0^{min}}^{r_0^{max}} \frac{\sigma_{f-i}\left(l,P\right)}{k\left(r_0\right)} p\left(r_0\right) dr_0 \tag{5.12}$$

In the absence of any fluid, $P = 0$ and $\sigma_{f-i} = 0$. Therefore, we identify the bulk modulus K of the solid skeleton as:

$$\frac{1}{K} = \int_{r_0^{min}}^{r_0^{max}} \frac{p\left(r_0\right)}{k\left(r_0\right)} dr_0 \tag{5.13}$$

The macroscopic fluid-induced stress is:

$$\sigma_{f-i} = \sigma - K\epsilon = K \int_{r_0^{min}}^{r_0^{max}} \frac{\sigma_{f-i}\left(l,P\right)}{k\left(r_0\right)} p\left(r_0\right) dr_0 \tag{5.14}$$

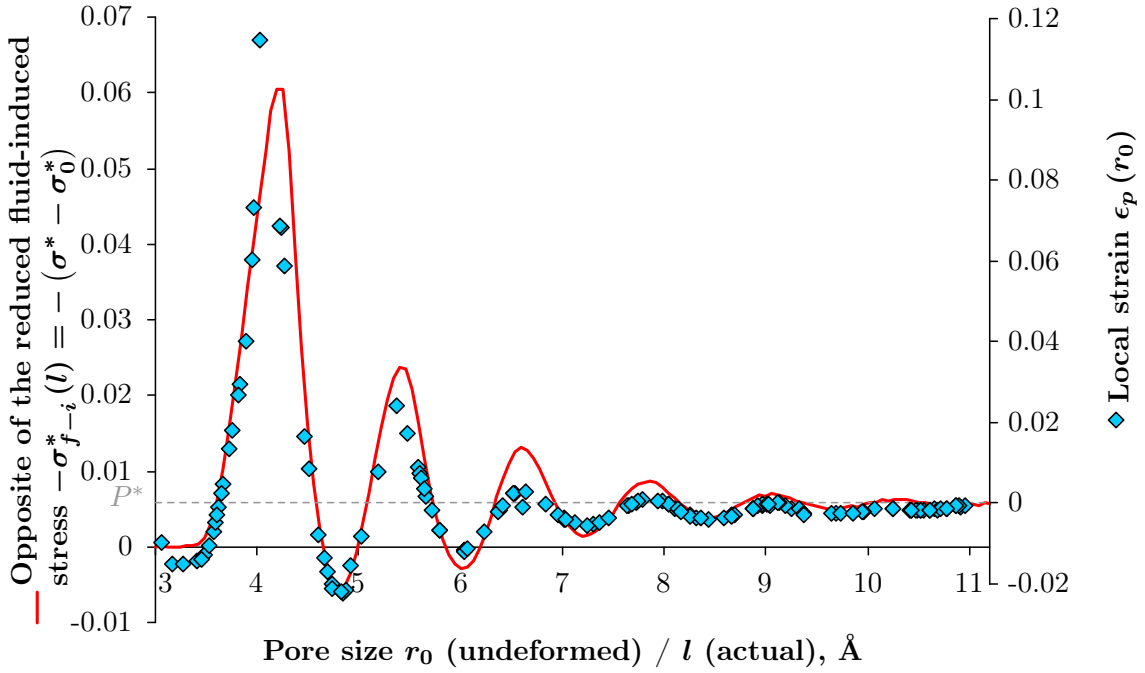

FIGURE 5.17. *Local strain of each micropore in the amorphous chain and fluid-induced stress.*

For a microporous solid with a wide uniform pore size distribution, we can show that this fluid-induced stress is nearly insensitive to the strain of the solid. In order to do so, let us consider a uniform pore size distribution $p(r_0) = 1/\left(r_0^{max} - r_0^{min}\right)$ on a range of pore sizes $\left[r_0^{min}; r_0^{max}\right]$ wide enough so that the smallest pore is too small to accommodate any fluid molecule even in strained conditions and so that the fluid-induced stress in the largest pore is nearly equal to the fluid bulk pressure. For the systems considered in this chapter, $r_0^{min} = 3.3$ Å and $r_0^{min} = 10.5$ Å fulfill those conditions. Considering this pore size distribution and making use of a change of variables, Eq. (5.14) becomes:

$$\sigma - K\epsilon = \frac{K}{r_0^{max} - r_0^{min}} \int_{l^{min}}^{l^{max}} \frac{\sigma_{f-i}(l, P)}{k(r_0(l))} \left.\frac{\partial r_0}{\partial l}\right|_{T,P,\epsilon} dl \tag{5.15}$$

where $l^{min} = r_0^{min}\left(1 + \epsilon_p\left(r_0^{min}\right)\right)$ and $l_0^{max} = r_0^{max}\left(1 + \epsilon_p\left(r_0^{max}\right)\right)$ are the minimum and maximum size of the pores in the deformed configuration. The parameters $k(r_0)$, $\partial r_0/\partial l|_{T,P,\epsilon}$, l^{min} and l^{max} depend on the total strain ϵ. The stiffness $k(r_0)$ of the pores is proportional to r_0. Since $r_0(l)$ and l differ by less than 10%, $k(r_0(l))$ and $k(l)$ also differ by less than 10%. Therefore, we can approximate $k(r_0(l))$ with $k(l)$ in the integral of Eq. (5.15): by doing so, the error is less than 10%. As for the derivative $\partial r_0/\partial l|_{T,P,\epsilon}$, there is no analytical formulation for this quantity, but numerical estimates show that this derivative is nearly independent of the strain (Fig. 5.18): due to the wide uniform pore size distibution, a strain of the solid modifies the deformed pore size distribution only by displacing the boundaries l^{min} and l^{max}, which vary from one strain ϵ to another. The variation of l^{min} and l^{max} with strain is of the order of magnitude of the strain, which has a negligible impact on the total value of the integral in Eq. (5.15), since the fluid-induced stress σ_{f-i} is small in the smallest and largest pores: $\sigma_{f-i}\left(l^{min}\right) \approx 0$ and $\sigma_{f-i}\left(l^{max}\right) \approx -P$. The latter value is negative, which implies that the macroscopic fluid-induced stress calculated with Eq. (5.15) should decrease with the strain. Therefore we conclude that the total fluid-induced stress $\sigma - K\epsilon$ for a wide uniform pore size distribution depends only slightly on the strain of the porous medium.

For the specific amorphous chain considered in this section, we display in Fig. 5.19 the excess stress for different strains ϵ. The fluid-induced stress decreased only slightly with the strain and, in a first approximation, can be considered nearly independent of the strain (up to 10%). Moreover, the excess stress is negative at all fluid pressures considered. This is due to the predominant contribution of the first peak of the fluid-induced stress isotherms (Fig. 5.15) in the integration of Eq. (5.15). The ocillations of the fluid-induced stress isotherm decrease exponentially with the size of the pore and the first peak is much larger than all other peaks. Since the first peak is negative, the total fluid-induced stress is negative, i.e., the fluid has a disjoining effect.

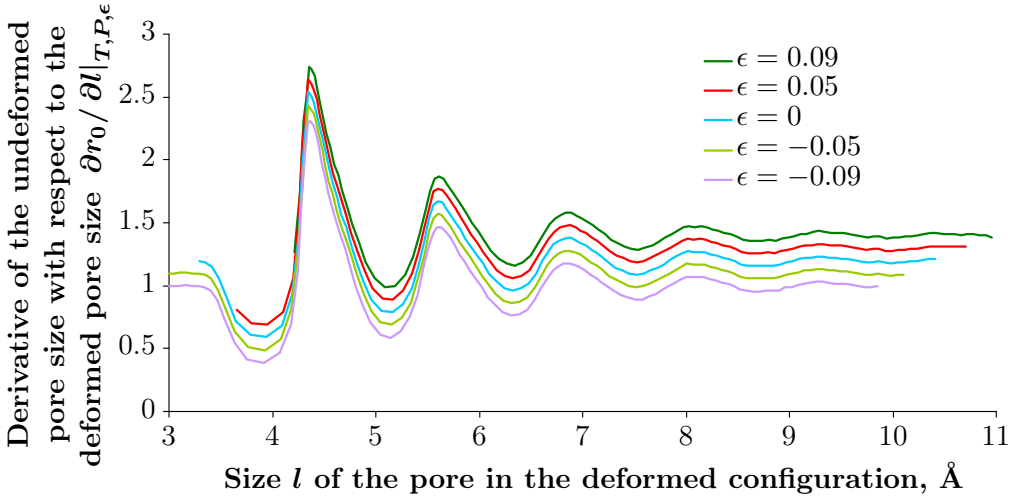

Figure 5.18. *Derivative of the pore size r_0 in the undeformed configuration with respect to the pore size l in the deformed configuration for various strains ϵ. For sake of clarity, the curves for $\epsilon = -0.05$, $\epsilon = 0$, $\epsilon = 0.05$ and $\epsilon = 0.09$ are shifted vertically by* 0.1, 0.2, 0.3 *and* 0.4 *units respectively. The maximum relative difference between the curves is* 1.25%.

According to our analysis, the mechanical behavior of an amorphous chain with a wide pore size distribution is nearly independent of the strain. The effect of the fluid is disjoining because of the predominance of the first oscillation in the fluid-induced stress isotherms (Fig. 5.15). Therefore, the smallest micropores, which can accommodate only one fluid molecule, play an important role in the macroscopic behavior of an amorphous chain. An amorphous chain for which the pore size distribution would not extend down to these small pores may contract at the smallest pressures of the fluid.

5.3.3 Inverse problem: back-calculation of the pore size distribution from macroscopic measurements

Adsorption isotherms are often used to attempt to characterize the microstructure of a material: from a macroscopic measurement of adsorbed amount of fluid, one wants to back-calculate the pore size distribution. The solution to such an inverse problem is not unique: many pore size distributions can lead to the same adsorption isotherm. How adsorption depends on the size of a pore can be estimated by DFT (Nguyen et al., 2005, Bae and Bhatia, 2006) but, as we saw in Sec. 5.3.1, can as well be estimated by Monte Carlo molecular simulations (see Fig. 5.20). Those adsorption isotherms at the scale of the pore are linked to the macroscopic adsorption isotherm $\widetilde{n}$ through:

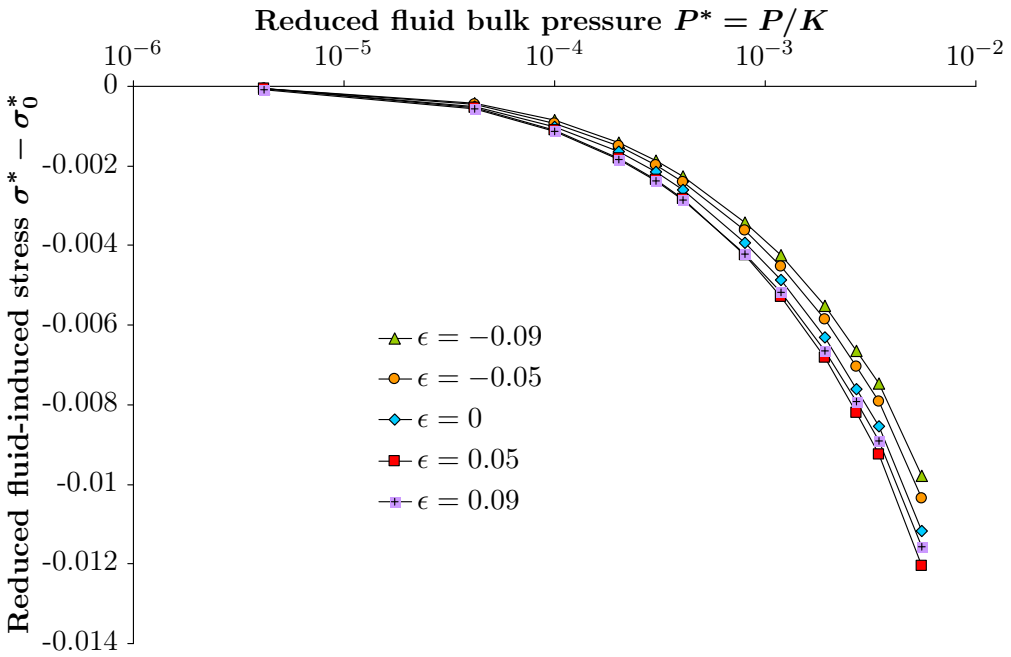

FIGURE 5.19. *Fluid-induced stress for a uniform pore size distribution between* 3.3 *Å and* 10.5 *Å.*

$$\widetilde{n} = \int_{r_0^{min}}^{r_0^{max}} \rho_p\left(l\right)\left(1+\epsilon_p\left(r_0\right)\right) p\left(r_0\right) dr_0 \tag{5.16}$$

where $\rho_p\left(l\right)$ is the apparent adsorbed density, which is defined as the amount adsorbed in a micropore of deformed size l per unit length in the deformed configuration. Like the fluid-induced stress, this quantity can be calculated from the molecular simulation of crystalline chains. We display in Fig. 5.20 $\rho_p\left(l\right)$ in function of the deformed pore size l for various fluid bulk pressures P.

In order to improve the quality of the estimate of pore size distributions from macroscopic measurements, we propose to use not only the macroscopic adsorption isotherms, but also the measurements of macroscopic volume strains upon adsorption as an additional information. Such an idea was already proposed by Kowalczyk et al. (2008), who thus characterized the pore size distribution of an activated carbon.

The macroscopic strain ϵ of the porous solid upon adsorption is linked to the poromechanical behavior at the pore scale through:

$$\epsilon = \int_{r_0^{min}}^{r_0^{max}} \epsilon_p\left(r_0\right) p\left(r_0\right) dr_0 \tag{5.17}$$
$$\text{where } \forall r_0, \epsilon_p\left(r_0\right) = \sigma_p^{-1}\left(-P\right) \text{ with } \sigma_p\left(\epsilon_p\right) = k\left(r_0\right)\epsilon_p + \sigma_{f-i}\left(r_0\left(1+\epsilon_p\right), P\right)$$

Considering such an additional information should improve the estimation of the pore size distribution, especially for very small micropores, for which the fluid-induced stress isotherms (Fig. 5.15) and the adsorbed density isotherms (Fig. 5.20) differ significantly from one pore size to the other.

As an application of the proposed approach, we considered a one-dimensional chain with pore sizes distributed around 5 and 9 Å. The actual pore size distribution is displayed in Fig. 5.21. By

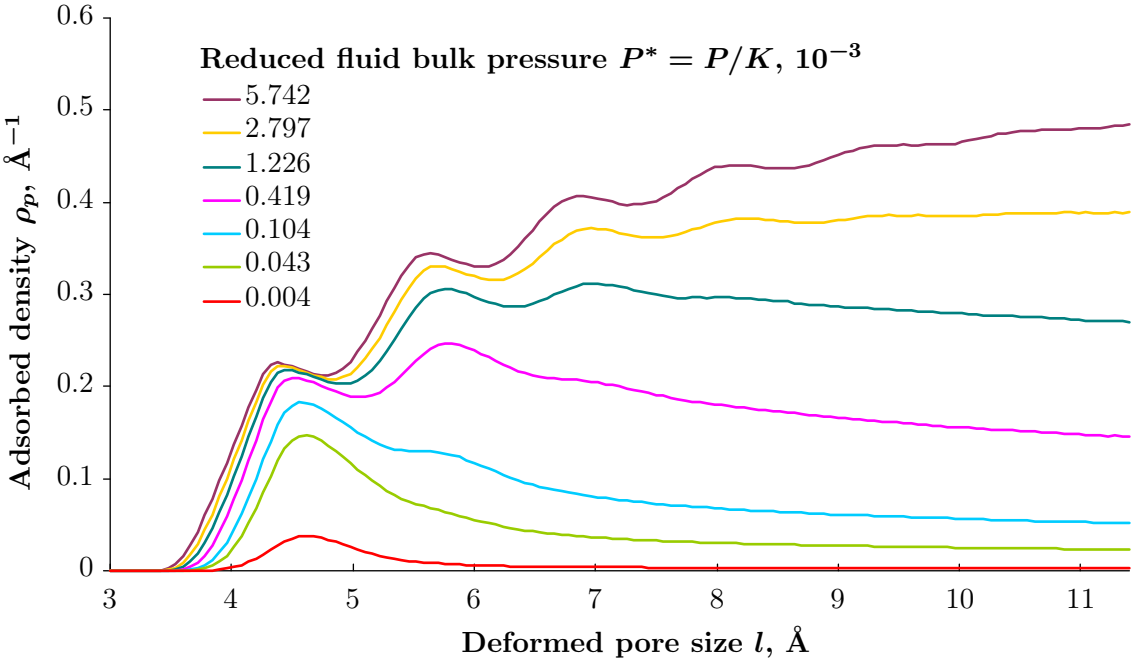

Figure 5.20. *Adsorbed density in function of the pore size. The bulk modulus K, used to make the fluid pressure dimensionless, is the bulk modulus of the crystalline chain studied in Sec. 5.1.*

using Monte Carlo simulations, we computed how adsorption in this porous solid and strain of the porous solid depend on the bulk fluid pressure when the porous solid is immersed in the fluid.

First, we estimated the pore size distribution by considering only as an input the macroscopic adsorption isotherm: out of all the pore size distributions that satisfy Eq. (5.16), we display in Fig. 5.21 the one that maximizes the entropy $\int_{r_0^{min}}^{r_0^{max}} p(r_0) \ln(p(r_0))\, dr_0$, i.e., the pore size distribution of maximum uncertainty.

Second, we estimated the pore size distribution by taking into account both the macroscopic adsorption isotherm and the swelling of the porous solid upon adsorption. Out of all the pore size distributions that satisfy simultaneously Eqs. (5.16) and (5.17), we display in Fig. 5.21 the one that maximizes the entropy $\int_{r_0^{min}}^{r_0^{max}} p(r_0) \ln(p(r_0))\, dr_0$.

For pores around 9 Å, both ways of estimating the pore size distribution yielded poor estimates. This is due to the fact that, in this range of pore sizes, the adsorption behavior and the poromechanical behavior do almost not depend on the pore size. By contrast, for pores around 5 Å, the pore size distribution estimated by taking into account both the macroscopic adsorption isotherm and the macroscopic strain induced by adsorption was significantly better than by taking into account the macroscopic adsorption isotherm only: the Euclidian distance between the actual distribution for $r_0 \in [3\text{ Å}; 7\text{ Å}]$ and the estimated one was twice as small with the former estimation as with the latter one. Therefore the use of both the macroscopic adsorption isotherm and the macroscopic adsorption-induced strain has clearly improved the estimation of the pore size distribution.

In conclusion, the coupling between mechanical behavior and adsorption can be a useful information to estimate the pore size distribution of a microporous solid.

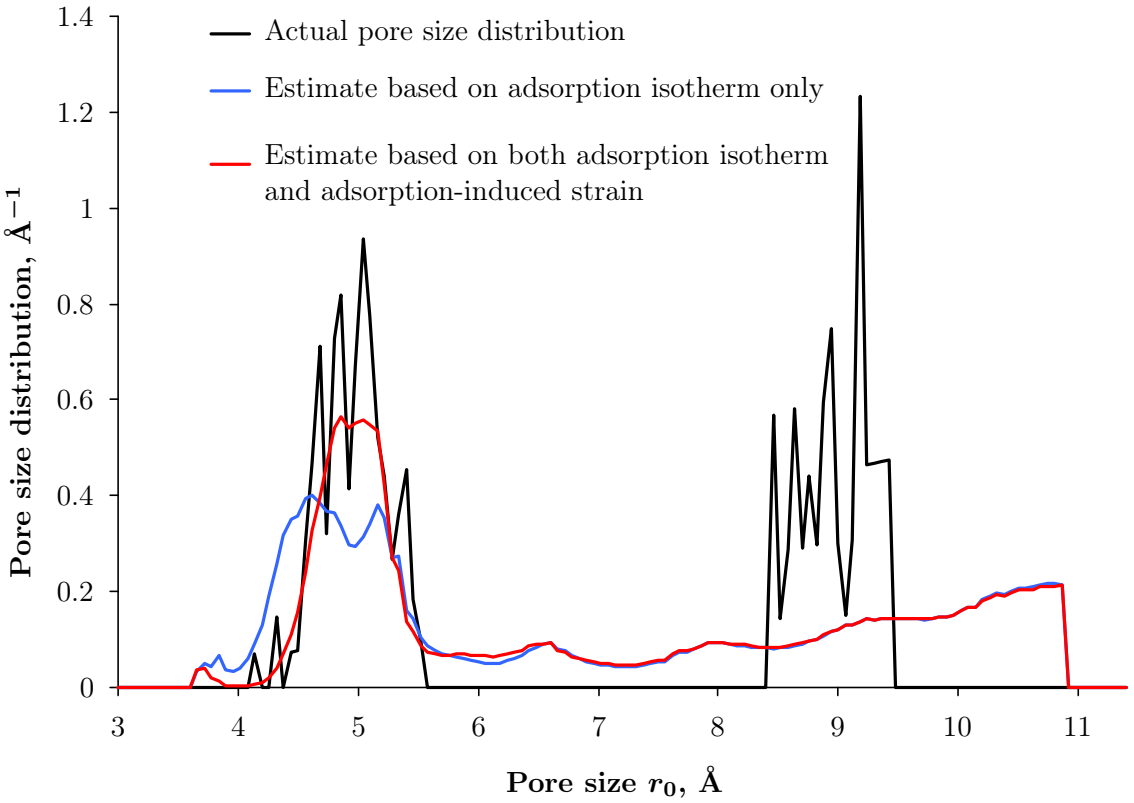

FIGURE 5.21. *Pore size distribution of a chain and its estimates obtained by two different means.*

5.4 Conclusions and discussion

We validated the constitutive equations (4.42) derived for microporous solids by performing molecular simulations of adsorption of fluid in one-dimensional microporous media. Those simulations also showed that microporous media can exhibit a counterintuitive behavior: their apparent drained bulk modulus can vary upon adsorption even when the medium behaves linearly in the absence of any fluid; their apparent Biot coefficient can be greater than unity and smaller than zero. How the amount of fluid in the porous medium depends on the strain of the medium governs how adsorption modifies the poromechanical behavior. But, often, the dependence of the isotherm of adsorption on the strain is disregarded since, for a macroporous medium, the amount of fluid in the system simply increases linearly with the strain. In contrast, in a microporous medium, we showed that the adsorbed amount can depend in a complex manner on the strain and that this dependence plays a significant role on how the medium will respond mechanically to adsorption. At the scale of the micropore, we explained this complex dependence by the commensurability of the size of the pores to the size of the fluid molecules. Interestingly, for a microporous medium with a wide pore size distribution, the amount of fluid in the system increases linearly with the strain of the medium, although this response at the scale of the system results from a complex combination of swelling and shrinkage of micropores. This linear dependence of the adsorbed amount of fluid on the strain leads to simplified constitutive equations. A detailed analysis shows that the fact that amorphous solids swell even at the lowest fluid pressures is due to the smallest micropores that can only accommodate one fluid molecule. An interesting perspective of our work is the use of both the macroscopic adsorption isotherm and the macroscopic adsorption-induced strain to estimate the pore size distribution by inverse analysis.

The whole chapter was based on one-dimensional systems, on which we studied the coupling between strain and adsorption. For three dimensional porous media however, the situation is more complex. In particular, the fluid may encounter phase transitions and the pores cannot be characterized by a pore size distribution only. However, two important conclusions of this chapter should hold for three dimensional systems, as long as no phase transition is involved:

- When all micropores are identical (i.e., when the solid is crystalline), how adsorption of fluid impacts the mechanical behavior of the porous solid is driven by the commensurability of the size of the pores to the size of the molecules of fluid.
- For a solid with a disordered porous network (for which the variability can come from a variability in size size and/or shape) the poromechanical behavior of the microporous solid is less complex than for a crystalline solid.

Coal is a disordered (and thus amorphous) microporous medium with a variety of pore sizes (Larsen et al., 1997, Takagi et al., 2004, Bae and Bhatia, 2006). One can wonder how the poromechanical behavior of coal is modified by fluid adsorption. In order to answer this question, Chaps. 6 and 7 are devoted to molecular simulations of adsorption of methane and carbon dioxide in a microporous carbon structure representative of a coal matrix.

Chapter 6

Molecular modeling of adsorption in coal

THIS CHAPTER *aims at presenting and validating the molecular modeling of adsorption of methane and carbon dioxide in coal, which we will use in Chap. 7 to study the adsorption-induced swelling of coal. Coal is not a material with a unique structure or composition but a family of materials characterized by a mass content in carbon larger than* 60%. *Adsorption occurs mostly in the organic regions of the coal matrix, which are made of macerals. From one maceral to the other, the adsorption capacities vary widely, which makes the adsorption-induced swelling heterogeneous at the scale of the coal matrix and leads to various magnitudes of swelling from one coal to the other. In addition, coal is anisotropic and can plasticize under high pressures of carbon dioxide. The molecular simulations of adsorption in coal are based on a realistic molecular model of the organic matrix of coal, which is called CS1000. These molecular simulations do not account for the variability of coal, for their anisotropy or for the plasticization, but provide estimates of adsorption in coal at the molecular scale which are as realistic as possible. The inter-atomic and inter-molecular interactions between atoms and/or molecules are modeled with Lennard-Jones potentials for the steric repulsion and for the dispersion forces, and with point charges for the electrostatic interactions. The simulated amounts of adsorbed methane and carbon dioxide in the microporous CS1000 compare well with the experimental amounts of adsorbed fluid in coal. By contrast, the simulated amounts of adsorbed fluid at the surface of mesopores differ significantly from the experimental amounts of adsorbed fluid in coal, which proves that most adsorption of fluid in coal occurs in micropores.*

Ce chapitre *a pour but de présenter et de valider la modélisation moléculaire de l'adsorption de méthane et de dioxyde de carbone dans du charbon, qui sera utilisée au Chap. 7 pour l'étude du gonflement du charbon induit par l'adsorption. Le charbon n'est pas un matériau précis mais une famille de matériaux caractérisés par une teneur massique en carbone supérieure à* 60%. *L'adsorption a lieu principalement dans la partie organique de la matrice de charbon, constituée de macérals. D'un macéral à l'autre les capacités d'adsorption sont très variables, ce qui se traduit par des gonflements hétérogènes à l'échelle de la matrice organique du charbon et par des amplitudes de gonflement assez différentes d'un charbon à l'autre. Par ailleurs, le charbon est anisotrope et peut plastifier en présence de dioxyde de carbone à haute pression. Les simulations moléculaires d'adsorption dans le charbon sont basées sur un modèle moléculaire réaliste de la matrice organique du charbon, le CS1000. Ces simulations ne tiennent pas compte de la variabilité du charbon, de leur anisotropie ou de la plastification, mais donne une première estimation aussi réaliste que possible de l'adsorption dans le charbon à l'échelle moléculaire. Les interactions inter-atomiques et inter-moléculaires entre les atomes et / ou molécules sont modélisées avec des potentiels de Lennard-Jones pour la répulsion stérique et les forces de dispersion, et par des points de charges pour les interactions électrostatiques. Les quantités estimées de méthane et de dioxyde de carbone adsorbés dans le CS1000 microporeux sont en bon accord avec les mesures expérimentales d'adsorption dans le charbon. En revanche, les quantités estimées de fluide adsorbé à la surface de mésopores sont très différents des quantités mesurées expérimentalement dans le charbon, ce qui prouve que l'essentiel de l'adsorption de fluide dans le charbon a lieu dans les micropores.*

Outline of Chapter 6

As illustrated in Chap. 5, molecular simulation enables easily to study adsorption in function of both strain and pressure. In this thesis, we decided to use this tool to study the adsorption of methane and carbon dioxide in coal. This chapter is dedicated to the selection of reliable molecular models and to the validation of our molecular modeling by comparison with experimental data. In Secs. 6.1 and 6.2, we discuss the complexity of natural coal and select a molecular model as representative as possible of natural coal. In Sec. 6.3, we present the molecular interactions that intervene in the adsorption of methane and carbon dioxide in coal. Section 6.4 is dedicated to the results of the molecular simulations and to the validation of our modeling by comparison with experimental measurements.

In this chapter and in the next one, we use the experimental data of Ottiger et al. (2006, 2008) to validate the results of our molecular simulations. Ottiger et al. (2006, 2008) published a full set of experimental data regarding adsorption of pure carbon dioxide, pure methane, and their mixture in coal. They reported excess and total amounts adsorbed as well as swelling measurements. These data are thus well adapted for a validation of our results.

6.1 The complexity of coal

According to the World Coal Institute[1]: *"Coal is a fossil fuel. It is a combustible, sedimentary, organic rock, which is composed mainly of carbon, hydrogen and oxygen. It is formed from vegetation, which has been consolidated between other rock strata and altered by the combined effects of pressure and heat over millions of years to form coal seams."* Coals are classified regarding their degree of maturity (or rank), ranging from peat (low rank) to anthracite (high rank). The more a coal has been altered over the years, the more mature it is. The carbon and energy content of low rank coals is low, while those of high rank coals is high. Table 6.1 gives an overview of the different types of coal.

Rank	Low Rank ⟶ High rank			
Name	Lignite	Sub-bituminous	Bituminous	Anthracite
Carbon content	60 wt%	75 wt%	85 wt%	95 wt%
Abundance in the Earth's crust	17%	30%	52%	1%

Table 6.1. *The different types of coal (According to the World Coal Institute). wt% holds for weight percent.*

Coal is a complex mixture of organic and inorganic matter, made of hundreds of elementary constituents (Vassilev and Vassileva, 1996). The residues of the coalified plants (called the macerals) are the main constituents of coal and of its organic matter. The remaining matter in coal is mostly inorganic minerals which contribute little to the adsorption of gases (Glass and Larsen, 1994, Bustin and Clarkson, 1998, White et al., 2005). Accordingly, we focused on the organic matter of coal in this work. The chemical composition of this organic matter is generally measured after incineration of coal and is expressed on a dry ash free basis (Tab. 6.2), even if this measure does not exactly correspond to the composition of the macerals in natural coal (Vassilev et al., 1997). Apart from carbon, the dry macerals contain mainly oxygen, hydrogen, nitrogen, and sulfur. The contents of oxygen and hydrogen are by far the most significant after the content of carbon, since oxygen and hydrogen each constitute more than 4% of the total mass of coal.

[1] http://www.worldcoal.org

Characteristics	Low rank coal (Lignite)	Medium rank coal (sub-bituminous)	High rank coal (Bituminous, Anthracite)
Carbon content	60 wt% to 75 wt%	75 wt% to 85 wt%	85 wt% to 95 wt%
Oxygen content	21.3 wt%	11.5 wt%	4.7 wt%
Hydrogen content	5.6 wt%	5.4 wt%	4.1 wt%
Nitrogen content	1.3 wt%	1.2 wt%	1.2 wt%
Sulfur content	2.9 wt%	0.8 wt%	1.6 wt%

TABLE 6.2. *Chemical composition of coal on a dry ash free basis (Vassilev et al., 1996). wt% holds for weight percent.*

The chemical composition, the maceral composition, and the mineral composition vary widely from one coal to another, even at a given carbon content. This intrinsic variability has consequences on the properties of coal and is readily visible to the naked eye: some coals are glossy, others are dull; some are rough, others are regular; some are powdery, others are solid (Fig. 6.1). Therefore, one cannot consider coal as a unique material, but rather as a collection of materials which share some common characteristics:

- Carbon represents at least 60% of the total mass of a coal sample,
- Oxygen, hydrogen, nitrogen and sulfur are the other major constituents of coal,
- The density of coal on a dry ash free basis is comprised between 1250 to 1600 kg/m^3 (Senel et al., 2001).

FIGURE 6.1. *Example of coal samples with various origins. Credit: Wikimedia Commons.*

Regarding adsorption, no simple relationship exists between the coal rank and the adsorption capacity (Levy et al., 1997, Bustin and Clarkson, 1998, Crosdale et al., 1998, White et al., 2005, Day et al., 2008a). Nevertheless, correlations are observed between the maceral composition and the adsorption capacity. Among the three major maceral groups (i.e., vitrinite, inertinite and liptinite), the adsorption capacity of vitrinite is the highest: vitrinite can adsorb up to five times as much gas as inertinite or liptinite. As a consequence, the swelling of coal upon adsorption varies widely from one coal sample to the other (Fig. 6.2) and the specific behavior of each grain of maceral makes coal swell in a heterogeneous manner (Özgen Karacan, 2003). In addition, the coal matrix is anisotropic because the deposits of vegetation are layered and consolidated in preferential directions: coal is stratified and its physical properties orthogonal to the bedding plane differ from the physical properties parallel to the bedding plane. In particular, the swelling of coal is larger in the direction orthogonal to the bedding plane than in the direction parallel to it, as can be observed in Fig. 6.3 (Day et al., 2008b). Also, the adsorption of carbon dioxide shows a specificity:

at high fluid pressures, the adsorbed molecules can induce structural rearrangements within the molecular structure of the coal matrix (Özgen Karacan, 2003). This effect, called 'plasticization', can be explained theoretically in polymer chemistry by the enhancement of a transition from a glassy to a rubbery structure by an adsorption of carbon dioxide (Larsen et al., 1997, Larsen, 2004). In a glassy structure, the movements of the atoms of a polymer are limited to small-scale vibrations and rotations around their equilibrium configuration, whereas in a rubbery structure the thermal energy is greater than the intra-molecular interaction energy, which makes structural rearrangements possible and thus enables to reach molecular structures with lower energy.

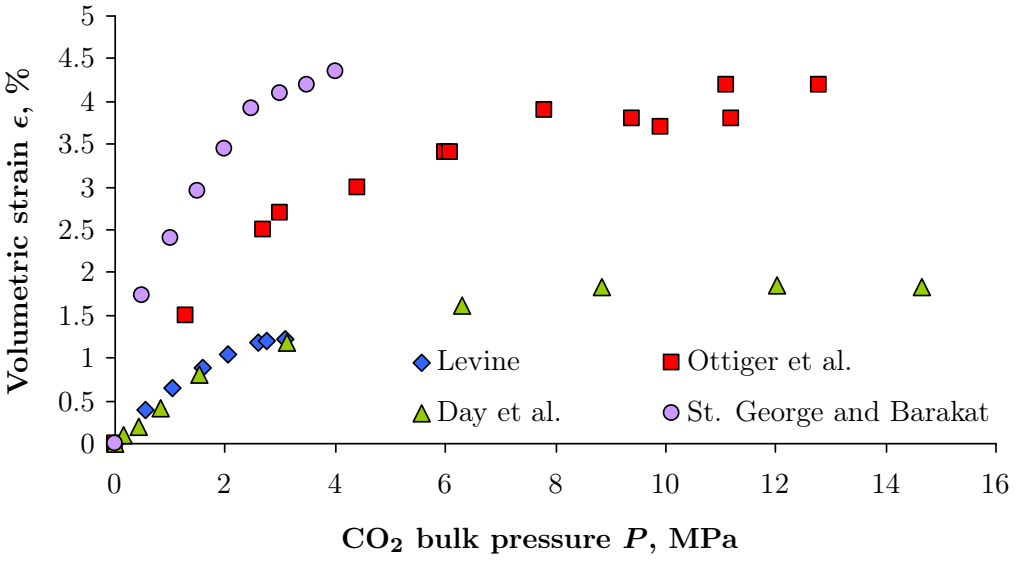

Figure 6.2. *Variability of the volumetric strain measured for coal immersed in carbon dioxide. The experimental measurements are from Levine (1996), St. George and Barakat (2001), Ottiger et al. (2008), Day et al. (2008b).*

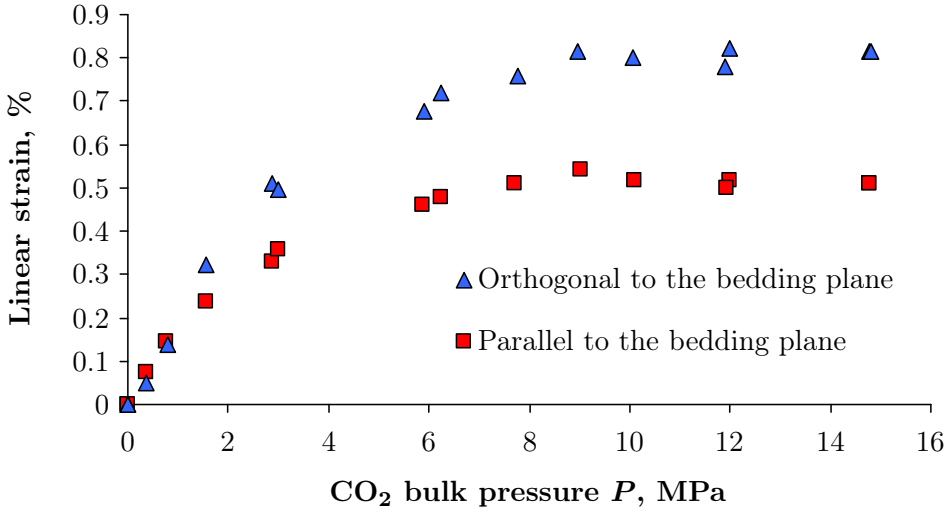

Figure 6.3. *Experimental measurements of the linear strain of coal orthogonal and parallel to the bedding plane. Adapted from Day et al. (2008b).*

As discussed in Sec. 4.3, how adsorption depends on the strain of the solid governs the poromechanical behavior of coal under adsorption. To the best of our knowledge, the effect of strain on adsorption has never been measured experimentally for coal. Ozdemir et al. (2003) proposed a quantitative model to account for the change of volume in the interpretation of the adsorption

isotherm: with their model, the fit of the adsorption isotherms in coal by analytical isotherms (Sec. 3.1.1) is very good, whereas the fit is poor when the volumetric strain is disregarded. A central hypothesis of their model is that one can define a density of the adsorbed phase, and thus a volume of this phase. The underlying consequence of this assumption is that adsorption depends linearly on the strain. The purpose of this chapter and of the next chapter is to study the adsorption of carbon dioxide and methane in coal and to determine whether the adsorbed amount of fluid depends indeed linearly on the strain of the coal sample.

In this chapter, we study the adsorption of methane and carbon dioxide by molecular simulation on a realistic molecular structure of coal. This study is based on one specific structure of coal and thus does not account for the variability of natural coal. Moreover, we disregard the anisotropy and the plasticization effect. Accordingly our results are not fully representative of the complexity of natural coal. This work aims at providing a first hint at the coupling between strain and adsorption in coal.

6.2 Molecular modeling of coal matrix

6.2.1 Molecular model

Coals are glassy, strained, cross-linked macromolecular systems (Larsen et al., 1997). X-ray diffraction (XRD) analysis indicates that the coal matrix exhibits an amorphous molecular structure with low crystallinity (Takagi et al., 2004). Smooth flat peaks are observed in the XRD profiles, which correspond to aromatic rings of various sizes stacked in a few (usually, two or three) layers. These aromatic rings recall the well-known crystalline structure of graphite, which only contains carbon atoms arranged in a hexagonal lattice. Different molecular models for porous carbons have been developed, which can be classified into three main categories according to their complexity:

- The slit pore model is a simple molecular model for graphite-like materials (Steele, 1973). The model is based on an analytic formulation of the solid-gas energy of interaction, the 'Steele $10-4-3$ potential', which assumes that the solid matrix is only composed of carbon atoms distributed in graphene layers. The implementation of this model is simple and its computational cost is low. Therefore, this model has been widely used to simulate physical adsorption of gases in porous carbons (Coasne et al., 2007, Nguyen et al., 2005, Do et al., 2008, Kowalczyk et al., 2008). However, independent and unconnected graphite-like slit pores are not representative of the amorphous and chemically heterogeneous structure of natural coal.

- Chemically heterogeneous models (Vishnyakov et al., 1998, Tenney and Lastoskie, 2006) account for the presence of oxygen and hydrogen atoms observed in bituminous and subbituminous coal. A model for coal is obtained by modifying graphite surfaces in order to account for topological and chemical heterogeneities. Selected carbon atoms from the top graphene layer are either removed entirely or replaced with oxygen- and hydrogen-containing functional groups, in order to obtain a content in oxygen and hydrogen similar to that observed in natural coal. Physical adsorption is then simulated by using Lennard-Jones and electrostatic interaction potentials.

- Molecular models obtained by reverse Monte Carlo methods (Pikunic et al., 2003, Jain et al., 2005, 2006b,a, Nguyen et al., 2008) account for both the structural and chemical hetero-

geneities in porous carbons. The reverse Monte Carlo methodology is a reconstruction technique that consists in creating a molecular structure by fitting simultaneously various experimental results such as X-ray scattering data, coordination number of the carbon atoms, average covalent bond angles and/or total interaction energy. The various fitting parameters are aggregated in a single cost function which is minimized. The models created exhibit amorphous porous structures with aromatics rings of various sizes. These amorphous structures are validated by comparing simulated adsorption in these structures to experimental adsorption data (Jain et al., 2006a). Those models are consistent with TEM image analysis (Pikunic et al., 2003).

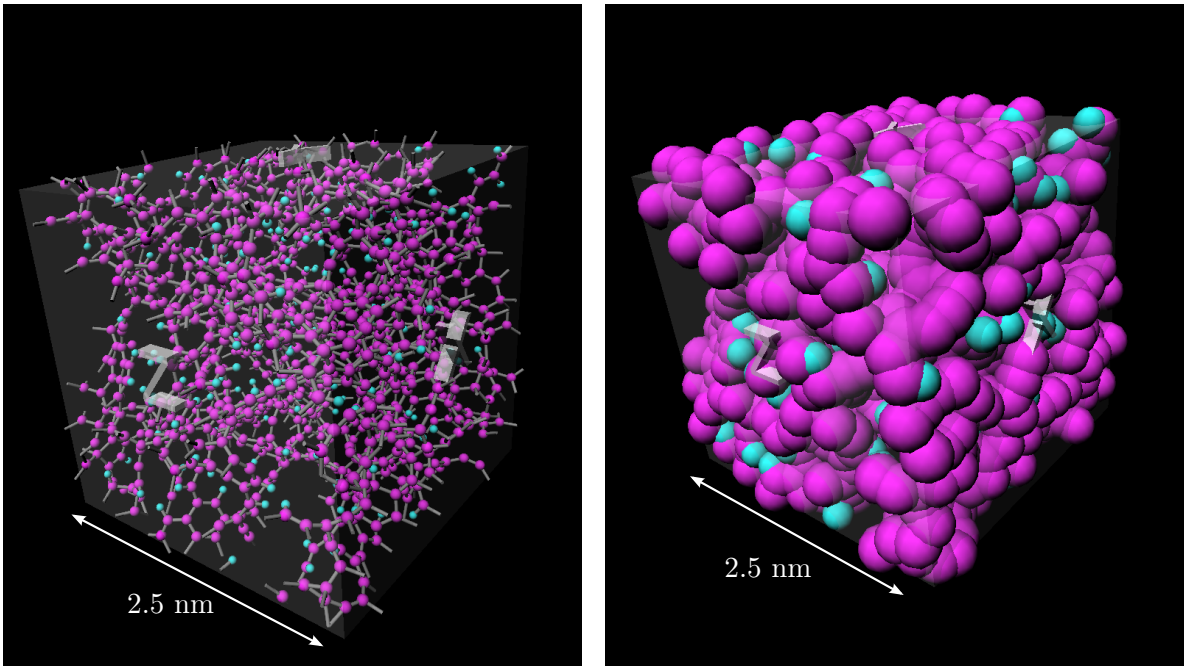

(a) (b)

Figure 6.4. *Representations of the CS1000 molecular model, representative of the nano-structure of coal. Representation of the covalent bonds (a) and representation of the volume occupied by the electron shell of the atoms (b).*

In this work, we used the reverse Monte Carlo models as molecular models for coal: their structural and chemical heterogeneities make them more suitable to reflect the adsorption behavior of natural coal. Among various reverse Monte Carlo models, we used the CS1000 model developed by Jain et al. (2006b) (Fig. 6.4). CS1000 is the molecular representation of a high density porous saccharose coke obtained by pyrolyzing pure saccharose at 1000°C in a nitrogen flow. The reconstruction method used is the 'Hybrid Reverse Monte Carlo' (HRMC) method, which aims at minimizing the total energy of interaction while fitting the experimental pair correlation function between the atoms of carbon. The energy potential used during the minimization was the reactive bond order potential developed by Brenner (1990) and Stuart et al. (2000), which adapts to any atomic arrangement of hydrogen and carbon atoms and predicts the chemical bonding in this structure. The chemical composition and the volume (and thus the density) are set at the beginning of the reconstruction. The HRMC method ensures that the molecular structure reconstructed is stable and exhibits the main morphological characteristics of the saccharose coke. We chose the CS1000 model of Jain et al. (2006b) because its characteristics, in terms of density, porosity and

composition are close to those of natural coal:

Porosity and pore size distribution: Due to its size ($25 \times 25 \times 25$ Å^3), the CS1000 sample does not contain mesopores. The porosity in the CS1000 model, probed by a hard sphere with a 3 Å diameter, is 14%. This value for the porosity, which accounts for the microporosity only, is in good agreement with experimental values (Bae and Bhatia, 2006). Micropores in coal vary in size but do not extend above 1 nm. CS1000 model contains micropores of various sizes (Fig. 6.5) and the maximum size of the micropores is 6 Å (Jain et al., 2006a).

Density: The density of the CS1000 model is 1584 kg/m^3, which is in the high range of helium densities of coal, generally measured between 1250 kg/m^3 and 1600 kg/m^3 (Senel et al., 2001, White et al., 2005, Bae and Bhatia, 2006).

Chemical heterogeneity: The CS1000 model includes carbon and hydrogen atoms. Oxygen is not accounted for, since oxygen represents less than 1% in mass in the saccharose coke. The proportion of hydrogen atoms in CS1000, which is equal to 1.2 wt%, is lower than the proportion observed in natural coal, which is around 5 wt%. The absence of oxygen atom is an important drawback of the CS1000 model. Indeed, the electronegativity of the atom of oxygen is high compared to that of carbon, which means that the distribution of charge in the coal matrix depends significantly on the presence of oxygen. Therefore, the CS1000 model should not be used to simulate the adsorption of polar fluids in coal, which strongly depends on the distribution of charge in the coal matrix. In this work, we focus on methane and carbone dioxide, which are nonpolar fluids and for the adsorption of which we disregard the effect of the presence of atoms of oxygen in the coal matrix.

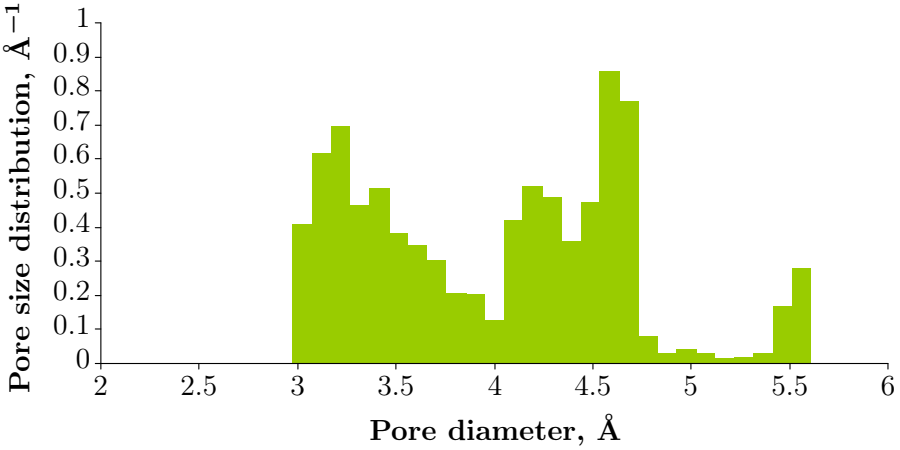

FIGURE 6.5. *Pore size distribution of the CS1000 model, probed by a hard sphere with a 3 Å diameter.*

6.2.2 Mesopores and micropores

The CS1000 molecular model cannot capture structural characteristics larger than half the size of the molecular sample. Therefore, features greater than 12.5 Å cannot be taken into account. CS1000 model can only account for the micropores of the coal matrix and not for the mesopores. Nevertheless, experimental measurements of the pore size distribution of coal indicate a clear separation between micropores, whose radius is smaller than 10 Å, and mesopores, whose radius is larger than 10 Å (Bae and Bhatia, 2006), as displayed schematically in Fig. 6.6.

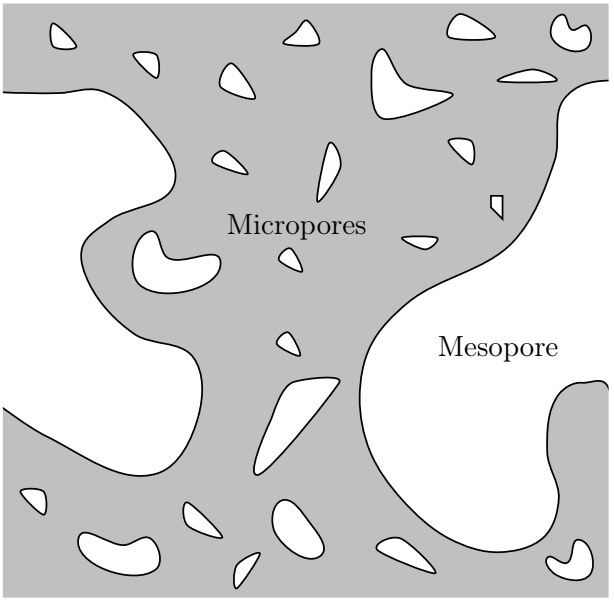

Figure 6.6. *Schematic representation of the micropores and mesopores of the coal matrix. The typical size of micropores is lower than a nanometer. The typical size of mesopores is a few nanometers and above.*

Simulation of adsorption in the CS1000 model only represents adsorption in micropores, whereas adsorption measured experimentally takes place in both micropores and mesopores. In order to compare the results of our simulations to experimental adsorption isotherms, we also aim at estimating adsorption in mesopores. In order to obtain this estimate, we simulated adsorption in a slit pore with walls made of CS1000: in a simulation box of dimensions $50 \times 50 \times 100$ Å^3, 8 elementary replicas of the CS1000 model were positioned as displayed in Fig. 6.7. Thus we created a 50 Å-large slit pore. The periodic boundary conditions of the CS1000 model ensure the continuity of the solid matrix, at the exception of the surfaces exposed to the mesopore: most carbon atoms on those surfaces lost the covalent bonds they were sharing with their direct neighbors in the periodic replica of CS1000 along the z-axis. To ensure the overall electroneutrality of the model, for each covalent bond lost, we positioned supplementary hydrogen atoms at a distance of 1.09 Å from the carbon atom (which is the optimum bond length for the C−H bond according to Jain et al. (2006b)) in the direction of the former covalent bond. Following Jain et al. (2006b), two carbon atoms are considered bonded if the distance from one to the other is comprised between 1.2 Å and 1.6 Å. We used this criterion to detect lost covalent bonds and add one supplementary hydrogen atoms for each lost bond. This technique ensures the electroneutrality of the model and was already used by Pellenq and Levitz (2001). The choice of a flat surface is somewhat arbitrary: mesopores in coal are not planar and adsorption may be influenced by the curvature of the pore. The adsorption isotherms obtained in this model of mesopore is a rough estimate of the adsorption at the surface of a mesopore in natural coal.

In summary, in order to simulate adsorption in micropores, we used the molecular structure displayed in Fig. 6.4, while we used the molecular structure displayed in Fig. 6.7 to simulate adsorption in mesopores.

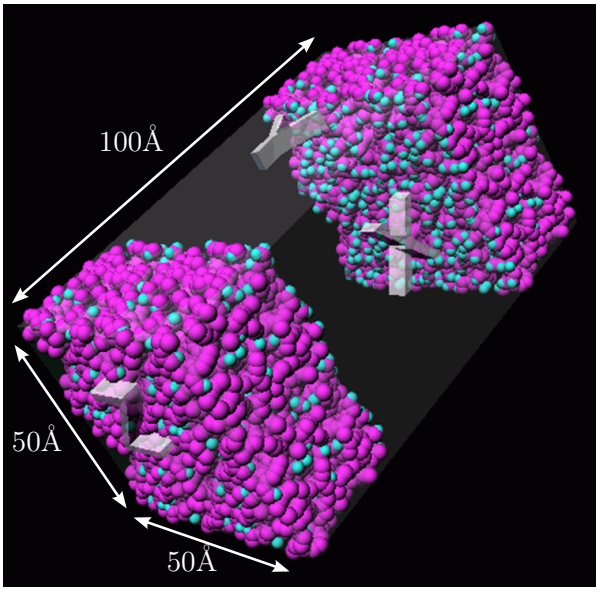

FIGURE 6.7. *Molecular model of mesopore built from the CS1000 model.*

6.3 Molecular interactions

In this section, we present the inter-atomic and inter-molecular potentials of interactions we used to simulate adsorption of carbon dioxide and methane in the molecular structures presented in Sec. 6.2.

6.3.1 Pure methane

A molecule of methane is composed of a carbon atom located at the center of four hydrogen atoms arranged in a tetrahedral structure. This molecule possesses no dipole and no quadrupole moment but an octopole moment. The electrostatic interaction between two octopoles decreases in r^{-7} (where r is the distance which separates two molecules) and can be neglected compared to the London dispersion force in r^{-6}. Therefore, as long as no chemical reaction is involved, the molecular interactions between two molecules of methane are only London dispersion forces and steric repulsion. As discussed in Sec. 2.3.3, a Lennard-Jones potential is a good approximation for the energy of interaction between two molecules of methane. The tetrahedral structure of methane implies that all orientations of the molecules are not equivalent one to the other, but an effective Lennard-Jones potential averaged over all possible orientations is a good approximation and significantly reduces the computational cost.

The interaction energy $U_{\mathrm{CH_4-CH_4}}$ between two molecules of methane depends on the distance r between the centers of the molecules:

$$U_{\mathrm{CH_4-CH_4}}(r) = 4\widetilde{\varepsilon}_{\mathrm{CH_4}} \left(\left(\frac{\widetilde{\sigma}_{\mathrm{CH_4}}}{r} \right)^{12} - \left(\frac{\widetilde{\sigma}_{\mathrm{CH_4}}}{r} \right)^{6} \right) \tag{6.1}$$

where $\widetilde{\sigma}_{\mathrm{CH_4}}$ and $\widetilde{\varepsilon}_{\mathrm{CH_4}}$ are the Lennard-Jones parameters for methane. We used the Lennard-Jones parameters proposed by Kurniawan et al. (2006), which are well-suited for the simulation of methane in underground conditions, i.e., for pressures up to 20 MPa and temperatures between 280 K and 340 K: $\widetilde{\sigma}_{\mathrm{CH_4}} = 3.751$ Å and $\widetilde{\varepsilon}_{\mathrm{CH_4}} = 148 \cdot k_B$.

To check the validity of this model for underground conditions, we performed molecular simulations of pure methane in the grand canonical ensemble at a temperature of 310 K and for fugacities ranging from 0 to 10 MPa in a cubic simulation box of size $50 \times 50 \times 50$ Å^3. For distances between molecules larger than 23 Å, the energy of interaction was set to zero, which is reasonable regarding the value of $\widetilde{\sigma}_{CH_4}$ and consistent with the size of the simulation box. For all these simulations, we computed the average density and the pressure with the virial estimate. We display in Fig. 6.10 the pressures and densities obtained by molecular simulation and those obtained with an experimental equation of state (Span and Wagner, 2003a). From this comparison, we conclude that the Lennard-Jones model used here enables to capture well the bulk properties of methane in the range of pressures and temperatures of interest for our study.

6.3.2 Pure carbon dioxide

The molecule of carbon dioxide is made of two oxygen atoms and of a carbon atom in-between the oxygen atoms and at an equal distance from each of those oxygen atoms. The oxygen atoms are tightly and stiffly bonded to the carbon atom with covalent chemical bonds. The length of the bonds and the angle between the bonds can hardly vary. Therefore, a first simplification in the molecular modeling of carbon dioxide is to consider the molecule as rigid. Since the oxygen atoms are more electronegative than the carbon atom, the electrons are delocalized toward the oxygen atom and thus the molecule possesses a quadrupole moment. Therefore, the inter-molecular interaction between two molecules of carbon dioxide includes the electrostatic interaction, the London dispersion forces, and the steric repulsion. Lennard-Jones potentials between the different atoms can be used to represent the London dispersion forces and the steric repulsion. The electrostatic interaction can be modeled with interaction between point charges. To do so, the distribution of charge in carbon dioxide is approximated by three point charges, each point charge being located at the center of each atom of the molecule (see Fig. 2.9). This representation is the representation of Harris and Yung (1995) in their 'Elementary Physical Model' (EPM), which we used in our work. The EPM model accounts for the underlying physical interactions, which is important for simulating adsorption. Other molecular models exist for carbon dioxide. Vrabec et al. (2001) developed the 2CLJQ model, which is made of two Lennard-Jones centers and a quadrupole in-between the two centers. This model is less representative of the the underlying physics, but is also less computationally expensive than the EPM model. The 2CLJQ model gives more accurate predictions than the EPM model for the bulk fluid at the pressures and temperatures of interest in our work. However, we favored the EPM model, which is more representative of the physics at short distance and thus is more adapted to simulate adsorption, especially in micropores. Harris and Yung (1995) and Zhang et al. (2005) developed a modified version of the EPM model in which the angle between the covalent bonds can vary. The energy due to the variation of angle is modeled with a harmonic potential; the angle at equilibrium is slightly different from 180°. This modification was introduced because a marginal deviation from the linear geometry is observed experimentally in supercritical conditions. This modified EPM model is more precise than the original EPM model in underground conditions, but its computational cost is higher because an additional degree of freedom has to be taken into account for each molecule. We decided to use the original EPM model in this work, because we were not interested in introducing much refinement to the molecular model of carbon dioxide, while the molecular modeling of the coal matrix is only partially representative of a natural coal.

According to the original EPM model of Harris and Yung (1995), the energy of interaction $U_{CO_2-CO_2}$ between two carbon dioxide molecules is:

$$U_{\mathrm{CO_2-CO_2}} = \sum_{i=1}^{3}\sum_{j=1}^{3}\left(4\widetilde{\varepsilon}_{ij}\left[\left(\frac{\widetilde{\sigma}_{ij}}{r_{ij}}\right)^{12} - \left(\frac{\widetilde{\sigma}_{ij}}{r_{ij}}\right)^{6}\right] + \frac{1}{4\pi\varepsilon_0}\frac{q_i q_j}{r_{ij}}\right) \tag{6.2}$$

where $(r_{ij})_{i,j=\{1,2,3\}}$ are the distances between two Lennard-Jones centers belonging to different molecules; $\widetilde{\sigma}_{ij}$ and $\widetilde{\varepsilon}_{ij}$ are the Lennard-Jones parameters for the interaction between atom i and atom j; q_i and q_j are the charges at the Lennard-Jones centers. The values of the parameters of the EPM model are given by Harris and Yung (1995): $\widetilde{\varepsilon}_{\text{C-C}} = 28.129k_B$, $\widetilde{\sigma}_{\text{C-C}} = 2.757$ Å, $\widetilde{\varepsilon}_{\text{O-O}} = 80.507k_B$, $\widetilde{\sigma}_{\text{O-O}} = 3.033$Å, $\widetilde{\varepsilon}_{\text{C-O}} = 47.588k_B$, $\widetilde{\sigma}_{\text{C-O}} = 2.892$ Å, $q_{\text{C}} = -2q_{\text{O}} = 0.6512e$ and the distance between the carbon and oxygen atoms $L_{\text{C-O}} = 1.149$ Å. The EPM model of Harris and Yung (1995) is sketched in Fig. 6.8 along with the Lennard-Jones model used for methane.

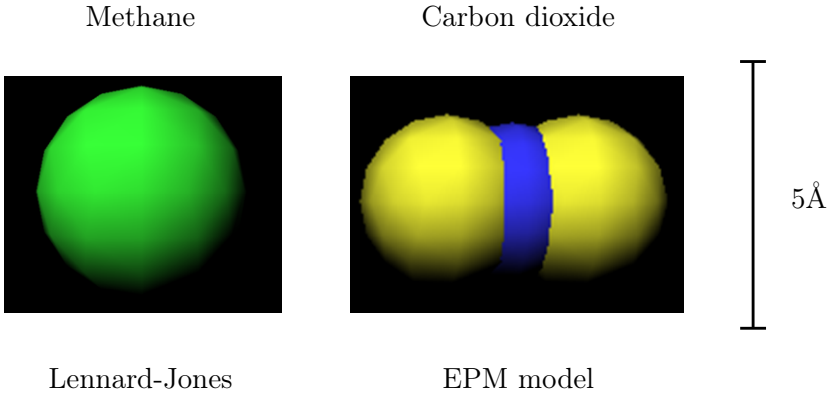

FIGURE 6.8. *Graphical representation of the molecular models chosen for simulating CO_2 and CH_4. The diameters of the balls correspond to the first Lennard-Jones parameter σ for each atom. The representations are at the same scale.*

The EPM model includes quadrupole-quadrupole interactions, whose range of interaction is larger than for the Lennard-Jones potential. In a first order expansion, the electrostatic energy of the quadrupole-quadrupole interaction is proportional to r^{-5} (Allen and Tildesley, 1989):

$$\begin{aligned}\frac{1}{4\pi\varepsilon_0}\sum_{i=1}^{3}\sum_{j=1}^{3}\frac{q_i q_j}{r_{ij}} \approx\ & \frac{3}{4}\frac{\mathcal{Q}^2}{r^5}\left(1 - 5\cos^2(\theta_1) - 5\cos^2(\theta_2) - 15\cos^2(\theta_1)\cos^2(\theta_2)\right.\\ & \left.+2\left(\mathbf{n}_1\cdot\mathbf{n}_2 - 5\cos(\theta_1)\cos(\theta_2)\right)^2\right)\end{aligned} \tag{6.3}$$

where $\mathcal{Q} = q_{\text{C}}\cdot(L_{\text{C-O}})^2$ is the moment of the linear quadrupole; θ_1, θ_2, and r are geometrical parameters defined in Fig. 6.9; $\mathbf{n}_1\cdot\mathbf{n}_2 = \cos(\theta_1)\cos(\theta_2) + \sin(\theta_1)\sin(\theta_2)\cos(\psi)$, with the unit vectors $\mathbf{n}_1$ and $\mathbf{n}_2$ and the angle ψ defined in Fig. 6.9.

Long range interactions need to be treated carefully if their range is greater than the size of the simulation box. In our study, we applied a cutoff radius: for distances between carbon dioxide molecules larger than 23 Å, we set the energy of interaction to zero. This approximation is valid since the energy which is not taken into account is negligible. Indeed, for pure carbon dioxide at a fugacity of 7 MPa, the electrostatic energy calculated by using a cutoff radius differed from the energy calculated with the Ewald sum (Allen and Tildesley, 1989, Frenkel and Smit, 2001) by less than 1%.

Using the EPM model for CO_2, we performed a series of simulations of bulk CO_2 and computed

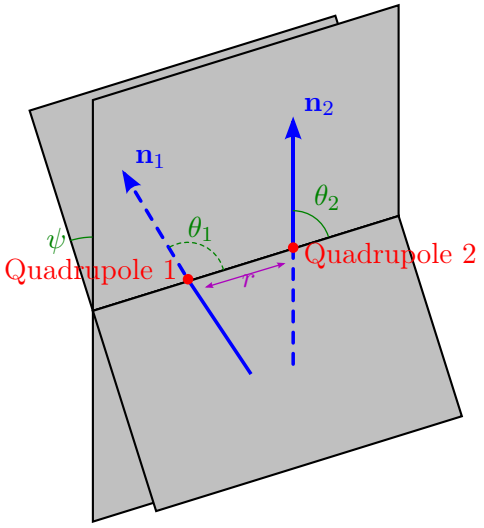

Figure 6.9. *Relative orientation of two linear quadrupoles of axis* $\mathbf{n}_1$ *and* $\mathbf{n}_2$*, adapted from Allen and Tildesley (1989).*

its density and pressure at a temperature $T = 310$ K. The results are displayed in Fig. 6.10 together with an experimental equation of state for CO_2 proposed by Span and Wagner (2003b). The EPM model captures well the experimental behavior for subcritical and supercritical pressures. Near the critical pressure $P_{cr} = 7.4$ MPa, the EPM model somewhat differs from the experimental values. The discrepancy observed between the experimental values and those calculated with the EPM model comes from the fact that the temperature considered, $T = 310$ K, is near the critical temperature $T_{cr} = 304$ K for CO_2, while the rigid EPM model was not developed originally to be used in supercritical conditions.

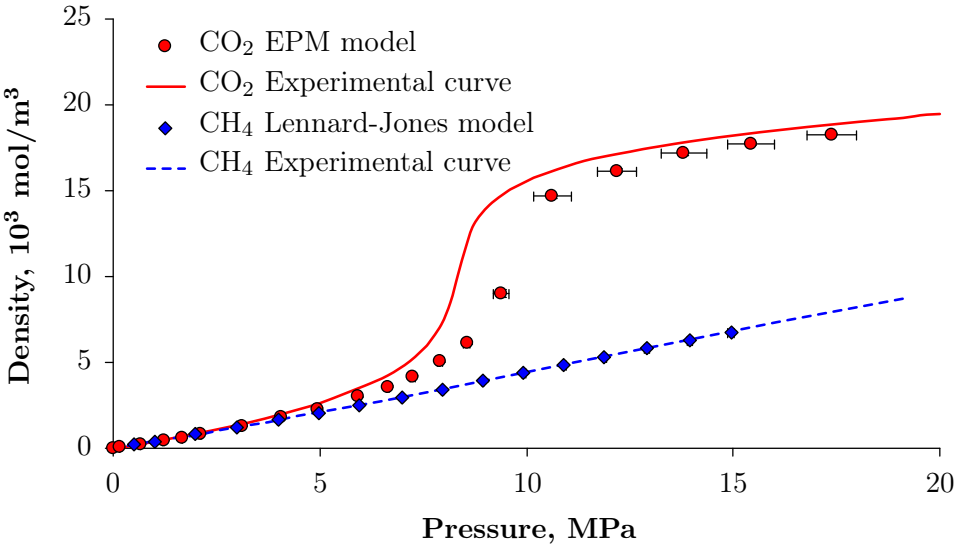

Figure 6.10. *Equation of state for* CH_4 *and* CO_2 *at a temperature* $T = 310$ *K: molecular models and experimental curves (Span and Wagner, 2003a,b).*

6.3.3 Fluid - solid interactions

In this work, we assumed that adsorption of methane and carbon dioxide in coal does not occur through chemical adsorption. This assumption is supported by the fact that the heats of adsorption

of carbon dioxide and methane in coal, either measured by calorimetry experiments (White et al., 2005) or estimated from experimental adsorption isotherms (Glass and Larsen, 1994, Ozdemir et al., 2004, White et al., 2005), are quite small (≈ 25 kJ/mol) which corresponds to physical adsorption. Nevertheless, detailed scanning calorimetry indicates that the first molecules of carbon dioxide adsorbed might be chemically bonded (Mirzaeian and Hall, 2006). Following the assumption of physical adsorption, the interactions between the CS1000 matrix and the fluids only involve the following types of interactions: steric repulsion, London dispersion forces, electrostatic interaction for carbon dioxide, and induced electrostatic interaction for methane.

The steric repulsion and the London dispersion forces can be modeled with Lennard-Jones potentials. A Lennard-Jones potential was used by Jain et al. (2006a) to simulate the adsorption of argon in CS1000. For the electrostatic and the induced electrostatic interactions, the distribution of charges in CS1000 can be modeled with point charges which mimic the electric field generated by the actual distribution of charge in CS1000. As discussed in Sec. 2.3.3, it is not possible to derive the electronic wave function in CS1000 by quantum mechanical calculation, because there are too many atoms in CS1000. Approximative methods were developed to determine a distribution of point charges (Leach, 2001). In this work, we compared two methods: the 'partial equalization of orbital electronegativity' (PEOE) developed by Gasteiger and Marsili (1980) and the 'charge equilibration method' (QEq) developed by Rappe and Goddard (1991). The point charges obtained are located at the centers of the carbon and hydrogen atoms of the CS1000. The distributions of probability of charges obtained with the two methods are displayed in Fig. 6.11. The two methods yield charge values between $-0.2e$ and $0.2e$, where e is the elementary charge. The hydrogen atoms are positively charged in both cases but their average charge predicted by the PEOE method is two times as low as their average charge predicted by the QEq method. The charges on the carbon atoms can be positive or negative, but there are significant discrepancies between the two methods: the correlation coefficient between the charges obtained by each method is only 0.50. Such approximative methods do not compare well with each other because they are based on different theories and because the methods were tested on small molecules and not on large structures like CS1000. In our work, we used the charge distribution predicted by the PEOE method.

We modeled the interaction of methane with CS1000 with the Lennard-Jones model and neglected the induced electrostatic interaction:

$$U_{\mathrm{CH_4-CS1000}}(r) = \sum_{i \in \mathrm{CS1000}} 4\widetilde{\varepsilon}_{i-\mathrm{CH_4}} \left(\left(\frac{\widetilde{\sigma}_{i-\mathrm{CH_4}}}{r_{i-\mathrm{CH_4}}} \right)^{12} - \left(\frac{\widetilde{\sigma}_{i-\mathrm{CH_4}}}{r_{i-\mathrm{CH_4}}} \right)^{6} \right) \tag{6.4}$$

where the parameters $\widetilde{\sigma}_{i-\mathrm{CH_4}}$ and $\widetilde{\varepsilon}_{i-\mathrm{CH_4}}$ are the appropriate Lennard-Jones parameters, which depend on the nature of the atom i (carbon or hydrogen). For a mixed Lennard-Jones potential between particles of different types A and B, a method commonly used to derive the values of the Lennard-Jones parameters is the Lorentz-Berthelot rules (Allen and Tildesley, 1989):

$$\widetilde{\sigma}_{A-B} = \frac{1}{2}\left(\widetilde{\sigma}_A + \widetilde{\sigma}_B\right) \tag{6.5}$$

$$\widetilde{\varepsilon}_{A-B} = \sqrt{\widetilde{\varepsilon}_A \widetilde{\varepsilon}_B} \tag{6.6}$$

where $(\widetilde{\sigma}_A, \widetilde{\varepsilon}_A)$ and $(\widetilde{\sigma}_B, \widetilde{\varepsilon}_B)$ are the Lennard-Jones parameters for the interactions between two

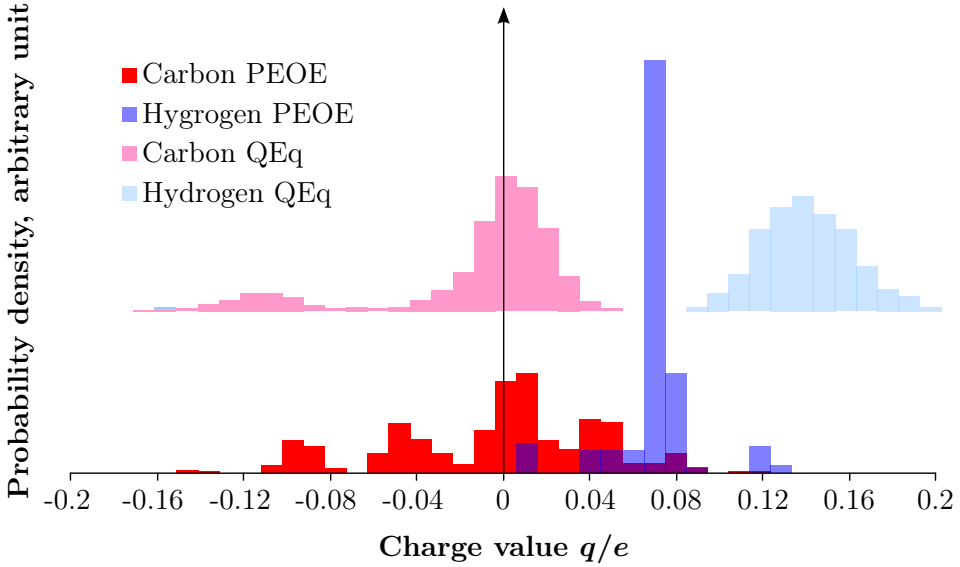

Figure 6.11. *Distribution of point charges in CS1000 obtained by the PEOE and QEq methods. The distributions obtained with the QEq method were shifted vertically, for sake of clarity.*

particles of type A and between two particles of type B, respectively. The Lorentz-Berthelot rule (6.5) is consistent with the fact that the steric repulsion originates from the volume occupied by the electrons shell of each atom: the minimum distance of approach for the particles of different types is the arithmetic mean of the diameters of the electron shells of the two particles. The Lorentz-Berthelot rule (6.6) is an approximative mixing rule for the London dispersion forces, which is exact if the first ionization potentials of the two particles are equal (Israelachvili, 1992).

Jain et al. (2006a) used the Lorentz-Berthelot rules for the Lennard-Jones potential between argon and the atoms of CS1000. We used the Lorentz-Berthelot rules as well, for the interactions between methane and the carbon and hydrogen atoms of CS1000:

$$\widetilde{\sigma}_{i-\mathrm{CH_4}} = \frac{1}{2}\left(\widetilde{\sigma}_i + \widetilde{\sigma}_{\mathrm{CH_4}}\right) \text{ and } \widetilde{\varepsilon}_{i-\mathrm{CH_4}} = \sqrt{\widetilde{\varepsilon}_i \widetilde{\varepsilon}_{\mathrm{CH_4}}} \tag{6.7}$$

where 'i' stands for an atom of carbon or of hydrogen in CS1000 and where $\widetilde{\sigma}_{\mathrm{C}} = 3.36$ Å, $\widetilde{\varepsilon}_{\mathrm{C}} = 28{\cdot}k_B$, $\widetilde{\sigma}_{\mathrm{H}} = 2.42$ Å, and $\widetilde{\varepsilon}_{\mathrm{H}} = 15.08 \cdot k_B$.

The induced electrostatic interaction between a molecule of methane and a point charge q_i in CS1000 is (Israelachvili, 1992):

$$U_{\text{ind.}} = -\frac{\alpha \left(q_i\right)^2}{2\left(4\pi\varepsilon_0\right)^2 r^4} \tag{6.8}$$

where α is the polarizability of methane. Considering a polarizability $\alpha = 2.89 \times 10^{-40}$ $\mathrm{C^2.m^2.J^{-1}}$ (Israelachvili, 1992), the energy of the induced electrostatic interaction is negligible compared to the Lennard-Jones potential, for most of the inter-particle distances r (Fig. 6.12). Only for inter-particle distances r around $\widetilde{\sigma}_{C-\mathrm{CH_4}}$, for which the Lennard-Jones potential is equal to zero, is the induced electrostatic interaction non negligible. Since this range is very small, we neglected the induced electrostatic energy in our simulations.

We modeled the interaction between carbon dioxide and CS1000 with Lennard-Jones potentials

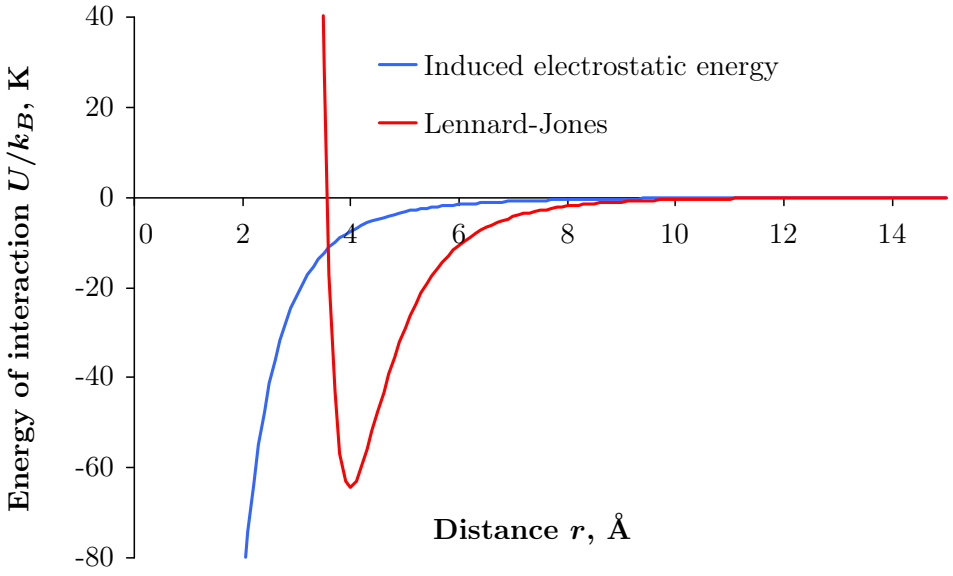

FIGURE 6.12. *Comparison of the induced electrostatic interaction with the Lennard-Jones potential for the interaction of methane with CS1000. We considered the case of an interaction with a carbon atom bearing a charge equal to* $0.1e$.

for the steric repulsion and the London dispersion forces and with point charges interactions for the electrostatic interactions:

$$U_{\mathrm{CO_2-CS1000}}(r) = \sum_{i\in \mathrm{CS1000}} \sum_{\substack{j=1 \\ j\in \mathrm{CO_2}}}^{3} \left(4\widetilde{\varepsilon}_{ij} \left[\left(\frac{\widetilde{\sigma}_{ij}}{r_{ij}} \right)^{12} - \left(\frac{\widetilde{\sigma}_{ij}}{r_{ij}} \right)^{6} \right] + \frac{1}{4\pi\varepsilon_0} \frac{q_i q_j}{r_{ij}} \right) \tag{6.9}$$

where $(r_{ij})_{j=\{1,2,3\}}$ are the distances between the Lennard-Jones centers of the EPM model and the atom i (carbon or hydrogen) of CS1000; $\widetilde{\sigma}_{ij}$ and $\widetilde{\varepsilon}_{ij}$ are the appropriate Lennard-Jones parameters for the interaction between atom i of CS1000 and center j of the EPM model; q_i and q_j are the point charges on an atom i of CS1000 and on a center j of the EPM model.

The Lennard-Jones parameters $\widetilde{\sigma}_{ij}$ and $\widetilde{\varepsilon}_{ij}$ are obtained following the Lorentz-Berthelot rules (6.5) and (6.6) with the same values of Lennard-Jones parameters as for the interactions between methane and CS1000: $\widetilde{\sigma}_{\mathrm{C}} = 3.36$ Å, $\widetilde{\varepsilon}_{\mathrm{C}} = 28 \cdot k_B$, $\widetilde{\sigma}_{\mathrm{H}} = 2.42$ Å, and $\widetilde{\varepsilon}_{\mathrm{H}} = 15.08 \cdot k_B$.

Figure 6.13 displays the electrostatic and the Lennard-Jones potentials for a CO_2 molecule interacting with an atom of carbon bearing a charge of $0.1e$. According to this comparison, the electrostatic contribution cannot be neglected. Like for pure carbon dioxide, we imposed a cutoff radius: for distances larger than 23 Å we set the electrostatic interaction to zero. The range of the electrostatic interaction is larger than the range of interaction of the Lennard-Jones potential, but we checked that the use of a cutoff radius is valid: on a sample of molecular configurations of CO_2 adsorbed in CS1000, the electrostatic energy calculated with the Ewald sum method or by introducing a cutoff radius differed by less than 1%.

6.3.4 Methane - carbon dioxide interactions

The intermolecular interaction between methane and carbon dioxide includes the steric repulsion, the London dispersion force, and the induced electrostatic interaction. As we did for the interaction of methane with CS1000, we neglected the induced electrostatic interaction. We modeled the

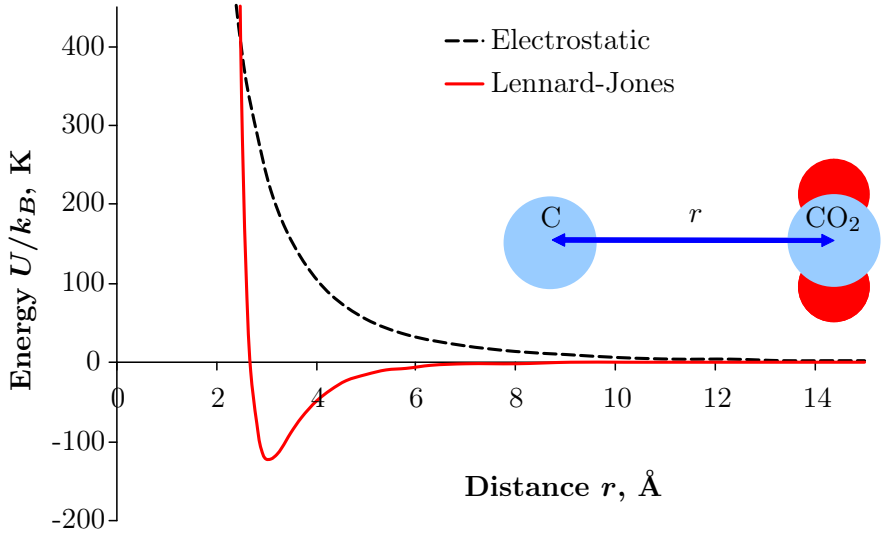

Figure 6.13. *Energy of interaction of a carbon dioxide molecule with an atom of carbon of CS1000. The point charge of the atom is set to* $0.1e$ *and the orientation of the carbon dioxide molecule with respect to the carbon atom is sketched.*

interactions with Lennard-Jones potentials. The total inter-molecular energy of interaction between a molecule of methane and a molecule of carbon dioxide is:

$$U_{\mathrm{CH_4-CO_2}} = \sum_{i=1}^{3} \left(4\widetilde{\varepsilon}_{\mathrm{CH_4}-i} \left[\left(\frac{\widetilde{\sigma}_{\mathrm{CH_4}-i}}{r_{\mathrm{CH_4}-i}} \right)^{12} - \left(\frac{\widetilde{\sigma}_{\mathrm{CH_4}-i}}{r_{\mathrm{CH_4}-i}} \right)^{6} \right] \right) \tag{6.10}$$

where $\widetilde{\sigma}_{\mathrm{CH_4}-i}$ and $\widetilde{\varepsilon}_{\mathrm{CH_4}-i}$ are the Lennard-Jones parameters for the interaction of methane with atom i (carbon or oxygen) of carbon dioxide. These parameters are derived from the Lennard-Jones parameters of the molecular model for pure methane and pure carbon dioxide following the Lorentz-Berthelot rules (6.5) and (6.6).

6.3.5 Inter-atomic potential for the coal matrix

In our work, we assumed that there is no plasticization of the coal matrix induced by adsorption: the molecular structure remains glassy and the atoms of CS1000 only are allowed to move around their equilibrium position. This assumption makes it possible to use non reactive energy potentials to model the chemical bonds in CS1000. The carbon-carbon interactions within CS1000 were modeled with a modified Morse potential proposed by Belytschko et al. (2002) for hybridized sp^2 atoms of carbon: such a potential should be well-suited to the study of coal, since most atoms of carbon in coal are hybridized sp^2. Moreover, this potential is expected to provide realistic results in strained conditions. The modified Morse potential is the sum of a conventional Morse potential $U_{\mathrm{C-C}}$ and of a bond angle bending potential $U_{\mathrm{C-C-C}}$. In this study, we only considered the second-order term in the bond angle bending potential. The equilibrium distance in the Morse potential was equal to the average equilibrium distance between atoms of carbon in the CS1000 sample:

$$U_{\mathrm{C-C}} = C_{morse} \left[\left(1 - e^{-\varsigma_{morse}(r-r_0)} \right)^2 - 1 \right] \text{ and } U_{\mathrm{C-C-C}} = \frac{1}{2} C^{\theta}_{harm} \left(\theta - \theta_0 \right)^2 \tag{6.11}$$

where r is the distance between two atoms of carbon, $r_0 = 1.423$ Å is the equilibrium distance between atoms of carbon, $C_{morse} = 6.03 \times 10^{-19}$ J and $\varsigma_{morse} = 2.625$ Å^{-1} are the parameters of the Morse potential, θ is the angle between three adjacent atoms of carbon, $\theta_0 = 2.094$ rad is the equilibrium angle, and $C^{\theta}_{harm} = 9.0 \times 10^{-19}$ J/rad^2 is the parameter for the bond angle bending potential.

Practically, the atoms of hydrogen within the solid skeleton have very little impact on the mechanical behavior of coal: this behavior is indeed mostly governed by the atoms of carbons and their interactions. Therefore, the potentials of interaction of atoms of hydrogen with atoms of carbon within the CS1000 sample have very little effect on the overall mechanical behavior of the sample. We chose those potentials in order to ensure the stability of the molecular structure. The carbon-hydrogen interaction within the CS1000 sample was modeled with a harmonic potential $U_{\mathrm{C-H}} = C_{harm}\left(r - r_0\right)^2/2$, where $r_0 = 1.09$ Å is the equilibrium distance between atoms of carbon and of hydrogen, and where $C_{harm} = 8 \times 10^{-18}$ J/Å^2 was such that the second-order derivative of this harmonic potential at equilibrium was the same as for the Morse potential for carbon-carbon interactions. We also accounted for the carbon-carbon-hydrogen and hydrogen-carbon-hydrogen bond angle bending energies by using the same potential as for the carbon-carbon-carbon bond angles. Finally, we also modeled the steric repulsion between non-bonded atoms of hydrogen and of carbon by using the repulsive potential $U_{rep} = 4\widetilde{\varepsilon}_{\mathrm{C-H}}(\widetilde{\sigma}_{\mathrm{C-H}}/r)^{12}$, where $\widetilde{\varepsilon}_{\mathrm{C-H}}$ and $\widetilde{\sigma}_{\mathrm{C-H}}$ were obtained following the Lorentz-Berthelot rules (6.5) and (6.6).

Two atoms of carbon of the CS1000 sample were considered bonded if the initial distance between them was less than 1.8 Å. This value is greater than the location of the first peak of the carbon-carbon pair correlation function of the initial CS1000 sample. Likewise, an atom of carbon and an atom of hydrogen were considered bonded if the initial distance between them was less than 1.4 Å. During the simulation, no bond could be added or removed. From the initial CS1000 sample obtained by reconstruction, we removed 8 atoms of hydrogen which were bonded to no atom of carbon but to another atom of hydrogen: indeed, the reactive potential of Brenner (1990) used by Jain et al. (2006b) in order to obtain the initial CS1000 structure by hybrid reverse Monte Carlo reconstruction allowed for the creation of dihydrogen molecules.

We checked that the CS1000 sample was stable with the potentials of interaction given above. In order to do so, we performed canonical simulations of CS1000 in the absence of any fluid and verified that atoms that were initially bonded would still verify the bond criteria at the end of a simulation, that there was no non-bonded pair of atoms that would verify the bond criteria at the end of a simulation, and that the pair correlation functions before and after a simulation were similar.

6.4 Molecular simulations of adsorption of pure fluid in rigid coal

In this section, we present the results of molecular simulations of adsorption of pure methane and pure carbon dioxide in micropores and mesopores and we compare those results to experimental data in order to validate our molecular modeling. Because of the large number of particles (more than a thousand) in the system, simulating adsorption in CS1000 is computationally expensive. In order to decrease this computational cost, we performed a first series of molecular simulations, in which the CS1000 matrix was considered rigid. Therefore, the results correspond to an adsorption at zero strain. The cases of adsorption in a flexible CS1000 and adsorption of a mixture is the focus of the next chapter.

6.4.1 Adsorption in micropores

We first simulated adsorption of pure methane and pure carbon dioxide in the CS1000 sample displayed in Fig. 6.4. Atomic interaction within the CS1000 skeleton were not taken into account, but the interaction energy of the atoms in CS1000 with the molecules of fluid was computed to estimate the adsorption isotherm at zero strain. The molecules of methane and carbon dioxide were simulated in the grand canonical ensemble. We display examples of sampled molecular states in Fig. 6.14, in which micropores filled with fluid molecules are clearly visible. In order to remain consistent with the cutoff radius of 23 Å, molecular simulations were actually not performed on one CS1000 model, but on a cubic box of $50 \times 50 \times 50$ Å^3 containing 8 replicas of the CS1000 model. Since CS1000 has been developed with periodic boundary conditions, we introduced no discontinuity by doing so and the resulting solid remained chemically stable.

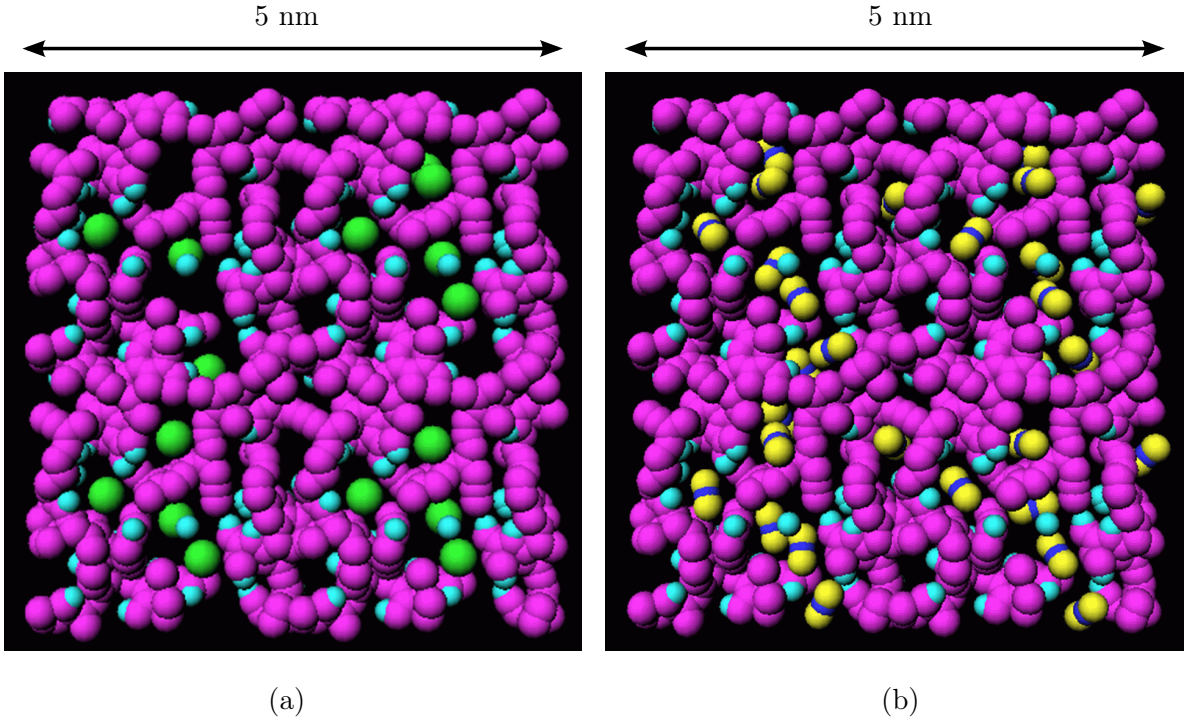

Figure 6.14. *Slices of sampled molecular configurations for the adsorption in CS1000 of methane (a) and of carbon dioxide (b). Carbon atoms are in pink, hydrogen atoms in light blue, methane molecules in green, and carbon dioxide molecules in yellow and dark blue. The size of the balls represents the first Lennard-Jones parameter $\widetilde{\sigma}$ of each atom.*

The total amount of methane and carbon dioxide in micropores per unit volume of CS1000 was computed for a temperature $T = 318.15$ K and is displayed in Fig. 6.15 in function of the bulk pressure of the fluid. We display on the same figure the experimental isotherms of Ottiger et al. (2006) obtained at the same temperature for coal from the Sulcis province, Italy. The results of the molecular simulations and the results of the experiments are displayed on different scales. As mentioned in Sec. 6.1, adsorption in coal varies widely from one coal to the other, but the general shape of the isotherm generally remains unchanged. In Fig. 6.15 the shape of the isotherms obtained by molecular simulations is consistent with the shape of the experimental isotherm. But the relative difference between the adsorptions of methane and of carbon dioxide obtained numerically is not as large as that observed experimentally.

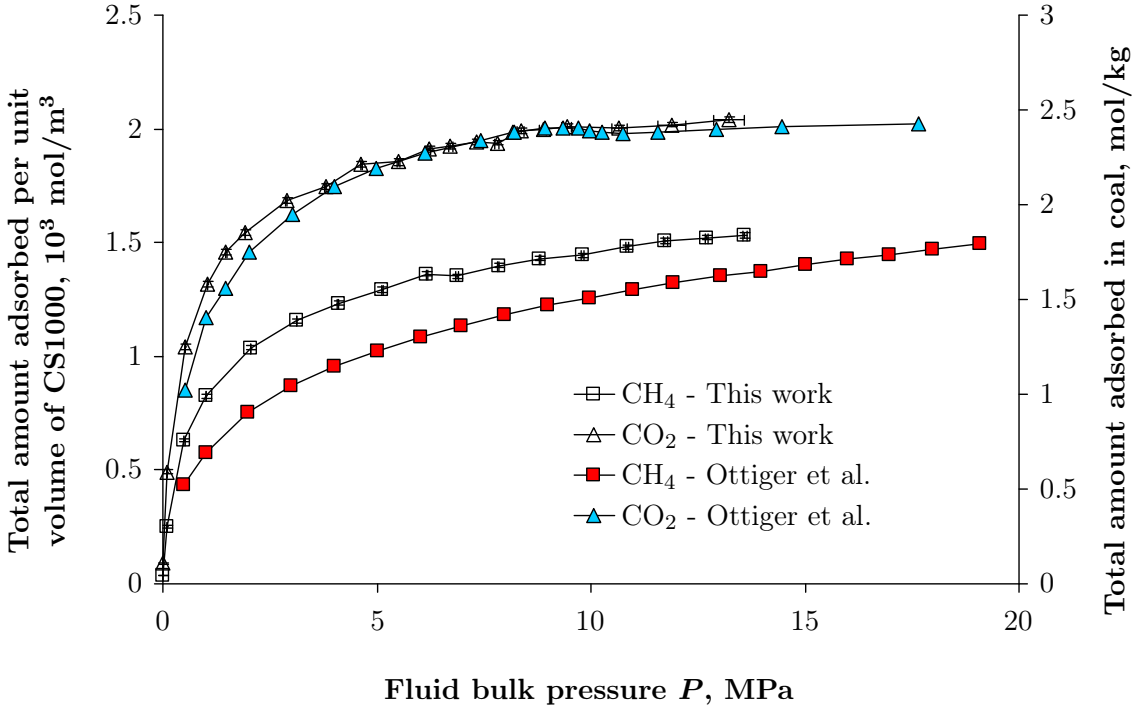

FIGURE 6.15. *Total amounts of methane and carbon dioxide adsorbed in micropores at a temperature $T = 318.15$ K.*

Actually, Ottiger et al. (2006) did not measure the total amount adsorbed, but the 'excess amount adsorbed', i.e., the increase of mass of a coal sample immersed in the bulk fluid. Because of the buoyancy, the excess amount adsorbed is the total amount adsorbed minus the amount that would occupy the volume of the adsorbed phase if the fluid mixture was at its bulk density in the pores. Ottiger et al. (2006) derived the total amount from the excess amount. To do so, they estimated the volume of the adsorbed phase from the nearly linear relationship between the excess amount of carbon dioxide and the bulk density of carbon dioxide that is observed at high pressure: the slope of this relationship is an estimate of the pore volume. By doing so, Ottiger et al. (2006) estimated a pore volume of 0.072 cm^3/g.

A possible estimate of the volume of micropores in CS1000 is the volume occupied by the maximum amount of fluid adsorbed at high pressure, assuming that the fluid is at a liquid density. The maximum amount of carbon dioxide adsorbed in micropores was around 155 molecules in the $50 \times 50 \times 50$ Å^3 CS1000 sample and was reached for a bulk pressure of 9 MPa. The volume of micropores was estimated with the volume occupied by the same amount of molecules at a liquid density. The liquid density of carbon dioxide at 260 K is between 2.29×10^4 mol/m^3 at a pressure $P = 4$ MPa and 2.43×10^4 mol/m^3 at a pressure $P = 20$ MPa. Thus we could estimate the volume of micropores to $155 \,/\left(2.35 \times 10^4 \cdot \mathcal{N}_A\right) \approx 1.1 \times 10^4$ nm^3 in a total volume of porous solid of 1.25×10^5 nm^3, which corresponds to a porosity of 9%. The same calculation with the maximum amount of methane adsorbed (around 115 molecules) and considering a methane liquid density of 2.56×10^4 mol/m^3 at a temperature $T = 120$ K yielded a porosity of 6%. An alternative estimate of the volume of micropore is the 'geometric porosity', i.e., the volume that can be occupied by a hard sphere with a 3Å diameter, considering the first Lennard-Jones parameter σ as geometric border of the solid atoms. By doing so, the geometric porosity was estimated to 14%, which is greater than the previous estimates of the volume of micropores obtained by other means. The difference is due to the fact that the whole geometric porosity cannot be fully filled with a set of

fluid molecules and to the fact that the fluid molecules we considered are larger than a sphere with a 3 Å diameter. Therefore, it is clear that defining a volume of micropore at the molecular scale is not straighforward: all estimates we obtained (6%, 9%, and 14%) are equally valid. In volume per unit mass, these estimates corresponds to porosities of 0.040, 0.060 and 0.093 cm^3/g respectively, which is consistent with the volume of micropores of 0.072 cm^3/g estimated by Ottiger et al. (2006). We estimated the microporosity at 6%, which is the value that allowed the best fit between the simulated isotherms and the experimental ones for adsorption of pure methane and pure carbon dioxide.

We display in Fig. 6.16 the experimental excess amounts of Ottiger et al. (2006) and the excess amounts derived from our molecular simulations. Like for the total amount, the general shape of the isotherms obtained by molecular simulations compares well to that obtained experimentally, but the relative difference between the isotherm of methane and the isotherm of carbon dioxide is underestimated in our simulation. There was a sharp decrease of the excess amount of carbon dioxide near the critical pressure. This decrease is due to the sharp increase of the bulk density of carbon dioxide at these pressures (Fig. 6.10), because the temperature considered here is not far from the critical temperature of carbon dioxide.

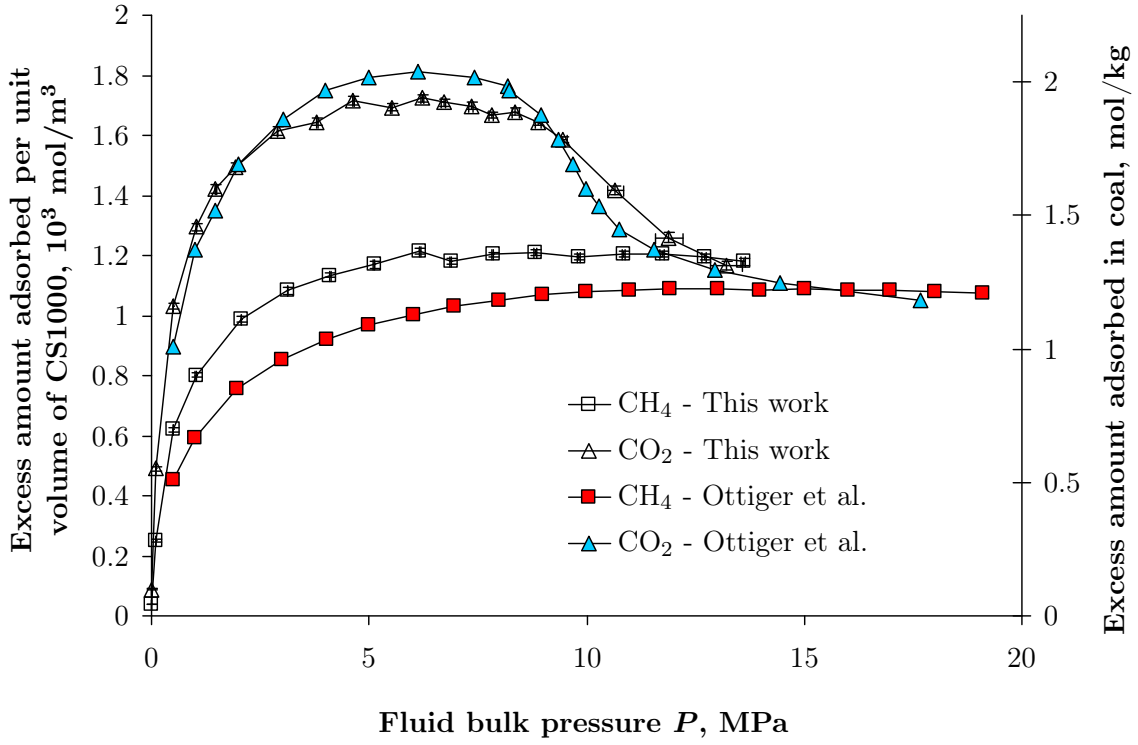

Figure 6.16. *Excess amounts adsorbed estimated by molecular simulations in CS1000 micropores, and measured by Ottiger et al. (2008) at* 318.15 *K.*

The underestimated relative difference between the adsorptions of methane and of carbon dioxide can be explained by the fact that, in a grand canonical Monte Carlo simulation, the molecules of methane and carbon dioxide have access to all micropores, whereas calorimetry experiments show that diffusion in the coal matrix does not provide equal access to all micropores: carbon dioxide can access micropores that are inaccessible to methane (Cui et al., 2004, Bae et al., 2009, Taraba, 2011). The difference in accessibility to micropores leads to a difference in volumes accessible to the adsorbed phase (Bae and Bhatia, 2006). In contrast, our simulations provided equal access to micropores for carbon dioxide and methane.

Although the relative difference between the isotherm of methane and the isotherm of carbon dioxide was slightly underestimated in our simulations, the good agreement between our isotherms of adsorption in CS1000 micropores and the experimental isotherms of Ottiger et al. (2006) indicates that the shape of the adsorption isotherms in natural coal can be explained by adsorption in micropores. One can wonder whether such a shape can also be explained by adsorption in mesopores. In order to answer this question, we study adsorption in mesopores in the next section.

6.4.2 Adsorption in mesopores

We performed molecular simulation of adsorption of pure carbon dioxide and pure methane in the mesoporous structure presented in Sec. 6.2.2 and displayed in Fig. 6.7. The temperature was set at 310 K. We display in Fig. 6.17 two examples of molecular configurations sampled. We computed the density profile of methane and carbon dioxide in the direction orthogonal to the slit mesopore. The density profiles for methane at different fugacities are displayed in Fig. 6.18. The density profiles of carbon dioxide and methane at a bulk fluid pressure of 5 MPa are displayed in Fig. 6.19.

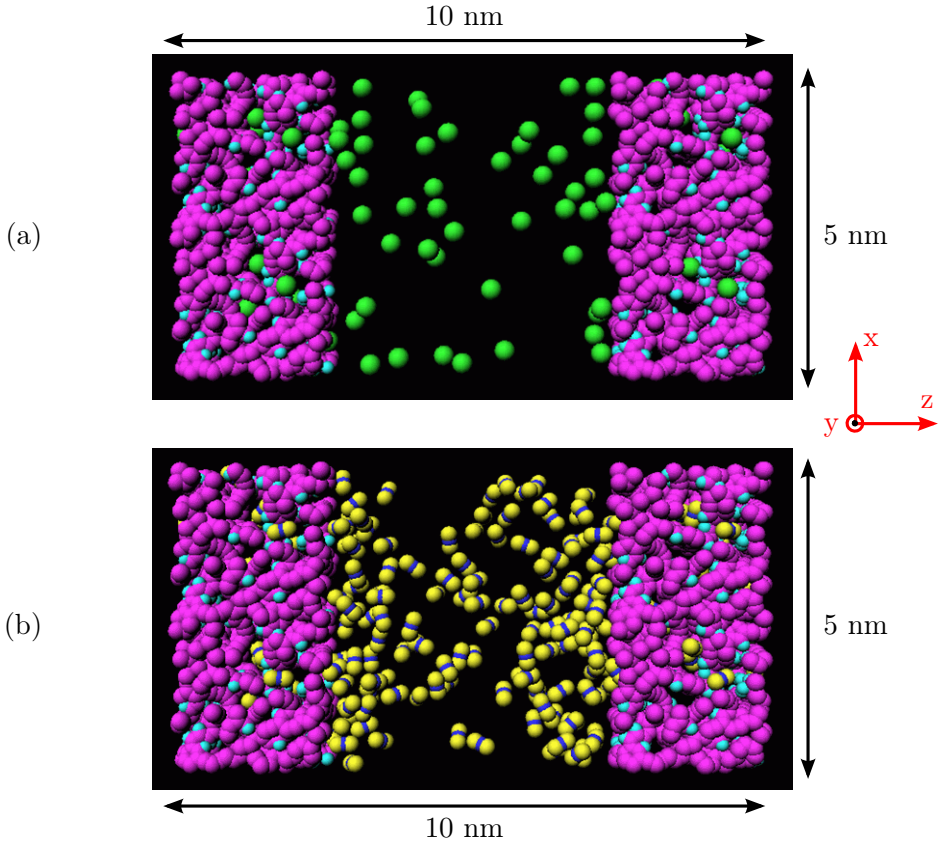

FIGURE 6.17. *Example of sampled molecular configurations for the adsorption of methane (a) and of carbon dioxide (b) in the mesoporous structure.*

For a 50 Å thick mesopore, the density of methane at the center of the mesopore was identical to the bulk density (see Fig. 6.20(a)). Therefore, a molecule of methane at a distance of 25 Å from a flat surface was not interacting with the solid. Such an observation also means that the inhomogeneous layers on each surface of the mesopore did not overlap. The inhomogeneous layers were up to 15 Å thick. Simulations performed for thinner mesopores showed that the adsorption isotherms obtained in 20 Å thick slit pores did not differ from the one obtained in the 50 Å thick

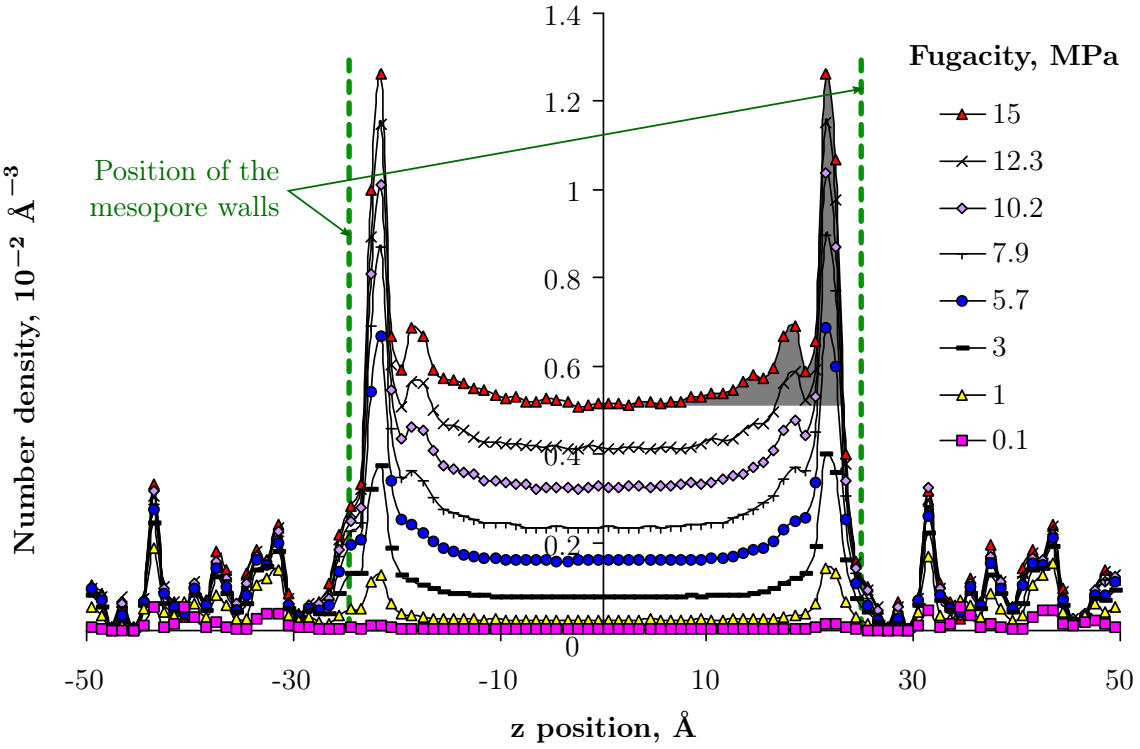

Figure 6.18. *Density profiles of methane in the mesopore at a temperature $T = 310$ K.*

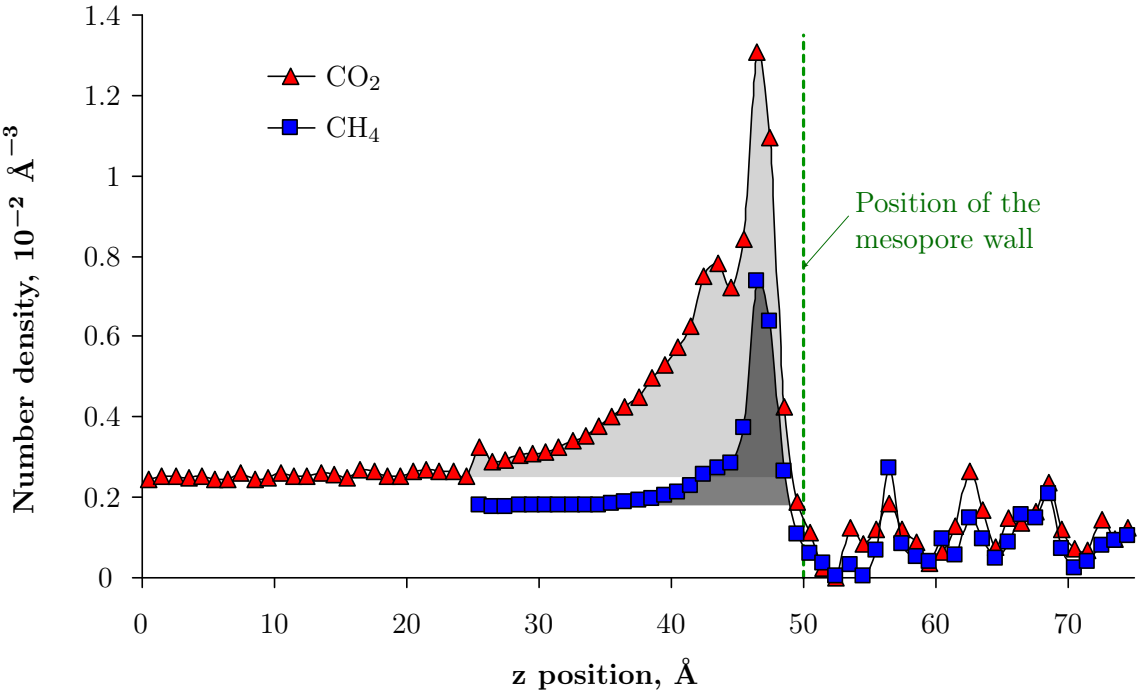

Figure 6.19. *Comparison of the density profiles of carbon dioxide and methane in the mesopore at a temperature $T = 310$ K and a bulk fluid pressure $P = 5$ MPa.*

mesopore. Therefore, the threshold in pore sizes between mesopores and micropores in coal can be estimated to 20 Å for methane as the adsorbed fluid. In contrast, for carbon dioxide a mesopore of 50 Å was too small to avoid the overlap of the inhomogeneous layers (see Fig 6.20(b)). We investigated several thicknesses of mesopores ranging from 25 Å to 100 Å. For mesopores thicker than 60 Å, the density at the center of the pore was equal to the bulk density of carbon dioxide. We estimated the threshold in pore size between mesopores and micropores to 60 Å for carbon dioxide, which is three times as large as for methane. The density profile of carbon dioxide displayed in Fig. 6.19 was obtained for a 100 Å thick mesopore.

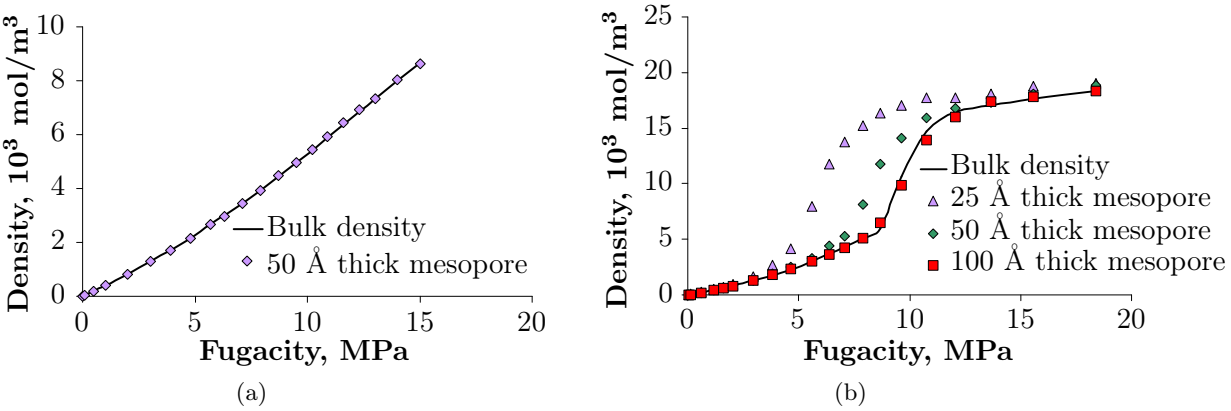

FIGURE 6.20. *Average density at the center of the mesopore and fluid bulk density for methane (a) and for carbon dioxide (b).*

The excess amounts adsorbed are the hatched areas in Figs. 6.18 and 6.19. We display in Fig. 6.21 the excess amounts adsorbed in function of the bulk fluid pressure, together with the adsorption isotherms measured by Ottiger et al. (2008). The adsorption isotherms obtained by simulation in mesopores clearly differed from the experimental one. The isotherm for carbon dioxide in mesopore was characteristic of a multilayer adsorption for bulk pressures lower than 9 MPa. For pressures larger than 9 MPa, carbon dioxide adsorbed in a single layer. Methane adsorbed in a single layer at all pressures and the adsorption took place for larger pressures than in the micropores. The experimental isotherms of carbon dioxide (also displayed in Fig. 6.21) do not exhibit the characteristic shape we obtained by simulation in mesopores, which shows that experimental adsorption isotherms cannot be explained by adsorption in mesopores.

6.5 Discussion

The study here performed by molecular simulations showed that experimental adsorption isotherms can be explained by adsorption in micropores (Sec. 6.4.1), but cannot be explained by adsorption in mesopores (Sec. 6.4.2). Therefore, we conclude that adsorption in natural coal mostly occurs in micropores.

The comparison of our simulated adsorption isotherms in micropores with the experimental isotherms is satisfactory (see Fig. 6.16). From this comparison, we conclude that molecular simulations of adsorption on CS1000 can yield realistic and meaningful results. In the following chapter, we will therefore use with confidence this approach for the study of more complex phenomena (i.e., multi-component adsorption, adsorption in a flexible coal structure). However, the relevance of such an approach can be discussed with respect to the following aspects:

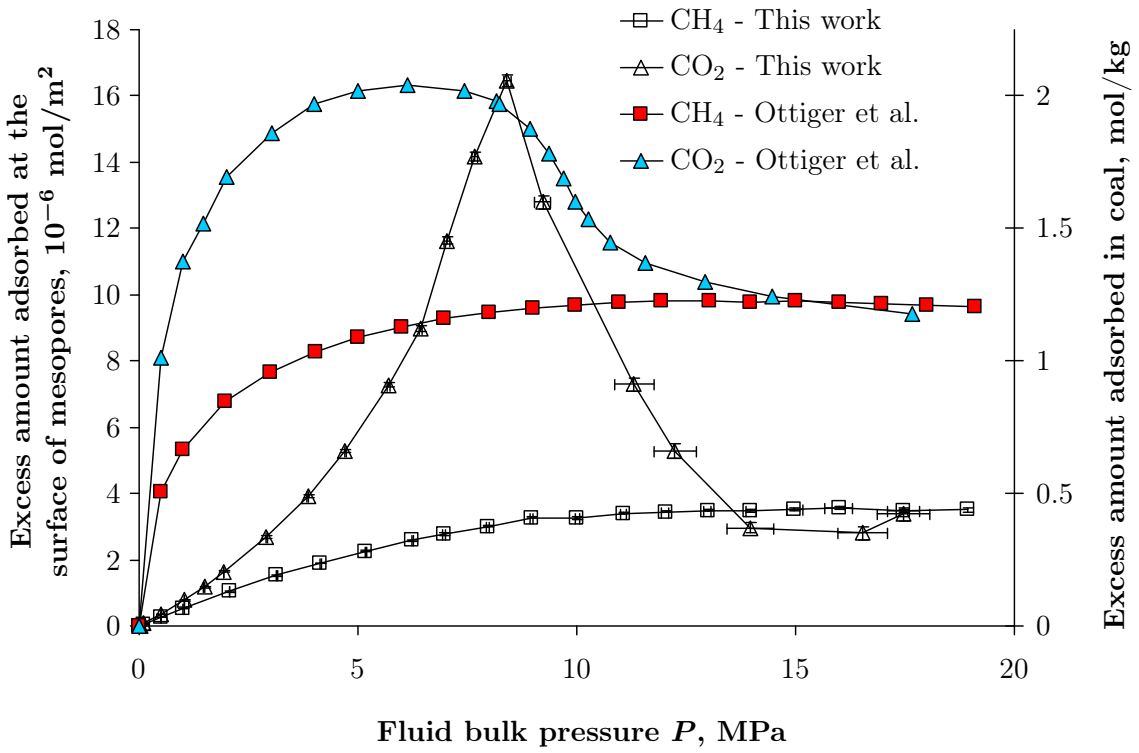

Figure 6.21. *Excess amounts adsorbed at the surface of a mesopore estimated by molecular simulation and excess amounts measured experimentally on coal by Ottiger et al. (2008).*

Accessibility to the micropores: In our simulations, all micropores are accessible because of the random insertion trials in the grand canonical Monte Carlo method. In natural coal, the microporous network is imperfectly connected and exhibits numerous constrictions which limit the accessibility of the fluid molecules to the micropore space (Radovic et al., 1997). To enter a micropore, an energy barrier may need to be overcome: the diffusion is said to be 'activated'. The activation energy is not the same for methane and for carbon dioxide (Cui et al., 2004, Bae et al., 2009). Some micropores are likely to remain inaccessible to both methane and carbon dioxide because the energy of activation to enter the micropores is much larger than the energy of the molecules. However, there exists other micropores that are accessible to carbon dioxide but remain closed for methane. Bae et al. (2009) estimated the volume of those latter micropores from the adsorption-desorption hysteresis: for the two coals they considered, 13% and 17% of the total volume of micropores presented a constricted access. In our simulation results, the underestimation of the relative difference between the amounts of carbon dioxide and of methane adsorbed (which is of about 15%) could therefore be explained by the fact that Monte Carlo simulations provide access to all micropores.

Chemical representativity of the CS1000 model: Oxygen atoms are not accounted for in the CS1000 model, whereas in natural coal oxygen amounts to about 10% of the total mass. Oxygen atoms significantly infuence the distribution of charge in a molecular structure because of their high electronegativity. For methane, we showed that the induced electrostatic interactions are small compared to the dispersion forces and steric repulsion (see Sec. 6.3.3). However, electrostatic interactions are significant for the adsorption of carbon dioxide. One can expect that higher electrostatic interactions with the solid skeleton favor specific orientations of the carbon dioxide molecules and may enhance the adsorption by lowering the total

energy of interaction with the solid. Tenney and Lastoskie (2006) simulated the adsorption of carbon dioxide on pure carbon surfaces and on carbon surfaces with chemical heterogeneities characteristic of coal: comparing this latter case with the former, the adsorption of carbon dioxide is enhanced in most cases but not always, adsorption occurs at lower pressures, and the maximum amount adsorbed is, on average, 5% larger. Therefore, the absence of oxygen is a drawback of our modeling. The error associated to this absence is somewhat difficult to quantify, but can be estimated to 5% in first order.

Size of the CS1000 model: The CS1000 model is 25 Å large and contains only a few micropores. As was discussed in Sec. 6.2.2, the CS1000 model cannot account for the mesoporosity of coal. We built a mesoporous structure based on the CS1000 model to overcome this difficulty. But one can even wonder whether the small number of micropores is sufficiently representative of the variety of pore sizes and morphologies present in a natural coal. Indeed, as was observed in Sec. 5.2, the dependence of adsorption on strain is significantly influenced by the pore size distribution. Therefore, the representativity of the CS1000 sample to study the coupling between strain and adsorption in coal is questionable.

Chapter 7

Mechanical behavior of coal under adsorption

THIS CHAPTER *is dedicated to the application of the poromechanical equations extended to microporous solids to adsorption of methane and carbon dioxide in coal. The coupling between adsorption and strain is estimated by molecular simulation of methane in a flexible microporous CS1000 model. For positive strains, the adsorption depends linearly on the strain, as was observed for the one-dimensional amorphous solid studied in Chap. 5. This conclusion is confirmed by an inverse analysis of experimental data of immersion of coal in a fluid, in which both the swelling of the sample and the adsorbed amounts were measured. The inverse analysis also shows that adsorption of carbon dioxide in coal exhibits a peculiar behavior when the temperature and pressure conditions are close to those at the critical point. Molecular aggregation of carbon dioxide molecules, which occurs in these conditions, could explain this peculiarity. The derived poromechanical constitutive equations, simplified for the case of a linear dependence of adsorption on the strain of the medium, are applied to coal immersed in pure methane and pure carbon dioxide: the swelling estimated with the derived constitutive equations combined with the adsorption isotherms obtained by molecular simulation compare well with the swelling measured experimentally. In a coal seam, the microporous matrix is exposed to a mixture of methane and carbon dioxide, the composition of which varies during the injection process. In order to estimate the differential swelling due to the progressive replacement of methane with carbon dioxide, molecular simulations of adsorption of CO_2-CH_4 mixtures are performed at temperatures and pressures representative of injection sites at various depths. The simulated adsorption isotherms are consistent with experimental ones and are used to estimate the differential swelling in various underground conditions in function of the carbon dioxide mole fraction of the pore fluid mixture. Finally, the limitations and the perspectives of this thesis are discussed.*

Ce chapitre *est dédié à l'application des équations poromécaniques étendues aux solide microporeux au cas de l'adsorption de méthane et de dioxyde de carbone dans le charbon. Le couplage entre adsorption et déformation est estimé par simulation d'adsorption de méthane dans le CS1000 microporeux considéré flexible. Pour les déformations positives, l'adsorption dépend linéairement de la déformation, comme observé pour le solide unidimensionnel amorphe étudié au Chap. 5. Cette conclusion est confirmée par une analyse inverse de résultats d'expériences d'immersion où sont mesurés à la fois le gonflement de l'échantillon et les quantités adsorbées. Pour le dioxyde de carbone, l'analyse inverse met en évidence un comportement particulier lorsque les conditions de température et de pression sont proches des conditions du point critique. L'agrégation des molécules de dioxyde de carbone qui apparaît dans ces conditions pourrait expliquer cette particularité. Les équations poromécaniques, simplifiées en considérant une adsorption linéaire en fonction de la déformation, sont appliquées au cas du charbon immergé dans du méthane pur et du dioxyde de carbone pur: les gonflements estimés à partir de ces équations et des isothermes d'adsorption obtenus par simulation moléculaire sont en bon accord avec les gonflements observés expérimentalement. Dans une veine de charbon, la matrice microporeuse est exposée à un mélange de méthane et de dioxyde de carbone dont la composition varie durant l'injection. Afin d'estimer le gonflement différentiel dû au remplacement progressif du méthane par du dioxyde de carbone, des simulations moléculaires d'adsorption d'un mélange CO_2-CH_4 sont réalisées à des températures et des pressions représentatives de sites d'injection à différentes profondeurs. Les résultats des simulations sont en bon accord avec les résultats expérimentaux et permettent d'estimer le gonflement différentiel en fonction de la fraction molaire de dioxyde de carbone pour des injections dans des veines à différentes profondeurs. Enfin, les limitations et les perspectives de ce travail de thèse sont discutées.*

Outline of Chapter 7

Coal is a mostly amorphous microporous medium which exhibits a variety of pore sizes. As was discussed in Chap. 4, the poromechanical behavior of a microporous solid is governed by how adsorption depends on the strain. As was discussed in Chap. 5, the dependence of adsorption on the strain can be significantly affected by the structure of the pore network. Therefore, one can wonder what the poromechanical behavior of coal under adsorption is. In particular, given the amorphous molecular structure of the coal solid skeleton, one can wonder whether the simplified constitutive equation (5.4) holds for this material. This chapter is dedicated to the study of the poromechanical behavior of coal under adsorption.

In the first section, we perform molecular simulations of adsorption of methane in a flexible CS1000 matrix. We study the coupling between adsorption and strain and we partially validate our results with the experimental data of Ottiger et al. (2008). In the second section, we use the constitutive equations derived in Sec. 4.3 to estimate the differential swelling during the progressive replacement of methane by carbon dioxide in geological conditions. In the last section, we discuss the limitations of our approach and the perspectives of our work for field application.

7.1 Mechanical behavior of coal under adsorption of pure component fluid

This section is devoted to the study of pure component adsorption in coal. We identified in Sec. 6.4 that adsorption in coal mostly occurs in micropores: from now on, we therefore focus on the study of adsorption in micropores. Molecular simulations of adsorption on a flexible CS1000 are performed in order to determine how adsorption and strain are coupled. The results from the simulations are validated with experimental data from the literature. A poromechanical model calibrated on the results of the molecular simulations is then used to estimate the swelling of a coal sample immersed in a fluid.

7.1.1 Molecular simulations of adsorption of methane in flexible coal matrix

In order to study adsorption in micropores, molecular simulations were performed on the CS1000 sample displayed in Fig. 6.4. In order to study the coupling between adsorption and strain, the CS1000 sample was kept flexible. A first series of molecular simulations was performed to identify the volume of the unstressed CS1000 sample in the absence of any fluid. Then, we applied various volumetric strains to the sample and let the atoms relax at each strain by performing a Monte Carlo canonical simulation. The final molecular configuration obtained at each strain was used as a starting configuration for the simulations of adsorption of methane. The simulations of adsorption were performed in the canonical ensemble regarding the atoms of the CS1000 sample and in the grand canonical ensemble regarding the molecules of methane. Volumetric strains from -6% to $+6\%$ and bulk pressures from 0 to 15 MPa were considered.

We display in Fig. 7.1 the adsorbed amount of methane per unit undeformed volume in function of the strain of the CS1000 sample for various bulk pressures of the methane. When the volumetric strain of the CS1000 sample was negative, the adsorbed amount of methane depended on the strain of the medium non-monotonically, which reminds of the response of the crystalline one-dimensional microporous solid to adsorption (Fig. 5.6). In contrast, when the volumetric strain of the CS1000 was positive, the adsorbed amount of methane increased almost linearly with the strain of the medium, which reminds of the response of the amorphous one-dimensional microporous solid to

adsorption (Fig. 5.10). Such an observation suggests that, at least for cases in which coal swells, approximating the adsorption isotherm by its first-order expansion with respect to the strain of the porous medium (Eq. 5.3) should be reasonable:

$$\widetilde{n}\left(\epsilon, P\right) \approx \widetilde{n}^{0}\left(1+\widetilde{C}\left(P\right)\epsilon\right) \tag{7.1}$$

where $\widetilde{n}^{0}$ is the adsorbed amount at zero strain.

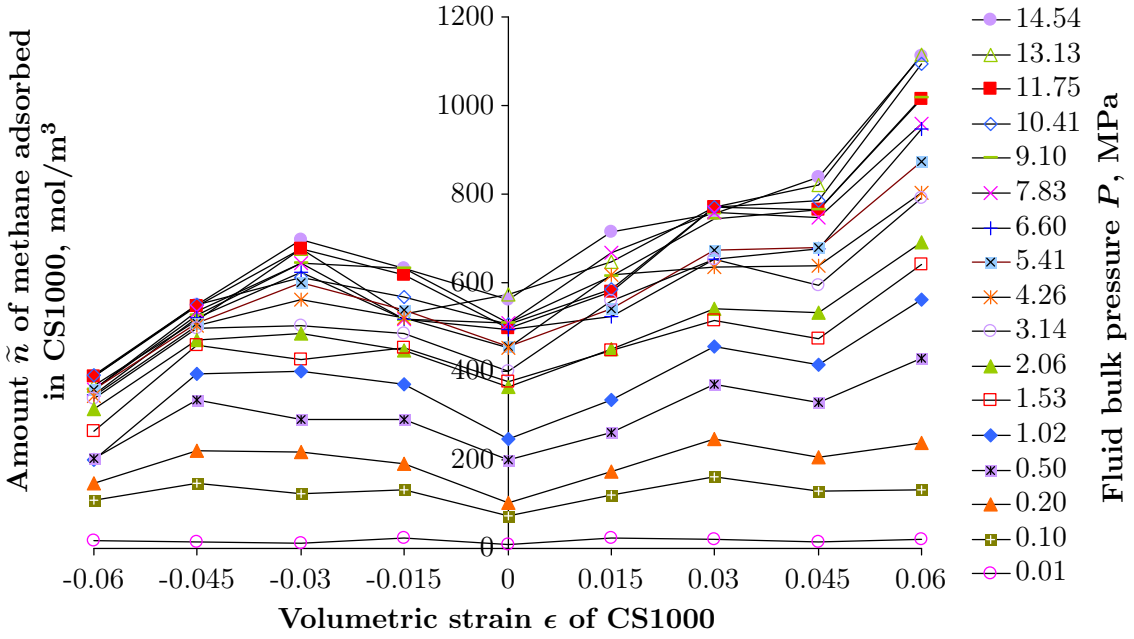

FIGURE 7.1. *Adsorbed amount of methane in CS1000 micropores per unit undeformed volume in function of both the fluid bulk pressure and the strain of the solid.*

We calculated the average of the derivative $\partial\widetilde{n}/\partial\epsilon|_{p}$ over all positive strains and compared this average to the amount $\widetilde{n}^{0}$ of fluid adsorbed at zero strain. The result of the comparison is displayed in Fig. 7.2. The comparison shows that the two quantities were almost proportional to each other, which means that the coupling coefficient $\widetilde{C}\left(P\right)$ in Eq. (7.1) (noted $\widetilde{C}_{\mathrm{CH_4}}$ in the specific case of methane) did almost not depend on the pressure P of the fluid: $\widetilde{C}_{\mathrm{CH_4}}\left(P\right) = 6.30 \pm 15\%$ on the whole range of pressures considered in this study. Therefore, since the first-order expansion (7.1) of the adsorption isotherm is valid, the simplified poroelastic constitutive equation (5.4) is valid for CS1000 upon swelling. By extension, we consider this simplified constitutive equation to be valid for coal as well. The poromechanical behavior can therefore be well described by the following set of constitutive equations:

$$\begin{aligned} \sigma &= K\epsilon - \widetilde{C}\int_{0}^{P}\widetilde{n}^{0}\overline{V}_{bulk}dP \\ \widetilde{n}\overline{V}_{bulk} &= \widetilde{n}\left(\epsilon, P\right)\overline{V}_{bulk}\left(P\right) \\ s_{ab} &= 2\overline{G}e_{ab} \end{aligned} \tag{7.2}$$

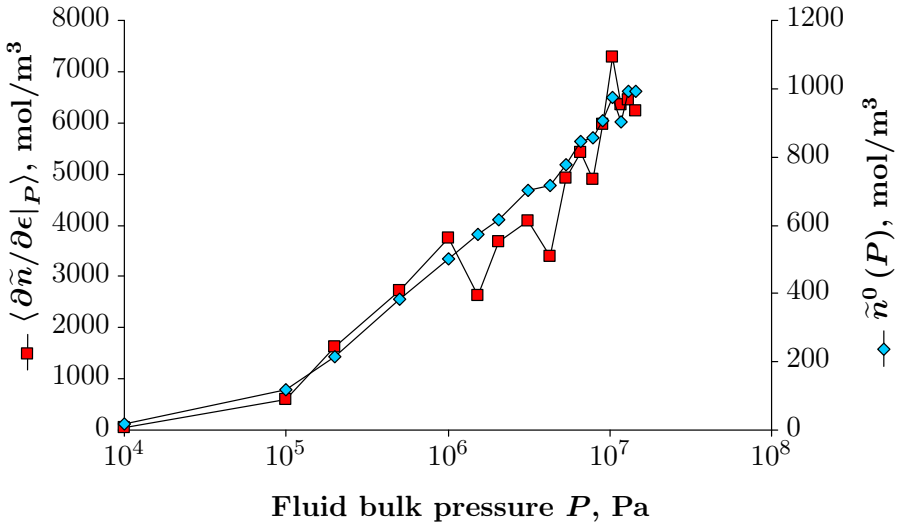

Figure 7.2. *Adsorption isotherm at zero strain and derivative of the adsorbed amount with respect to the strain.*

7.1.2 Comparison with laboratory experiments

The results of the molecular simulations must be validated with experimental data. In order to do so, we considered the work of Ottiger et al. (2006, 2008) who immersed coal samples in methane and measured the total amount of fluid adsorbed in the sample and the swelling of the sample. In such an experiment, the porous solid is in unjacketed conditions: the volumetric stress σ is equal to the opposite $-P$ of the fluid bulk pressure. The strain ϵ^u and the amount $\widetilde{n}^u$ of fluid adsorbed both depend on the fluid bulk pressure only. The linear poroelastic constitutive equations for microporous solids (Eqs. 4.44) yield a relation that the volumetric strain $\epsilon^u(P)$ must verify:

$$-P = K\epsilon^u(P) - \frac{\partial}{\partial \epsilon}\left(\int_0^P \widetilde{n}(\epsilon, P)\,\overline{V}_{bulk} dP\right)\Big|_{\epsilon=\epsilon^u} \tag{7.3}$$

Assuming that the adsorption isotherm can be well approximated by its first-order expansion with respect to the strain (i.e., assuming that Eq. (7.1) is valid: $\widetilde{n}(\epsilon, P) \approx \widetilde{n}^0\left(1 + \widetilde{C}(P)\,\epsilon\right)$ where $\widetilde{n}^0 = \widetilde{n}(\epsilon = 0, P)$), a differentiation of Eq. (7.3) with respect to the pressure P of the fluid yields:

$$\widetilde{C}(P) = \frac{1 + K d\epsilon^u/dP}{\widetilde{n}^u \overline{V}_{bulk} - \epsilon^u(1 + K d\epsilon^u/dP)} \tag{7.4}$$

Using this equation, the coupling coefficient $\widetilde{C}(P)$ can be fully determined from an immersion experiment in which both the adsorption isotherm $\widetilde{n}^u(P)$ and the volumetric strain $\epsilon^u(P)$ are measured.

In order to calculate the coupling coefficient $\widetilde{C}(P)$ with Eq. (7.4), one needs to know the bulk modulus K of the sample in the absence of any fluid and its density. For the coal tested by Ottiger et al. (2006, 2008), we estimated the density of the coal sample to 1300 kg/m^3, which is a characteristic value for an average coal (Senel et al., 2001). Based on the results reported by Ottiger et al. (2006, 2008), we display in Fig. 7.3 the coupling coefficient $\widetilde{C}_{\mathrm{CH_4}}(P)$ calculated for methane for bulk moduli K ranging from 1 GPa to 4 GPa, which is the range of values usually observed for coal (Pan and Connell, 2007, Wang et al., 2009). The back-calculated coupling coefficient was the least pressure-dependent for a bulk modulus $K = 2.65$ GPa. For such a bulk modulus, we

back-calculated a coupling coefficient $\widetilde{C}_{\mathrm{CH_4}}(P) = 6.05 \pm 7\%$, i.e., a coupling coefficient $\widetilde{C}_{\mathrm{CH_4}}(P)$ which hardly depended on the bulk fluid pressure. The coupling coefficient $\widetilde{C}_{\mathrm{CH_4}} = 6.05$ back-calculated from the experimental data of Ottiger et al. (2006, 2008) compares very well with the coupling coefficient $\widetilde{C}_{\mathrm{CH_4}} = 6.30$ obtained from molecular simulations (see Sec. 7.1.1). Moreover, experimental data shows that the coupling coefficient $\widetilde{C}_{\mathrm{CH_4}}(P)$ depends little on the fluid bulk pressure, as was also inferred from the molecular simulations (see Sec. 7.1.1). This comparison brings confidence in the results of the molecular simulations and therefore validates the use of the poroelastic constitutive equations (7.2) to describe the poromechanical behavior of coal saturated with methane:

$$\begin{aligned} \sigma &= K\epsilon - \widetilde{C}_{\mathrm{CH_4}} \int_0^P \widetilde{n}^0_{\mathrm{CH_4}} \overline{V}^{bulk}_{\mathrm{CH_4}} dP \\ \widetilde{n}_{\mathrm{CH_4}} \overline{V}^{bulk}_{\mathrm{CH_4}} &= \widetilde{n}_{\mathrm{CH_4}}(\epsilon, P)\, \overline{V}^{bulk}_{\mathrm{CH_4}}(P) \\ s_{ab} &= 2\overline{G} e_{ab} \end{aligned} \tag{7.5}$$

with $\widetilde{C}_{\mathrm{CH_4}} = 6.05$.

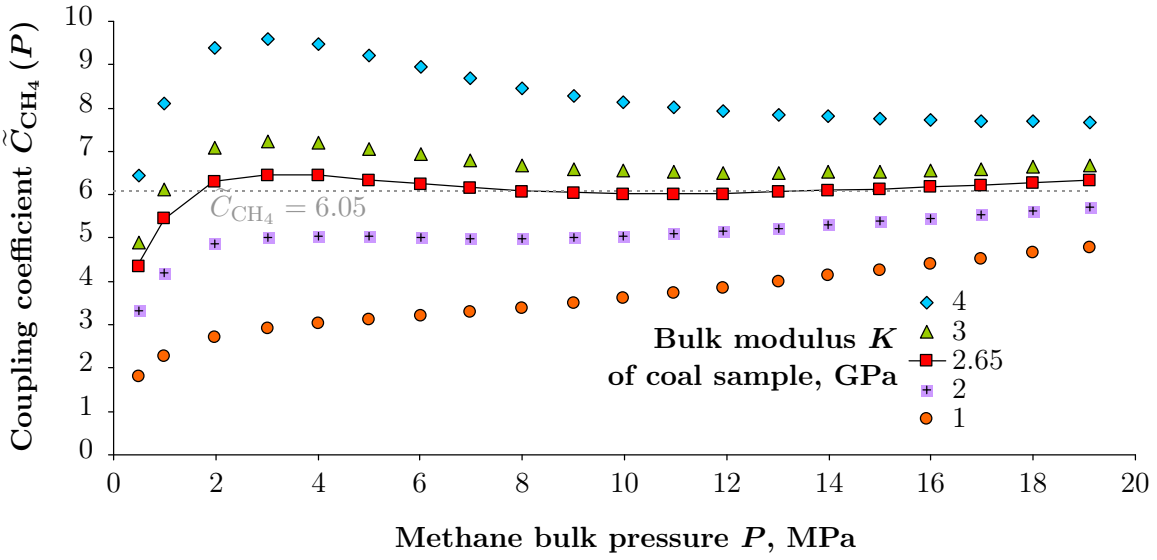

FIGURE 7.3. *Coupling coefficient $\widetilde{C}_{CH_4}(P)$ for the adsorption of methane in coal estimated from the immersion experiments of Ottiger et al. (2006, 2008).*

7.1.3 Case of coal saturated with carbon dioxide

There is no evidence that the coupling coefficient $\widetilde{C}(P)$ that determines the poromechanical behavior of coal does not depend on the nature of the adsorbed fluid: this coefficient may well vary from one fluid to the other, even if the two fluids are at the same bulk pressure. Therefore, a complete investigation would require to simulate the adsorption of carbon dioxide in flexible CS1000 as well. But performing such simulations proved to be very expensive computationally, mostly because the simulation of carbon dioxide is much more computationally expensive than that of methane. Therefore, those simulations were not performed.

However, as we did for methane, we back-calculated the coupling coefficient $\widetilde{C}_{\mathrm{CO_2}}(P)$ for carbon dioxide from the immersion experiments of Ottiger et al. (2006, 2008). The results of this calculation

are displayed in Fig. 7.4. For fluid bulk pressures lower than 8 MPa, the values of $\widetilde{C}_{CO_2}(P)$ calculated for a bulk modulus of 2.65 GPa hardly depended on the fluid pressure and were very similar to the values obtained for methane: $\widetilde{C}_{CO_2}(P < 8 \text{ MPa}) = 6.40 \pm 7\%$. But for pressures larger than 8 MPa, the coupling coefficient $\widetilde{C}_{CO_2}(P)$ became pressure dependent and reached a maximum value for a pressure of CO_2 of 10.76 MPa: $\widetilde{C}_{CO_2}(P = 10.76 \text{ MPa}) = 10.53$. At higher pressures, the coupling coefficient $\widetilde{C}_{CO_2}(P)$ decreased back to $\widetilde{C}_{CO_2}(P = 17.66 \text{ MPa}) = 7.03$.

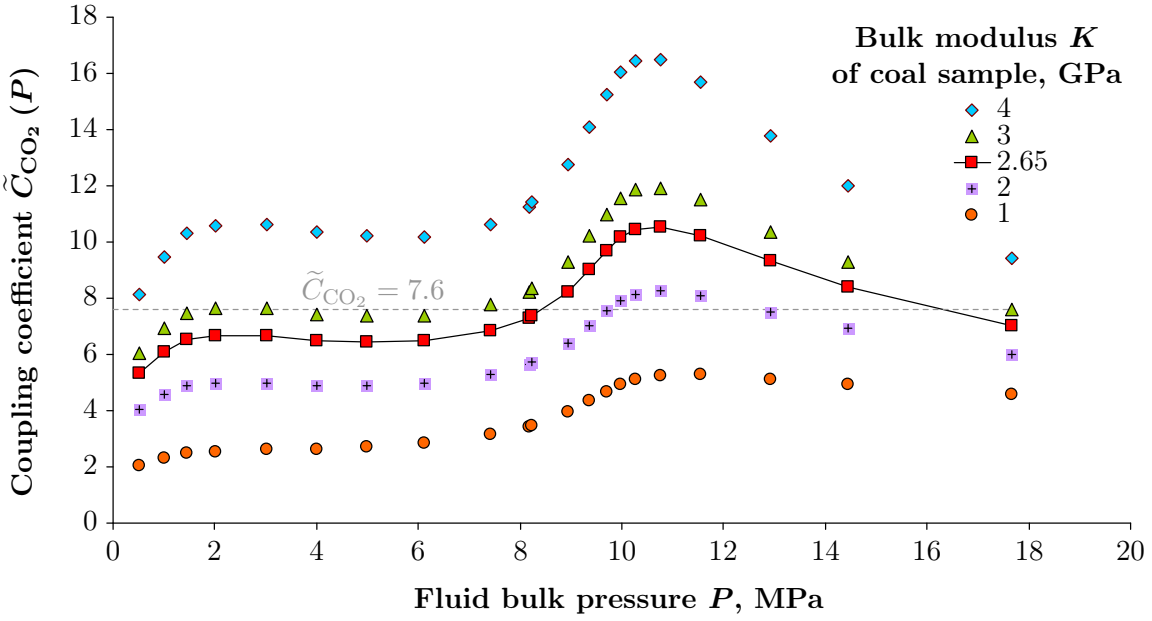

Figure 7.4. *Coupling coefficient $\widetilde{C}_{CO_2}(P)$ for the adsorption of carbon dioxide in coal estimated from the immersion experiments of Ottiger et al. (2006, 2008).*

The fluid pressure at which the coupling coefficient $\widetilde{C}_{CO_2}(P)$ increased sharply corresponds to the pressure at which the bulk density of carbon dioxide increases sharply (Fig. 6.10). The specificity of supercritical carbon dioxide around this pressure is that significant fluctuations of density are observed at the molecular scale: clusters of a few molecules large form. This aggregation is not observed for conditions of temperature and pressure far from the critical point. The size of these clusters can be estimated from scattering and diffraction experiments (Chu and Lin, 1970, Lunacek and Cannell, 1971, Nishikawa et al., 1996, Ishii et al., 1996). From the experimental results of Nishikawa et al. (1996), the maximum size of the clusters for the temperature considered in the experiments of Ottiger et al. (2006, 2008) (318.15 K) is about 10 Å at $P = 10$ MPa, which corresponds to a cluster of 5 or 6 molecules. The aggregation of carbon dioxide molecules is responsible for the multilayer adsorption of carbon dioxide in mesopores (Figs. 6.19 and 6.21). By contrast, the aggregation does not affect the adsorption in the micropores of CS1000, which are too small compared to the characteristic size of a cluster, and which are already filled at a fluid pressure $P = 10$ MPa. Therefore, we interpret the pressure dependence of the coupling coefficient $\widetilde{C}_{CO_2}(P)$ (Fig. 7.4) as due to aggregation of carbon dioxide. When aggregation occurs, adsorption in micropores larger than $10 - 15$ Å and in mesopores increases significantly. As discussed in Sec. 6.5, most of adsorption in coal occurs in micropores and the contribution of adsorption in mesopores is almost negligible. This observation is strictly valid for conditions of temperature and pressure far from the critical point. But adsorption in mesopores might play a significant poromechanical role when aggregation occurs. The pressure dependence of the coupling coefficient $\widetilde{C}_{CO_2}(P)$ could be explained by the fact that, around the critical point, adsorption in pores of intermediate sizes (i.e., mesopores and large micropores) increases significantly and affects the poromechanical behavior of

the medium.

The poromechanical modeling of coal for the adsorption of carbon dioxide should account for the fact that the coupling coefficient $\widetilde{C}_{CO_2}(P)$ for carbon dioxide depends on the fluid pressure. As discussed at the beginning of this section, this dependence on pressure is very small for pressures up to 8 MPa (for which $\widetilde{C}_{CO_2} = 6.40 \pm 7\%$) and varied between $\widetilde{C}_{CO_2} = 6.40$ and $\widetilde{C}_{CO_2} = 10.53$ for higher pressures. As a rough modeling, in what follows, we considered that the constitutive equations (7.2) remain valid to describe the poromechanical behavior of coal saturated with carbon dioxide, in which the coupling coefficient $\widetilde{C}_{CO_2}(P)$ is assumed independent of the pressure. We chose the value $\widetilde{C}_{CO_2} = 7.60$, which is an average value over the range of fluid pressures considered in this study:

$$\begin{aligned} \sigma &= K\epsilon - \widetilde{C}_{CO_2} \int_0^P \widetilde{n}^0_{CO_2} \overline{V}^{bulk}_{CO_2} dP \\ \widetilde{n}_{CO_2} \overline{V}^{bulk}_{CO_2} &= \widetilde{n}_{CO_2}(\epsilon, P)\, \overline{V}^{bulk}_{CO_2}(P) \\ s_{ab} &= 2\overline{G} e_{ab} \end{aligned} \tag{7.6}$$

with $\widetilde{C}_{CO_2} = 7.60$.

7.1.4 Estimation of adsorption-induced swelling with poromechanical model

According to the constitutive equations (7.2), the strain ϵ^u of a coal sample immersed in a fluid is related to the amount $\widetilde{n}^0$ of fluid adsorbed at zero strain:

$$\epsilon^u(P) = -\frac{P}{K} + \frac{\widetilde{C}}{K} \int_0^P \widetilde{n}^0 \overline{V}_{bulk} dP \tag{7.7}$$

By using this equation, we could estimate the swelling of a coal sample immersed in a fluid. For an immersion in methane, we used a coupling coefficient $\widetilde{C}_{CH_4} = 6.05$ (which is the value back-calculated in Sec. 7.1.2) and the adsorption isotherm obtained by molecular simulations on the rigid CS1000 sample (see Sec. 6.4.1 and Fig. 6.15). For an immersion in carbon dioxide, we used a coupling coefficient $\widetilde{C}_{CO_2} = 7.60$ (which is the value back-calculated in Sec. 7.1.3) and the adsorption isotherm obtained by molecular simulations on the rigid CS1000 sample (see Sec. 6.4.1 and Fig. 6.15). For each case, we considered the same bulk modulus $K = 2.65$ GPa for the sample. We display in Fig. 7.5 the results of our calculation together with the measurements performed by Ottiger et al. (2008). The swelling estimated with the poromechanical equation (7.7) together with the adsorption isotherms obtained by molecular simulation is consistent with the experiments. At pressures lower than 2 MPa, the swelling was overestimated for both fluids. Such a discrepancy is due to the fact that the coupling coefficients $\widetilde{C}_{CH_4} = 6.05$ and $\widetilde{C}_{CO_2} = 7.60$ overestimate the actual coupling coefficients in this range of pressure (see Figs. 7.3 and 7.4). At larger fluid pressures, because of the integral form of Eq. (7.7), the initial overestimation is propagated. Nevertheless the swellings estimated with the poromechanical model combined with the simulated adsorption isotherms obtained by molecular simulation and the swellings measured experimentally followed very similar evolutions. Since we observed experimentally that the coupling coefficient $\widetilde{C}_{CO_2}(P)$ for carbon dioxide depends more on the pressure than the coupling coefficient $\widetilde{C}_{CH_4}(P)$ for methane, the comparison with experiment was not as satisfactory for carbon dioxide as for methane.

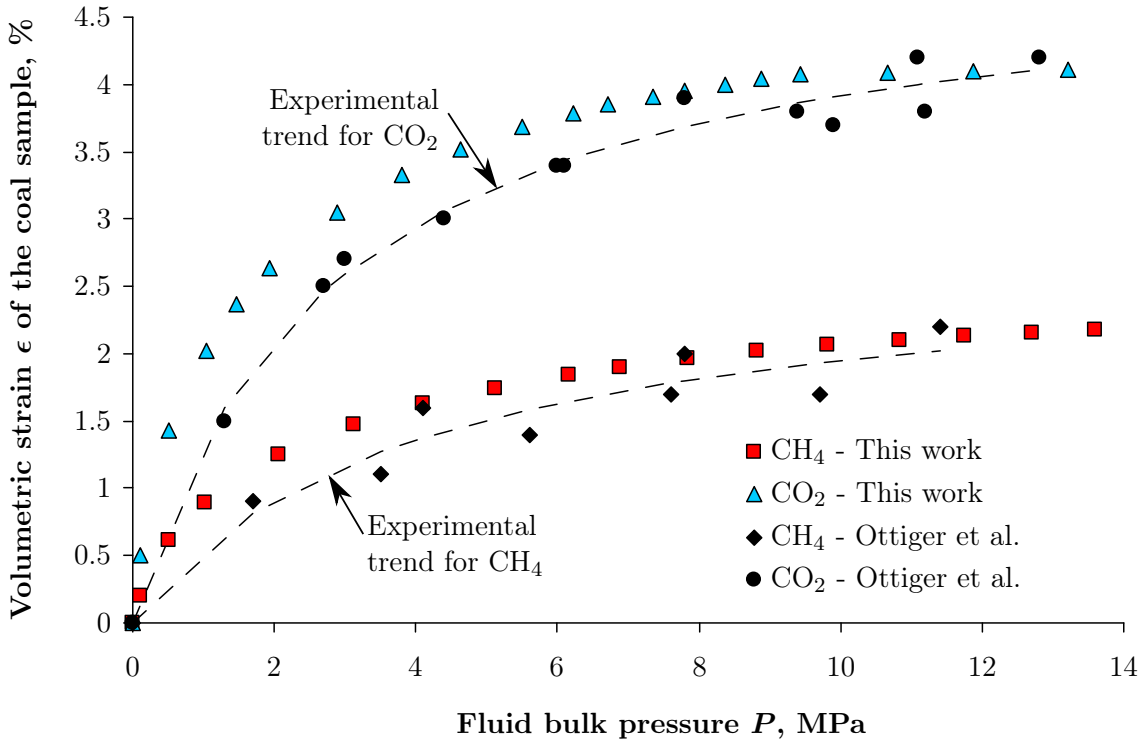

Figure 7.5. *Swelling of a coal sample immersed in a fluid, measured experimentally and estimated with the poromechanical model combined with adsorption isotherms obtained by molecular simulations. The experimental data are from Ottiger et al. (2008).*

7.2 Mechanical behavior of coal under adsorption of multi-component fluid in underground conditions

In an actual coal bed reservoir in which carbon dioxide is injected, the coal matrix is exposed to a mixture of CO_2 and CH_4 whose composition varies. Indeed, during the injection process, CO_2 gradually replaces CH_4. In this section, we aim at determining how coal adsorbs a mixture of CO_2 and CH_4, and how this adsorption of mixture leads to a swelling. In order to estimate adsorption isotherms of the mixture, we employ molecular simulations. The swelling induced by adsorption of the mixture is estimated by combining the poromechanical constitutive equations obtained in Sec. 7.1 with the simulated adsorption isotherms.

In a first approximation, we will consider that, during this process, the temperature and the fluid pressure remain constant and equal to the geothermal temperature and to the hydrostatic pressure, respectively. Such a description is approximative: the temperature may vary with the heat transported by the injected fluid and the fluid is injected at a pressure higher than the pressure that prevails in the reservoir. However, we considered this approximation sufficient for the purpose of our work.

We selected five sets of temperature and pressure that correspond to the following injection site depths: 300 m, 600 m, 900 m, 1200 m, and 1500 m. These depths correspond to the range of injection site depths considered for carbon dioxide sequestration. The corresponding temperatures and pressures are given in Tab. 7.1. The values were obtained by considering an average geothermal gradient of 25°C/km, a surface temperature of 15°C, a hydrostatic pressure gradient and a surface pressure of 101325 Pa. For the pressure gradient, we considered a water density $\rho_{H_2O} = 1000$ kg/m^3 and a gravitational acceleration of $g = 9.81$ m/s^2.

Depth	Temperature, K	Fluid bulk pressure, MPa
300 m	295.7	3.04
600 m	303.2	5.99
900 m	310.7	8.93
1200 m	318.2	11.87
1500 m	325.7	14.82

TABLE 7.1. *Temperature and pressure conditions that prevail in coal bed reservoirs at various depths.*

7.2.1 Simulations of adsorption of carbon dioxide - methane mixture

Prior to the simulation of mixture adsorption, we performed simulations of the CO_2-CH_4 bulk mixture in the isobaric-isothermal ensemble for the five sets of temperature and pressure (see Tab. 7.1) and for mixture compositions ranging from pure methane to pure carbon dioxide. We computed the fugacities of each fluid with the Widom insertion method (Eq. 2.46). The results are displayed in Fig. 7.6. We used these values of fugacities for the adsorption simulations of the mixture in the grand canonical ensemble.

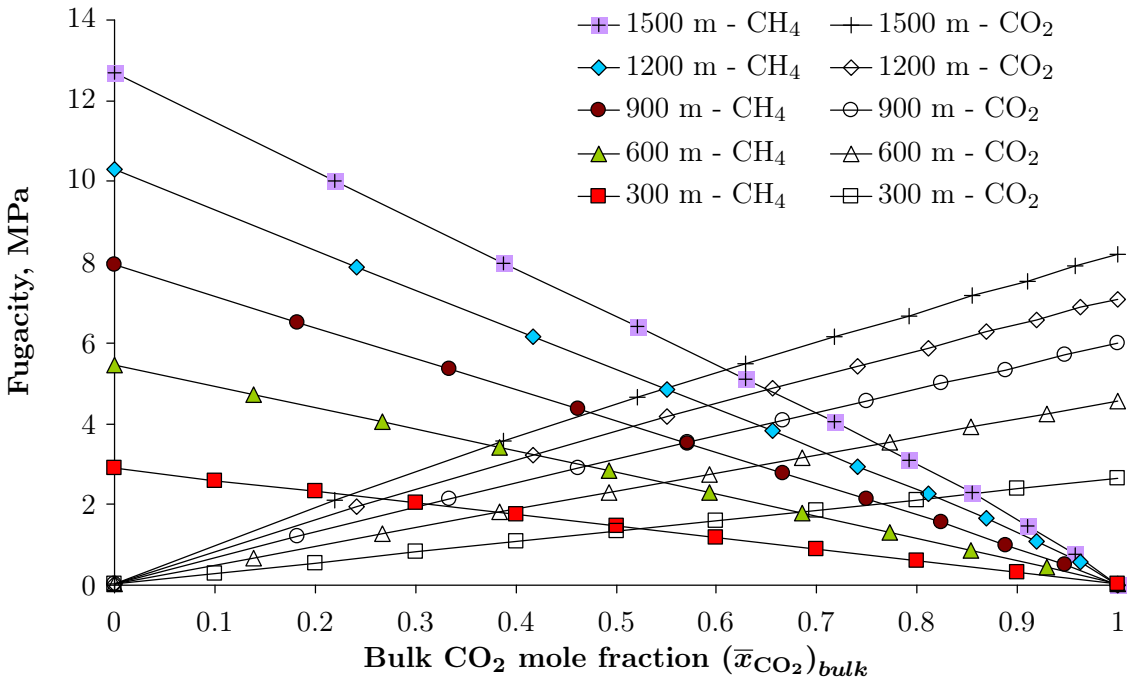

FIGURE 7.6. *Fugacities of methane and carbon dioxide in function of the mixture composition for the various geological depths considered.*

We simulated adsorption of the CO_2-CH_4 mixture in coal micropores by using the CS1000 model displayed in Fig. 6.4. One of the molecular configurations sampled is displayed in Fig. 7.7. The total amount of methane and carbon dioxide in micropores per unit volume of CS1000 was computed and is displayed in Fig. 7.8. As expected, carbon dioxide adsorbed preferentially to methane: the total amount of carbon dioxide in CS1000 exceeded that of methane for a bulk CO_2 mole fraction as small as 0.25. We also observe that the total amounts adsorbed did not evolve significantly with the depth of the injection site considered, although a slight trend could be identified: the amount of adsorbed methane increased slightly with the depth of the site, whereas the amount of adsorbed carbon dioxide decreased slightly.

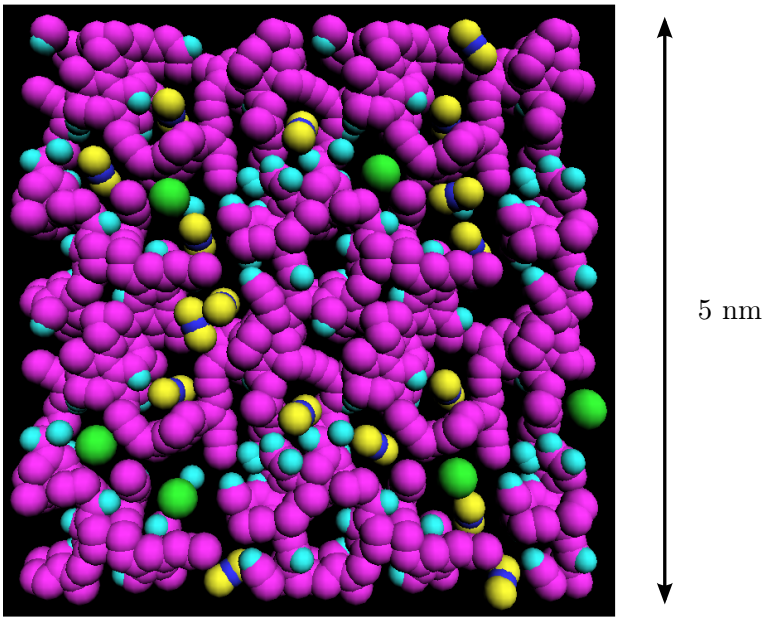

Figure 7.7. *Example of molecular configuration sampled for the adsorption of a mixture of CO_2 and CH_4 in the CS1000 sample. The molecules of CO_2 are in yellow and dark blue, the molecules of CH_4 are in green, the carbon and hydrogen atoms of CS1000 are in pink and light blue.*

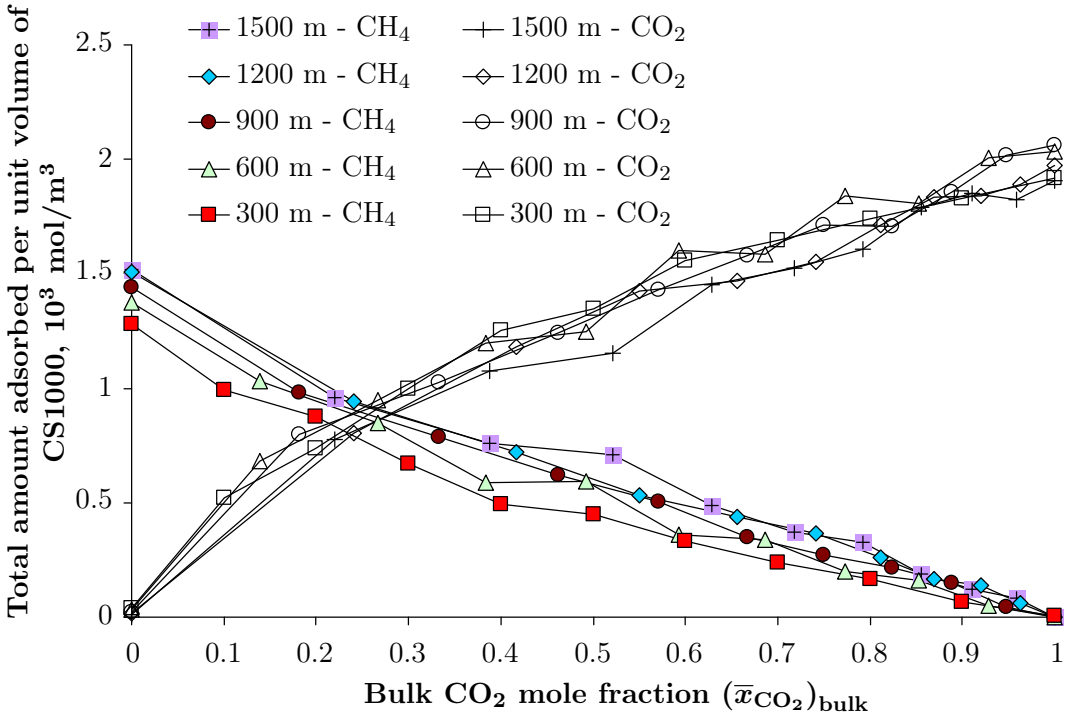

Figure 7.8. *Total amounts of CO_2 and CH_4 adsorbed in a CS1000 sample exposed to a mixture of CO_2-CH_4 for the various geological depths considered.*

The selectivity, also called separation factor, is a criterion to assess the performance of the CS1000 sample to preferentially adsorb carbon dioxide in a mixed CO_2-CH_4 atmosphere. The carbon dioxide selectivity $\overline{S}_{CO_2}$ is defined as (Ruthven, 1984, Ettre, 1993):

$$\overline{S}_{CO_2} = \left(\frac{\overline{x}_{CO_2}}{\overline{x}_{CH_4}}\right)_{CS1000} \Big/ \left(\frac{\overline{x}_{CO_2}}{\overline{x}_{CH_4}}\right)_{bulk} \tag{7.8}$$

where $\overline{x}_{CO_2}$ and $\overline{x}_{CH_4}$ are the mole fractions of carbon dioxide and of methane, respectively. The subscript $\square_{bulk}$ means that the mole fractions are those in the bulk, whereas the subscript $\square_{CS1000}$ means that the mole fractions are those in the CS1000 sample. We calculated the selectivity of carbon dioxide in CS1000: the results are displayed in Fig. 7.9. The selectivity was always greater than unity, meaning that, at all temperatures and pressures here considered, carbon dioxide was adsorbed preferentially to methane. Two trends are observed: the deeper the reservoir considered, the lower the selectivity was; and the higher the CO_2 mole fraction, the lower the selectivity was. The fact that the selectivity decreased with the depth means that, for the same amount of methane recovered, less carbon dioxide is sequestered in deep injection sites than in shallow ones. Therefore, a deep site may appear more interesting for methane recovery; whereas a shallow site seems preferable for carbon sequestration. Note however that such a conclusion is based on the selectivity curves only and does not take into account the kinetic effects due to variations of permeability of the reservoir induced by a potential swelling of the coal matrix.

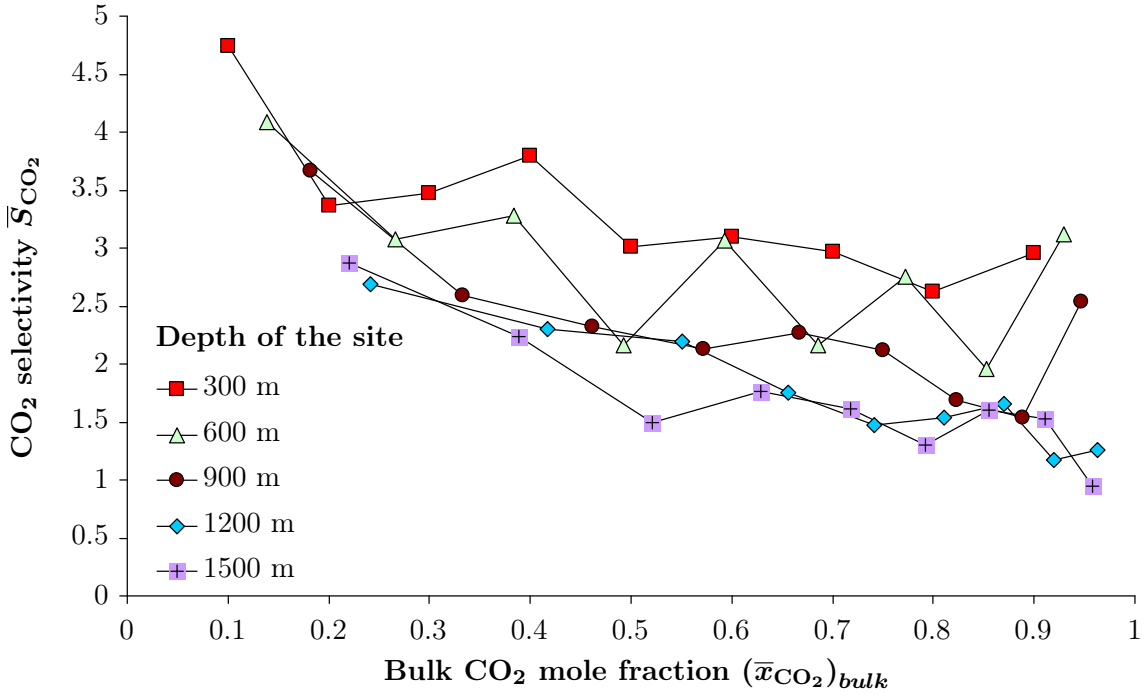

FIGURE 7.9. *Selectivity of CO_2 in the CS1000 sample.*

7.2.2 Comparison with laboratory experiments

Ottiger et al. (2008) performed laboratory experiments of adsorption of mixtures of CO_2 with CH_4 in coal. The amounts measured by Ottiger et al. are amounts in excess of the bulk density. Therefore, we converted the total adsorbed amounts displayed in Fig. 7.8 into excess amounts by considering a porosity of 6% for CS1000 (see Sec. 6.4.1). The excess amounts isotherms obtained

are displayed in Fig. 7.10. The shape of the isotherms was similar to that of the total amount isotherms. The excess amount of adsorbed carbon dioxide was larger than the excess amount of adsorbed methane for bulk CO_2 mole fractions as small as 0.2. The excess amount of adsorbed carbon dioxide decreased with an increasing depth. The excess adsorbed amounts in conditions corresponding to sites at depths of 300 m and 600 m were very close to the total adsorbed amount. However, at the three deeper sites considered, the excess adsorbed amounts were significantly lower than the total adsorbed amounts, because of the high bulk density of carbon dioxide for sites deeper than 800 m (Fig. 1.3).

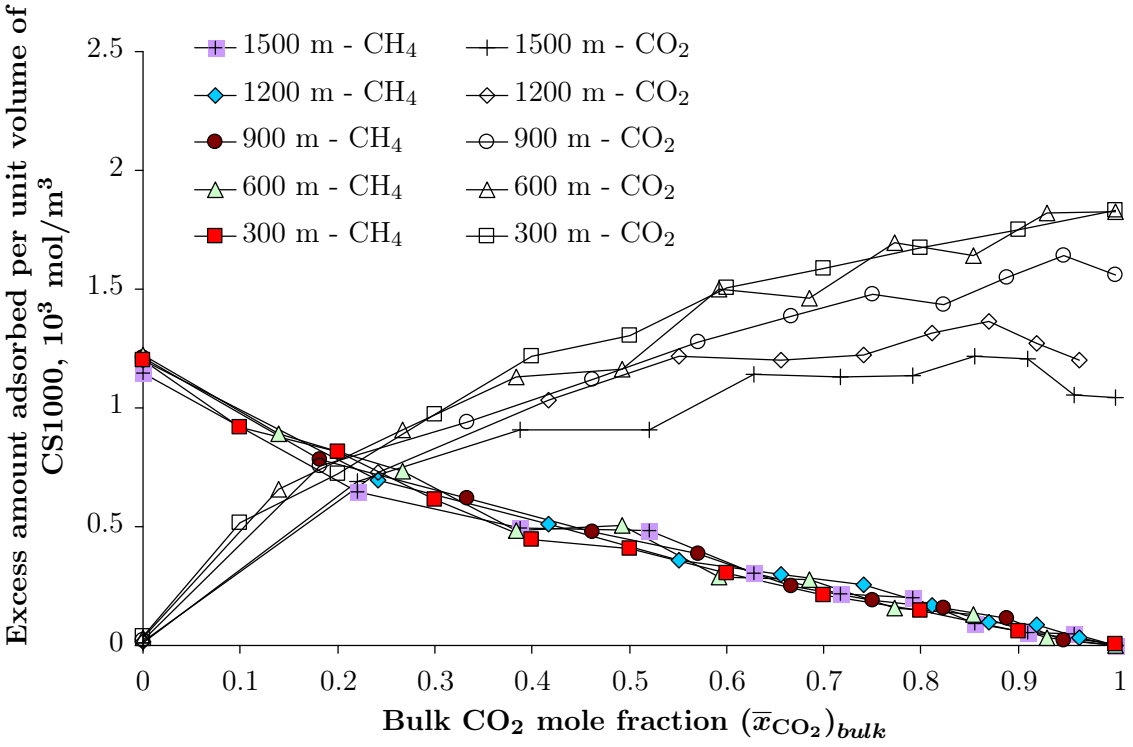

Figure 7.10. *Excess amounts isotherms for the adsorption of the CO_2-CH_4 mixture in CS1000 for the various geological depths considered.*

The experimental isotherms adapted from Ottiger et al. (2008) are displayed in Fig. 7.11. One should note that Ottiger et al. (2008) only varied the pressure of the mixture, while keeping the temperature constant and equal to 318.15 K. The adsorbed amounts at the five pressures we considered were obtained by linearly interpolating the data of Ottiger et al. (2008). In addition, we display in Fig. 7.12 the excess amounts estimated by molecular simulation together with those measured experimentally for sites at depths of 900 m and 1200 m, for which the temperature considered in the simulations and in the experiments are the closest. The comparison of the experimental isotherms with the isotherms computed by molecular simulation is quite satisfactory, although the amounts of methane were overestimated by the molecular simulations, as was the case for pure fluid adsorption (see Sec. 6.4.1). Moreover, the excess amount of adsorbed CO_2 depends less on the pressure of the mixture (i.e., on the depth of the site of injection) experimentally than what could be inferred from the molecular simulations. As discussed in Sec. 6.5, the accessibility of methane to micropores, which is not accounted for in our molecular simulations, could explain why the amounts of adsorbed methane were overestimated in our simulations.

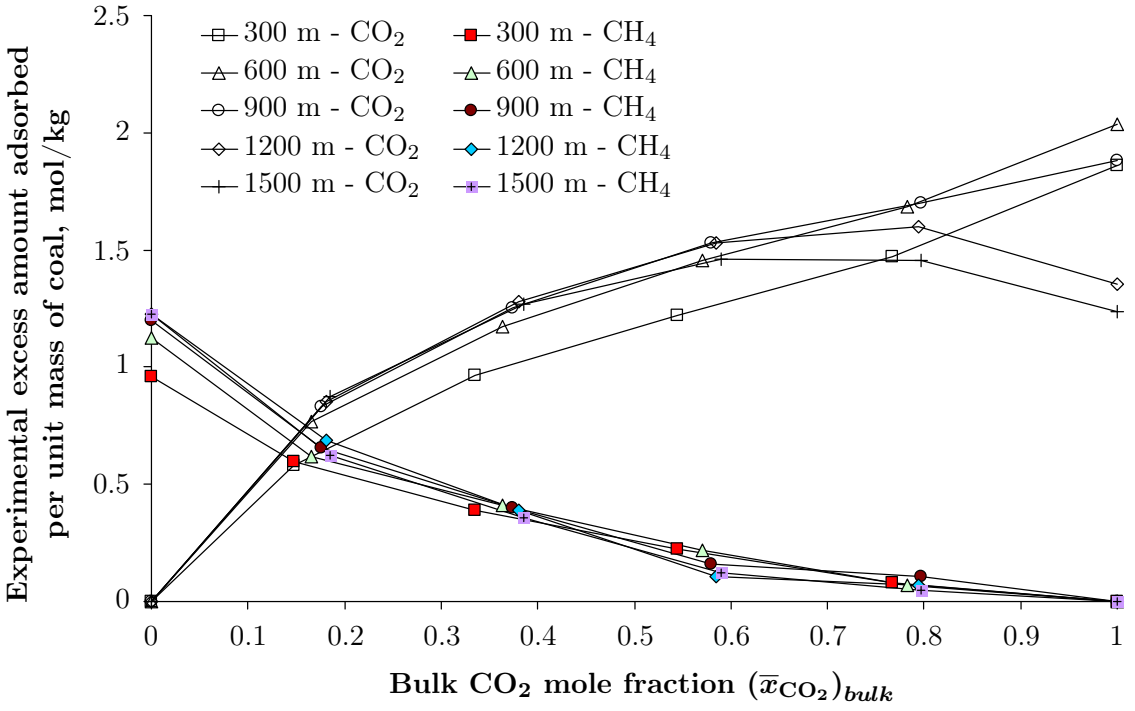

FIGURE 7.11. *Experimental isotherms for the competitive adsorption of the CO_2-CH_4 mixture in coal at the various geological depths considered. Adapted from Ottiger et al. (2008).*

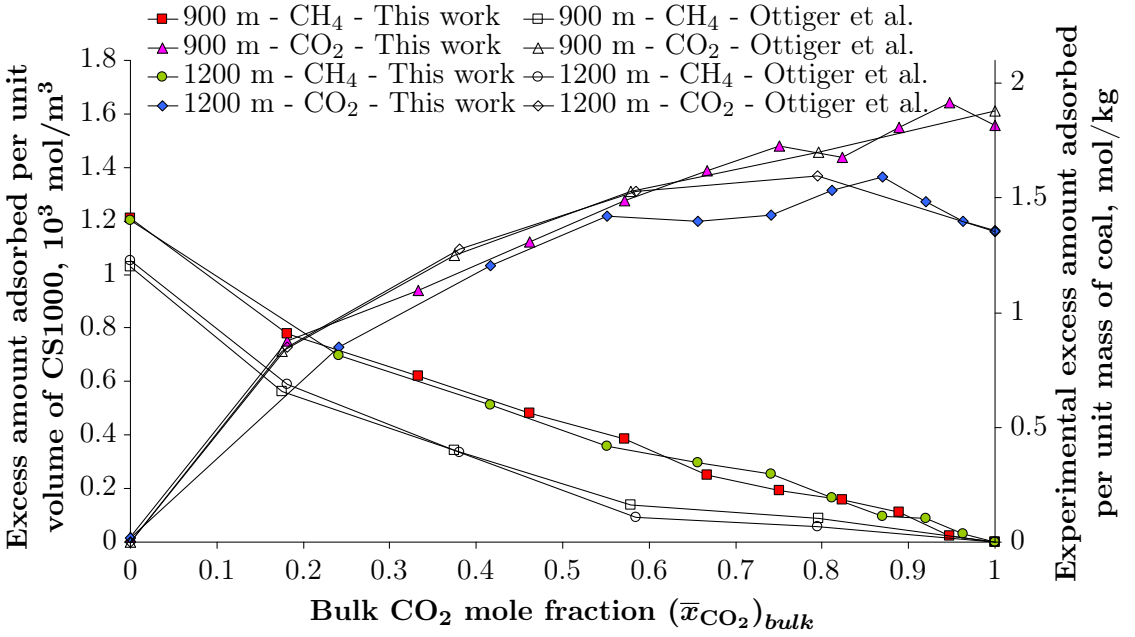

FIGURE 7.12. *Excess amounts adsorbed estimated by molecular simulation and measured experimentally by Ottiger et al. (2008) for the competitive adsorption of the CO_2-CH_4 mixture in coal at two of the geological depths considered.*

7.2.3 Estimation of differential swelling in geological conditions

Using the adsorption isotherms of CO_2-CH_4 mixture obtained by molecular simulations (see Sec. 7.2.1 and Fig. 7.8), we aim at predicting the differential swelling of the coal matrix induced by the progressive replacement of methane with carbon dioxide for sites at the various depths considered. To do so, the poromechanical constitutive equations (7.2) derived in Sec. 7.1 needed to be extended to the case of fluid mixtures. We assumed that the adsorption of the CO_2-CH_4 mixture depends linearly on the strain of the coal matrix with the same coupling coefficients $\widetilde{C}_{CH_4}$ and $\widetilde{C}_{CO_2}$ as for the adsorptions of pure methane and pure carbon dioxide, respectively. Therefore, the first equation of the set of constitutive equations (7.2) becomes:

$$\sigma = K\epsilon - \int_{(-\infty,-\infty)}^{(\mu_{CH_4},\mu_{CO_2})} \left(\widetilde{C}_{CH_4}\widetilde{n}^0_{CH_4}d\mu_{CH_4} + \widetilde{C}_{CO_2}\widetilde{n}^0_{CO_2}d\mu_{CO_2}\right) \tag{7.9}$$

with $\widetilde{C}_{CH_4} = 6.05$ and $\widetilde{C}_{CO_2} = 7.6$. The integration does not depend on the path of integration. At given bulk pressure of the fluid mixture, the replacement of methane with carbon dioxide in coal corresponds to specific values of chemical potentials which depend on the bulk CO_2 mole fraction $(\overline{x}_{CO_2})_{bulk}$. The corresponding fugacities are displayed in Fig. 7.6. Comparing a coal sample exposed to a mixture of CO_2 and CH_4 with a coal sample exposed to a fluid at the same pressure as the mixture but made of pure methane, the variation $\Delta\sigma$ of volumetric stress, the variation $\Delta\epsilon$ of volumetric strain and the adsorbed amounts are related according to:

$$\Delta\sigma = K\Delta\epsilon - \int_{\left(\mu^{pure}_{CH_4},-\infty\right)}^{\left(\mu_{CH_4}(\overline{x}_{CO_2}),\mu_{CO_2}(\overline{x}_{CO_2})\right)} \left(\widetilde{C}_{CH_4}\widetilde{n}^0_{CH_4}d\mu_{CH_4} + \widetilde{C}_{CO_2}\widetilde{n}^0_{CO_2}d\mu_{CO_2}\right) \tag{7.10}$$

The so-called differential swelling ϵ_{diff} is the variation of volumetric strain when the volumetric stress is constant (i.e., when $\Delta\sigma = 0$). This differential swelling is not the swelling that would be observed in situ, since in a coal bed reservoir the coal matrix is not free to swell. Nevertheless, the differential swelling quantifies the mechanical effect induced by adsorption. From Eq. (7.10), the differential swelling ϵ_{diff} can be expressed as:

$$\epsilon_{diff} = \frac{1}{K}\int_{\left(\mu^{pure}_{CH_4},-\infty\right)}^{\left(\mu_{CH_4}(\overline{x}_{CO_2}),\mu_{CO_2}(\overline{x}_{CO_2})\right)} \left(\widetilde{C}_{CH_4}\widetilde{n}^0_{CH_4}d\mu_{CH_4} + \widetilde{C}_{CO_2}\widetilde{n}^0_{CO_2}d\mu_{CO_2}\right) \tag{7.11}$$

The amounts $\widetilde{n}^0_{CH_4}(\mu_{CH_4},\mu_{CO_2})$ of adsorbed methane and $\widetilde{n}^0_{CO_2}(\mu_{CH_4},\mu_{CO_2})$ of adsorbed carbon dioxide are known from the adsorption simulations performed in Sec. 7.2.1 (see Fig. 7.8). Using Eq. (7.11), we estimated the differential swelling of the coal matrix consecutive to a progressive replacement of methane with carbon dioxide. We display in Fig. 7.13 the differential swelling estimated for coal beds in sites at various depths. The strain depended concavely on the bulk CO_2 mole fraction: almost half of all the differential swelling was achieved for a bulk CO_2 mole fraction of 0.2. According to this result, the differential swelling occurs at the early stage of the injection process. The differential swelling was mostly independent of the injection site depth, although for bulk CO_2 mole fractions below 0.7 the differential swelling was smaller at the shallowest sites considered, while for bulk CO_2 mole fractions above 0.8 the differential swelling was smaller at the deepest sites considered.

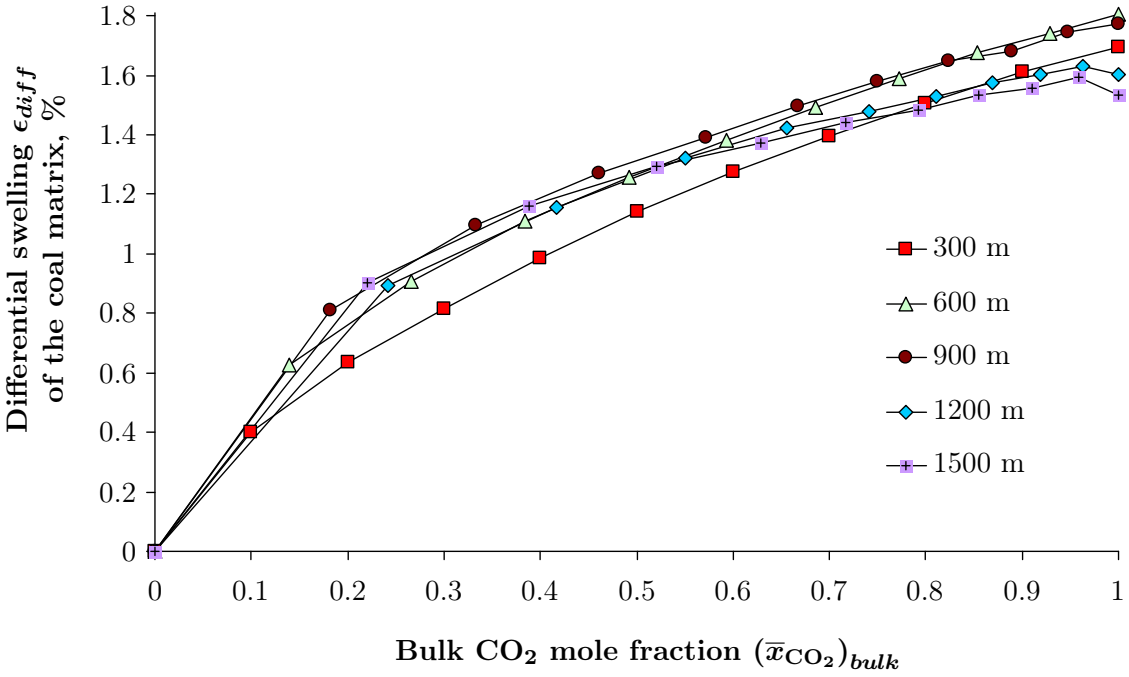

FIGURE 7.13. *Differential swelling of the coal matrix estimated for the different site depths considered.*

We display in Fig. 7.14 the estimated differential swelling in function of the CO_2 mole fraction in CS1000: The differential swelling was almost proportional to the CO_2 mole fraction in CS1000. The swelling in conditions corresponding to a site depth of 300 m was slightly lower than for conditions corresponding to sites at other depths, except for $(\overline{x}_{CO_2})_{CS1000} > 0.9$. In practice, for field application, this proportional relationship between differential swelling and CO_2 mole fraction in coal could help to estimate quickly the differential swelling of the coal matrix.

7.3 Discussion and perspectives

In Secs. 7.1 and 7.2, we combined molecular simulations of adsorption in coal with poromechanical constitutive equations extended to microporous solids in order to explain the adsorption-induced swelling of coal and estimate the differential swelling that would occur at conditions of temperature and pressure representative of injection sites at various depths. However, several aspects of our approach may be discussed. Such a discussion is the focus of this section.

7.3.1 Assumptions of the poromechanical model extended to microporous solids

The poromechanical model that we developed for microporous solids relies on several assumptions, which we summarize and discuss in this section.

The poromechanical equations (4.44) were derived assuming an isotropic porous medium, which implies that these equations are unable to capture the anisotropy of the adsorption-induced swelling of coal observed experimentally (see Fig. 6.3). Our derivation could be adapted to account for anisotropic materials, for which the amount $\widetilde{n}$ of adsorbed fluid molecules per unit undeformed volume of the porous medium may depend not only on the volumetric strain but also on the deviatoric strain, and for which the mechanical properties of the solid skeleton also are anisotropic.

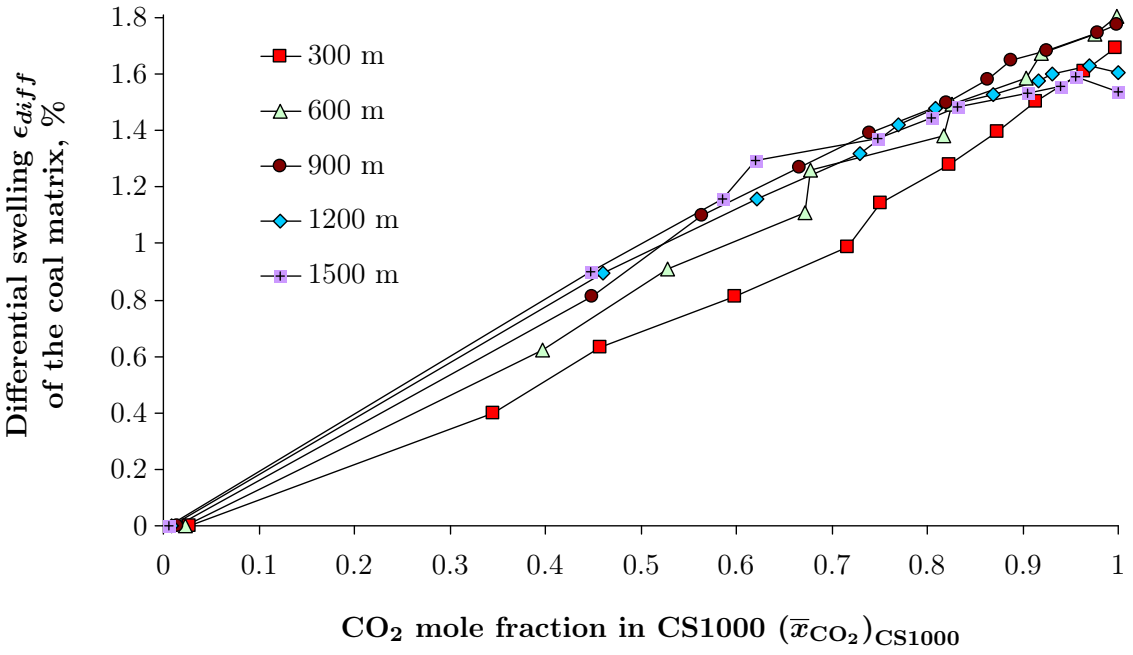

Figure 7.14. *Differential swelling of the coal matrix in function of the CO_2 mole fraction in CS1000.*

Applying such constitutive equations practically would require to know how adsorption depends not only on the volumetric strain but also on other components of the strain tensor. Therefore, accounting for the anisotropy would make the problem significantly more complex. Moreover, the CS1000 molecular structure would not be adapted to such a study since CS1000 is isotropic. On the other hand, it may well be that the anisotropy observed at the scale of the reservoir does not originate from the coal matrix, but from the anisotropic cleat system or from the layered microsctructure.

In our derivation of the poromechanical model, we only considered reversible adsorption: we assumed no hysteresis in the adsorption and the desorption processes. However, adsorption of carbon dioxide and methane in coal may present hystereses (Busch et al., 2003, Ozdemir et al., 2004, Bae et al., 2009). The observed hystereses are generally small. Moreover, their physical origin is unclear. Potential origins for such hystereses are: chemical adsorption, constricted diffusion, insufficient equilibration of the samples... Other experimental studies did not report any hysteresis (for instance Levine (1996) and Ottiger et al. (2006)). Therefore, neglecting the hysteresis of adsorption seems a reasonable assumption.

We assumed that the mechanical behavior of the solid skeleton was elastic. However, the plasticization of coal (see Sec. 6.1) can induce non-elastic behaviors. Regarding plasticization, only adsorption of carbon dioxide at pressures larger than 3 MPa and temperatures larger than 330 K may induce plasticization (Larsen, 2004). In our work, the largest temperature considered was 325.7 K, which is lower than the temperature threshold for plasticization. Nevertheless, the temperature at injection sites may well exceed 330 K. In such cases, the effect of plasticization can no more be neglected and our model should be modified.

We considered that the solid skeleton was not altered during injection. But, in field applications, the injection of carbon dioxide at high pressures may trigger fracturation. Moreover, while the adsorptions of carbon dioxide and methane in coal are generally considered to be physical, the very first molecules of adsorbed carbon dioxide might be chemically bonded (Mirzaeian and Hall,

2006). Those two phenomena may modify the elastic properties of the skeleton and the transport properties of the coal matrix.

Finally, we neglected how the coupling coefficient $\widetilde{C}_{CO_2}(P)$ for carbon dioxide depends on the bulk fluid pressure, whereas experimental results show that this coefficient varies near the critical pressure of carbon dioxide (see Sec. 7.1.3). Our approximation gives satisfactory results at a temperature of 318.15 K for what concerns the swelling of an immersed sample (see Fig. 7.5), but the coupling coefficient $\widetilde{C}_{CO_2}$ should nevertheless be adjusted in function of the temperature and pressure considered. The singular behavior of a supercritical fluid near its critical point may explain the fact that $\widetilde{C}_{CO_2}(P)$ depends significantly on the pressure of the fluid: this singular behavior is indeed very sensitive to conditions of temperature and pressure near the critical point. In Sec. 7.2.3, we used a pressure-independent coupling coefficient $\widetilde{C}_{CO_2}$ to predict the differential swelling at various site depths. This approximation is questionable, especially at a depth of 900m, at which the temperature and pressure are the closest to the critical point of carbon dioxide.

7.3.2 Reliability of the molecular modeling

A second aspect which is important to discuss is the reliability of the molecular modeling of adsorption in coal. This modeling is very convenient to distinguish adsorption in micropores and in mesopores or to explore how adsorption depends on both the strain and the fluid pressure, but it only remains a model. As such, the results of the molecular simulations are not results of laboratory experiments and must be used with caution. In this section, we discuss the main approximations of our molecular modeling.

We did not account for the accessibility of methane and carbon dioxide to the micropores of CS1000. In Chap. 6, we attributed most of the discrepancy between the adsorption isotherms estimated by molecular simulation and those measured experimentally to the question of accessibility. How carbon dioxide and methane molecules diffuse in the coal matrix and have access to the micropores could be explained by activated diffusion, as discussed in Sec. 6.5. The activated diffusion cannot be simulated by Monte Carlo simulation, since the Metropolis algorithm does not predict the evolution of a molecular system over time. Molecular dynamics does, but is limited to very short time scales (on the order of 1 ns), which may be insufficient since the rate of diffusion in the coal matrix is low. Metadynamics (Laio and Parrinello, 2002) could be an alternative technique to reach larger time scales.

The CS1000 model, which is $25 \times 25 \times 25$ Å^3 large, is too small to be representative of all the morphologies and sizes of pores in natural coal. How adsorption in rigid CS1000 depends on the pressure was satisfactorily predicted (see Sec. 6.4). But how adsorption depends on strain may be much more sensitive to the sizes and morphologies of the pores, as was the case for the one-dimensional solids studied in Chap. 5. Since no experimental data exists for the dependency of adsorption on strain in coal, we are unable to fully validate the dependence of adsorption on strain that we simulated (Fig. 7.1).

As discussed in Sec. 6.1, the characteristics of coal vary widely from one coal to the other and no single molecular model can be representative of all types of coal. We considered one molecular modeling (i.e., the CS1000 model), which was validated with one set of experimental data for a specific coal from the Sulcis coal province (Ottiger et al., 2006, 2008). A more thorough validation of our approach would require to check its repeatability by considering other sets of experimental data and other molecular models of microporous carbon.

Finally, like any model, our molecular modeling is perfectible:

- The PEOE method we used to determine the distribution of effective point charges in CS1000 (Sec. 6.3.3) only provided a rough estimate of this distribution, as we showed by comparison with the results of the Qeq method.
- The potentials of interaction between the atoms of CS1000 are a rough approximation of the actual interactions between atoms in coal. In particular, the interaction between carbon atoms was modeled with a potential valid for hybridized sp^2 carbon atoms like in graphite. A better modeling would require to distinguish the different types of carbon atoms and use a potential that would distinguish the different atomic orbitals, while being representative of the elastic behavior of natural coal.
- The absence of oxygen in CS1000 is an important limitation of this model. In particular, the adsorption of water, which is a polar molecule, could not be simulated reliably with such a model. In the recent development of the reactive potential REBO used to reconstruct the CS1000 model, the oxygen atoms were included, which makes it possible to obtain molecular models that are more representative of the actual chemical heterogeneity in coal.

7.3.3 Other factors influencing adsorption-induced swelling of coal during ECBM

Several factors, which may affect the swelling of coal, were not studied in our work and could be interesting research topics in the future.

Liquid water is commonly present in coal seams and is known to affect the injection process. At the scale of the coal matrix, water molecules are adsorbed in micropores only on hydrophilic sites (White et al., 2005). Therefore, water contributes to the adsorption-induced swelling of coal. Moreover, the access to the micropores and the amount of stored carbon dioxide are reduced in presence of water. We did not consider the effect of the presence of water on the differential swelling of coal, but, for field application, this effect cannot be ignored. At the scale of the cleat network, water reduces the apparent permeability of the coal reservoir to carbon dioxide. Indeed, liquid water is not miscible with pure carbon dioxide and thus restrains the flow of carbon dioxide inside the cleats. In addition, carbon dioxide molecules can dissolve in liquid water, which increases the acidity, thus inducing chemical reactions with the mineral matter in coal (Massarotto et al., 2010). Moreover, the dissolved CO_2 can be transported away from the coal seam, which is a potential leakage route (White et al., 2005). These other impacts of water should be assessed as well.

We also did not consider the presence of nitrogen. Nitrogen can indeed be injected into coal seams along with carbon dioxide, as is the case for flue gas-ECBM (see Sec. 1.2.1). Nitrogen is adsorbed in coal, but the affinity of nitrogen for coal is lower than that of carbon dioxide and methane (Fitzgerald et al., 2005). Therefore, the competitive adsorption of a CO_2-CH_4-N_2 mixture should induce a swelling which differs from the swelling induced by a CO_2-CH_4 mixture. Therefore, in the perspective of flue gas-ECBM, the effect of nitrogen should be studied.

Plasticization of coal (see Sec. 6.1), which corresponds to structural rearrangements within the molecular structure of the coal matrix, usually occurs at temperatures larger than 700 K. The adsorption of CO_2 induces plasticization at temperatures near 330K and pressures larger than 3 MPa (Larsen, 2004). Such temperatures and pressures may be encountered in many injection sites. How plasticization impacts the mechanical behavior of the coal matrix and thus affects the adsorption-induced swelling of coal should be assessed in detail.

7.3.4 Perspective: reservoir simulation

The model we developed enables to estimate the strain of the coal matrix when subjected to a confining stress and to an adsorption of a CO_2-CH_4 mixture of given bulk composition and bulk pressure. As such, the model we developed cannot be used to model the behavior of an entire coal reservoir. Our model must first be upscaled at the scale of the representative elementary volume of fractured coal, i.e., at a scale at which cleats enter the picture; the upscaled model must then be implemented together with a relevant permeability model for fractured media in a code simulating an entire geological site (Fig. 7.15). How differential swelling impacts the permeability of the coal bed is a complex issue, which depends not only on the amplitude of the differential swelling, but also on the mechanical constraints at the boundary of the coal bed, on the size and morphology of the cleats, on the stress and strain distribution inside the coal bed, and so on. The injectivity rebound observed at the Allison unit injection pilot (see Fig. 1.5) shows that the evolutions of permeability over time are nontrivial: indeed the permeability does not evolve monotonically with time.

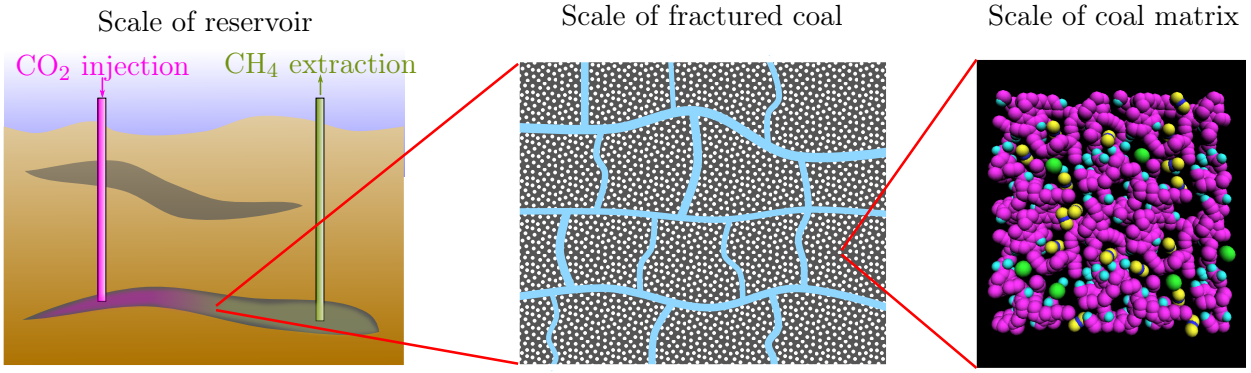

FIGURE 7.15. *The simulation of a reservoir involves three different scales.*

In order to illustrate the complex relation between differential swelling and permeablity, we considered a very simple situation: a sample of fractured coal is held at zero strain and we assume that all differential swelling of the coal matrix contributes to the closure of the cleat network:

$$\Delta\phi^{cleats} = \left(1 - \phi_0^{cleats}\right) \epsilon_{diff} \tag{7.12}$$

where $\Delta\phi^{cleats} = \phi^{cleats} - \phi_{ini}^{cleats}$ is the variation of porosity of the cleats due to the differential swelling ϵ_{diff} given by Eq. (7.11) and ϕ_0^{cleats} is the porosity of the cleats at zero stress and zero bulk pressure.

The porosity of the cleats before injection is a decreasing function of the site depth, since the opposite of the confining stress σ increases more with the depth z than the pore pressure P in the cleats. Assuming an incompressible solid matrix, we obtain:

$$\phi_{ini}^{cleats}(z) = \phi_0^{cleats} + \frac{\sigma(z) + P(z)}{K} \tag{7.13}$$

Considering a hydrostatic fluid pressure gradient of 10 kPa/m and a gradient for the confining stress of -25 kPa/m, a reference cleat porosity of $\phi_0^{cleats} = 4\%$, a bulk modulus of $K = 1$ GPa, and using the differential swelling which we estimated and display in Fig. 7.13, we computed the cleat porosity in function of the composition of the CO_2-CH_4 mixture for sites at various depths. In

addition, assuming that the permeability of the fractured coal sample depends on the cleat porosity ϕ^{cleats} according to the Kozeny-Carman relationship ($\kappa \propto \left(\phi^{cleats}\right)^3 \Big/ \left(1-\phi^{cleats}\right)^2$), we estimated how the permeability of a constrained fractured coal sample evolves with the composition of the fluid mixture. The results are displayed in Fig. 7.16. How the permeability of the fractured coal sample depends on the composition of the mixture is very sensitive to the depth: the deeper the injection site, the larger the loss of permeability. By constrast, the differential swellings we estimated in Sec. 7.2.3 were almost insensitive to the depth. Therefore, the relation between permeability and differential swelling needs to be studied carefully.

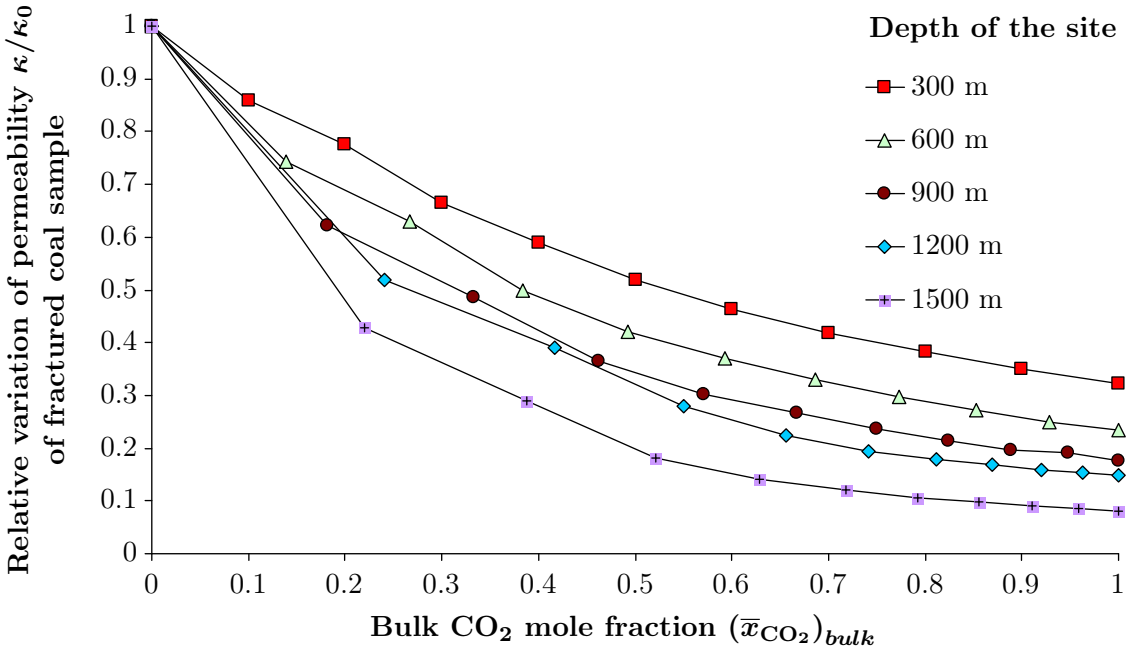

Figure 7.16. *Relative variation of permeability of fractured coal sample in function of the composition of the CO_2-CH_4 mixture for injection sites at various depths.*

Conclusions (en)

The differential swelling of coal during the geological storage of carbon in coal seams hinders the development of this type of carbon storage at an industrial scale. In this thesis, we studied this swelling by combining an extension of poromechanics to microporous solids with molecular simulations of adsorption in the coal matrix. On a theoretical level, this work led us to better understand how adsorption can lead a porous solid to deform. On a practical level, we derived constitutive equations well-suited for the modeling of carbon storage in coal seams and estimated numerically the adsorption of carbon dioxide, methane, and their mixtures in coal.

The swelling of the coal matrix during carbon storage originates from the preferential adsorption of carbon dioxide in coal over the methane in place in the seams. Adsorption (i.e., a variation of the concentration of fluid in the vicinity of a solid) can induce deformations of the adsorbent: in addition to the CO_2-induced swelling of coal, the water-induced dimensional changes of wood and the swelling of clays are other examples of adsorption-induced strain. The coupling between the strain of a porous solid and adsorption is often neglected: adsorption is generally studied in function of the bulk pressure of the fluid only. In this thesis, a first theoretical work consisted in taking into account the coupling between adsorption and deformation by extending the constitutive equations of poromechanics to cases in which adsorption on surfaces or in micropores is significant. The poromechanical behavior of the medium depends not only on the bulk pressure of the fluid (as is correctly captured by classical poromechanics) but also on its composition: such dependence explains on a theoretical level why the replacement of methane by carbon dioxide can make coal swell.

The derived poromechanical equations are valid independent of the state of the fluid in the pores (bulk, adsorbed on surfaces, or adsorbed in micropores). Therefore, these equations apply to a generic porous medium. An analysis of these equations shows that the mechanical effect of the fluid is closely related to the amount of adsorbed fluid molecules per unit undeformed volume and in particular to how this quantity depends on the strain of the medium. Since most models of adsorption do not take explicitly into account the dependence on strain, it is not possible to estimate a priori how adsorption will modify the mechanical behavior of a solid. In order to make this estimation possible, the coupling between adsorption and strain needs to be studied first. However, studying this coupling experimentally requires very specific setups, since one needs to control independently the bulk pressure of the pore fluid and the confining stress applied to the solid. Moreover, all strains (in particular tensile strains) are not accessible by experimentation. In this thesis, we used molecular simulation, which consists in modeling matter numerically at the scale of the atoms and molecules. Molecular simulation is an investigation tool which interestingly complements laboratory experiments, by making it possible to investigate adsorption in mesopores and in micropores separately and to apply any strain to the medium.

A significant part of this PhD thesis was dedicated to the study of model one-dimensional mi-

croporous solids by molecular simulation. We verified the validity of the derived poromechanical equations on those model systems, on which we also investigated the coupling between adsorption and strain. This numerical study improved our understanding of this coupling: when all micropores are identical, the adsorption depends on the strain in a complex manner because of the commensurability of the size of the pores to the size of the fluid molecules. For such a solid, depending on the conditions, adsorption can induce shrinkage or swelling. By contrast, when the sizes of the pores are uniformly distributed, the adsorbed amount of fluid depends linearly on the strain and the fluid induces a disjoining effect for any strain of the medium. Therefore, a disordered solid with micropores of random sizes exhibits a relatively simple macroscopic poromechanical behavior. Even though these results are derived from the study of one-dimensional model systems, they give a first hint as to the coupling between mechanics and adsorption in microporous solids.

In order to apply the derived poromechanical equations to carbon storage in coal, one needs to know how the adsorption of methane and carbon dioxide evolves in function of the chemical potentials of both species and in function of the strain of the coal sample. With this aim in mind, we performed molecular simulations of adsorption in a realistic molecular model of the organic matrix of coal. The validity of the molecular modeling is assessed by comparing the isotherms estimated by molecular simulation to those measured experimentally. The results of the simulations showed that the amount of adsorbed fluid in coal depends linearly of the volumetric strain, which is confirmed by inverse analysis of immersion experiments. Since the organic matrix of coal is almost amorphous, this result is consistent with the results of the molecular simulations of one-dimensional solids. The adsorption of carbon dioxide exhibits a peculiarity at temperatures and pressures close to the critical point, which could be explained by molecular aggregation. What was observed for carbon dioxide suggests that liquid-gas phase changes can significantly modify the coupling between adsorption and mechanics. In this thesis, phase changes were not considered since carbon dioxide and methane are gaseous or supercritical in geological conditions. This is however a question of interest for other fluids and in particular for water.

In a final part, we applied the derived poromechanical equations to coal by using the adsorption isotherms estimated by molecular simulation for carbon dioxide, methane, and their mixture. The swelling estimated for coal samples immersed in pure methane and pure carbon dioxide compared well with the swelling measured experimentally. The same approach was then used to estimate the differential swelling during the progressive replacement of methane by carbon dioxide, at temperatures and pressures corresponding to coal seams at various depths. Our modeling is in itself restricted to the scale of the coal matrix and should therefore be considered as a necessary first elementary step toward modeling a whole coal seam.

The main contributions of this work are theoretical on one hand and applied on the other hand. Regarding theory, the constitutive equations we derived are general and apply to any situation where a fluid is adsorbed in a porous material in absence of irreversibility. The main contribution of this extension of poromechanics is to overcome the reference to any notion of porosity or specific surface and to consider only well defined quantities even for microporous media. The use of these equations is difficult because it is necessary to know how adsorption depends on the pressure of the fluid and on the deformation independently. We focused on the specific case of supercritical fluids in amorphous materials for which we highlighted a linear dependency between adsorption and strain. As is the case for methane and carbon dioxide adsorbed in coal, this specific behavior is likely to apply to disordered nanoporous carbons in general. However, such a behavior is not valid when a porous material has an ordered structure, or when the fluid exhibits a phase change. What is the adsorption behavior in these situations and how the constitutive equations are impacted are

research orientations to further study. The poromechanical framework developed in this thesis do not account for the irreversibilities such as adsorption hysteresis, plasticity or chemi-sorption. In order to account for these irreversibilities, it is necessary to introduce new appropriate macroscopic state parameters. In this thesis, we limited our derivation to an elementary combination of state parameters. The extension to more complex combination is a promising subject of research.

Regarding application, we developed a modeling of the poromechanical behavior of coal during the geological storage of carbon dioxide. In dry conditions, i.e., in absence of water, and for injection sites deeper than 200 m, this modeling gives relevant estimations with an accuracy of $\pm 15\%$. The strength of this modeling stems from the physics behind. Only one parameter was calibrated in our modeling: the bulk modulus of coal. Therefore this modeling is a significant improvement compared to the previous modeling, mostly empirical and involving a lot of parameters to calibrate. This approach can be considered robust and transferable from one coal to the other. In order to apply this modeling, the coupling coefficient for the coal considered must be determined first, for instance by inverse analysis of immersion experiments. For shallow injection sites (< 200 m), however, our modeling our modeling is not reliable since the poromechanical model overestimates the adsorption-induced swelling at low pressures ($P < 2$ MPa). The major drawback for field application is the fact that this model does not account for the presence of water, whereas in most cases, coal beds are filled with water. Accounting for water in the molecular simulation requires first to use a molecular model of the coal matrix including oxygen atoms, in order to have more realistic electrostatic interactions which are critical for a polar molecule such as water. A second step is to include the notion of saturation in the poromechanical model since water and carbon dioxide are non miscible. The extension to the presence of water is a challenging research direction. Beyond the differential swelling of coal, the quantity of interest is the loss of permeability of the coal reservoir induced by the swelling. How the swelling impacts the permeability needs to be studied in detail.

We hope that this work will be useful for those aiming at modeling or developing carbon storage and for those interested in microporous materials in general.

Conclusions (fr)

Le gonflement différentiel du charbon lors de la séquestration géologique du carbone est un obstacle au déploiement industriel de ce type de stockage de carbone. Dans cette thèse, nous avons étudié ce phénomène de gonflement en associant la théorie poromécanique étendue aux solides microporeux à des simulations moléculaires d'adsorption dans la matrice de charbon. Sur un plan théorique, ce travail nous a permis de mieux comprendre comment l'adsorption peut induire la déformation d'un solide poreux. Sur le plan applicatif, nous avons dérivé des équations constitutives adaptées à la modélisation de la séquestration du carbone dans des veines de charbon et nous avons estimé numériquement l'adsorption du dioxyde de carbone, du méthane et de leur mélange dans le charbon.

Le phénomène de gonflement du charbon lors du stockage de carbone a pour origine l'adsorption préférentielle du dioxyde de carbone dans le charbon par rapport au méthane présent naturellement dans les veines. L'adsorption (c'est à dire la variation de concentration de fluide près d'un solide) peut induire des déformations mécaniques de l'adsorbant: Au delà du gonflement du charbon induit par le CO_2, le travail du bois et le gonflement des argiles sont d'autres exemples de déformations induites par l'adsorption. Le couplage entre la déformation d'un solide poreux et l'adsorption est souvent négligé: l'adsorption est généralement étudiée en fonction de la pression du fluide uniquement. Dans cette thèse, un premier travail théorique a consisté à coupler adsorption et déformation en étendant les équations constitutives de poromécanique à l'adsorption de surface ou dans des micropores. Le comportement mécanique du milieu poreux ne dépend plus seulement de la pression du fluide, comme en poromécanique classique, mais aussi de sa composition; ce qui explique, sur le plan théorique, pourquoi le charbon peut gonfler lorsque le méthane est remplacé par du dioxyde de carbone.

Les nouvelles équations poromécaniques sont valides quelque soit l'état du fluide dans les pores (bulk, adsorbé sur des surface, ou adsorbé dans des micropores). Ces équations sont donc valides pour un milieu poreux quelconque. Une conséquence importante de ces équations est que l'effet du fluide sur la mécanique est étroitement lié à la quantité de fluide adsorbé par unité de volume non déformé et en particulier comment cette quantité dépend de la déformation du milieu poreux. Comme la plupart des modèles d'adsorption ne tiennent pas compte de la déformation, il n'est pas possible d'estimer a priori comment l'adsorption affectera le comportement mécanique d'un solide. Afin de rendre possible cette estimation, le couplage entre adsorption et déformation doit d'abord être étudié. Cependant, sur le plan expérimental, l'étude du couplage entre adsorption et déformation nécessite des dispositifs très spécifiques, dans la mesure où il faut pouvoir contrôler indépendamment la pression du fluide dans les pores et la contrainte de confinement qui s'applique au solide. Par ailleurs, tous les états de déformation (en particuliers les états en tractions) ne sont pas accessibles par l'expérience. Dans cette thèse, nous avons utilisé la simulation moléculaire, qui consiste à reproduire numériquement le comportement de la matière à l'échelle des atomes et des molécules. La simulation moléculaire est un complément intéressant aux expériences de laboratoire,

qui permet d'étudier séparément l'adsorption à la surface des mésopores et dans les micropores et qui permet d'appliquer n'importe quel état de déformation au milieu poreux.

Une étape importante de ce travail de thèse a été consacrée à l'étude de systèmes modèles, des solides microporeux unidimensionnels, par simulation moléculaire. Nous avons vérifié la validité des nouvelles équations poromécaniques sur ces systèmes modèles, pour lesquels nous avons également étudié le couplage entre adsorption et déformation. Cette étude numérique nous a permis de mieux comprendre ce couplage: lorsque tous les micropores sont identiques, l'adsorption dépend de la déformation de façon complexe en raison de la commensurabilité de la taille des pores à la taille des molécules de fluide. Pour un tel solide, l'adsorption peut induire aussi bien des contractions que des gonflements suivant les conditions. A l'inverse, lorsque les pores sont de tailles variées uniformément réparties, l'adsorption macroscopique dépend linéairement de la déformation et le fluide induit un effet de disjonction quelque soit la déformation. Ainsi, un solide désordonné avec des micropores de tailles aléatoires présente un comportement macroscopique relativement simple. Bien que ces résultats soient obtenus à partir de l'étude de systèmes unidimensionnels, ils donnent une première idée générale du couplage entre mécanique et adsorption pour des solides microporeux.

Pour appliquer les nouvelles équations poromécaniques à la séquestration du carbone dans le charbon, il est nécessaire de connaitre comment l'adsorption de méthane et de dioxyde de carbone évolue en fonction des potentiels chimiques de ces deux espèces et en fonction de la déformation du charbon. Dans ce but, nous avons réalisé des simulations moléculaires d'adsorption dans un modèle moléculaire réaliste de la matrice organique du charbon. La validité de la modélisation moléculaire est vérifiée en comparant les isothermes d'adsorption estimées par simulation moléculaire à des isothermes expérimentales. Les simulations nous ont permis de montrer que la quantité de fluide adsorbé dans le charbon dépend linéairement de la déformation, ce qui est confirmé par analyse inverse d'expériences d'immersion. La matrice organique du charbon étant quasi-amorphe, ce résultat est cohérent avec les résultats des simulations de solides unidimensionnels. L'adsorption de dioxyde de carbone présente une particularité pour des températures et pressions proche du point critique. L'agrégation moléculaire qui apparait dans ces conditions pourrait expliquer cette particularité. Ce qui a été observé pour de dioxyde de carbone suggère que les changements de phases gaz-liquide peuvent modifier sensiblement le couplage entre adsorption et mécanique. Dans toute cette thèse, la question des changements de phases n'a pas été abordée dans la mesure où le dioxyde de carbone et le méthane sont gazeux ou supercritiques dans les conditions géologiques. Il s'agit d'une question importante pour d'autres fluides, en particulier pour l'eau.

Ce travail s'est achevé avec la mise en œuvre des équations poromécaniques dans le cas du charbon à partir des isothermes d'adsorption estimés par simulation moléculaire pour le dioxyde de carbone, le méthane et leur mélange. Les gonflements estimés pour du charbon immergé dans du méthane pur et du dioxyde de carbone pur sont en bon accord avec les résultats expérimentaux d'expériences d'immersion. Par ailleurs, la même démarche est mise en œuvre pour estimer le gonflement différentiels durant le remplacement progressif du méthane par du dioxyde de carbone à des températures et pressions représentatives de veines de charbon à différentes profondeurs. Notre modélisation en soi se limite à l'échelle de la matrice organique du charbon, mais constitue la brique élémentaire indispensable à la mise en place d'un modèle de réservoir.

Les principaux apports de ce travail sont d'une part théoriques et d'autre part appliqués. Sur le plan théorique, les équations constitutives que nous avons dérivées sont générales et s'appliquent à toutes situations où un fluide est adsorbé dans un milieu poreux en l'absence d'irréversibilité. L'apport principal de cette extension des équations poromécaniques est de s'affranchir des notions de porosité et de surface spécifiques et de ne faire intervenir que des quantités bien définies même

pour des milieux microporeux. La mise en œuvre de ces équations est difficile car nécessite de connaitre le comportement d'adsorption en fonction de la pression de fluide et de la déformation. Nous nous sommes focalisés sur le cas spécifique de fluides supercritiques et de matériaux amorphes pour lesquels nous avons mis en évidence une dépendance linéaire de l'adsorption en fonction de la déformation. A l'image du méthane et du dioxyde de carbone adsorbés dans le charbon, ce comportement spécifique est susceptible de s'appliquer aux carbones microporeux désordonnées en général. Cependant un tel comportement n'est pas valable dès qu'un matériau présente une structure ordonnée, ou bien que le fluide présente un changement de phase. Quel est le comportement d'adsorption dans ces situations et comment cela se traduit-il au niveau des équations constitutives sont des orientations de recherche qu'il convient d'étudier. Le cadre poromécanique mis en place dans cette thèse ne prend pas en compte les irréversibilités telles que l'hystérésis d'adsorption, la plasticité ou la chimie-sorption. La prise en compte de ces irréversibilités nécessite d'introduire de nouveaux paramètres d'état macroscopiques les caractérisant. Dans cette thèse, nous nous sommes limités à une combinaison élémentaire de paramètres d'état. L'extension à des combinaisons plus complexes est un sujet de recherche à poursuivre.

Sur le plan appliqué, nous avons mis en place une modélisation du comportement poromécanique du charbon lors du stockage géologique du carbone. En conditions sèches, i.e., en l'absence d'eau, et pour des sites d'injection à plus de 200 m de profondeur, cette modélisation donne des estimations fiables à $\pm 15\%$. La force de cette modélisation réside dans son approche véritablement physique et non empirique. Seul un paramètre a été calibré dans notre modélisation : le module de compressibilité du charbon. Aussi s'agit-il d'un progrès conséquent par rapport aux modélisations antérieures, majoritairement empiriques et nécessitant la calibration d'un grand nombre de paramètres. Cette approche peut être jugée robuste et transposable d'un charbon à l'autre. Pour pouvoir appliquer cette modélisation, les coefficients de couplage pour le charbon considéré doivent être déterminés au préalable, par exemple par l'analyse inverse d'expériences d'immersion. Pour des sites d'injection peu profond (< 200 m), cependant, notre modélisation n'est pas fiable car le modèle poromécanique surestime le gonflement induit par l'adsorption à faible pression ($P < 2$ MPa). Pour une mise en œuvre concrète, le principal défaut de cette modélisation est de ne pas tenir compte de la présence d'eau, alors que des aquifères sont souvent présents dans les réservoirs de charbon. La prise en compte de l'eau dans les simulations moléculaires suppose dans un premier temps d'utiliser un modèle moléculaire de la matrice de charbon incluant les atomes d'oxygènes, afin d'être plus représentatifs des interactions électrostatiques cruciales pour l'adsorption d'une molécule polaire comme l'eau. Dans un second temps, le modèle poromécanique doit être adapté pour tenir du compte du fait que le dioxyde de carbone et l'eau ne sont pas miscibles, en introduisant une notion de saturation. La prise en compte de la présence d'eau est une piste de recherche à étudier. Au-delà du gonflement différentiel du charbon, il s'agit de déterminer la perte de perméabilité du réservoir suite à ce gonflement. Comment le gonflement impacte la perméabilité doit être étudié en détail.

Nous espérons que ce travail permettra d'apporter des réponses utiles concernant le développement de la séquestration du carbone. Nous espérons également que ce travail sera utile à ceux qui s'intéressent aux matériaux microporeux en général.

List of Notations

Symbol	Description
	Latin letters
a	Specific surface
A	Area
b	Biot coefficient
B	Parameter of the BET adsorption isotherm
$\mathcal{B}$	Number of blocks (Block averaging method)
C	Parameter for potential of interaction
$\widetilde{C}$	Coefficient characterizing the linear dependency adsorption on strain, also called 'coupling coefficient'
Cst	Constant scalar value
D	Parameter of the Dubinin-Radushkevich adsorption isotherm
e	Elementary charge
$e_{\square}$ (with subscript)	Component of the deviatoric strain tensor
$\underline{\underline{e}}$	Deviatoric strain tensor
$\widetilde{e}$	Thickness
E	Internal energy
$\mathbf{E}$	Electric field
f	Helmholtz free energy per unit undeformed volume
F	Helmholtz free energy
$\mathbf{F}$	Force vector
fug	Fugacity
G	Gibbs free energy
$\overline{G}$	Shear modulus
h	Planck constant
$\hbar$	Reduced Planck constant: $h/(2\pi)$
I and J	Phases
k	Local bulk modulus (scale of a micropore)
k_B	Boltzmann constant
K	Bulk modulus
$\mathcal{K}$	Number of chemical species
l	Actual size of a pore
L	Length

Continued on next page ...

continued from previous page

Symbol	Description
m	Mass of a particle
M	Constant scalar value
n	Number of molecular configurations sampled during a molecular simulation
$\overline{n}$	Minimum number of consecutive molecular configurations sampled, for which the molecular configuration are not correlated, also called decorrelation threshold
$\widetilde{n}$	Number of particles per unit undeformed volume
$\mathbf{n}$	Unit vector
N	Number of particles
$\overline{N}$	Biot modulus
$\mathcal{N}_A$	Avogadro number
O	Macroscopic property of a system, also called observable
$\widetilde{O}$	Empirical estimator of observable O
p	Probability
$\mathbb{P}$	Distribution of probability of occurrence of micro-states
$\mathbf{p}$	Impulsion of a particle
P	Pressure
q	Electric charge
Q	Heat
$\mathbb{Q}$	Instrumental distribution of probability (rejection sampling method)
$\mathcal{Q}$	Moment of a linear quadrupole
r	Distance
R	Geometrical radius
$\mathbf{r}$	Position of a particle
$\mathbb{R}$	Set of real numbers
s	Component of the deviatoric stress tensor
$\underline{\underline{s}}$	Deviatoric stress tensor
$\widetilde{s}$	Entropy per unit undeformed volume
S	Entropy
$\overline{S}$	Selectivity, also called separation factor
$\overline{SD}$	Standard deviation
$\widetilde{SD}$	Empirical estimator of the standard deviation
t	Time
T	Temperature
$\mathbf{u}$	Electric dipole moment
U	Energy of interaction
V	Volume
$\overline{V}$	Volume per molecule
$\widetilde{V}$	Proposed volume (Metropolis algorithm)
$\mathcal{V}$	Number of virtual insertions for the computation of the instantaneous chemical potential of a molecular configuration (Widom insertion method)

Continued on next page ...

continued from previous page

Symbol	Description
w	Internal virial (virial equation)
W	Total number of micro-states in the accessible phase space
$\overline{x}$	Mole fraction
x, y and z	Cartesian coordinates, also used to name the different axes
$\mathbf{x}$	Set of positions $(\mathbf{r}_i)_{i\in\{1,\dots,N\}}$ of a molecular state, also called molecular configuration
$\widetilde{\mathbf{x}}$	Proposed molecular configuration (Metropolis algorithm)
Y	Random value (rejection sampling method)
Z	Partition function
	Greek letters
α	Polarizability
$\alpha^{\square}_{\square}$ (with subscript and superscript)	Derivative of the specific surface with respect to the variable in subscript, at constant value of the variable(s) in superscript (Temperature is omitted)
β	Affinity coefficient, parameter of the Dubinin-Radushkevich adsorption isotherm
χ	Function characterizing the proportionality of the grand potential with respect to the volume for a bulk fluid
δ_{ab}	Kronecker delta
$\widetilde{\varepsilon}$	Parameter of the Lennard-Jones potential
ε	Permittivity
ϵ	Component of the strain tensor if with a subscript, volumetric strain otherwise
$\underline{\underline{\epsilon}}$	Strain tensor
γ	Interface energy
Γ	Excess amount adsorbed per unit area
η	Variable of integration
ϕ	Lagrangian porosity
φ	Variation of Lagrangian porosity
κ	Permeability
λ	Lagrange multiplier
Λ	Thermal de Broglie wavelength
$\widetilde{\Lambda}$	Lagrange function (method of Lagrange multipliers)
μ	Chemical potential
ν	Parameter of the Dubinin-Astakhov adsorption isotherm
Π	Disjoining pressure
θ	Angle
ρ	Density
σ	Component of the stress tensor if with a subscript, volumetric stress otherwise
$\underline{\underline{\sigma}}$	Stress tensor
$\widetilde{\sigma}$	Parameter of the Lennard-Jones potential
Σ	Accessible phase space of positions and impulsions

Continued on next page ...

continued from previous page

Symbol	Description
ς	Parameter for potential of interaction
υ	Exponent of the inverse power law for steric repulsion
ω	Grand potential per unit undeformed volume
ω_{hyb}	Hybrid potential per unit undeformed volume
ω^r_{hyb}	Hybrid potential per unit undeformed volume without the interface energy
ω_{os}	Osmotic potential per unit undeformed volume (minimum at equilibrium in the osmotic ensemble)
Ω	Grand potential
Ω_{hyb}	Hybrid potential (minimum at equilibrium in the hybrid canonical - grand canonical ensemble, canonical for the atoms of the solid skeleton, grand canonical for the molecules of the fluid)
ψ	Angle
Ψ	Wave function in quantum mechanics
	Subscripts and superscripts
$\square_a$	Component of vectors ($a \in \{x, y, z\}$) • $\mathbf{F}_a$: component of the force vector • $\mathbf{r}_a$: component of the position vector
$\square_A$ or $\square_B$	Particles of type A or B • $\widetilde{\varepsilon}_A$ or $\widetilde{\varepsilon}_B$: Lennard-Jones parameter for the interaction between two particles of type A or two particles of type B • $\widetilde{\varepsilon}_{A-B}$: Lennard-Jones parameter for the interaction between a particle of type A and a particle of type B • $\widetilde{\sigma}_A$ or $\widetilde{\sigma}_B$: Lennard-Jones parameter for the interaction between two particles of type A or two particles of type B • $\widetilde{\sigma}_{A-B}$: Lennard-Jones parameter for the interaction between a particle of type A and a particle of type B
$\square_{aa}$, $\square_{ab}$ and $\square_{bb}$	Component of a tensor ($(a, b) \in \{x, y, z\}^2$) • e_{aa}, e_{ab} and e_{bb}: components of the deviatoric strain tensor • s_{aa}, s_{ab} and s_{bb}: components of the deviatoric stress tensor • ϵ_{aa}, ϵ_{ab} and ϵ_{bb}: components of the strain tensor • σ_{aa}, σ_{ab} and σ_{bb}: components of the stress tensor
$\square_b$	Block index (Block averaging method) • $\widetilde{O}_b$: empirical estimator over the b^{th} block
$\square_{ads}$	'Adsorption' • U_{ads}: interaction energy of adsorption
$\square_{bl}$	'Block' (Block averaging method) • n_{bl}: number of molecular configurations per block
$\square^{bulk}$ or $\square_{bulk}$	'Bulk' • $\overline{V}_{bulk}$: volume per molecule in the bulk • $\overline{x}_{bulk}$: mole fraction in the bulk • ρ_{bulk}: bulk density • σ^{bulk}: mechanical stress in the bulk

Continued on next page ...

continued from previous page

Symbol	Description
$\square_{\mathrm{C}}$	'Carbon atom' • q_{C}: electric charge on a carbon atom • $U_{\mathrm{C-C}}$: energy of interaction between two atoms of carbon • $U_{\mathrm{C-C-C}}$: energy of interaction between three atoms of carbon • $\widetilde{\varepsilon}_{\mathrm{C}}$: Lennard-Jones parameter for the carbon atom • $\widetilde{\varepsilon}_{\mathrm{C-C}}$: parameter for the Lennard-Jones interaction between carbon atoms • $\widetilde{\sigma}_{\mathrm{C}}$: Lennard-Jones parameter for the carbon atom • $\widetilde{\sigma}_{\mathrm{C-C}}$: parameter for the Lennard-Jones interaction between carbon atoms
$\square_{\mathrm{C-H}}$	Property of the interaction between a carbon atom and a hydrogen atom • $U_{\mathrm{C-H}}$: energy of interaction between a carbon atom and a hydrogen atom • $\widetilde{\varepsilon}_{\mathrm{C-O}}$: parameter for the Lennard-Jones interaction between a carbon atom and a hydrogen atom • $\widetilde{\sigma}_{\mathrm{C-O}}$: parameter for the Lennard-Jones interaction between a carbon atom and a hydrogen atom
$\square_{\mathrm{C-O}}$	Property of the interaction between a carbon atom and an oxygen atom • $L_{\mathrm{C-O}}$: distance between a carbon atom and an oxygen atom • $\widetilde{\varepsilon}_{\mathrm{C-O}}$: parameter for the Lennard-Jones interaction between a carbon atom and an oxygen atom • $\widetilde{\sigma}_{\mathrm{C-O}}$: parameter for the Lennard-Jones interaction between a carbon atom and an oxygen atom
$\square_{\mathrm{CH_4}}$	'Methane' • $\widetilde{C}_{\mathrm{CH_4}}$: coupling coefficient for methane • $\widetilde{n}_{\mathrm{CH_4}}$: amount of adsorbed methane per unit undeformed volume of porous medium • $U_{\mathrm{CH_4-CH_4}}$: energy of interaction between molecules of methane • $\overline{V}_{\mathrm{CH_4}}$: volume per molecule for methane • $\overline{x}_{\mathrm{CH_4}}$: mole fraction of methane • $\widetilde{\varepsilon}_{\mathrm{CH_4}}$: Lennard-Jones parameter for methane • $\mu_{\mathrm{CH_4}}$: chemical potential of methane • $\widetilde{\sigma}_{\mathrm{CH_4}}$: Lennard-Jones parameter for methane
$\square_{\mathrm{CO_2}}$	'Carbon dioxide' • $\widetilde{C}_{\mathrm{CO_2}}$: coupling coefficient for carbon dioxide • $\widetilde{n}_{\mathrm{CO_2}}$: amount of adsorbed carbon dioxide per unit undeformed volume of porous medium • $U_{\mathrm{CO_2-CO_2}}$: energy of interaction between molecules of carbon dioxide • $\overline{V}_{\mathrm{CO_2}}$: volume per molecule for carbon dioxide • $\overline{x}_{\mathrm{CO_2}}$: mole fraction of carbon dioxide • $\mu_{\mathrm{CO_2}}$: chemical potential of carbon dioxide
$\square_{cr}$	'Critical'

Continued on next page ...

continued from previous page

Symbol	Description
	• P_{cr}: critical pressure • T_{cr}: critical temperature
$\square_{\mathrm{CS1000}}$	'CS1000' • $U_{\mathrm{CH_4-CS1000}}$: energy of interaction between a molecule of methane and the solid skeleton of CS1000 • $U_{\mathrm{CO_2-CS1000}}$: energy of interaction between a molecule of carbon dioxide and the solid skeleton of CS1000 • $\overline{x}_{\mathrm{CS1000}}$: mole fraction when adsorbed in CS1000
$\square_{disp}$	'Dispersion forces' • C_{disp}: characteristic coefficient of the dispersion forces
$\square_f$	'Fluid' • E_f: internal energy of the fluid • N_f: number of molecules of the fluid • S_f: entropy of the fluid • U_f: energy of interaction between molecules of the fluid • V_f: volume of the fluid • $\widetilde{\varepsilon}_f$: Lennard-Jones parameter for a molecular interaction between fluid molecules • ω_f: grand potential of the fluid per unit undeformed volume • Ω_f: grand potential of the fluid • $\widetilde{\sigma}_f$: Lennard-Jones parameter for a molecular interaction between fluid molecules
$\square_{f-i}$	'Fluid-induced' • σ_{f-i}: fluid-induced stress
$\square_{fs}$	'Fluid-solid' • U_{fs}: energy of interaction between a molecule of the fluid and an atom of the solid skeleton • $\widetilde{\varepsilon}_{fs}$: Lennard-Jones parameter for a molecular interaction between a fluid molecule and an atom of the solid skeleton • $\widetilde{\sigma}_{fs}$: Lennard-Jones parameter for a molecular interaction between a fluid molecule and an atom of the solid skeleton
$\square_{GC}$	Quantity in the grand canonical ensemble • Z_{GC}: partition function in the grand canonical ensemble
$\square_{\mathrm{H}}$	'Hydrogen atom' • q_{H}: electric charge on a hydrogen atom • $\widetilde{\varepsilon}_{\mathrm{H}}$: Lennard-Jones parameter for the hydrogen atom • $\widetilde{\sigma}_{\mathrm{H}}$: Lennard-Jones parameter for the hydrogen atom
$\square_{harm}$	'Harmonic' • C_{harm}: characteristic coefficient of the harmonic potential
$\square_i$ and $\square_j$	Particle index • Λ_i and Λ_j: thermal de Broglie wavelength of the i^{th} and j^{th} particles • m_i and m_j: mass of the i^{th} and j^{th} particles

Continued on next page ...

continued from previous page

Symbol	Description
	• $\mathbf{p}_i$ and $\mathbf{p}_j$: impulsions of the i^{th} and j^{th} particles • q_i and q_j: electric charges of the i^{th} and j^{th} particles • $\mathbf{r}_i$ and $\mathbf{r}_j$: positions of the i^{th} and j^{th} particles • $\widetilde{\varepsilon}_i$ and $\widetilde{\varepsilon}_j$: Lennard-Jones parameter for the i^{th} and j^{th} particles • $\widetilde{\sigma}_i$ and $\widetilde{\sigma}_j$: Lennard-Jones parameter for the i^{th} and j^{th} particles
$\square_{ij}$	'From particle i to particle j' or 'exerted by particle i on particle j' or 'between particles i and j' • r_{ij}: distance between particle i and particle j • $\mathbf{r}_{ij}$: vector from particle i to particle j • $\mathbf{F}_{ij}$: force exerted by particle i on particle j • U_{ij}: potential of energy of interaction between particle i and particle j • w_{ij}: internal virial between particle i and particle j • $\widetilde{\varepsilon}_{ij}$: parameter for the Lennard-Jones interaction between particle i and particle j • $\widetilde{\sigma}_{ij}$: parameter for the Lennard-Jones interaction between particle i and particle j
$\square_I$ and $\square_J$	Quantity related to phases I and J, respectively • P_I and P_J: pressures in phases I and J • V_I and V_J: volumes of phases I and J
$\square_{IdG}$	Quantity for an ideal gas • μ_{IdG}: chemical potential of an ideal gas
$\square_{ind}$	'Induced' • $\mathbf{u}_{ind}$: induced electric dipole moment • U_{ind}: induced electrostatic energy of interaction
$\square_{ini}$	'Initial' • P_{ini}: initial pore pressure • ϵ_{ini}: initial deformation • φ_{ini}: initial change of porosity • σ_{ini}: initial stress
$\square^{int}$	'Interaction' • σ^{int}: stress due to the molecular interactions
$\square_k$	Chemical species index • $\widetilde{C}_k$: Coefficient characterizing the linearity of the adsorption with respect to the strain for the k^{th} chemical species • $\widetilde{n}_k$: number of particles of the k^{th} chemical species per unit undeformed volume • N_k: number of particles of the k^{th} chemical species • Γ_k: Excess amount adsorbed of the k^{th} chemical species per unit area • Λ_k: thermal de Broglie wavelength of the k^{th} chemical species

Continued on next page ...

continued from previous page

Symbol	Description
	• μ_k: chemical potential of the k^{th} chemical species • ρ_k: numeral density of the k^{th} chemical species • $\overline{V}_k$: volume per molecule of the k^{th} chemical species
$\square^{kin}$	'Kinetic' • σ^{kin}: kinetic part of the mechanical stress
$\square_l$ and $\square_m$	Index of the sampled molecular configurations (Metropolis algorithm) • $\mathbf{x}_l$ and $\mathbf{x}_m$: l^{th} and m^{th} molecular configurations sampled • $\widetilde{\mathbf{x}}_l$ and $\widetilde{\mathbf{x}}_l$: proposed molecular configurations at the l^{th} and m^{th} Monte Carlo steps • V_l and V_m: volume of the l^{th} and m^{th} molecular configurations sampled • $\widetilde{V}_l$ and $\widetilde{V}_l$: proposed volumes at the l^{th} and m^{th} Monte Carlo steps
$\square_{LJ}$	'Lennard-Jones' • U_{LJ}: Lennard-Jones potential energy of interaction
$\square_{max}$ or $\square^{max}$	'Maximum' • l^{max}: Maximum actual size of a micropore • r_0^{max}: Maximum undeformed size of a micropore • Γ_{max}: Maximum excess adsorbed amount per unit area
$\square_{mech}$	'Mechanical' • P_{mech}: mechanical pressure
$\square^{min}$	'Minimum' • l^{min}: Minimum actual size of a micropore • r_0^{min}: Minimum undeformed size of a micropore
$\square_{morse}$	Parameter of the Morse potential • C_{morse}: characteristic coefficient of the Morse potential • ς_{morse}: parameter of the Morse potential
$\square_{NPT}$	Quantity in the isobaric-isothermal ensemble • Z_{NPT}: partition function in the isobaric-isothermal ensemble
$\square_O$	Quantity related to the observable O • $\overline{SD}_O$: Standard deviation of an observable O
$\square_{\widetilde{O}}$	Quantity related to the empirical estimator of an observable O • $\overline{SD}_{\widetilde{O}}$: Standard deviation of the empirical estimator of O (Metropolis algorithm) • $\widetilde{SD}_{\widetilde{O}}$: Standard deviation of the empirical estimator of O (Metropolis algorithm)
$\square_{\mathrm{O}}$	'Oxygen atom' • q_{O}: electric charge on an oxygen atom • $\widetilde{\varepsilon}_{\mathrm{O-O}}$: parameter for the Lennard-Jones interaction between oxygen atoms • $\widetilde{\sigma}_{\mathrm{O-O}}$: parameter for the Lennard-Jones interaction between oxygen atoms

Continued on next page ...

continued from previous page

Symbol	Description
$\square_p$	'Pore' • ϵ_p: strain of a pore • ρ_p: fluid density in a pore • σ_p: stress in a pore
$\square_{rep}$	'Repulsive' • U_{rep}: repulsive potential energy of interaction
$\square^s$	'Surface' • E^s: excess internal energy in the inhomogeneous layer of an interface • N^s: excess number of particles in the inhomogeneous layer of an interface • S^s: excess entropy in the inhomogeneous layer of an interface • ϵ^s: surface strain • σ^s: surface stress • Ω^s: excess grand potential in the inhomogeneous layer of an interface
$\square_s$	'Solid' • E_s: internal energy of the solid • f_s: Helmholtz free energy per unit undeformed volume of the solid • F_s: Helmholtz free energy of the solid • K_s: bulk modulus of the solid • N_s: Number of atoms of the solid • $\widetilde{s}_s$: entropy per unit undeformed volume of the solid • S_s: entropy of the solid • U_s: energy of interaction between atoms of the solid • ϵ_s: volumetric strain of the solid
$\square_{sat}$	'Saturation' • P_{sat}: saturation pressure
$\square^{sec}$	'Secant' • b^{sec}: secant drained Biot coefficient • K^{sec}: secant drained bulk modulus
$\square_{site}$	'Adsorption sites' • N_{site}: Number of sites where fluid particles can adsorbed
$\square^{Supp}$	'Supplementary' • U^{Supp}: supplementary energy of interaction due to the insertion of a particle (Widom insertion method)
$\square_T$	System made of a molecular system and the large reservoir with which the small system can exchange different type(s) of energy • E_T: internal energy of the whole system • S_T: entropy of the whole system
$\square^{tan}$	'Tangent' • b^{tan}: tangent drained Biot coefficient • K^{tan}: tangent drained bulk modulus

Continued on next page ...

continued from previous page

Symbol	Description
$\square_{th}$	'Thermostat' or large reservoir of heat, particle, volume, and so on • E_{th}: internal energy of the reservoir • N_{th}: number of particles of the reservoir • S_{th}: entropy of the reservoir • T_{th}: temperature of the reservoir • V_{th}: Volume of the reservoir • W_{th}: Number of accessible micro-states for the reservoir
$\square^u$	'Unjacketed' • $\widetilde{n}^u$: amount adsorbed per unit undeformed volume of the porous medium in unjacketed conditions • ϵ^u: volumetric strain in unjacketed conditions
$\square_u$ and $\square_v$	Micro-state index • E_u: internal energy of the u^{th} micro-state • N_u: number of particles of the u^{th} micro-state • O_u: value of observable O for the u^{th} micro-state • p_u: probability of occurrence of the u^{th} micro-state • V_u: volume of the u^{th} micro-state
$\square_{un}$	'Unnecessary' • $\mathbf{x}_{un}$: set of unnecessary degrees of freedom (simplified models of inter-atomic and inter-molecular interactions)
$\square^v$	Virtual particle index (Widom insertion method) • $\mathbf{r}^v$: Position of the v^{th} virtual particle
$(\square)_x$, $(\square)_y$ and $(\square)_z$	Component of a vector in the x, y and z directions respectively, or quantity related to the x, y and z directions respectively • $(\mathbf{F})_x$, $(\mathbf{F})_y$ and $(\mathbf{F})_z$: force in the x, y and z directions • $(\mathbf{p})_x$, $(\mathbf{p})_y$ and $(\mathbf{p})_z$: impulsion in the x, y and z directions • $(\mathbf{r})_x$, $(\mathbf{r})_y$ and $(\mathbf{r})_z$: positions in the x, y and z directions
$\square_x$, $\square_y$ and $\square_z$	Quantity related to the x, y and z directions respectively • L_x, L_y and L_z: lengths of a system in the x, y and z directions
$\square_{xx}$, $\square_{xy}$, ... $\square_{zz}$	Component of a tensor • ϵ_{xx}, ϵ_{xy}, ... ϵ_{zz}: components of the strain tensor • σ_{xx}, σ_{xy}, ... σ_{zz}: components of the stress tensor
$\square_0$ or $\square^0$	'Reference' or 'initial' or 'undeformed' • a^0: specific surface at zero volumetric strain • a_0: specific surface in the undeformed configuration • K_0: bulk modulus in the absence of any fluid • L_0: undeformed length of a one-dimensional solid • $\widetilde{n}^0$: number of particles per unit undeformed volume at zero volumetric strain • P_0: reference pressure (parameter of the Langmuir isotherm) • r_0: equilibrium distance of a potential energy of interaction • s_0: deviatoric stress of a porous medium in the absence of any fluid

Continued on next page ...

continued from previous page

Symbol	Description
	• t_0: initial time • V_0: volume in the undeformed configuration • ϕ^0: Lagrangian porosity at zero volumetric strain • Γ^0: Excess adsorbed amount per unit area at zero volumetric strain • μ_0: Chemical potential at a bulk pressure of 1 Pa • μ^0_{IdG}: reference chemical potential of an ideal gas at a density of 1 particle per cubic meter • ϕ_0: porosity at zero strain and zero fluid bulk pressure • ε_0: vacuum permittivity • κ_0: initial permeability • σ_0: volumetric stress of a porous medium in the absence of any fluid • θ_0: equilibrium angle
	Mathematical notations
$\delta(X)$	Dirac delta function
$\exp(X)$ or e^X	Exponential function
$\ln(X)$	Natural logarithm function
$\min(X, Y)$	Minimum of two values X and Y
$X \propto Y$	X proportional to Y
$\lvert X \rvert$	Euclidean norm
$(X \otimes Y)$	Tensor product
$\mathcal{N}(m, var)$	Normal probability distribution of mean value m and variance var
$N!$	Factorial N
$X \in V$	X is an element of V
$\sum_{X \in V} f(X)$	Summation over a discrete space
$\prod_{X \in V} f(X)$	Product over a discrete space
$\int_{X \in V} f(X)\, dX$	Integral
$\frac{\partial f}{\partial X_\cdot}\Big\rvert_{Y,Z,\ldots}$	Partial derivative of the function f with respect to X at constant values of Y, Z ,...
$\langle f \rangle$	Average value
$\nabla_X f$	Gradient of the function f with respect to the parameter X
$\nabla \cdot f$	Divergence

Bibliography

Allen, M. P. and Tildesley, D. J. (1989). Computer Simulation of Liquids. Oxford University Press, USA.

André, L., Azaroual, M., and Menjoz, A. (2010). Numerical simulations of the thermal impact of supercritical co2 injection on chemical reactivity in a carbonate saline reservoir. Transport in Porous Media, 82(1):247–274.

Andrieu, S. and Müller, P. (2005). Les surfaces solides: concepts et méthodes. EDP Sciences.

Anger, R. and Fontaine, L. (2009). Bâtir en terre : du grain de sable à l'architecture. Belin ; Cité des sciences et de l'industrie, 2009.

Bae, J. H., Lim, Y. R., and Sung, J. (2008). Statistical mechanics of molecular adsorption: Effects of adsorbate interaction on isotherms. Langmuir, 24(6):2569–2572.

Bae, J.-S. and Bhatia, S. K. (2006). High-pressure adsorption of methane and carbon dioxide on coal. Energy & Fuels, 20(6):2599–2607.

Bae, J.-S., Bhatia, S. K., Rudolph, V., and Massarotto, P. (2009). Pore accessibility of methane and carbon dioxide in coals. Energy & Fuels, 23(6):3319–3327.

Balbuena, P. B., Berry, D., and Gubbins, K. E. (1993). Solvation pressures for simple fluids in micropores. The Journal of Physical Chemistry, 97(4):937–943.

Belytschko, T., Xiao, S. P., Schatz, G. C., and Ruoff, R. S. (2002). Atomistic simulations of nanotube fracture. Phys. Rev. B, 65(23):235430–.

Bemer, E. and Lombard, J. (2010). From injectivity to integrity studies of co2 geological storage. Oil Gas Sci. Technol. Rev. IFP, 65(3):445–459.

Bernstein, L., Bosch, P., Canziani, O., Chen, Z., Christ, R., Davidson, O., Hare, W., Huq, S., Karoly, D., Kattsov, V., Kundzewicz, Z., Liu, J., Lohmann, U., Manning, M., Matsuno, T., Menne, B., Metz, B., Mirza, M., Nicholls, N., Nurse, L., Pachauri, R., Palutikof, J., Parry, M., Qin, D., Ravindranath, N., Reisinger, A., Ren, J., Riahi, K., Rosenzweig, C., Rusticucci, M., Schneider, S., Sokona, Y., Solomon, S., Stott, P., Stouffer, R., Sugiyama, T., Swart, R., Tirpak, D., Vogel, C., and Yohe, G. (2007). IPCC Fourth Assessment Report: Climate Change 2007 Synthesis Report. IPCC.

Bloomberg, editor (2010). A fresh look at the costs of reducing US carbon emissions. Bloomberg New Energy Finance.

Botan, A., Rotenberg, B., Marry, V., Turq, P., and Noetinger, B. (2010). Carbon dioxide in montmorillonite clay hydrates: Thermodynamics, structure, and transport from molecular simulation. The Journal of Physical Chemistry C, 114(35):14962–14969.

Boutin, A., Couck, S., Coudert, F.-X., Serra-Crespo, P., Gascon, J., Kapteijn, F., Fuchs, A. H., and Denayer, J. F. (2011). Thermodynamic analysis of the breathing of amino-functionalized mil-53(al) upon co2 adsorption. Microporous and Mesoporous Materials, 140(1-3):108–113.

Brenner, D. W. (1990). Empirical potential for hydrocarbons for use in simulating the chemical vapor deposition of diamond films. Phys. Rev. B, 42(15):9458–.

Brunauer, S., Emmett, P. H., and Teller, E. (1938). Adsorption of gases in multimolecular layers. Journal of the American Chemical Society, 60(2):309–319.

Busch, A., Gensterblum, Y., and Krooss, B. M. (2003). Methane and co2 sorption and desorption measurements on dry argonne premium coals: pure components and mixtures. International Journal of Coal Geology, 55(2-4):205–224.

Bustin, R. M. and Clarkson, C. R. (1998). Geological controls on coalbed methane reservoir capacity and gas content. International Journal of Coal Geology, 38(1-2):3–26.

Chen, S. G. and Yang, R. T. (1994). Theoretical basis for the potential theory adsorption isotherms. the dubinin-radushkevich and dubinin-astakhov equations. Langmuir, 10(11):4244–4249.

Chevoir, F. (2010). Physique Statistique. Ecole des Ponts ParisTech.

Christensen, N. P. and Holloway, S. (2004). Assessing european potential for geological storage of co2 from fossil fuel combustion. Technical report, The GESTCO project.

Chu, B. and Lin, J. S. (1970). Small-angle scattering of x rays from carbon dioxide in the vicinity of its critical point. J. Chem. Phys., 53(12):4454–4466.

Churaev, N. V. (2003). Derjaguin's disjoining pressure in the colloid science and surface phenomena. Advances in Colloid and Interface Science, 104(1-3):xv – xx.

Coasne, B., Jain, S. K., Naamar, L., and Gubbins, K. E. (2007). Freezing of argon in ordered and disordered porous carbon. Physical Review B, 76(8):085416.

Coudert, F.-X., Jeffroy, M., Fuchs, A. H., Boutin, A., and Mellot-Draznieks, C. (2008). Thermodynamics of guest-induced structural transitions in hybrid organic-inorganic frameworks. Journal of the American Chemical Society, 130(43):14294–14302.

Coussy, O. (2004). Poromechanics. John Wiley & Sons, Ltd.

Coussy, O. (2010). Mechanics and Physics of Porous Solids. John Wiley & Sons, Ltd.

Crosdale, P. J., Beamish, B. B., and Valix, M. (1998). Coalbed methane sorption related to coal composition. International Journal of Coal Geology, 35(1-4):147–158.

Cui, X., Bustin, R. M., and Dipple, G. (2004). Selective transport of co2, ch4, and n2 in coals: insights from modeling of experimental gas adsorption data. Fuel, 83(3):293–303.

Day, S., Duffy, G., Sakurovs, R., and Weir, S. (2008a). Effect of coal properties on co2 sorption capacity under supercritical conditions. International Journal of Greenhouse Gas Control, 2(3):342–352.

Day, S., Fry, R., and Sakurovs, R. (2008b). Swelling of australian coals in supercritical co2. International Journal of Coal Geology, 74(1):41–52.

Derjaguin, B. and Obuchov, E. (1936). Ultramicrometric analysis of solvate layer and elementary expansion effects. Acta Physicochimica URSS, 5:1.

Derjaguin, B. V. and Landau, L. (1941). The theory of stability of highly charged lyophobic sols and coalescence of highly charged particles in electrolyte solutions. Acta Physicochim URSS, 14(11):633–652.

Derome, D., Griffa, M., Koebel, M., and Carmeliet, J. (2011). Hysteretic swelling of wood at cellular scale probed by phase-contrast x-ray tomography. Journal of Structural Biology, 173(1):180–190.

Diu, B., Guthmann, C., Lederer, D., and B., R. (1989). Physique Statistique. Hermann, Editeur des Sciences et des Arts.

Do, D. D., Nicholson, D., and Do, H. D. (2008). Effects of adsorbent deformation on the adsorption of gases in slitlike graphitic pores: A computer simulation study. The Journal of Physical Chemistry C, 112(36):14075–14089.

DOE/EIA, editor (2010). Energy Information Administration - Annual Energy Outlook 2011. Department of Energy / Energy Information Administration.

Dolino, G., Bellet, D., and Faivre, C. (1996). Adsorption strains in porous silicon. Phys. Rev. B, 54(24):17919–.

Dubinin, M. M. (1967). Adsorption in micropores. Journal of Colloid and Interface Science, 23(4):487–499.

Dubinin, M. M. and Astakhov, V. A. (1971). Development of the concepts of volume filling of micropores in the adsorption of gases and vapors by microporous adsorbents. Russian Chemical Bulletin, 20(1):3–7.

Edmiston, P. L. and Underwood, L. A. (2009). Absorption of dissolved organic species from water using organically modified silica that swells. Separation and Purification Technology, 66(3):532–540.

EIA, editor (1996). U.S. Coal Reserves: A Review and Update. Energy Information Administration.

Einstein, A. (1905). On the movement of small particles suspended in stationary liquids required by the molecular-kinetic theory of heat. Annalen der Physik, 17:549–560.

Ettre, L. S. (1993). Nomenclature for chromatography (iupac recommendations 1993). Pure Appl. Chem., 65(4):819–872.

Fitzgerald, J., Pan, Z., Sudibandriyo, M., Robinson, Jr., R., Gasem, K., and Reeves, S. (2005). Adsorption of methane, nitrogen, carbon dioxide and their mixtures on wet tiffany coal. Fuel, 84(18):2351–2363.

Frenkel, D. and Smit, B. (2001). Understanding Molecular Simulation. Academic Press, Inc.

Gale, J. and Freund, P. (2001). Coal-bed methane enhancement with co2 sequestration worldwide potential. Environmental Geosciences, 8(3):210–217.

Gasteiger, J. and Marsili, M. (1980). Iterative partial equalization of orbital electronegativity–a rapid access to atomic charges. Tetrahedron, 36(22):3219 – 3228.

Gaus, I. (2010). Role and impact of co2-rock interactions during co2 storage in sedimentary rocks. International Journal of Greenhouse Gas Control, 4(1):73–89.

Gibbs, J. W. (1902). Elementary principles in statistical mechanics: developed with especial reference to the rational foundations of thermodynamics. C. Scribner's sons.

Gibbs, J. W. (1928). The collected works, volume I. Longmans (New-York), Green (New-York).

Glass, A. S. and Larsen, J. W. (1994). Coal surface properties. specific and nonspecific interactions for polar molecules and surface tensions for hydrocarbons at the surface of illinois no. 6 coal. Energy & Fuels, 8(3):629–636.

Gloor, G. J., Jackson, G., Blas, F. J., and de Miguel, E. (2005). Test-area simulation method for the direct determination of the interfacial tension of systems with continuous or discontinuous potentials. The Journal of Chemical Physics, 123(13):134703.

Günther, G., Prass, J., Paris, O., and Schoen, M. (2008). Novel insights into nanopore deformation caused by capillary condensation. Phys. Rev. Lett., 101(8):086104–.

Gor, G. Y. and Neimark, A. V. (2010). Adsorption-induced deformation of mesoporous solids. Langmuir, 26(16):13021–13027.

Gor, G. Y. and Neimark, A. V. (2011). Adsorption-induced deformation of mesoporous solids: Macroscopic approach and density functional theory. Langmuir, 27(11):6926–6931.

Grosman, A. and Ortega, C. (2008). Influence of elastic deformation of porous materials in adsorption-desorption process: A thermodynamic approach. Phys. Rev. B, 78(8):085433–.

Harpalani, S. and Schraufnagel, A. (1990). Measurement of parameters impacting methane recovery from coal seams. Geotechnical and Geological Engineering, 8(4):369–384.

Harris, J. G. and Yung, K. H. (1995). Carbon dioxide's liquid-vapor coexistence curve and critical properties as predicted by a simple molecular model. The Journal of Physical Chemistry, 99(31):12021–12024.

Hastings, W. K. (1970). Monte carlo sampling methods using markov chains and their applications. Biometrika, 57(1):97–109.

Heisenberg, W. (1927). Über den anschaulichen inhalt der quantentheoretischen kinematik und mechanik. Zeitschrift für Physik A Hadrons and Nuclei, 43(3):172–198.

Herman, T., Day, J., and Beamish, J. (2006). Deformation of silica aerogel during fluid adsorption. Phys. Rev. B, 73(9):094127–.

Hill, T. L. (1946). Statistical mechanics of multimolecular adsorption. i. The Journal of Chemical Physics, 14(4):263–267.

Hutson, N. D. and Yang, R. T. (1997). Theoretical basis for the dubinin-radushkevitch (d-r) adsorption isotherm equation. Adsorption, 3(3):189–195.

IEA, editor (2008). Energy Technology Perspectives 2008- Scenarios & Strategies to 2050. International Energy Agency.

IEA, editor (2010). Carbon Capture and Storage Roadmap. International Energy Agency.

Irving, J. H. and Kirkwood, J. G. (1950). The statistical mechanical theory of transport processes. iv. the equations of hydrodynamics. The Journal of Chemical Physics, 18(6):817–829.

Ishii, R., Okazaki, S., Okada, I., Furusaka, M., Watanabe, N., Misawa, M., and Fukunaga, T. (1996). Density dependence of structure of supercritical carbon dioxide along an isotherm. J. Chem. Phys., 105(16):7011–7021.

Israelachvili, J. N. (1992). Intermolecular and Surface Forces, Second Edition: With Applications to Colloidal and Biological Systems (Colloid Science). Academic Press.

Jain, S. K., Gubbins, K. E., Pellenq, R. J.-M., and Pikunic, J. P. (2006a). Molecular modeling and adsorption properties of porous carbons. Carbon, 44(12):2445 – 2451.

Jain, S. K., Pellenq, R. J.-M., Pikunic, J. P., and Gubbins, K. E. (2006b). Molecular modeling of porous carbons using the hybrid reverse monte carlo method. Langmuir, 22(24):9942–9948.

Jain, S. K., Pikunic, J. P., Pellenq, R. J.-M., and Gubbins, K. E. (2005). Effects of activation on the structure and adsorption properties of a nanoporous carbon using molecular simulation. Adsorption, 11(0):355–360.

Jakubov, T. S. and Mainwaring, D. E. (2002). Adsorption-induced dimensional changes of solids. Phys. Chem. Chem. Phys., 4(22):5678–5682.

Jouanna, P. and Brocas, S. (2001). Approche statistique du tenseur des contraintes par le viriel généraliséstatistical approach of the stress tensor by the generalised virial. Comptes Rendus de l'Académie des Sciences - Series IIB - Mechanics, 329(11):775 – 782.

Kirkwood, J. G. and Buff, F. P. (1949). The statistical mechanical theory of surface tension. The Journal of Chemical Physics, 17(3):338–343.

Kondepudi, D. K. (2008). Introduction to modern thermodynamics. John Wiley and Sons.

Kowalczyk, P., Ciach, A., and Neimark, A. V. (2008). Adsorption-induced deformation of microporous carbons: Pore size distribution effect. Langmuir, 24(13):6603–6608.

Kramer, D. and Weissmüller, J. (2007). A note on surface stress and surface tension and their interrelation via shuttleworth's equation and the lippmann equation. Surface Science, 601(14):3042–3051.

Kurniawan, Y., Bhatia, S. K., and Rudolph, V. (2006). Simulation of binary mixture adsorption of methane and CO_2 at supercritical conditions in carbons. AIChE Journal, 52(3):957–967.

Laio, A. and Parrinello, M. (2002). Escaping free-energy minima. Proceedings of the National Academy of Sciences, 99(20):12562–12566.

Langmuir, I. (1916). The constitution and fundamental properties of solids and liquids. part 1. solids. Journal of the American Chemical Society, 38(11):2221–2295.

Laplace, P.-S. (1808). Supplément au dixième livre du traité de méchanique céleste sur l'action capillaire. Duprat.

Larsen, J. W. (2004). The effects of dissolved co2 on coal structure and properties. International Journal of Coal Geology, 57(1):63–70.

Larsen, J. W., Flowers, R. A., Hall, P. J., and Carlson, G. (1997). Structural rearrangement of strained coals. Energy & Fuels, 11(5):998–1002.

Leach, A. R. (2001). Molecular modelling : principles and applications. Prentice Hall.

Levine, J. R. (1996). Model study of the influence of matrix shrinkage on absolute permeability of coal bed reservoirs. Geological Society, London, Special Publications, 109(1):197–212.

Levy, J. H., Day, S. J., and Killingley, J. S. (1997). Methane capacities of bowen basin coals related to coal properties. Fuel, 76(9):813–819.

London, F. (1937). The general theory of molecular forces. Trans. Faraday Soc., 33:8b–26.

Lunacek, J. H. and Cannell, D. S. (1971). Long-range correlation length and isothermal compressibility of carbon dioxide near the critical point. Phys. Rev. Lett., 27(13):841–.

Malani, A., Ayappa, K. G., and Murad, S. (2009). Influence of hydrophilic surface specificity on the structural properties of confined water. The Journal of Physical Chemistry B, 113(42):13825–13839.

Martinez, R. E., Augustyniak, W. M., and Golovchenko, J. A. (1990). Direct measurement of crystal surface stress. Phys. Rev. Lett., 64(9):1035–.

Massarotto, P., Golding, S., Bae, J.-S., Iyer, R., and Rudolph, V. (2010). Changes in reservoir properties from injection of supercritical co2 into coal seams – a laboratory study. International Journal of Coal Geology, 82(3-4):269–279.

Mazumder, S. and Wolf, K. H. (2008). Differential swelling and permeability change of coal in response to co2 injection for ecbm. International Journal of Coal Geology, 74(2):123 – 138.

Mazzotti, M., Pini, R., and Storti, G. (2009). Enhanced coalbed methane recovery. The Journal of Supercritical Fluids, 47(3):619–627.

McKinsey&Company, editor (2010). Impact of the financial crisis on carbon economics: Version 2.1 of the global greenhouse gas abatement cost curve. McKinsey & Company.

Metropolis, N., Rosenbluth, A. W., Rosenbluth, M. N., Teller, A. H., and Teller, E. (1953). Equation of state calculations by fast computing machines. J. Chem. Phys., 21(6):1087–1092.

Metz, B., Davidson, O., de Coninck, H., Loos, M., and Meyer, L. (2005). Carbon Dioxide Capture and Storage. Cambridge University Press, UK. pp 431.

Mirzaeian, M. and Hall, P. J. (2006). The interactions of coal with co2 and its effects on coal structure. Energy & Fuels, 20(5):2022–2027.

Mushrif, S. H. and Rey, A. D. (2009). An integrated model for adsorption-induced strain in microporous solids. Chemical Engineering Science, 64(22):4744–4753.

Neimark, A. V., Coudert, F.-X., Triguero, C., Boutin, A., Fuchs, A. H., Beurroies, I., and Denoyel, R. (2011). Structural transitions in mil-53 (cr): View from outside and inside. Langmuir, 27(8):4734–4741.

Nguyen, T. X., Bhatia, S. K., and Nicholson, D. (2005). Prediction of high-pressure adsorption equilibrium of supercritical gases using density functional theory. Langmuir, 21(7):3187–3197.

Nguyen, T. X., Cohaut, N., Bae, J.-S., and Bhatia, S. K. (2008). New method for atomistic modeling of the microstructure of activated carbons using hybrid reverse monte carlo simulation. Langmuir, 24(15):7912–7922.

Nishikawa, K., Tanaka, I., and Amemiya, Y. (1996). Small-angle x-ray scattering study of supercritical carbon dioxide. The Journal of Physical Chemistry, 100(1):418–421.

OECD, editor (2008). Measuring Material Flows and Ressource Productivity - Synthesis report. Organisation for Economic Co-operation and Development.

Ottiger, S., Pini, R., Storti, G., and Mazzotti, M. (2008). Competitive adsorption equilibria of co2 and ch4 on a dry coal. Adsorption, 14(4):539–556.

Ottiger, S., Pini, R., Storti, G., Mazzotti, M., Bencini, R., Quattrocchi, F., Sardu, G., and Deriu, G. (2006). Adsorption of pure carbon dioxide and methane on dry coal from the sulcis coal province (sw sardinia, italy). Environ. Prog., 25(4):355–364.

Ozdemir, E., Morsi, B. I., and Schroeder, K. (2003). Importance of volume effects to adsorption isotherms of carbon dioxide on coals. Langmuir, 19(23):9764–9773.

Ozdemir, E., Morsi, B. I., and Schroeder, K. (2004). Co2 adsorption capacity of argonne premium coals. Fuel, 83(7-8):1085–1094.

Özgen Karacan, C. (2003). Heterogeneous sorption and swelling in a confined and stressed coal during co2 injection. Energy & Fuels, 17(6):1595–1608.

Pan, Z. and Connell, L. D. (2007). A theoretical model for gas adsorption-induced coal swelling. International Journal of Coal Geology, 69(4):243 – 252.

Pauli, W. (1925). Über den zusammenhang des abschlusses der elektronengruppen im atom mit der komplexstruktur der spektren. Zeitschrift für Physik A Hadrons and Nuclei, 31(1):765–783.

Pekot, L. J. and Reeves, S. R. (2002). Modeling coal matrix shrinkage and differential swelling with co_2 injection for enhanced coalbed methane recovery and carbon sequestration applications. Topical report, U.S. Department of Energy.

Pellenq, R. J. M. and Levitz, P. E. (2001). Adsorption/condensation of xenon in a disordered silica glass having a mixed (micro and meso) porosity. Molecular Simulation, 27(5):353–370.

Perrin, J. (1913). Les atomes. Félix Alcan.

Pikunic, J., Clinard, C., Cohaut, N., Gubbins, K. E., Guet, J.-M., Pellenq, R. J.-M., Rannou, I., and Rouzaud, J.-N. (2003). Structural modeling of porous carbons. constrained reverse monte carlo method. Langmuir, 19(20):8565–8582.

Planck, M. (1901). Ueber das gesetz der energieverteilung im normalspectrum. Ann. Phys., 309(3):553–563.

Pruess, K. (2009). Formation dry-out from co2 injection into saline aquifers: 2. analytical model for salt precipitation. Water Resources Research, 45(3):W03403–.

Pruess, K. and Müller, N. (2009). Formation dry-out from co2 injection into saline aquifers: 1. effects of solids precipitation and their mitigation. Water Resources Research, 45(3):W03402–.

Radovic, L. R., Menon, V. C., Leon Y Leon, C. A., Kyotani, T., Danner, R. P., Anderson, S., and Hatcher, P. G. (1997). On the porous structure of coals: Evidence for an interconnected but constricted micropore system and implications for coalbed methane recovery. Adsorption, 3(3):221–232.

Rappe, A. K. and Goddard, W. A. (1991). Charge equilibration for molecular dynamics simulations. The Journal of Physical Chemistry, 95(8):3358–3363.

Ravikovitch, P. I. and Neimark, A. V. (2006). Density functional theory model of adsorption deformation. Langmuir, 22(26):10864–10868.

Reeves, S. (2004). The coal-seq project: Key results from field, laboratory, and modeling studies. In 7th International Conference on Greenhouse Gas Control Technologies (GHGT-7).

Reeves, S., Taillefert, A., Pekot, L., and Clarkson, C. (2003). The allison unit co_2-ecbm pilot: A reservoir modeling study. Topical report, U.S. Department of Energy.

Reichenauer, G. and Scherer, G. W. (2000). Nitrogen adsorption in compliant materials. Journal of Non-Crystalline Solids, 277(2-3):162–172.

Rubinstein, R. Y. and Kroese, D. P. (2008). Simulation and the Monte Carlo method. Wiley-Interscience, 2 edition.

Ruthven, D. M. (1984). Principles of adsorption and adsorption processes. Wiley-Interscience.

Scherer, G. W. (1986). Dilatation of porous glass. Journal of the American Ceramic Society, 69(6):473–480.

Schrödinger, E. (1926). An undulatory theory of the mechanics of atoms and molecules. Phys. Rev., 28(6):1049–.

Seibel, B. A. and Walsh, P. J. (2001). Potential impacts of co2 injection on deep-sea biota. Science, 294(5541):319–320.

Senel, A. G., Guruz, A. G., Yucel, H., Kandas, A. W., and Sarofim, A. F. (2001). Characterization of pore structure of turkish coals. Energy & Fuels, 15(2):331–338.

Shi, J.-Q. and Durucan, S. (2004). A numerical simulation study of the allison unit co2-ecbm pilot: the effect of matrix shrinkage and swelling on ecbm production and co2 injectivity. In Proceedings of the 7th International Conference on Greenhouse Gas Control Technologies (GHGT-7), pages 431–442.

Shuttleworth, R. (1950). The surface tension of solids. Proceedings of the Physical Society. Section A, 63(5):444.

Sing, K. S. W., Everett, D. H., Haul, R. A. W., Moscou, L., Pierotti, R. A., Rouquerol, J., and T., S. (1985). Reporting physisorption data for gas/solid systems, with special reference to the determination of surface area and porosity (recommendations 1984). Pure and applied chemistry, 57(4):603–619.

Span, R. and Wagner, W. (2003a). Equations of state for technical applications. ii. results for nonpolar fluids. International Journal of Thermophysics, 24(1):41–109.

Span, R. and Wagner, W. (2003b). Equations of state for technical applications. iii. results for polar fluids. International Journal of Thermophysics, 24(1):111–162.

St. George, J. D. and Barakat, M. A. (2001). The change in effective stress associated with shrinkage from gas desorption in coal. International Journal of Coal Geology, 45(2-3):105–113.

Steele, W. A. (1973). The physical interaction of gases with crystalline solids: I. gas-solid energies and properties of isolated adsorbed atoms. Surface Science, 36(1):317 – 352.

Stuart, S. J., Tutein, A. B., and Harrison, J. A. (2000). A reactive potential for hydrocarbons with intermolecular interactions. J. Chem. Phys., 112(14):6472–6486.

Takagi, H., Maruyama, K., Yoshizawa, N., Yamada, Y., and Sato, Y. (2004). Xrd analysis of carbon stacking structure in coal during heat treatment. Fuel, 83(17-18):2427–2433.

Taraba, B. (2011). Flow calorimetric insight to competitive sorption of carbon dioxide and methane on coal. Thermochimica Acta, In Press, Corrected Proof:–.

Tenney, C. and Lastoskie, C. (2006). Molecular simulation of carbon dioxide adsorption in chemically and structurally heterogeneous porous carbons. Environmental Progress, 25(4):343–354.

Tolman, R. C. (1949). The superficial density of matter at a liquid-vapor boundary. The Journal of Chemical Physics, 17(2):118–127.

Tsuzuki, S., Uchimaru, T., and Tanabe, K. (1998). A new ab initio based model potential for methane. Chemical Physics Letters, 287(3-4):327 – 332.

Ustinov, E. and Do, D. (2006). Effect of adsorption deformation on thermodynamic characteristics of a fluid in slit pores at sub-critical conditions. Carbon, 44(13):2652–2663.

Vassilev, S. V., Kitano, K., and Vassileva, C. G. (1996). Some relationships between coal rank and chemical and mineral composition. Fuel, 75(13):1537 – 1542.

Vassilev, S. V., Kitano, K., and Vassileva, C. G. (1997). Relations between ash yield and chemical and mineral composition of coals. Fuel, 76(1):3–8.

Vassilev, S. V. and Vassileva, C. G. (1996). Occurrence, abundance and origin of minerals in coals and coal ashes. Fuel Processing Technology, 48(2):85–106.

Verwey, E. J. W. and Overbeek, J. T. G. (1948). Theory of the stability of lyophobic colloids. Elsevier.

Vishnyakov, A., Piotrovskaya, E. M., and Brodskaya, E. N. (1998). Capillary condensation and melting/freezing transitions for methane in slit coal pores. Adsorption, 4:207.

Vrabec, J., Stoll, J., and Hasse, H. (2001). A set of molecular models for symmetric quadrupolar fluids. The Journal of Physical Chemistry B, 105(48):12126–12133.

Walton, J. P. R. B., Tildesley, D. J., Rowlinson, J. S., and Henderson, J. R. (1983). The pressure tensor at the planar surface of a liquid. Molecular Physics: An International Journal at the Interface Between Chemistry and Physics, 48(6):1357–1368.

Wang, G., Massarotto, P., and Rudolph, V. (2009). An improved permeability model of coal for coalbed methane recovery and co2 geosequestration. International Journal of Coal Geology, 77(1-2):127–136.

Washburn, E. W. (1926-1933). International critical tables of numerical data, physics, chemistry and technology. Published for the National Research Council by McGraw-Hill.

WEC, editor (2010). 2010 Survey of Energy Resources. World Energy Council.

Wheeler, J. A. and Zurek, W. H. (1983). Quantum theory and measurement. Princeton University Press.

White, C. M., Smith, D. H., Jones, K. L., Goodman, A. L., Jikich, S. A., LaCount, R. B., DuBose, S. B., Ozdemir, E., Morsi, B. I., and Schroeder, K. T. (2005). Sequestration of carbon dioxide in coal with enhanced coalbed methane recovery a review. Energy & Fuels, 19(3):659–724.

Widom, B. (1963). Some topics in the theory of fluids. J. Chem. Phys., 39(11):2808–2812.

Yang, K., Lu, X., Lin, Y., and Neimark, A. V. (2010). Deformation of coal induced by methane adsorption at geological conditions. Energy & Fuels, 24(11):5955–5964.

Young, T. (1805). An essay on the cohesion of fluids. Philosophical Transactions of the Royal Society of London, 95:65–87.

Zhang, Y., Yang, J., and Yu, Y.-X. (2005). Dielectric constant and density dependence of the structure of supercritical carbon dioxide using a new modified empirical potential model: A monte carlo simulation study. The Journal of Physical Chemistry B, 109(27):13375–13382.

Zhou, M. (2003). A new look at the atomic level virial stress: on continuum-molecular system equivalence. Proceedings of the Royal Society of London. Series A: Mathematical, Physical and Engineering Sciences, 459(2037):2347–2392.

Poromechanics and adsorption: Application to coal swelling during carbon geological storage

The geological storage of carbon in coal seams is a transitory solution to mitigate climate change. The feasibility of this type of storage at an affordable cost is still uncertain, in particular because the rate of injection of carbon dioxide in coal seams is low. Pilot projects have shown that the permeability of the reservoir decreases during injection, as a consequence of the swelling of the coal matrix induced by the preferential adsorption of carbon dioxide over the methane in place. This PhD thesis is dedicated to the study of this swelling. A first theoretical work consisted in extending the constitutive equations of classical poromechanics to cases for which adsorption on surfaces or in micropores becomes significant. We showed that the poromechanical behavior of the medium can only be determined if the dependence of adsorption on the strain of the porous medium is known. The coupling between adsorption and strain is little studied in the literature and is difficult to measure experimentally. In this work, we used molecular simulations which make it convenient to control independently the bulk pressure of the adsorbed fluid and the strain of the porous medium. By performing molecular simulations of adsorption in model one-dimensional systems, we validated the derived constitutive equations. We also showed that adsorption can depend on the strain of the medium in a complex manner and depends significantly on the structure of the micropores. Based on the simulation results on a realistic molecular model of coal, we concluded that the swelling of coal in presence of fluid can be explained by adsorption in micropores but not by adsorption in mesopores. We studied numerically the coupling between adsorption and strain in coal. The swelling estimated by combining the simulated adsorption isotherms with the derived poromechanical equations compared well with data obtained experimentally. We also simulated adsorption of mixtures of carbon dioxide and methane in coal at temperatures and pressures representative of the underground conditions. The results of those simulations were used to estimate the differential swelling during the injection of carbon dioxide in coal seams at various depths.
Keywords: poromechanics, adsorption, coal swelling, molecular simulation, ECBM, CO_2 storage.

Poromécanique et adsorption : Application au gonflement du charbon lors du stockage géologique du carbone

Le stockage géologique du carbone dans les veines de charbon est une solution transitoire pour lutter contre le réchauffement climatique. La faisabilité de ce stockage à un coût abordable reste incertaine, en particulier parce que l'injection de dioxyde de carbone dans les veines de charbon est lente. Les projets pilotes ont montré que la perméabilité du réservoir diminue lors de l'injection, suite au gonflement du charbon induit par l'adsorption préférentielle du dioxyde de carbone par rapport au méthane présent naturellement. Ce mémoire de thèse est consacré à l'étude de ce gonflement. Un premier travail théorique a consisté à étendre les équations constitutives de poromécanique classique dans les cas où l'adsorption sur des surfaces ou dans des micropores devient significative. Nous avons montré que le comportement poromécanique du solide ne peut être compris que si la dépendance de l'adsorption en fonction de la déformation du milieu poreux est connue. Le couplage entre adsorption et déformation est peu étudié dans la littérature et difficile à mesurer expérimentalement. Dans ce travail, nous avons utilisé la simulation moléculaire qui permet facilement de contrôler indépendamment la pression du fluide adsorbé et la déformation du milieu poreux. À l'aide de simulations moléculaires d'adsorption dans des systèmes modèles unidimensionnels, nous avons validé les nouvelles équations constitutives. Nous avons montré également que l'adsorption peut dépendre de la déformation de façon complexe et qu'elle est très sensible à la structure des micropores. Les résultats de simulations moléculaires d'adsorption dans un modèle moléculaire réaliste de la matrice organique du charbon nous ont permis de montrer que le gonflement du charbon en présence de fluide peut être expliqué par l'adsorption dans les micropores, mais pas dans les mésopores. Nous avons étudié numériquement le couplage entre adsorption et déformation dans le charbon. Le gonflement estimé en associant les simulations moléculaires d'adsorption aux nouvelles équations constitutives de poromécanique est en bon accord avec les mesures expérimentales. De même, nous avons simulé l'adsorption de mélanges de dioxyde de carbone et de méthane dans le charbon à des températures et pressions représentatives des conditions souterraines. Le résultat de ces simulations a permis d'estimer le gonflement différentiel durant l'injection de carbone pour des veines de charbon à différentes profondeurs.
Mots clefs: poromécanique, adsorption, gonflement du charbon, simulation moléculaire, ECBM, stockage de CO_2.